



Combined multi-scale modelling and experimentation for lignin-rich biomass pyrolysis

Andrés Gabriel Chico Proaño

A dissertation submitted in partial fulfillment

of the requirements for the degree of

Doctor of Philosophy

of

University College London.

Department of Chemical Engineering

University College London

August 3, 2023

I, Andrés Gabriel Chico Proaño, confirm that the work presented in this thesis is my own. Where information has been derived from other sources, I confirm that this has been indicated in the work.

”Reason is a torch that lights every spiritual being, giving color and light to the operations of the soul.”

-Eugenio Espejo

”Reason is immortal, all else mortal.”

-Phytagoras

Impact statement

Over the last decades, major efforts have been directed to change our energy dependence on fossil fuels. Such dependence goes beyond energy generation as local industries rely on oil-derived platform chemicals for their operation. Agro-industrial wastes represent an opportunity to bring together the needs for renewable energy, green chemicals and waste management. Biomass pyrolysis can address both energy generation and chemicals production. Pyrolysis usually considers cellulose-rich woody materials as feedstock. Nonetheless, there are many communities and local industries, specially in the tropics, where lignin-rich biomass is produced as waste. Such wastes are usually related to oil seeds, coffee and food crops and they do not have a current use.

Process industries and industries with agro-industrial wastes. In this work, a mechanistic model for capturing biomass pyrolysis behaviour was developed. The model predicts temperatures and product distribution in thermally-thick particles relatively easy, in comparison with other complex and time consuming modelling approaches like computational fluid dynamics (CFD). Having an easier to model and easier to manipulate pyrolysis process, in terms of available data and tools for simulation, will support the development of feasibility and techno-economical analysis, which eventually will lead to more pyrolysis projects being proposed. A model that is easier and quicker to solve also allows to include early-stage economic, environmental and energy efficiency outcomes that biomass producers, local governments or decision makers require.

Small, medium and big size companies that currently have high-lignin residues. The physical, chemical, thermal and pyrolysis-related characteristics of palm kernel shells, provide valuable information of non woody materials. This information can serve as input for small to big oil seeds extracting companies for using the wastes they generate. From

the waste-to-value perspective, this work provides some inputs that could serve to decision makers to evaluate alternatives for using such wastes. These inputs include palm kernel shells properties but also information for simulations and processing in auger reactors. For a company to have the opportunity to assess the type of products that might arise from their residues is not only a solution for managing wastes, but an opportunity to increase the lines of business, looking up to alternatives that were not part of their offer.

Communities located in rural areas with biomass resources. Rural communities in tropical regions rely on agricultural activities for their incomes. Usually, their location, prevents such communities of having regular services such as electricity. The developed model and multi-scale approach could be used for determined potential energy generation from biomass in rural communities as a decentralized generation alternative [1].

Catalytic processes and new materials. Given the range of different products that can arise from biomass pyrolysis, the area of functional materials might benefit from having information regarding the components of high-lignin content biomass, as well as data related to char yields and properties from biomass pyrolysis. Biochar is a material that is currently being used as catalyst, energy storage conductivity modifier and as pollutants removal [2]. Therefore, having a clear idea of the amount and properties of char that can be produced from a given biomass feedstock can support the development of these materials.

Similarly, the academia can access to experimental and simulation data generated through this work, for comparison purposes or to apply different methods for comparing new biomass processing technologies.

Abstract

Biomass pyrolysis is a key alternative for supporting a shift towards more environmental-friendly energy generation and chemicals production. However, pyrolysis' complexity and the missing information for high-lignin biomass, require robust and easy-to-implement modelling approaches, but also demands information regarding lignin-rich biomass properties for supporting future process design and large-scale operations. This work initially presents a particle model, based on energy, mass and momentum conservation, which includes a boundary immobilisation technique to describe thermally-thick biomass pyrolysis for different combinations of moisture and heating temperatures. Temperature gradients and pyrolysis product distribution are determined by solving the resulting model with gPROMS ModelBuilder®. The easy-to-solve model allows to include preliminary economic, environmental and energy efficiency indicators. The variety of kinetic models, and the lack of a specialized one in lignin-rich biomass made it necessary to select one, palm kernel shells (PKS), to study its properties and kinetic model. Finally, this work explores an approach to couple the particle model, with the characterization of PKS, and of a pilot scale auger reactor, to have some insight regarding the required steps for a multi-scale pyrolysis strategy.

The results from the particle model suggest that it can predict temperature and composition within a thermally-thick particle. Furthermore, the PKS experimental analysis performed with the PKS show that lignin-rich biomass behaves differently than conventional cellulose-rich biomass during pyrolysis and it highlights the need of having experimental data for this type of biomass. Finally, pyrolysis shows the difficulties regarding the description of granular flow and its coupling with a particle model and experimental kinetics to describe an auger reactor. In conclusion, multi-scale biomass pyrolysis is a complex and information demanding process. However, if the required knowledge is available, it is possible to describe pyrolysis effectively so as to support future process design and optimization.

Acknowledgements

This thesis was developed at the Department of Chemical Engineering, UCL, under the supervision of Prof. Eric Fraga, Dr. George Manos and Prof. Lazaros Papageorgiou. I would like to express my gratitude to my supervisors, in particular Professor Eric Fraga, who kindly received me in his research group and supported me in the development of this project. Similarly, my sincere thanks to Dr. George Manos and Professor Lazaros Papageorgiou for the support and thoughtful advice. I would like to thank Instituto de Investigación Geológico Energético (IIGE) and its staff, for welcoming in my research stay.

I would like to acknowledge the support of my sponsors. I deeply appreciate the support from Escuela Politécnica Nacional (EPN), without them it would have been impossible to continue with my studies. I also want to acknowledge the Ecuadorian people through the Secretaría de Educación Superior, Ciencia, Tecnología e Innovación (Senescyt) and their scholarship program, which allowed me to study at the highest level possible.

Many of my friends and colleagues deserve credit for making this experience something unforgettable. Thank you Carlos, Isabel, Daniela, Giorgios, Alexandra, Marco, Harry, Diana, Jay, Yodaly, Zuzanna, Mohammad, Sergio and Erika. Similarly, thank you all at the PPSE and UCL, Ricky, Fabio, Panos, Alba, Pedro, Mariam, Olie, Arun, Costas, Ioannis, Katerina, Andrea, Alberto, Philip, Conor, Sarah, Aitana and many others.

Lastly but most importantly, I would like to thank my family, who have given me the strength and peace to continue in moments of doubt to finish this endeavor. No words will suffice to express how lucky and grateful I am to have you all in my life. This work is for my brothers Sebas and Faby, my nephew Maty, my aunts Paty(†) and Esperanza(†), María(†); but specially for my father Fabian and my loving mother Yolanda.

Contents

1	Introduction	24
1.1	Biomass pyrolysis from a particle perspective	25
1.2	Biomass pyrolysis from the molecular point of view	26
1.2.1	Biomass composition	27
1.2.2	Interaction between biomass components in pyrolysis	28
1.2.3	Kinetic models for describing biomass pyrolysis	28
1.2.4	Residual lignocellulosic biomass	30
1.3	Biomass pyrolysis	31
1.4	Relevant parameters that influence pyrolysis operations	32
1.4.1	Operating temperature and heating rate	32
1.4.2	Moisture content and particle size	32
1.5	Pyrolysis from a macro perspective and the multi-scale challenges in biomass pyrolysis	33
1.5.1	Pyrolysis energy intensive nature	34
1.5.2	Modelling approaches that target multi-scale pyrolysis	34
1.5.3	Supply chain	35
1.6	Motivation and objectives of the present work	36
1.6.1	Work to be done at a particle scale	36
1.6.2	Remaining work at a molecular scale	37
1.6.3	Work at a reactor scale	37
1.7	Modelling and experimental approach	38
1.8	Thesis objectives	39
1.9	Outline of the thesis	39
1.10	Computational resources	40

	<i>Contents</i>	9
2 Literature review		41
2.1 Biomass	41	
2.1.1 Lignocellulosic biomass components	41	
2.2 Biomass pyrolysis	43	
2.2.1 Thermal degradation of biomass main components in pyrolysis	43	
2.2.2 Biomass pyrolysis kinetics	45	
2.2.3 Review of relevant biomass pyrolysis kinetic models	45	
2.2.4 Lumped models for biomass pyrolysis based on thermal decomposition analysis	46	
2.2.5 Detailed reaction schemes for biomass pyrolysis	50	
2.2.6 Applications of pyrolysis products	53	
2.2.7 Energy efficiency in biomass pyrolysis	55	
2.3 Experimental determination of biomass pyrolysis kinetics	56	
2.4 The multi-scale nature of biomass pyrolysis	57	
2.4.1 Biomass pyrolysis at a particle scale	57	
2.4.2 Reactor scale modelling strategies for pyrolysis	59	
2.5 Concluding remarks	61	
3 Single thermally-thick biomass particle pyrolysis model		62
3.1 Introduction	62	
3.2 Model description	64	
3.2.1 Preliminary analysis	64	
3.2.2 Kinetic models used in this work	67	
3.2.3 Moisture	69	
3.2.4 Required physical properties	71	
3.2.5 Estimation of thermophysical properties used in the model	71	
3.2.6 Particle model development	71	
3.2.7 Initial and boundary conditions	78	
3.2.8 Numerical solution and validation	79	
3.3 Results and discussion	82	
3.3.1 Temperature and product distribution from the particle model	82	
3.3.2 Applications of the developed particle model	86	
3.3.3 Thermal efficiency of the pyrolysis process	87	

<i>Contents</i>	10
3.4 Concluding remarks	93
4 Characterization and pyrolysis kinetic modeling of lignin-rich biomass	96
4.1 Introduction	96
4.2 Materials and experimental methods	98
4.2.1 Materials	98
4.2.2 Experimental methods	98
4.2.3 Determination of physical properties of palm kernel shells	99
4.2.4 Chemical characterization of PKS	105
4.2.5 Energy content analysis	110
4.2.6 Thermal analysis and kinetic model determination	114
4.3 Results	117
4.3.1 Physical, chemical and thermal characterization: general findings .	117
4.3.2 PKS size and density	120
4.3.3 PKS chemical composition and its relationship with the energy con- tent	121
4.3.4 Crystallographic structure	126
4.3.5 Functional groups and FTIR analysis	127
4.3.6 Microscopy	130
4.4 Thermal analysis and kinetic model determination	131
4.4.1 Thermal analysis and behaviour throughout pyrolysis	132
4.4.2 Kinetic model for the pyrolysis of palm kernel shells	138
4.5 Concluding remarks	145
5 Pyrolysis of coarse biomass in a single screw auger reactor	147
5.1 Introduction	147
5.1.1 Granular flow in auger reactors	148
5.2 Description of the feed material and the reaction system	149
5.2.1 Feed material	149
5.2.2 Description of the reactor system	150
5.3 Determination of residence time distributions with an empirical mathemat- ical model	152
5.3.1 Data collection	152

5.4	Determination of residence times distributions from a DEM approach	154
5.4.1	Materials and methods	154
5.4.2	PKS characterization	154
5.4.3	Discrete element model approach	157
5.4.4	DEM calibration: procedure and experiments	159
5.4.5	Residence time using a DEM approach	162
5.5	Results	164
5.5.1	Determination of residence time distributions with an empirical mathematical model	164
5.5.2	Determination of residence time distributions using a DEM approach	166
5.6	Multi-scale modelling approach for describing an auger reactor	176
5.6.1	Issues arising from using a different kinetic model	176
5.6.2	Initial and boundary conditions	182
5.6.3	Numerical solution	183
5.6.4	Preliminary results	183
5.7	Concluding remarks	184
6	Conclusions and future research	186
6.1	Single thermally-thick biomass particle pyrolysis model	187
6.2	Characterization and pyrolysis kinetic modelling of lignin-rich biomass . .	188
6.3	Pyrolysis of coarse biomass in a single screw auger reactor	188
6.4	Summary of the most relevant contributions from this work	189
6.5	Future research	190
6.5.1	Extending the applicability of the developed particle model	190
6.5.2	To associate the characteristics of more types of lignin-rich biomass undergoing pyrolysis to establish a general behaviour for lignin-rich biomass.	190
6.5.3	Further work at a reactor level and multi-scale strategy	191
6.5.4	Incorporation of the developed approach into the context of biorefineries	192
Appendices		195

A Single thermally-thick biomass particle	195
A.1 Determination of temperature ranges for applying the ideal gas equation of state for the considered components in the model	195
A.1.1 Kinetic models used for describing pyrolysis	195
A.2 Detailed reaction scheme, RAC scheme, with the complete the reactions and compounds involved in pyrolysis.	199
A.3 Estimation of specific heat at constant pressure for developing the particle model	204
B Characterization and pyrolysis kinetic modeling of lignin-rich biomass	208
B.1 Materials	208
B.1.1 Sample preparation	208
B.1.2 PKS bulk and apparent density	209
B.1.3 Particle size distribution	212
B.1.4 Proximal analysis	215
B.1.5 X-Ray Diffraction characterization	216
B.1.6 Microscopy	218
B.1.7 Extractives determination and quantification	218
B.1.8 Elemental analysis determination	225
B.1.9 Energy content high heating value determination	228
B.2 Thermal analysis and kinetic model determination	229
B.2.1 Thermogravimetric analysis (TGA)	229
C Pyrolysis of coarse biomass in a single screw auger reactor	232
C.1 Determination of residence time distributions using a DEM approach	232
C.1.1 Convergence analysis for interaction properties in PKS	232
C.1.2 Density adjustment	232
C.1.3 Simulations for determining particle-particle sliding and rolling friction coefficients.	232
Bibliography	238

List of Figures

1.1	Representation of a reacting biomass particle undergoing pyrolysis.	26
1.2	Different types of biomass and their composition, modified from [3].	27
1.3	Multiscale approach for modelling complex processes from particle to reactors and applications in process design [4].	34
1.4	Number of research performed with the different types of pyrolysis reactors [5].	37
2.1	Main components of lignocellulosic biomass, modified from [6].	42
2.2	Structure of cellulose linear polymeric chains, modified from [7]	43
2.3	Thermal decomposition of cellulose, hemicellulose and lignin during a differential scanning calorimetry (DSC) analysis under pyrolysis conditions. Required enthalpy as a function of temperature, modified from [8].	44
2.4	Cellulose thermal decomposition under pyrolysis conditions evidenced as: a) mass loss (m) with temperature during thermogravimetric analysis (TGA) within a helium atmosphere [9], and b) differential thermogravimetric profiles for different heating rates [10].	46
2.5	Cellulose pyrolysis reaction scheme with simple first order reactions and lumped products. Modified from [11].	47
2.6	Lumped cellulose pyrolysis reaction scheme with an intermediate active cellulose stage. Modified from [12, 13].	47
2.7	Approach for taking a rotary kiln a) as a reference for modelling an auger reactor b)	60
3.1	Representation of a shrinking biomass particle undergoing pyrolysis when a heat flux Q_{in} is supplied.	65

3.2	Schematic representation of the followed steps for developing the pyrolysis particle model.	65
3.3	Biot numbers and corresponding Py^I numbers for different particle sizes and operating conditions. Conduction-limited pyrolysis lies in the shaded area of the plot	67
3.4	Schematic of kinetic model 1 describing a lumped pyrolysis reaction scheme.	68
3.5	Schematic of kinetic model 2 describing pyrolysis for biomass components.	69
3.6	a) Temperature gradient, from the core (0.0) to the border (1.0), for 5 mm diameter particles undergoing fast pyrolysis with $T_0=250^\circ\text{C}$ and after 5 s. b) Predicted particle's core temperature for a 5 mm diameter particle, 9 wt. % initial moisture and 60 kW m^{-2} of incident heat flux; and corresponding experiments from literature [14].	83
3.7	Product distribution at different temperatures using a cellulose particle model with a lumped kinetic model.	83
3.8	Product distribution for the gaseous phase using a cellulose particle model with detailed kinetics model.	84
3.9	Levoglucosan yields from the developed model and from experiments [15]. Pyrolysis for cellulose particles with $r = 9 \cdot 10^{-3}\text{m}$, $T_0 = 250^\circ\text{C}$ and $T_\infty = 800^\circ\text{C}$. LVG yields obtained as average from different charring degrees: 0.025, 0.030 and 0.035.	84
3.10	Mass fraction of LVG at different charring degrees (X_{cell}) for slow pyrolysis ($X_{\text{cell}} = 0.100$), intermediate pyrolysis ($X_{\text{cell}} = 0.063$) and fast pyrolysis ($X_{\text{cell}} = 0.025$).	85
3.11	Energy consumption for different heating alternatives (a). Product distribution represented as mass fraction for different heating alternatives considering a lumped model for cellulose as feedstock (b).	87
3.12	Diagram of the energy balance involved in the calculation of thermal efficiencies in the pyrolysis process. Adapted from Kodera & Kaiho (2016). . .	87
3.13	Outcomes for normalized Y_{energy} , η_{th} , EP and $-ENV$ for different conditions of initial biomass temperature (T_0), external temperature (T_∞) and percentage of moisture content for pyrolysis, described by lumped model.	92

3.14 Differences in the resulting outcomes when the normalized economic potential (<i>EP</i>) is maximized and the normalized environmental outcome (- <i>ENV</i>) is minimized, considering a lumped model and varying T_{inlet} , T_{∞} and biomass moisture content.	94
4.1 a) Density kit scheme using distilled water and b) assembled in the laboratory scale. Scheme modified from [16].	101
4.2 PKS sample preparation and analysis with a precision cutter a), polisher b), microscope c), using PKS cross sectional samples of 1.00 mm thick d) and e).105	105
4.3 Soxhlet extraction unit with its components for extractives analysis a), extraction process after 4 hours b) and after 24 hours of extraction c).	107
4.4 Soxhlet extraction unit with its components for extractives analysis a), extraction process after 4 hours b) and after 24 hours of extraction c).	108
4.5 Elemental analyzer a) and micro balance b) used in the determination of the elemental composition in PKS.	110
4.6 JASCO FT/IR 4600 series infrared spectrometer used for analyzing PKS and the synthetic mixture.	111
4.7 Calorimeter used for the determination of HHV in biomass, manual press and crucible with PKS pellet.	112
4.8 TGA equipment in operation a), and before the operation with the sample-containing platinum crucible.	114
4.9 Cumulative share for different particle sizes for 3 different PKS samples. . .	121
4.10 Van Krevelen diagram for the PKS from this work and for other types of biomass from literature [17, 18, 19]; with a lignin-rich biomass zone identified and coloured (> 43.9 wt.% of lignin).	123
4.11 Higher heating values determined for PKS and retrieved from literature [17, 18, 19].	123
4.12 Higher heating values for dry lignin-rich for different carbon contents. . .	125
4.13 XRD analysis for a) palm kernel shells and b) the synthetic mixture. . . .	127
4.14 FTIR spectra of PKS.	129
4.15 FTIR spectra of the synthetic mixture resembling PKS composition. . . .	130
4.16 Section of the $1400\text{-}400\text{ cm}^{-1}$ of the FTIR spectra of PKS.	131

4.17 Morphology of the PKS in the polarized light microscope, zone 3 with 20X magnification and without Toluidine (n/T)	132
4.18 Morphology of the PKS in the polarized light microscope, zone 3 with 50X magnification and without Toluidine (n/T)	133
4.19 Potential location of lignin and morphology of the PKS in the polarized light microscope, zone 2 with 50X magnification and with Toluidine blue as dyeing agent (w/T)	133
4.20 Average remaining mass determined through a TG analysis of palm kernel shells undergoing pyrolysis at different heating rates	134
4.21 Comparison of average remaining mass from a TGA for palm kernel shells, undergoing pyrolysis at 5, 20, 35 and 50°C.	135
4.22 Remaining mass at the end of pyrolysis with palm kernel shells and the synthetic mixture, for heating rates of 5, 20, 35 and 50°C presented as an interval plot considering 95% CI for the mean. Individual standard deviations are used to calculate the intervals.	135
4.23 Thermal analysis of PKS pyrolysis at different heating rates considering TGA.	136
4.24 Differential thermal analysis of PKS pyrolysis at different heating rates.	137
4.25 Thermal analysis of the synthetic mixture under pyrolysis at different heating rates considering TGA.	138
4.26 Differential thermal analysis of the synthetic mixture under pyrolysis at different heating rates.	139
4.27 Mass loss rate for different samples undergoing pyrolysis at $50^{\circ}\text{min}^{-1}$ obtained from TGA.	139
4.28 Linear regression for different conversions resulting from the TGA PKS analysis using the KAS method	140
4.29 Linear regression for different conversions resulting from the TGA PKS analysis using the FWO method.	142
4.30 Tendency of the activation energy E_a for different values of conversion α calculated using the FWO and KAS methods	143
5.1 Cumulative share for different particle sizes for 3 different PKS samples. . .	150
5.2 Configuration of the auger reactor used for PKS pyrolysis.	151
5.3 Plan of the auger reactor and the internal screw.	152

5.4	Tilting surface and configuration for measuring the coefficient of friction.	156
5.5	Device for evaluating particle's discharge.	161
5.6	Evaluation of discharge for PKS particles.	161
5.7	Mass flow rate in steady state for 25%, 50%, 75% and 100% of the maximum rotational velocity. Average of three measurements.	165
5.8	Negative step-change effect over the mass flow rate of the pyrolysis screw operating at different percentages of the maximum rotational velocity. Average for three measurements.	166
5.9	Comparison between experimental setup and DAE simulation for determining friction coefficients.	168
5.10	Part of the results considering front and back repose angles using a DEM simulation in LIGGGTHS. Sliding coefficient-Rolling coefficient. F=front, B=back, L=left, R=right.	168
5.11	Effect over the repose angle of varying the sliding coefficient for a) constant rolling coefficient $\mu_{rolling} = 0.47$, and of varying the rolling coefficient for b) constant sliding coefficient $\mu_{sliding} = 0.39$	169
5.12	Average repose angle for different combinations of particle-particle sliding friction and rolling friction coefficients.	170
5.13	Comparison of mass flow rates at the outlet of the reactor from the DEM simulation and the experimental results for 25% and 50% of the maximum rotational velocity.	171
5.14	Comparison of mass flow rates at the outlet of the reactor from the DEM simulation and the experimental results for 75% and 100% of the maximum rotational velocity.	172
5.15	Multi-scale modeling strategy for describing biomass pyrolysis inside and auger reactor	177
5.16	Devolatilization reaction for palm kernel shells undergoing pyrolysis.	177
5.17	Comparison thermal decomposition during pyrolysis.	178
5.18	Scheme of the heat transfer phenomena involved in the auger reactor, considering the wall temperature T_w , the biomass bed temperature T_b and the gas temperature T_g	179

5.19 Definition of the differential volume in the PFR to perform mass and energy balances	181	
5.20 Normalized char production for different screw velocities.	184	
B.1 Cellulose a), D-xylose b) and Lignin c) used for preparing the synthetic mixture to resemble PKS.		208
B.2 Palm kernel shells sampling before characterization and thermal analysis. .		210
B.3 Cyclone blade mill used for palm kernel shells size reduction.		210
B.4 Vibratory sieve shaker and sieves of different size used for PKS size distribution determination.		213
B.5 Digital dry oven used for moisture content determination.		215
B.6 Furnace used for volatile matter determination.		216
B.7 XRD equipment, sampler and sample holder.		217
B.8 PKS zones studied in the microscopy analysis.		218
B.9 Compiled microscopy of PKS, zone 1 without Toluidine.		219
B.10 Compiled microscopy of PKS, zone 2 without Toluidine.		219
B.11 Compiled microscopy of PKS, zone 3 without Toluidine.		220
B.12 Compiled microscopy of PKS, zone 1 without Toluidine.		220
B.13 Compiled microscopy of PKS, zone 2 without Toluidine.		221
B.14 Compiled microscopy of PKS, zone 3 without Toluidine.		221
B.15 Compiled microscopy of PKS, zone 1 with Toluidine.		222
B.16 Compiled microscopy of PKS, zone 2 with Toluidine.		222
B.17 Compiled microscopy of PKS, zone 3 with Toluidine.		223
B.18 Compiled microscopy of PKS, zone 1 with Toluidine.		223
B.19 Compiled microscopy of PKS, zone 2 with Toluidine.		224
B.20 Compiled microscopy of PKS, zone 3 with Toluidine.		224
B.21 HB43-S Halogen Mettler Toledo moisture balance before a) and during analysis b).		225
B.22 Linear regressions between predicted and measured HHV for the current work and three other correlations from literature [20, 21, 22].		230
C.1 Convergence of the mean for evaluating the tilting angle using for determining wall-particle coefficients of static friction and rolling friction.		233

C.2	Convergence of the deviation for evaluating the tilting angle using for determining wall-particle coefficients of static friction and rolling friction. . .	234
C.3	Results from the simulation in LIGGGHTS for the calculation of repose angle for different combination of sliding and rolling particle-particle friction coefficients. Sliding coefficient-Rolling coefficient. F=front, B=back, L=left, R=right.	234
C.4	Results from the simulation in LIGGGHTS for the calculation of repose angle for different combination of sliding and rolling particle-particle friction coefficients. Sliding coefficient-Rolling coefficient. F=front, B=back, L=left, R=right.	235
C.5	Results from the simulation in LIGGGHTS for the calculation of repose angle for different combination of sliding and rolling particle-particle friction coefficients. Sliding coefficient-Rolling coefficient. F=front, B=back, L=left, R=right.	236
C.6	Repose angle for left and right sides of the experimental set up for finding sliding and rolling friction coefficients between particle-particle. Sliding coefficient-Rolling coefficient. F=front, B=back, L=left, R=right.	237

List of Tables

1.1	General operating conditions and main products for different types of pyrolysis [23].	32
2.1	Identification of the crystalline structure of biomass components evaluated through XRD analysis	42
2.2	Particular species considered for the stoichiometry of detailed reaction schemes [24, 25].	52
2.3	Properties and specifications for pellets made from lignocellulosic and aquatic biomass, blends and mixtures	54
2.4	Correlations for predicting HHV in MJ kg ⁻¹ for biomass samples from elemental and carbohydrates analysis.	55
3.1	Order of magnitude for the estimated characteristic times through pyrolysis for lower and upper limits	68
3.2	Reactions, kinetic parameters and enthalpy of reaction for biomass pyrolysis considering a lumped kinetic model [26].	68
3.3	Detailed reaction scheme and kinetic parameters for biomass pyrolysis [27, 25].	72
3.4	Parameters for biomass water evaporation [28, 29]	73
3.5	Parameters for biomass water evaporation [28, 29]	73
3.6	Properties of the substances used by the model	79
3.7	Pyrolysis products properties considered for the energy efficiency analysis [30, 31]	89
3.8	Market prices for raw materials and products involved in pyrolysis	90
3.9	Global warming potential (GWP) for a 100 years horizon for the products of cellulose pyrolysis.	91

4.1	Methods applied for palm kernel shell characterization	99
4.2	Correlations used for comparison purposes for predicting HHV in MJ kg ⁻¹ for lignocellulosic biomass.	113
4.3	Results from the palm kernel shell characterization	118
4.4	Proximal analysis comparison between different types of lignocellulosic feedstock	120
4.5	Average results of particle size distribution for PKS	121
4.6	Comparison between experimental results, the correlation developed in this work and correlations from previous works.	125
4.7	Comparison of statistical parameters between correlations for predicting HHV from composition of biomass.	126
4.8	Identification of characteristic groups in PKS using FTIR spectra.	129
4.9	Activation energy for palm kernel shell pyrolysis, for $0.2 \leq \alpha \leq 0.7$, using the KAS method	141
4.10	Activation energy for palm kernel shell pyrolysis, for $0.2 \leq \alpha \leq 0.7$, using the FWO method	142
4.11	Comparison of the activation energy (E_a) and pre-exponential factor A for palm kernel shell pyrolysis	143
4.12	Composition of palms kernel shells and kinetic parameters for pyrolysis . .	144
5.1	Average results of particle size distribution for PKS	150
5.2	Results from the palm kernel shell characterization	150
5.3	Relevant dimensions from the auger reactor	151
5.4	PKS size distribution considered for the DEM approach	155
5.5	Parameters used for the DEM	160
5.6	Parameters found for the mean residence time mathematical equation . . .	167
5.7	Values of the particle-wall coefficients determined experimentally	167
5.8	Parameters used in the DEM simulation	173
5.9	Mean residence time determined from experiments.	173
5.10	Mean residence time determined from empirical correlation using experiments.	173
5.11	Mean residence time determined from DEM simulations followed by an empirical correlation.	174

5.12 Mean residence time determined from DEM simulations tracking particles.	174
5.13 Comparison of statistical parameters between correlations for predicting residence time.	174
5.14 Comparison between simulations using the DEM	175
5.15 Activation energy (E_a) and pre-exponential factor A in s^{-1} , for palm kernel shell pyrolysis	176
5.16 Parameters for the mean residence time mathematical equation	178
A.1 Reactions, kinetic parameters and enthalpy of reaction for biomass pyrolysis considering lumped kinetic models [26].	
A.2 Particular species considered for the stoichiometry of detailed reaction schemes [24, 25].	198
A.2 (Continued.)	199
A.3 Detailed reaction scheme and kinetic parameters for biomass pyrolysis [27, 25].	200
A.4 Reactions for softwood biomass pyrolysis corresponding to the RAC reaction scheme [24, 25].	201
A.4 (Continued.)	202
A.4 (Continued.)	203
A.5 Correlations for estimating specific heat for different species involved in pyrolysis in $\text{J K}^{-1} \text{ kg}^{-1}$.	205
A.5 (Continued.)	206
B.1 Cellulose properties provided by the manufacturer [32].	209
B.2 D-Xylose properties provided by the manufacturer [33].	209
B.3 Lignin properties provided by the manufacturer [34].	209
B.4 Bulk density measurements for PKS	211
B.5 Density for distilled water in g cm^3 at different temperatures [16].	211
B.6 Measurements and calculationS of PKS apparent density	212
B.7 Results of the particle size distribution for sample 1 of PKS	213
B.8 Results of the particle size distribution for sample 2 of PKS	214
B.9 Results of the particle size distribution for sample 3 of PKS	214
B.10 Results of calculation of d_{50} for three samples of PKS	214

B.11 Results of calculation of d ₈₀ for three samples of PKS	215
B.12 Moisture measurements	216
B.13 Volatile matter determination measurements	216
B.14 Ash content determination measurements	217
B.15 Milled PKS moisture content determined with the moisture balance.	225
B.16 Determination of water-soluble extractives in PKS samples	226
B.17 Determination of ethanol-soluble extractives in PKS samples	226
B.18 Elemental analysis results for moist PKS, synthetic mixture and coffee husk	226
B.19 Moisture corrected elemental analysis results for moist PKS, synthetic mixture and coffee husk	227
B.20 Comparison between the elemental composition for different types on dry basis.	227
B.21 Detail of the measurements for the determination of HHV in biomass samples without corrections	228
B.22 High calorific value including moisture and sulfur content corrections. . . .	228
B.23 Results from the characterization of coffee husk	229
B.24 Summary of the design of experiments for pyrolysis analysis	230
B.25 Design of experiments for randomized PKS and synthetic mixture pyrolysis tests at different heating rates	231
C.1 Comparison of densities for PKS, particle and bulk	232

Chapter 1

Introduction

The present work deals with lignin-rich biomass pyrolysis at particle, molecular (kinetics and properties) and reactor scales, each one with its own limitations and particular way of being addressed. In this chapter biomass pyrolysis is described from different points of view, the main goals of the research are presented and an outline of the thesis is included at the end of this chapter.

Transportation has been the main driver for oil demand growth over the last years; however, it is expected that for the next decade, petrochemicals will account for nearly 60% of the new oil demands [35]. As concerns grow regarding reserves depletion, market volatility and negative environmental impacts associated with the use of fossil fuels [36, 37], there is an increasing need for finding renewable alternatives for producing both fuels and petrochemicals [38]. Biomass is an abundant and renewable resource that could be transformed into both energy and platform chemicals. As an energy vector, biomass could be considered to be nearly neutral in terms of green house gas emissions [14].

Pyrolysis is one of the key technologies for transforming biomass into both fuels and platform chemicals. In spite of its potential to produce a variety of chemical products, pyrolysis has been mainly studied for energy generation purposes. To scale up pyrolysis and to incorporate it into biorefineries for energy generation and chemicals production, the understanding of the complex thermochemical processes that take place during pyrolysis, the interactions between biomass components, the effect of heating rates over pyrolysis and its operating conditions is required. The inherent complexity of pyrolysis makes it necessary to describe it at a molecular scale, where the reaction takes place, at a particle scale, where gaseous products and reactants interact inside a defined volume, and finally at a reactor scale, where mass and heat transfer limitations and the type of technology for pyrolysis

play a fundamental role in the distribution of products and in the energy requirements of the pyrolysis process [15, 26].

1.1 Biomass pyrolysis from a particle perspective

Modelling enables the study of complex systems such as pyrolysis. Particle scale modelling approaches have been applied to deal with such complexity and to capture pyrolysis behaviour. Previous works [25, 36, 26, 27, 39] have modelled pyrolysis at a particle scale to predict product distribution and the temperature of the particles. As it is schematized in Figure 1.1, while biomass reacts, the biomass particle gets consumed and gases and condensibles are formed. This is a dynamic process, and if the particle is big enough, biomass' low thermal conductivity will generate a temperature gradient inside the particle. This type of particle is known as thermally-thick particle [40]. While the particle reacts, it shrinks, its porosity increases and its surface changes in temperature, area and composition. Biomass pyrolysis kinetics and the different transfer phenomena that take place throughout pyrolysis at a particle level add complexity to biomass pyrolysis models [39], and computational fluid dynamics (CFD) is usually applied to simulate the behaviour of such systems [26, 41]. Moreover, when reliable models are required for biomass pyrolysis at a particle scale, the change in the particle's size over time needs to be considered [36, 27]. This creates an additional modelling challenge, the constantly changing dimension, composition and temperature at the surface of the particle, which represents a not-easy-to-solve moving boundary problem. Moving boundaries pose additional difficulties for finding numerical solutions, especially when traditional mesh methods are used in CFD [42]. As a result, increasingly complex models, high computational times and scaling-up difficulties would be expected in pyrolysis particle models [26]. Therefore there is a need to solve the problems related to pyrolysis at a particle scale, in a way that guarantees the obtained results but also in a way that presents approaches for such issues using an easier and less time consuming alternative.

Most of the available information regarding biomass pyrolysis considers the thermal behaviour of fine biomass particles (< 1 mm) [43, 44]. Considering small particle sizes and, consequently, low masses, aims to avoid heat and mass transfer resistances during pyrolysis [45]. However, even for small biomass masses (0.3-3.0 mg), whenever high heating rates

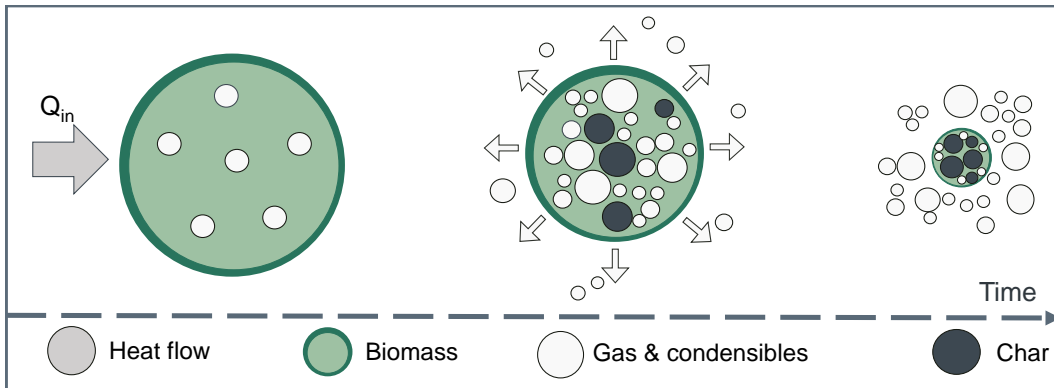


Figure 1.1: Representation of a reacting biomass particle undergoing pyrolysis.

are applied ($\geq 50 \text{ }^{\circ}\text{C min}^{-1}$) between 250 and 400 $^{\circ}\text{C}$, deviations between experimental data and kinetic model-calculated values appear [9]. Bigger particles with internal temperature gradients, *i.e.* thermally thick particles, are common in most industrial scale pyrolysis applications [46], and the study of thermally thick biomass particles undergoing pyrolysis is needed when considering the poor thermal conductivity of the biomass and the consequent influence of biomass size on pyrolysis yields and product distribution [47].

Previous works have addressed the effect of heating rate over product distribution in thermally thick particles [14, 48, 39] and the application of particle models for their use in multi-scale systems for fluidized bed, fixed bed and moving grates reactors [27, 36]. The mentioned research has mainly addressed dry thermally thick biomass pyrolysis. However, biomass moisture content should not be overlooked given its impact over product distribution, drying-associated energy requirements, and because it can reduce biomass milling energy consumption in pre-treatment stages [46]. Therefore, there is the need to understand how different operating conditions, biomass and processing temperatures, and biomass moisture content influence thermally thick particles pyrolysis.

1.2 Biomass pyrolysis from the molecular point of view

When discussing biomass from the molecular point of view, biomass components and composition, pyrolysis kinetics, and biomass characteristics will be involved.

1.2.1 Biomass composition

Lignocellulosic biomass is an abundant resource that contains cellulose, hemicellulose, lignin, water, inorganic components and extractives. Cellulose, hemicellulose and lignin usually represent more than 90 wt.% of biomass constituents. Although lignocellulosic biomass could be represented as a combination of moisture, cellulose, hemicellulose and lignin; the presence of extractives and the variations in the combination of the previously mentioned components, have a direct effect over the product distribution from pyrolysis [49]. As it is evidenced in Figure 1.4, most of the studied lignocellulosic biomass is mainly composed of cellulose and hemicellulose. Moreover, the lignin content in most studies regarding biomass do not exceed 35%. Indeed, out of the 70 different types of biomass included in Figure 1.4, only 5 types of biomass could be considered as lignin-rich biomass. This highlights the need of more studies that characterize lignin-rich biomass and at the same time it shows a potential lack of information regarding the behaviour of lignin-rich biomass in pyrolysis. Such missing information is valuable for developing waste-to-energy and waste-to-value alternatives in regions where lignin-rich biomass might be abundant and ready to be used, but where also the lack of information regarding such type of feedstock has hindered potential applications in the areas of renewable energies, biorefineries and biomass processing technologies.

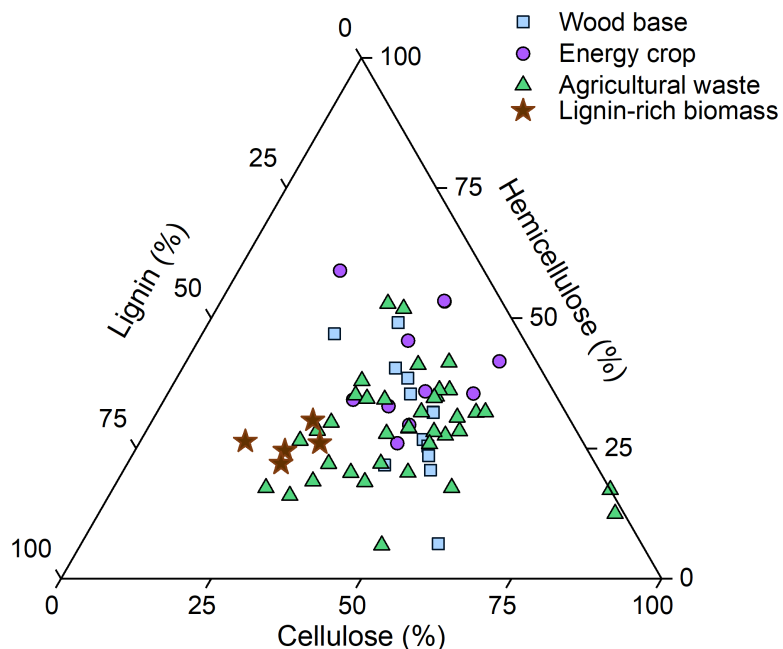


Figure 1.2: Different types of biomass and their composition, modified from [3].

1.2.2 Interaction between biomass components in pyrolysis

Biomass composition changes significantly due to differences in crops' varieties and maturity, location, environment, used fertilizers and soil, irrigation and growing and harvesting practices. The chemical composition of agricultural wastes present variability even for the same type of crop and residue. Such variation could be as high as 23% for cellulose, 15% for hemicellulose and 15% for lignin, in sugarcane bagasse. This behavior responds to the multiple aforementioned factors [50] and if such variations could be expected in the same type of crop, lignin-rich biomass would be expected to have completely different properties when compared with cellulose or hemicellulose-rich biomass. Consequently, if high-lignin biomass is to be described, experimental analysis are required to provide the missing physical, chemical and thermal properties of a given high-lignin feedstock.

The thermochemical decomposition of biomass in pyrolysis occurs through a complex system of primary and secondary chemical reactions. Consequently, the determination of biomass pyrolysis reaction mechanisms and their associated kinetic parameters is a challenging task. Such kinetic parameters are particularly difficult to determine for lignin because of the differences in composition and structure that lignin presents in biomass, which has an effect over the reaction mechanism [51].

1.2.3 Kinetic models for describing biomass pyrolysis

Previous biomass pyrolysis modelling strategies had addressed pyrolysis complexity by considering biomass as a cellulose, hemicellulose and lignin only mixture [52]. Other modelling approaches had included extractives in the analysis by grouping them under hydrophilic or hydrophobic species that follow lumped pyrolysis reactions [49, 36]. Inorganic components are not usually included in biomass pyrolysis models; however, such components catalyze secondary reactions that modify pyrolysis product distribution [53]. Existing interactions between cellulose, hemicellulose and lignin had been identified in previous biomass pyrolysis experiments [54, 55]; however, such information is limited to pure components only and the effect of these interactions over pyrolysis kinetics is not fully understood yet. Moreover, further research needs to be developed in order to understand the way such interactions could be incorporated in biomass pyrolysis models, as an alternative to improve the agreement between predicted and experimental pyrolysis results [56]. The combination of modelling approaches and experimental analysis for describing complex

thermochemical processes like pyrolysis, stands out as an opportunity to develop reliable pyrolysis models with views to future process design and optimization. This work aims to combine modelling and experimental strategies as an alternative for improving pyrolysis model's product distribution prediction.

In complex thermochemical processes such as biomass pyrolysis, describing the reaction mechanism and determining pyrolysis kinetic parameters are challenging tasks. One of the alternatives to describe biomass pyrolysis considers a parallel reaction scheme where biomass is represented by a combination of three components (cellulose, hemicellulose and lignin) that react without interacting with each other. Although such approach is widely used for describing biomass pyrolysis, it has some shortcomings that can result in deviations between predicted and experimental results. Another of the limitations of the previously mentioned three component reaction approach, is that all the other components that can be found in biomass, besides cellulose, hemicellulose and lignin, are neglected. Biomass variability, in terms of composition and morphology, can also affect the behaviour of biomass and the way it decomposes in pyrolysis [36].

Biomass morphology had not been considered for modelling pyrolysis kinetics. However, morphology could be an indicative of how easy or difficult biomass' components could react in pyrolysis. Such availability represents, in a way, how easy it is for biomass structural components to undergo pyrolysis as a result of their morphology and configuration. Such analysis could be relevant when explaining the differences in pyrolysis kinetics between biomass feedstocks that share similar cellulose, hemicellulose and lignin contents, but that exhibit different pyrolysis behaviour. Even cellulose, the least variable of biomass' structural components, could present different aggregation degrees, and consequently, different configurations, depending on the biomass source. Such behaviour is a result of the existence of different combinations of crystalline and amorphous zones in cellulose. The mentioned amorphous zones in cellulose are also known as accessible regions and they represent the sectors where water can be absorbed [57]. Cellulose thermal decomposition is highly dependent on cellulose composition and structure, as well as the used atmosphere, temperatures and heating rates [58].

Biomass pyrolysis has been studied extensively. Experimentally and modelling strategies have been developed for unraveling pyrolysis' complex kinetics and reaction mechanisms

[45, 9, 59, 60]. Depending on the required level of detail, simple lumped kinetic models or complex detailed kinetic models could be used to predict pyrolysis product distribution. Whereas lumped kinetics group all products under three categories or phases: gas, condensibles (tar or bio-oil) and solids (char), detailed kinetic models identify the individual components of each product phase. Detailed kinetics incorporate secondary charring reactions to account for the amount of initial products from pyrolysis that undergo additional reactions. Consequently, in pyrolysis there is a trade-off between the complexity of the kinetic model and the information it provides [25, 36, 26].

Biomass pyrolysis kinetics and the different transfer phenomena that take place throughout pyrolysis add complexity to biomass pyrolysis models [39], and computational fluid dynamics (CFD) is generally used to simulate the behaviour of such systems [26, 41]. Moreover, when reliable models are required for biomass pyrolysis at a particle scale, the change in the particle's size over time needs to be considered [36, 27]. This creates an additional modelling challenge: the constantly changing dimension, composition and temperature at the surface of the particle. Considering these aspects results in a moving boundary problem. Moving boundaries pose additional difficulties for finding numerical solutions, especially when traditional mesh methods are used in CFD [42]. As a result, increasingly complex models, high computational times and scaling-up difficulties would be expected in pyrolysis particle models [26]. The mentioned drawbacks and model-related complexities hinder the application of particle models in process design and new alternatives to overcome such difficulties need to be developed.

1.2.4 Residual lignocellulosic biomass

Biomass is an abundant resource that could support a transition from our oil-driven economy towards more sustainable and environmental-friendly alternatives, while contributing to reduce oil consumption. Among the different types of biomass, lignocellulosic residues emerge as one of the most promising feedstocks for obtaining fuels and platforms chemicals due to their potential to underpin the development of biorefineries, especially in industries with large waste generation such as the palm oil extracting industry [61]. Palm oil is the most widely used vegetable oil and 75.5 million of metric tons of palm oil were produced in 2021 [62]. The demand of palm oil is only expected to grow in the upcoming years;

unfortunately, such volume of production goes hand in hand with the generation of wastes. Indeed, considering that palm oil only represents near 10 wt.% of the dry mass available in the palms, there are plenty of residual lignocellulosic biomass that could be either potentially used, or that will require appropriate disposal [63]. Palm kernel shells (PKS) are one of the residues from the palm oil extraction process that have received attention in the past years as a potential source of energy, mainly because of its relatively high energy content when compared with other lignocellulosic wastes [64, 63, 61, 65]. Within this context, the purpose of this work is to provide some insights into the use of particle models for describing pyrolysis, not only as an alternative to predicting product distributions and temperature gradients but also as a tool for providing early stage information on the effect of operating conditions over potential economic, environmental and energy impacts. Such information is obtained by combining a pyrolysis mechanistic modelling approach, at a particle scale, with a boundary immobilization technique that has not been applied yet to pyrolysis modelling. This technique, however, has shown to be useful for modelling changing water-air interfaces in tablet coating [66] and for describing transient two-phase diffusion [67], and this success motivates the application to a particle model for pyrolysis.

Despite the potential benefits of using lignocellulosic biomass for energy or industrial purposes, its seasonal behaviour and the variation of physico-chemical properties within crops, are main drawbacks for achieving continuous operations [68, 69]. Therefore, a detailed characterization of the residual biomass of interest, and a flexible technology to process such feedstock are required. Pyrolysis is one of the most relevant technologies for transforming biomass into valuable fuels and platform chemicals [68]. However, the complexity of the reactions that take place throughout pyrolysis, the effect of biomass variability over pyrolysis performance and the role that the existing interactions between biomass main components (cellulose, hemicellulose and lignin) play in pyrolysis kinetics need to be better understood to develop scalable pyrolysis units [25]

1.3 Biomass pyrolysis

Pyrolysis is a key technology for transforming biomass into both fuels and platform chemicals, which could support the transformation of agro-industries into biorefineries. However, the integration of pyrolysis into biorefineries requires a better understanding of the complex interactions between biomass components and also more information about the effect of

Table 1.1: General operating conditions and main products for different types of pyrolysis [23].

Pyrolysis	Temperature [°C]	Vapour residence time [s]	Solid residence time [s]	Heating rate [°C min ⁻¹]	Main product
Fast	500	< 2	< 10	High (>> 20)	Bio-oil
Intermediate	400	5-20	< 20	-	Process-depending
Slow	400	several hours	several hours	Slow (\approx 20)	Char

different operating conditions over pyrolysis products is needed. This is particularly critical for the development of reliable models for pyrolysis process design [23].

1.4 Relevant parameters that influence pyrolysis operations

There are many parameters that can influence a complex process like pyrolysis. Temperature, heating rates and residence times are among the most commonly studied parameters in pyrolysis. However, parameters such as the composition of the biomass, the particle size or biomass' moisture content, are also relevant for pyrolysis operations; however, they are not widely studied.

1.4.1 Operating temperature and heating rate

Small changes in pyrolysis operating conditions can deeply impact product distribution. While high heating rates favor tar production, high pyrolysis temperatures increase char concentration in the products [14]. The heating rate and the residence time of the produced vapours is what defines a slow, intermediate or fast pyrolysis. Table 1.1 shows a general perspective of the differences between the types of pyrolysis. Whereas the limits of the operating conditions, as well as the resulting main products, are usually well defined for slow and fast pyrolysis, intermediate pyrolysis remains a grey area in which product distribution prediction and kinetics determination remain a challenge.

1.4.2 Moisture content and particle size

Moisture content plays a significant role in biomass handling and processing. For instance, moisture has an effect over biomass preservation during storage and biomass densification processes. While moisture contents below 20% are required for biomass storage, moisture contents between 10 – 14 % are needed for biomass densification. Moisture content is variable in biomass and in lignocellulosic feedstocks it could range anywhere from 7.30% or lower, as in rice husk, to 60.0% or higher, as in grape residues [3, 18]. Moisture acts differently during pyrolysis depending on the size of the biomass particle. For small particles (thermally thin), higher initial moisture contents foster charring reactions and decrease tar

yields, specially in fluidized bed reactors [70]. There is little information regarding the effect of moisture over pyrolysis of thermally thick particles [71, 72, 73]. A previous work [74] found that although the initial moisture content does not affect char, tar and gases yields in the pyrolysis of thermally thick wood particles, higher initial moisture contents are associated with higher conversion times and delays in pyrolysis. For high heating rates (40 kW m^{-2}), there is little difference in pyrolysis when comparing biomass moisture contents between 0.0% and 11.0 %. However, this could change in thermally thick particles as we approach the centre of the particle, where high water contents could reduce the overall char production while increasing the gaseous products [14]. Higher biomass moisture contents in pyrolysis are also related to higher overall energy requirements. The mentioned behaviour responds to biomass slow temperature rise as a consequence of the additional energy requirements for heating and evaporating biomass-associated water. For this reason, fast pyrolysis applications require moisture contents below 10%. In addition, high moisture contents could affect bio-oil's viscosity, heating value, stability and homogeneity [75].

1.5 Pyrolysis from a macro perspective and the multi-scale challenges in biomass pyrolysis

Multi-scale modelling in pyrolysis presents several challenges associated with the complexity of biomass thermochemical decomposition and with the variability in properties among different feedstocks [5]. Molecular, particle and reactor levels are required for describing biomass pyrolysis accurately. Moreover, considering the complexity of biomass pyrolysis, the determination of appropriate kinetics is a key factor for developing models that represent pyrolysis and that could be scaled-up [27]. Biomass pyrolysis is heavily dependent on its composition and in the used heating rates [36, 25, 76].

The variability on biomass composition, the coexistence of liquid, gaseous and solid phases and transport phenomena at particle and reactor scales make modelling of biomass pyrolysis complex. As it is presented schematically in Figure 1.3, a multi-scale approach offers the possibility to address complex processes by breaking down the difficult problem into smaller pieces that could be addressed separately. Such smaller pieces are referring to molecular properties and kinetics, particle transport mechanisms and reaction level models, all of this within a unified framework. Whereas molecular models are usually related with the estimation of physical, chemical, kinetic and thermodynamic properties; particle level

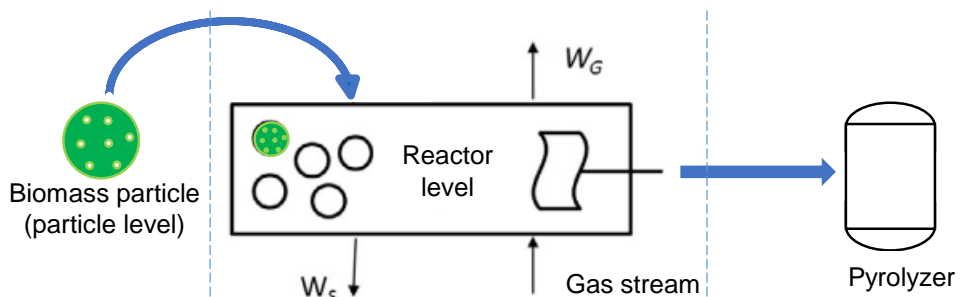


Figure 1.3: Multiscale approach for modelling complex processes from particle to reactors and applications in process design [4].

models aim to determine product concentration and temperature profiles during pyrolysis by taking into consideration kinetics and transfer phenomena. Finally, reactor models make use of particle models to evaluate pyrolysis at pilot and industrial scales. If pyrolysis is to be described through modelling approaches, the three levels: molecular, particle and reactor, need to be considered [27].

1.5.1 Pyrolysis energy intensive nature

Energy efficient pyrolysis could facilitate more environmentally-friendly and cost-effective pyrolysis operations [77]; therefore, alternatives such as auto-thermal pyrolysis reactors, combined heating strategies and biomass radiative pyrolysis, using solar concentration, have been considered [78, 14, 79]. Despite the mentioned options for supplying pyrolysis thermal energy needs, energy efficiency is not commonly addressed when studying biomass pyrolysis. Little information is available about the influence of pyrolysis operating conditions, product distribution, and their correlation with the associated energy generation and consumption [30]. Moreover, information on how energy efficiency in pyrolysis could be considered at particle level, for modelling applications, is also limited. Energy inefficient biomass processing and biofuels production could generate higher emissions than fossil fuels processing chains [80]. There is a need to understand the existing nexus between biomass, operating conditions, energy consumption/generation, environmental footprint and economic outcomes so as to consider pyrolysis as a viable candidate for replacing fossil fuels in energy generation and industrial applications.

1.5.2 Modelling approaches that target multi-scale pyrolysis

Biomass pyrolysis is a complex thermochemical process in which reactions take place at a molecular level and transfer phenomena occur both at micro and macro scales. As a result, to describe pyrolysis accurately it is necessary to combine micro and macro approaches at

the same time, having lengths and scales which could vary in orders of magnitude. Reactions that take place at atomic or molecular levels are included within particles where transfer phenomena becomes relevant. Particles are usually fed to reactors and pyrolysis is described in terms of mass, heat and energy transport. All the mentioned stages are considered in order to describe a chemical process [25]. Moreover, if additional information such as logistics and market constraints are also relevant, pyrolysis becomes extremely challenging by combining different scales simultaneously. Regardless of the complexity in multi-scale approaches, the core of the process will always be the reaction system [27].

1.5.3 Supply chain

There are many challenges that biomass needs to overcome before it can be established as an energy vector and as a source for platform chemicals. One of such challenges is biomass low density and the consequent densification processes required for its transportation and processing. This low density can potentially increase the cost of biomass-derived biofuels given that moving biomass from fields to processing or pre-processing facilities has a considerable impact over biomass feedstock costs [81]. Distributed energy generation has been regarded as an alternative to avoid transportation-associated costs, but also as an opportunity to provide renewable energy in remote locations with biomass availability.

1.5.3.1 Pyrolysis technologies for decentralized processing

Biomass pyrolysis represents an opportunity for supporting distributed renewable energy generation, an alternative to generate liquid and gaseous fuels that could be used in small-scale CHP units. In contrast with other energy-oriented biomass processing technologies, pyrolysis is flexible enough to produce both fuels and a variety of platform chemicals, using the same equipment but changing the operating conditions. Similarly, different types of pyrolysis technologies can be used for different scales of operation. In spite of its potential, pyrolysis remains as an under exploited waste-to-value technology. This is particularly evident in tropical regions, where more traditional alternatives such as anaerobic digestion or combustion are preferred [82]. The decentralized use of biomass opens the possibility to use readily available biomass where ever and when ever it becomes available. Such decentralized vision is particularly interesting for agrarian countries with large pools of waste biomass that currently are not used, nor involved as part of a productive system. Auger reactors, also known as screw reactors, are one of the alternatives for pyrolyzing biomass at pilot and medium scales ($20\text{-}700 \text{ kg h}^{-1}$) [83, 84]. Such type of pyrolyzers could support

decentralized pyrolysis. However, there are only a few models to describe biomass pyrolysis in auger reactors and more work is required to develop robust modelling strategies that can predict biomass behaviour, energy requirements and product distribution in this type of equipment [85]. A recent review on bio-oil production evaluated more than 230 works with different pyrolysis technologies [5]. If the mentioned works are categorized by type of reactor in their research, Auger reactors represent only 3% of the studied technologies. Therefore, more efforts need to be directed towards developing models and experimentation considering Auger reactors.

Despite the advances in describing biomass pyrolysis, there are many challenges that need to be addressed before pyrolysis can be considered as a scalable, cost-efficient and environmental friendly technology with a future role in replacing energy and petrochemicals-driven oil demands. Among the many process-related challenges that still remain for pyrolysis to become a widely available technology, its energy-intensive nature and a deeper understanding of pyrolysis behaviour for different types of feedstock and different operating conditions, as well as the associated economic and environmental performance, need to be addressed [86, 77]. Moreover, the dynamic nature of pyrolysis and its complexity demand the development of modelling strategies that are capable of capturing biomass pyrolysis behaviour and with the appropriate level of detail to facilitate process design applications.

1.6 Motivation and objectives of the present work

As presented in the previous lines, there is missing information in each one of the stages of a multi-scale approach for describing pyrolysis, which opens several working areas at molecular, particle and reactor scales. Similarly, to couple each one of this components to have an effective description of pyrolysis also remains a challenge. The areas that require further development are presented briefly in the next lines on the basis of the information described in the introduction.

1.6.1 Work to be done at a particle scale

At a particle-scale further research needs to be performed in order to describe thermally-thick biomass particles with different moisture contents, inlet temperatures, heating temperatures, among others conditions. All of this, using an approach that could be replicated

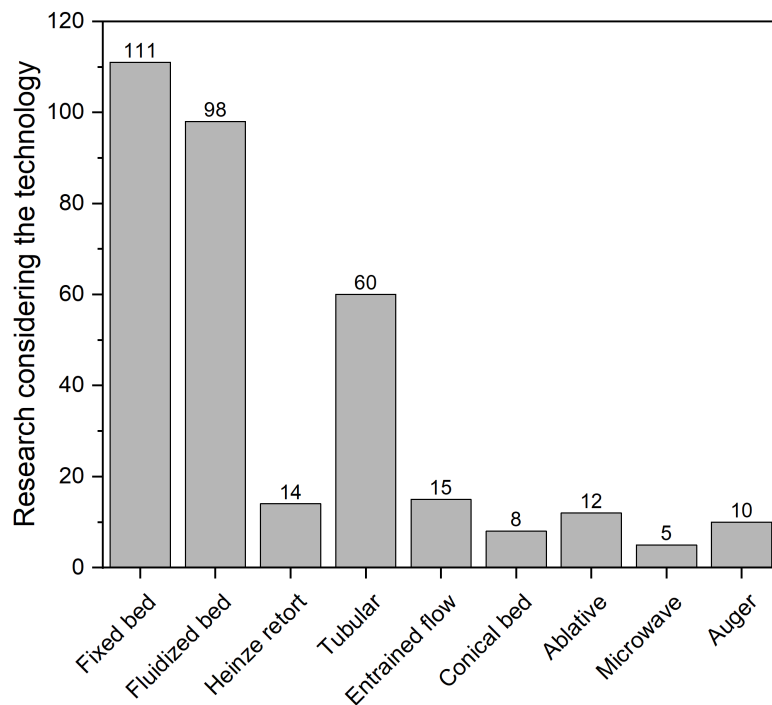


Figure 1.4: Number of research performed with the different types of pyrolysis reactors [5].

easily by other researchers and industry practitioners. Reducing the complexity in solving particle models remains a challenge that hinders its application.

1.6.2 Remaining work at a molecular scale

As presented before, lignin-rich biomass is a type of feedstock, whose properties are not readily available yet. Moreover, the differences in behaviour during pyrolysis between high-lignin and high-cellulose should also be addressed. Lignin-rich biomass requires a dedicated analysis and characterization in order to find the most appropriate operating conditions for their use with energy or industrial purposes.

1.6.3 Work at a reactor scale

Regarding the reactor scale, the retrieved information evidenced that auger reactors are one of the reactors for pyrolysis with less studies regarding its operation, optimization, use of different feedstocks, product yields, operational cost, etc. Before all this missing information could be addressed, there is a first obstacle to tackle. This obstacle is the characterization of the granular flow inside auger reactors. Furthermore, the granular flow needs to be coupled with a compatible particle model and an appropriate kinetic model in order to fully describe pyrolysis. The need for research in this area is accentuated by the fact that there are no previous experiences, that the author is aware of, for combining

shrinking particle models with a granular flow model and with pyrolysis kinetics calculated at the Laboratory. Within this context, the aim of this work is to develop a multi-scale strategy that describes pyrolysis for lignin-rich biomass, using mathematical models and experimental results.

1.7 Modelling and experimental approach

This section describes the approach undertaken throughout the thesis for connecting biomass pyrolysis at different scales. This thesis combines modelling and experimental approaches to bridge the gaps found in the current knowledge, so a complete multi-scale strategy could be used to describe the pyrolysis of lignin-rich biomass, covering the particle scale, the molecular scale and the reactor level. The particle scale level is covered in Chapter 3 by developing a mechanistic model to describe pyrolysis at a particle level.

The lack of information regarding properties and kinetic models for palm kernel shells, made it necessary to undertake the complete characterization of this agricultural waste. Moreover, given that PKS is a lignin-rich biomass, certain particularities of this type of biomass could be identified through the experimental analysis. Chapter 4 addresses data collection at a molecular level through experiments for high-lignin biomass.

Finally, a combined experimental and modelling approach are followed in Chapter 5 with views on characterizing the flow pattern in a single auger reactor, and to model such behaviour for different operating conditions.

The mathematical models generated in this thesis are oriented towards:

- Describing pyrolysis of thermally thick biomass particles in such a way that relevant economic, environmental and energy-efficiency outcomes are included.
- Describing the granular flow that appears when thermally-thick biomass is transported within an auger reactor.
- Providing a common working framework for incorporating results from obtained pyrolysis

The experiments developed in this thesis have the purpose of:

- Characterize lignin-rich biomass so it can be compared with other types of biomass and en function of the develop kinetic model
- Characterize experimentally the granular flow from the auger reactor so empirical correlations could be used for predicting biomass properties.

1.8 Thesis objectives

With the information presented previously, the proposed objectives for this work are:

- To develop a particle model that captures the behaviour of lignin-rich biomass throughout pyrolysis.
- To characterize palm kernel shells and to establish its pyrolysis kinetic parameters.
- To develop a multi-scale alternative to use the generated experimental information for building a multi-scale approach that describes pyrolysis in auger reactors.

1.9 Outline of the thesis

This thesis is organised as presented in the next lines:

- **Chapter 1.** This chapter covers the current challenges associated with the scales of a pyrolysis problem.
- **Chapter 2.** This chapter presents the state-of-the-art of particle model alternatives, pyrolysis kinetic models and alternatives for modelling pyrolysis at a reactor level.
- **Chapter 3.** This chapter presents a particle model capable of describing temperature and concentration during pyrolysis. Moreover, lumped and detailed kinetic models are considered for delivering economic, environmental and energy efficiency-related information.
- **Chapter 4.** This chapter considers a series of laboratory analysis to characterize palm kernel shells, a lignin-rich type of biomass, and to define its kinetic parameters for pyrolysis.
- **Chapter 5.** This chapter considers both an experimental and a simulation approach for characterizing the granular flow of the particle. Additionally, friction coefficients are also determined for future experiences.

- **Chapter 6.** This chapter presents the main findings from this work and concludes with potential areas in which the future work could be developed. Finally, the molecular information and the particle level are combined at a reactor scale.

1.10 Computational resources

Several computational resources were required for the development of this thesis. The particle model was developed and solved in gPROMS®ModelBuilder 7.0.9 2021, Process Systems Enterprise-A Siemens business. This software is a general-purpose software capable of solving ODEs and PDEs. The DAEBDF solver was used for the particle model. The numerical results are gathered from a 64-bit Windows portable computer with Intel®Core™i7-106 CPU @ 1.80GHz 2.30 GHz with 16 GB of RAM.

LIGGGHTS, a DEM software was also used for characterizing the granular flow of the screw reactor. In this case, a Intel® Xeon® CPU E5-2650 v4 @ 2.2 GHz 2.2 GHz (2 physical processors - 24 cores per processor 48 logic processors) was used. The generated results, any other additional information is available through the repository <https://github.com/AndresCh2018/PhDCombinedmultiscaleAchP>

Chapter 2

Literature review

This chapter summarizes some of the developments found in literature for describing pyrolysis at a particle scale, reactor scale and also through laboratory analysis. Moreover, the relevance and potential applications and limitations of pyrolysis, their products and available technologies are discussed and compared.

2.1 Biomass

Biomass is a renewable resource that includes the organic plant and algae-originated components present in woody and herbaceous materials, agricultural products and wastes, human and animal wastes and aquatic sources [87]. It is widely regarded as a renewable and potentially CO₂-neutral source for generating thermal energy and electricity [27]. In spite of its energy application, one of the most promising uses of biomass is as an alternative for replacing platform chemicals and marketable products that currently rely on oil derivatives for being manufactured. Indeed, biomass can be transformed into solvents, bulk chemicals, polymers and biofuels [88, 89]. Lignocellulosic biomass is one of the most abundant types of biomass. This resource is non-edible for humans and it is vastly available in agricultural wastes and woody materials; therefore, it does not compromise food security [5].

2.1.1 Lignocellulosic biomass components

Lignocellulosic biomass is formed mainly by cellulose, hemicellulose and lignin; yet it also contains small amounts of ashes and extractives (resins, triglycerides, phenolic compounds and tannins). As it is presented in Figure 2.1 cellulose molecules group together to form microfibers that provide structural support while surrounded by amorphous hemicellulose and lignin. Woody biomass is perhaps one of the most studied type of biomass, and it has cellulose as its most abundant component (40-60 wt. %), followed by hemicellulose (15-30 wt. %) and lignin (10-20 wt. %). Whereas for lignocellulosic biomass, cellulose usually

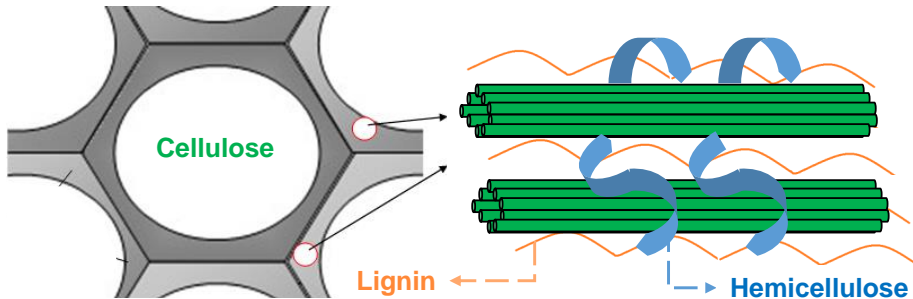


Figure 2.1: Main components of lignocellulosic biomass, modified from [6].

Table 2.1: Identification of the crystalline structure of biomass components evaluated through XRD analysis

Component	θ_{\max} °	Additional peaks found in 2θ (°)	Reference
Cellulose I β	21.1-22.3	14.25- 16.25	[90, 91, 92]
Hemicellulose			
D-xylose	18.30-19.10	10.80-12.5, 16.60-17.50, 19.2-21.60, 32.5-35.0	[93]
L-xylose	18.30-19.10	10.80-12.5, 16.60-17.50, 19.2-21.60, 32.5-35.0	[93]
D-arabinose	20.00-20.80	13.40-15.00, 16.20-19.20, 22.5-24.00, 32.5-33.3, 40.00-40.83	[93]
L-arabinose	20.00-20.80	13.40-15.00, 16.20-19.20, 22.5-24.00, 32.5-33.3, 40.00-40.83	[93]
Lignin		Amorphous zone from 10.00-40.00 degrees	[94]

remains around 50 wt. %, the composition of lignin and hemicellulose can differ greatly from one type of biomass to another [6, 7]. Cellulose can be described as a polymer formed by glucose molecules arranged in long chains. Cellobiose, a glucose dysaccharide, is the structural unit of the cellulose chain. As it is evidenced in Figure 2.2, cellulose chains have a reducing and a non-reducing end [7]. Moreover, cellulose long chains can have different degrees of crystallinity, including allomorph groups, which modifies their properties and thermal behaviour. Cellulose could be found in two crystalline forms: cellulose I α and cellulose I β , the latter being the most abundant. The crystalline structure of cellulose I β is also more thermodynamically stable than the one formed in cellulose I α . Cellulose I α can be identified experimentally using X-Ray difraction (XRD) and electron diffraction analysis [90].

Cellulose and lignin interactions and their effect over pyrolysis product distribution have been identified in previous works [54, 95]. Indeed, the combined pyrolysis of cellulose and lignin affects the yield of light products by promoting the synthesis of oxygenated compounds with low molecular weights such as ketones, esters and aldehydes. In spite of the cellulose-lignin interactions not generating new reaction paths; biomass thermal decompo-

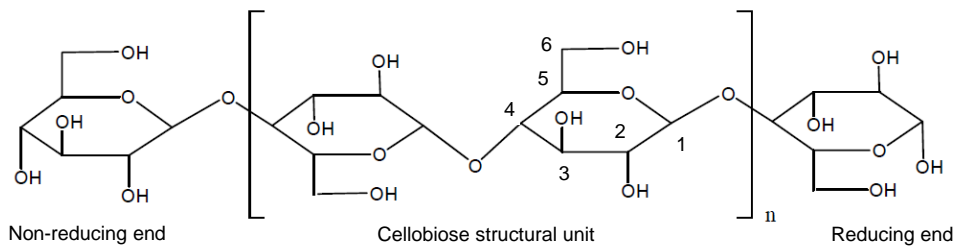


Figure 2.2: Structure of cellulose linear polymeric chains, modified from [7]

sition is affected by the mentioned interactions above 700 °C [54]. Cellulose-hemicellulose interactions have also been studied throughout biomass pyrolysis, they are expected to appear over 327 °C and such interactions mainly result in higher char yields [95]. Lignin and hemicellulose are relevant in the first stages of pyrolysis, below 327 °C [56]. In addition to these three main components, biomass also has extractives and inorganic salts. Biomass extractives comprise a variety of compounds such as tannins, fatty acids, resins, terpenes and alkaloids [96, 97]. The inorganic salts that are present in biomass are sometimes referred to as ashes and they might include calcium, magnesium, potassium, aluminium, copper, cobalt and iron metallic compounds; but also silicon, phosphorus and sulphur, among many other non-metallic compounds [6]. High contents of ash in biomass are not desirable for thermochemical processes such as pyrolysis or gasification. In cases of biomass with alkaline ash, even small amounts of ash can modify pyrolysis product distribution. Indeed, a 3.0 wt.% of added ash can increase CO₂ and char production in pyrolysis. Ashes can also poison the catalyst whenever catalytic pyrolysis or gasification is used [98].

2.2 Biomass pyrolysis

2.2.1 Thermal degradation of biomass main components in pyrolysis

During biomass pyrolysis, hemicellulose and cellulose are the first biomass constituents to decompose, followed by lignin. As it is evidenced in Figure 2.3, hemicellulose decomposition starts in the 220 to 250 °C range, releasing energy in the mentioned process. However, even at high temperatures (990 °C), hemicellulose thermal decomposition is not complete and a solid residue, representing as much as 20 % of the initial biomass weight, could remain. In terms of cellulose pyrolysis, this polysaccharide begins to decompose between 315 and 400 °C, with a highly endothermic process. Contrary to hemicellulose, when higher temperatures are reached, cellulose decomposes almost completely, leaving very little solid

residue left. Lignin is the most thermally stable component, compared to the previous ones; consequently, it has a slow decomposition in the 200-900 °C range and it experiences both endothermic and exothermic reactions. Lignin's stability is evidenced in the solid residue that remains after pyrolysis, which could reach near 47 % of its initial weight [8].

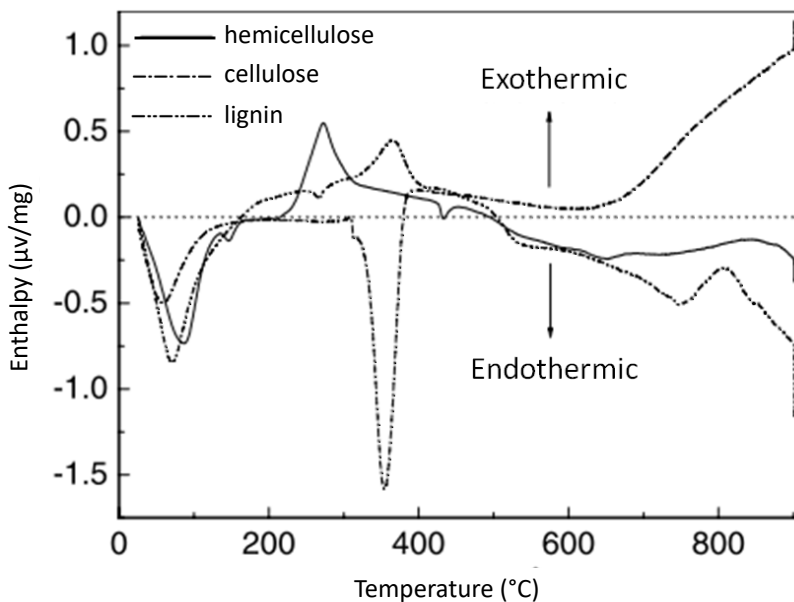


Figure 2.3: Thermal decomposition of cellulose, hemicellulose and lignin during a differential scanning calorimetry (DSC) analysis under pyrolysis conditions. Required enthalpy as a function of temperature, modified from [8].

Biomass thermal decomposition is a complex combination of endothermic and exothermic processes, as described in Figure 2.3. Thus, the energy requirements of pyrolysis change with biomass composition and with the temperature of the process [8]. Given that cellulose decomposition is highly endothermic between the 200 to 400 °C range, cellulose pyrolysis requires more energy at low temperatures. In the same way, for higher temperatures, both hemicellulose and lignin decomposition are responsible for pyrolysis energy requirements. As it is evidenced in the previous figure, when the pyrolysis temperature reaches 350 °C, cellulose experiences a highly endothermic process. The mentioned thermal behaviour is opposed to the exothermic processes that take place for both hemicellulose and lignin between the 200-500 °C range. The thermal decomposition of lignocellulosic materials had been used in previous works to describe the heat of reaction of pyrolysis [8, 99, 27]. Even though the thermal behaviour of cellulose, hemicellulose and lignin is well documented for each component separately, the effect of the interactions between these three components

over the heat of reaction is not completely understood yet. Indeed, further research is required in the area of biomass pyrolysis in order to determine more accurate heats of reaction considering temperature, biomass composition and the interactions between components.

Besides the effect of interactions between components during pyrolysis, the heating rate at which pyrolysis occurs also affects the overall process. For a particular type of biomass, variations in the heating rate result in higher or lower conversion, different product distribution and different heats of reaction. As it is presented in Figure 2.4 a) and b), an increase in the heating rate will have a positive effect on the overall conversion of cellulose and biomass for each temperature, evidenced as a higher mass loss during pyrolysis [9]. In spite of the increase in the overall conversion, the composition of products is highly dependent on the heating rate due to the presence of secondary charring reactions [52]. Cellulose, hemicellulose and lignin are affected in different ways by changes in the heating rate. Such behaviour corresponds with the relatively narrow range of temperatures for thermal decomposition of cellulose, compared with the broader decomposition range of lignin or hemicellulose. In general, higher heating rates favors the production of volatile species, whereas lower heating rates favors char generation from lignin and hemicellulose [95]. The complexity of the interactions between biomass components, and the effect of the heating rate over the distribution of products and over the energy requirements of the pyrolysis process need to be addressed in the future in order to develop more reliable and more flexible biomass pyrolysis models. Flexible pyrolysis models could facilitate an optimal allocation of resources in terms of feedstock and correspondent pyrolysis technology.

2.2.2 Biomass pyrolysis kinetics

2.2.3 Review of relevant biomass pyrolysis kinetic models

Depending on the required level of detail, simple lumped kinetic models or complex detailed kinetic models could be used to predict pyrolysis product distribution. Consequently, in pyrolysis there is a trade-off between the complexity of the kinetic model and the information it provides [25, 36, 26]. The existing kinetic models for biomass pyrolysis have been developed to describe either the thermal decomposition of biomass through mass loss, or the distribution of pyrolysis products. Most of the existing models aim to obtain kinetic parameters for pyrolysis on the basis of mass loss observations in thermal decomposition experiments, mainly through regression and curve fitting [6, 100, 11]. Curve fitting is a simple way to provide kinetic parameters that are good enough to represent particular py-

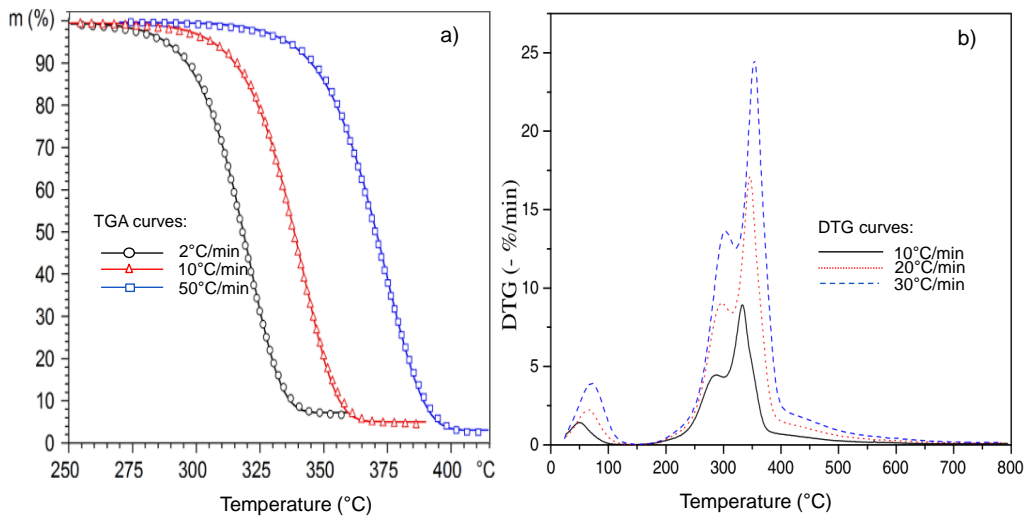


Figure 2.4: Cellulose thermal decomposition under pyrolysis conditions evidenced as: **a)** mass loss (m) with temperature during thermogravimetric analysis (TGA) within a helium atmosphere [9], and **b)** differential thermogravimetric profiles for different heating rates [10].

rolysis conditions. Previous works include detail information regarding the many and varied kinetic models for biomass pyrolysis that have been developed through model-fitting. However, such models cannot be extrapolated to another type of biomass or different operating conditions than the ones used to build the fitted model [100, 11]. Such limitations have generated the need for more general models that describes pyrolysis for a range of feedstocks and different operating conditions, such as lumped and detailed reaction models for pyrolysis.

2.2.4 Lumped models for biomass pyrolysis based on thermal decomposition analysis

Lumped models provide a general understanding of the pyrolysis process in terms of three main products: a solid product (biochar), a liquid product (bio-oil or tar) and a gaseous product. The mentioned products could be a result of one stage (primary) or two stages (secondary) degradation processes of volatile species during pyrolysis. Cellulose, hemicellulose and lignin thermal decomposition have been described extensively through lumped pyrolysis models [13, 11].

One of the most applied methodologies for building biomass pyrolysis kinetic models considers the experimental information from thermal decomposition analysis to describe pyrolysis. In such cases, mass loss data for decomposing biomass in non-reactive atmospheres is

used to determine kinetic parameters and reaction models. Such thermal decomposition is evaluated through thermogravimetric analysis (TGA) and the final products from pyrolysis are grouped under three categories: char, tar and gases. The mentioned categories have been used extensively to describe biomass pyrolysis; however, pyrolysis is a complex process with multiple reactions and with a variety of products that are not considered in mass loss pyrolysis models. Through TGA experiments, biomass pyrolysis had been initially described as a group of three parallel first order reactions, as it is presented in Figure 2.5. One

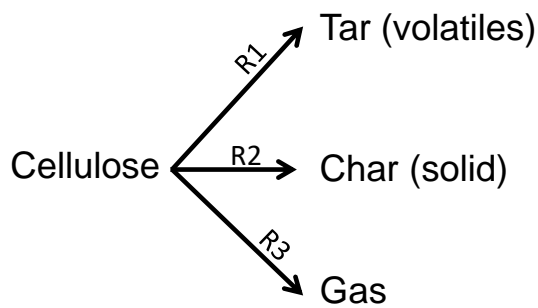


Figure 2.5: Cellulose pyrolysis reaction scheme with simple first order reactions and lumped products. Modified from [11].

of the first works that described in detail the pyrolysis reaction scheme for cellulose, considered active cellulose as an intermediate [12]. The mentioned model, which is presented in Figure 2.6 provides an initial idea of the potential products and yields, by grouping them into solid, liquid or gaseous products. The same proposed reaction schemes for cellulose have been extended for hemicellulose and lignin. However, such lumped models do not provide information regarding the distribution of the products in a detailed way [12, 13]. Indeed, such distribution refers to the type and amount of each potential specie formed during pyrolysis. For evaluating the effect of operating conditions or biomass variability in the distribution of the products, more detailed reaction schemes are required [27]. Ho-



Figure 2.6: Lumped cellulose pyrolysis reaction scheme with an intermediate active cellulose stage. Modified from [12, 13].

mogeneous reactions' modelling is usually addressed through macroscopic kinetic models; however, due to the heterogeneous character of pyrolysis, one alternative is to use solid-

phase conversion (α) instead of the concentration of reactants. Moreover, α determination follows Eq. 2.1, and the reaction rate is described by Arrhenius theory, as presented in Eq. 2.2 [101]:

$$\frac{d\alpha}{dt} = k(T)f(\alpha) \quad (2.1)$$

$$k(T) = A \exp\left(-\frac{E}{RT}\right) \quad (2.2)$$

Where:

α = solid-phase conversion

T = temperature (K)

E = activation energy (J mol⁻¹)

A = pre-exponential factor (s⁻¹)

k = reaction rate (s⁻¹)

t = time (s)

R = ideal gas constant (J K⁻¹ mol⁻¹)

The kinetic parameters included in the previous Arrhenius equation are usually determined using curve fitting-methods. When biomass pyrolysis is assumed as an isothermal process, the solid-phase conversion is a function of time. On the contrary for non-isothermal processes, a constant heating rate (β) is considered and experimental data from derivative thermogravimetric (DTG) or TGA analysis could be used for solving such type of non-isothermal approaches, as described in Equation 2.3 [6].

$$\frac{d\alpha}{dt} = \frac{1}{\beta}k(T)f(\alpha) \quad (2.3)$$

Reliability and consistency are two of the main issues of linear fitting in TGA data, and they are a consequence of the limited conversion ranges from which linear fitting can provide good enough kinetic parameters [11]. A previous work [100] include detailed information regarding the many and varied kinetic models for lignocellulosic pyrolysis that have been developed through model-fitting. Because of the mentioned limitations, more robust models have been developed for obtaining kinetic parameters in biomass pyrolysis.

2.2.4.1 Distributed activation energy models

Distributed activation energy models (DAEM) consider multiple parallel and independent reactions, each one with its own activation energy. Consequently, a series of parallel first-order reactions take place at the same time, but with different kinetic parameters and different products. Moreover, the activation energy distribution of the pyrolysis reactions is a continuous function. With this approach, more accurate kinetic parameters can be provided for a broader conversion range, compared with conventional fitting-methods. The DAEM model is a lumped model that also uses model-fitting methods and requires an assumed function for estimating the value of α in advance. The assumed α function comes from the analysis of the reaction-order model of pyrolysis. In a general form, the DAEM can be represented by Eq. 2.4. [6].

$$1 - \alpha = \begin{cases} \int_0^{\infty} \exp \left[- \int_{T_o}^T \frac{A}{\beta} \exp \left(-\frac{E}{RT} \right) dT \right] f(E) dE; & n = 1 \\ \int_0^{\infty} \left[1 - (1-n) \int_{T_o}^T \frac{A}{\beta} \exp \left(-\frac{E}{RT} \right) dT \right]^{\left(\frac{1}{1-n}\right)} f(E) dE; & n \neq 1 \end{cases} \quad (2.4)$$

Where:

α = solid-phase conversion

T = temperature (K)

T_o = initial temperature (K)

E = activation energy ($J \text{ mol}^{-1}$)

$f(E)$ = distribution function for the activation energy

A = pre-exponential factor (s^{-1})

β = heating rate ($K \text{ s}^{-1}$)

n = reaction order, $n \geq 1$

k = reaction rate

t = time (s)

R = ideal gas constant ($J \text{ K}^{-1} \text{ mol}^{-1}$)

One of the simplest alternatives to define an activation energy distribution function $f(E)$ is to assume the same constant frequency factor k_0 for the set of reactions that take place. In the case of a first-order occurring single reaction, the Arrhenius plots for different heating rates

converge in a straight line; whereas for a single non-first order reaction, the Arrhenius plots are heating rate dependent. The previous approach for estimating kinetic parameters has several limitations that are mainly associated to different experimental conditions, biomass composition, type of equipment used and scale of the experiment, among others. Moreover, the constant frequency factor and an assumed Gaussian distribution for $f(E)$ can generate deviations from real behaviour [102].

Lumped models are useful for predicting, in general terms, the products from pyrolysis. Moreover, such models allows certain understanding of the correlation between temperature, composition and the overall generation of products. One of the most attractive features of lumped models is that they manage to by-pass the inherent complexity of pyrolysis reactions, providing overall yields of groups of products (tar, char and gases). All of the previously mentioned characteristics however, are not sufficient when more information regarding the composition of products is required. Furthermore, if the potential use of pyrolysis products within biorefineries is to be assessed, lumped models could only give partial information. In such cases, one of the alternatives for overcoming the mentioned limitations is the development of models that considers a detailed reaction scheme [27, 25].

2.2.5 Detailed reaction schemes for biomass pyrolysis

The products from pyrolysis have been studied extensively by different authors [103, 104, 5, 15, 105, 52, 106]. Most of the research regarding the distribution of pyrolysis products is focused in determining or predicting product composition in terms of its solid, liquid and gaseous fractions, correspondingly, the fractions of char, bio-oil and gases. Such composition has been studied experimentally for a variety of lignocellulosic feedstocks, and for different operating conditions: heating rates, operating pressures and reaction temperatures [107, 108, 109]. However, pyrolysis products, specifically bio-oil, contain many valuable chemicals that could be used as platforms chemicals for a future development of biorefineries, or to incorporate them into existing oil & gas refineries [5]. In order to do it so, the composition of feedstocks, the interaction between biomass components and processing conditions are required to be considered.

Detailed reaction schemes for pyrolysis have been developed over the last decade in order to describe, as accurately as possible, the distribution of products from biomass pyrolysis.

Such models are empirical and they consider cellulose, hemicellulose and lignin as the sole components of biomass. The three mentioned components decompose independently to form solids, gases and condensables that are well identified and described in literature [110, 111, 25]. However, when only cellulose, lignin and hemicellulose are considered, kinetic models might fail to predict the distribution of products from pyrolysis in cases where biomass presents a high content of extractives ($> 10\% \text{ w/w}$) [49]. One of the first works that considered a detailed pyrolysis product description worked within experimental results in the 400 to 550 °C temperature range [15]. Moreover, such model only considered a limited number of products from the fast pyrolysis, mainly glucose-associated carbohydrates. The mentioned pyrolysis process required less than 3 seconds to reach complete conversion, and it showed that for the 400-500 °C range, longer cellulose chains generate higher Levoglucosan yield [15].

Detailed reaction schemes are complex, mainly because they incorporate secondary charring reactions in order to account for the amount of initial products from pyrolysis that undergo additional (secondary) reactions in order to form char, tar and gases. The detailed reaction scheme developed by Ranzi et al., (2014) and modified by Anca-Couce & Scharler (2017) also referred to as RAC scheme, is one of such models and it has been previously used in literature to describe continuous pyrolysis and torrefaction processes [25, 27]. The detailed reaction scheme differs from other models because it considers intermediate species for describing pyrolysis. For instance, active cellulose (cellA), is considered to form from cellulose before any other gaseous or solid component. This intermediate state for cellulose corresponds with observations from experiments and it takes into account the physical changes that cellulose undergoes before it decomposes during pyrolysis [108]. In order to describe a complex process like pyrolysis, several intermediate species need to be included as part of the reactions. Moreover, certain gaseous species are considered to remain trapped in the solid phase when pyrolysis starts. In order to clarify the reactions and species associated with biomass pyrolysis, some of the components that required additional explanation are presented in the following Table. The detail of the reactions involved in the RAC detailed kinetic scheme is presented in the Appendix A.

Table 2.2: Particular species considered for the stoichiometry of detailed reaction schemes [24, 25].

Identification	Species	Observation
CELL	Cellulose	
CELLA	Active cellulose	
HAA	Hydroxyacetaldehyde	
GLYOX	Glyoxal	
HMFU	Hydroxymethylfurfural	
G{H2}	Hydrogen	Trapped in solid phase
G{H4}	Methane	Trapped in solid phase
LVG	Levoglucosan	
HCE	Hemicellulose	
AA (HW)	Acetic acid	For high molecular weight HCE
AA (SW)	Acetic acid	For low molecular weight HCE
HCEA1	Active cellulose	Type 1, intermediate
G{CO2}	Carbon dioxide	Trapped in solid phase
G{COH2}	Formaldehyde	Trapped in solid phase
G{CH3OH}	Methanol	Trapped in solid phase
G{CO}	Carbon monoxide	Trapped in solid phase
G{C2H4}	Ethylene	Trapped in solid phase
XYL	Xylan	
HCEA2	Active cellulose	Type 2, intermediate
LIG-C	Lignin	Lignin with -C radicals
LIG-CC	Active lignin	Intermediate from LIG-C
pCOUMARYL	p-coumaryl alcohol	
LIG-H	Lignin	Lignin with -H radicals
LIG-OH	Lignin	Lignin with -OH radicals
LIG	Lignin	
G{H2}	Hydrogen	Trapped in solid phase

In spite of the level of detail in the RAC scheme, regarding product distribution; one of its major limitations is the incorporation of empirical factors (charring factors) in the kinetic model. Such empirical factors are intended to adjust the stoichiometry of the reac-

tions in order to account for the amount of primary products from pyrolysis that undergo secondary charring reactions. Moreover, charring factors for cellulose (X_{cell}), lignin (X_{lig}) and hemicellulose (X_{hce}) depend on the heating rate, biomass characteristics and the pyrolysis process itself. Such factors need to be defined beforehand in order to differentiate fast pyrolysis processes from slow pyrolysis processes. For instance, charring factors for cellulose are selected within a range from 0.025 (fast pyrolysis) to 0.10 (slow pyrolysis) [4, 112, 25, 26, 113]. The information previously presented for lumped and detailed kinetic models is one of the main components required to represent pyrolysis with views to process design and optimization. The information from the kinetic models needs to be coupled with mass and energy balances in order to develop applications that can describe biomass pyrolysis at small and large scales.

2.2.6 Applications of pyrolysis products

Pyrolysis is one of the key technologies for transforming biomass into both fuels and diverse platform chemicals that can be used in different industries [114, 69]. The different kinetic models that have been developed to represent complex thermochemical processes such as biomass pyrolysis, also define and limit the application of the products from pyrolysis. Pyrolysis most common application is the production of fuels with energy purposes. When lumped kinetic models are considered, and regardless of the operating conditions, processing technology or feedstock; pyrolysis produces a blend of solid (biochar), liquid (bio-oil) and gaseous products. The proportions of such products are dependant on the characteristics of the biomass, the type of reactor, the selected operating conditions and the presence/absence of a catalyst. The production of a solid fuel (biochar) via pyrolysis, increases the energy density of the original biomass and transforms it into a renewable fuel that could be used onsite or as an end-product [115]. Currently, it is difficult to find dedicated specifications for energy applications of biochar, bio-oil or gases produced via pyrolysis from non-woody biomass. The specifications will most likely depend on the application for each pyrolysis product. Perhaps biochar energy applications could consider the specifications for non-woody pellets for combustion as initial properties that biochar needs to meet for energy applications. In such case, type A and type B pellets, and their specifications, could be considered, as presented in Table 2.3.

The yield and the energy content are the main criteria for selecting either a type or biomass

Table 2.3: Properties and specifications for pellets made from lignocellulosic and aquatic biomass, blends and mixtures

Property	Type A pellet	Type B pellet
Origin and source	-Herbaceous biomass -Fruit biomass -Aquatic biomass -Blends and mixtures	-Herbaceous biomass -Fruit biomass -Aquatic biomass -Blends and mixtures
Diameter, D and Length, L [mm]	D06 to D25, $D \pm 1$ $3.15 \leq L \leq 40$, for D06 to D10 $3.15 \leq L \leq 50$, for D12 to D25	D06 to D25, $D \pm 1$ $3.15 \leq L \leq 40$, for D06 to D10 $3.15 \leq L \leq 50$, for D12 to D25
Moisture, M [%] in mass, wet basis	M12 \leq 12	M15 \leq 15
Ash, A [%] in mass, wet basis	A6 \leq 6	A10 \leq 10
Net calorific value, Q [MJ/kg]	Q14.5 \geq 14.5	Q14.5 \geq 14.5

or a produced biochar or bio-oil as energy sources. The yield could be related to either the amount of biomass produced per unit of area, in the case of a particular type of crop, or to the amount of produced biochar or bio-oil, per mass of fed biomass, in the case of pyrolyzed biomass [116]. The energy content, on the other hand, is evaluated through the higher heating value, or HHV; a property that is usually measured in a laboratory using a calorimeter. A calorimeter is energy content analysis-dedicated equipment that contains a vessel in which biomass, biochar or bio-oil are combusted in the presence of oxygen. As the exothermic reaction of combustion takes place, the heat of reaction is registered and reported in energy units per unit of mass, usually MJ kg⁻¹. Due to the importance of the energy content in biomass, biochar and bio-fuels, several works have been developed for predicting biomass higher heating value using empirical correlations; thus avoiding the need of special instruments such as calorimeters. The aforementioned works have taken either the elemental composition of biomass, its cellulose, hemicellulose or lignin content, and even the fixed carbon present in biomass, to determine biomass HHV [20, 21, 22]. Some of the mentioned correlations developed for lignocellulosic biomass and fuels in general are presented in Table 2.4. In spite of the many contributions that are available regarding HHV prediction in lignocellulosic biomass, most of these works focus their attention in feedstocks that have either cellulose or hemicellulose as their main component.

Table 2.4: Correlations for predicting HHV in MJ kg⁻¹ for biomass samples from elemental and carbohydrates analysis.

Correlation	Type of fuel	Observations	Reference
HHV = 0.0877(L)+16.4951	Non-woody lignocellulosic biomass	L = lignin content in wt.%	[20]
HHV={33.5[C] + 142.3[H] - 15.4[O] - 14.5[N]} · 10 ⁻²	Fuels in general	[C]=carbon content in wt.% [H]=hydrogen content in wt.%	[118]
HHV = 0.3856(C+H)-1.6938	Lignocellulosic biomass	(C+H) = carbon + hydrogen in wt.%	[21]
HHV = 0.196(FC)+14.119	Lignocellulosic biomass	FC = fixed carbon wt.%	[118]
HHV = 0.0979(L)+16.292	biomass	L = lignin content in wt.%	[22]

Indeed, the information retrieved from literature do not show a particular focus on lignin-rich biomass and some of the correlations found in literature identified potential limitations for determining HHV in cases where lignin exceeded 15 wt.% [117]. Lignin-rich biomass characterization and energy applications remain as opportunities for further research to have a better understanding of the behaviour of lignin-rich biomass, that serves as a complement to the already existing information on cellulose and hemicellulose-rich biomass.

The energy application of biomass and pyrolysis products presented in the previous lines are not the only nor the most valuable products from pyrolysis. Indeed, when detailed kinetic models are used and each of the volatiles and condensable compounds are identified, a broader range of applications besides energy, opens up for pyrolysis and biomass. For instance levoglucosan, furfurals, aldehydes, furanes, acetone, formaldehyde, among others, are valuable platform chemicals with higher market prices than any of pyrolysis energy applications [53]. Moreover, using biomass pyrolysis as a reaction path to obtain such platform chemicals has proven to be economically feasible and if the appropriate separation technologies are used, the production costs of such chemicals could be as low as 10% of the current market price [119].

2.2.7 Energy efficiency in biomass pyrolysis

In spite of the versatility of pyrolysis for generating energy and for producing platform chemicals; one of its main drawbacks is its energy-intensive nature. Reducing pyrolysis'

energy requirements is critical for expanding the use of this technology and for the design of competitive biorefineries [114]. Previous works have dealt with energy efficiency in pyrolysis. However, most of the available information considers energy efficiency of the process from a macro perspective. Correspondingly, energy generation is defined on the basis of produced thermal energy and generated electricity from burning char, tar or gases from pyrolysis [120]. Thermal efficiency in pyrolysis had been studied in previous works whenever biochar or biofuels are products of interest [31, 121, 122]. In such circumstances, the higher heating value (HHV) of both feed and products, as well as latent heats and the external heat used in pyrolysis, could be considered to define either an energy densification ratio, a percentage of energy recovery [30] or thermal energy efficiencies [31, 121]. Whereas the standard formation enthalpies for biomass pure components (cellulose, hemicellulose and lignin) are available in literature [123, 124], the standard enthalpies for char, tar and gases from pyrolysis are not that readily available. However, such enthalpies can be determined using the HHV of tar, char and pyrolysis gases, as well as the elemental composition of pyrolysis products [31, 121, 30]. One of the few works that addresses energy efficiency in thermochemical processes considers torrefaction's energy efficiency as a ratio between the higher heating values of the products and reactants [125]. This ratio is defined as energy yield (Y_{energy}).

2.3 Experimental determination of biomass pyrolysis kinetics

Pyrolysis is one of the most relevant technologies for transforming biomass into valuable fuels and platform chemicals. However, the effect of biomass variability over pyrolysis performance and the role of biomass main components over pyrolysis kinetics need to be better understood to develop scalable pyrolysis units. Physical and chemical properties are required to develop robust modelling strategies, especially in complex thermochemical processes like pyrolysis. Such properties and pyrolysis associated-kinetics are available for pure components and woody materials; however, they are scarce for residual biomass and particularly difficult to find for lignin-rich biomass such as palms kernel shells, coconut shells, coffee and Jatropha Curcas endocarpus, among others [126]. Kinetic parameters, enthalpy of reaction and pyrolysis-related thermophysical properties of biomass and pyrolysis products can serve to support biomass pyrolysis modelling; however, such information is not readily available in databases [124]. Previous works have addressed the determination of biomass pyrolysis reaction mechanisms using thermal analysis methods [36, 127].

The kinetic parameters for biomass pyrolysis can be affected by the heterogeneity of the feedstock, different processing conditions and heat and mass transfer limitations [50]. Thermal analysis is one of the most broadly applied techniques for determining kinetic parameters, experimentally. Thermogravimetric analysis (TGA) is one of such techniques. Throughout TGA, the mass of a particular sample is heated using a defined heating rate, and it is monitored over time. Furthermore, if a differential analysis is conducted considering the variation of mass with time, maximum reaction rates could be identified. The latter method is also known as derivative thermogravimetry (DTG) [128, 50]. Differential scanning calorimetry (DSC) is another thermal analysis method that compares the heat flux that goes in and out of the required sample and of a reference material, while both are heated or cooled. DSC is broadly used for quantifying heat of reaction, heat of phase transition and specific heats [128, 50].

2.4 The multi-scale nature of biomass pyrolysis

2.4.1 Biomass pyrolysis at a particle scale

2.4.1.1 Single particle modelling approaches

Biomass pyrolysis modelling requires to couple heat and mass transfer in order to develop applications that could be scaled-up and further integrated within pilot and industrial applications. Particle models have been used in a limited way, to describe mainly biomass gasification and combustion. Pyrolysis has also been described using particle models, mainly for representing fluidized bed and transporting bed pyrolyzers [4, 24].

Single particle models had been used in previous works [27, 24, 26, 25], to describe biomass pyrolysis by coupling information from pyrolysis kinetics, heat transfer, mass transfer and biomass physicochemical properties. Through particle models, temperature and product distribution could be predicted in biomass pyrolysis processes. Moreover, when thermally-thick particles undergo pyrolysis, intra and inter-phase heat and mass transfer need to be coupled with kinetics in order to apply models at reactor scale. During pyrolysis, biomass particles shrink, which leads to changes in particles' shape and size. The mentioned dimensional changes make it necessary to evaluate transport properties at the different stages of the pyrolysis process.

To simplify intra-particle analysis during pyrolysis, spherical biomass particles could be considered [25]. When spherical biomass particles are considered, biomass pyrolysis needs to take into consideration the presence of intra-particle temperature and concentration gradients [129]. The geometry and physical properties of biomass particles have an effect over the pyrolysis process. Particle size changes does not affect bio-oil yields during fast pyrolysis in fixed bed reactors, for particles within the 0.2 to 1.0 mm range [130]. Indeed, whenever the size of biomass particles is in the order of micrometres, the temperature across the particle can be considered constant for modelling purposes [105, 131]. In contrast, when the size of biomass particles is in the order of millimetres, intraparticle temperature gradients exist. Indeed, it has been found that differences in particle size also affects product yield and distribution during pyrolysis, whenever the main components in bio-oil are quantified individually. The mentioned behaviour is evidenced when comparing cellulose pyrolysis from thin-film samples ($3\text{ }\mu\text{m}$) and powder samples (0.29-0.78 mm), and their corresponding levoglucosan yields (27 % for thin-films and 48 % for powders) at $500\text{ }^{\circ}\text{C}$ [76]. This suggests that in biomass particles, even at a micrometric scale, intraparticle temperature and concentration gradients exist.

In single particle approaches, geometry of the particles, molecular properties and kinetic models need to be included within mass, energy and momentum balances. One of the major complications for modelling biomass pyrolysis is the constantly changing properties at the boundary of the particle. There is limited information regarding the use of a single particle model for describing pyrolysis from lumped and detailed kinetics point of view. Moreover, for simplicity of an already complex problem, the developed models in literature usually deal with biomass pyrolysis as a one-dimensional problem. For the majority of single particle problems for describing pyrolysis, computational fluid dynamics (CFD) has been used to solve the resulting complex systems of ordinary differential equations (ODE). The implementation of the particle model in CFD software can provide a deeper understanding of the fluid's behaviour during pyrolysis; however, it can also halts the implementation of optimization techniques at the particle level. Particle models had been used to model gasification at a reactor level. Indeed, the particle approach can be used for modelling fluidized bed and moving bed gasifiers, processes that can be included into biorefineries [26, 25, 111].

2.4.2 Reactor scale modelling strategies for pyrolysis

The variability on biomass composition, the coexistence of liquid, gaseous and solid phases and transport phenomena at particle and reactor scales make modelling of biomass pyrolysis complex. Because of pyrolysis' inherent complexity, Previous works have addressed the effect of heating rate over product distribution in thermally thick particles [14, 48, 39] and the application of particle models for their use in multi-scale systems for fluidized bed, fixed bed and moving grates reactors [27, 36]. Therefore, further work is required to understand how different operating conditions, biomass and processing temperatures, and biomass moisture content influence thermally thick particles pyrolysis.

2.4.2.1 Auger reactors for pyrolysis

There is limited information regarding the development of models for describing biomass pyrolysis in auger reactors. A previous work [132] couples heat and mass transfer with a distributed activation energy kinetic model (DAEM) for modelling steady state biomass pyrolysis inside an auger reactor, in the axial direction. The mentioned model consider the auger reactor to behave as a rotary kiln. Moreover, it provides insights regarding temperature profiles and product distribution for an specific biomass. In spite of the lack of models describing pyrolysis in auger reactors, there are previous experimental works with a focus on biomass processing conditions [133, 37].

One of the alternatives to model auger reactors considers to represent this reactor as a rotary kiln. The different phenomena that take place throughout pyrolysis in rotary kilns, make it difficult to develop modelling strategies that describe biomass pyrolysis in such reactors. A previous work developed by Klose & Wiest (1999) considered a plug flow reactor (PFR) approach to model slow pyrolysis in a rotary kiln [134]. Such work considered that heat and mass transfer occur faster than the pyrolysis reaction. Consequently, only thermally-thin particles were considered and no internal temperature or concentration gradients are included in the analysis. A previous work dealt with modelling slow pyrolysis for dry wood chips [135]. The mentioned work considered a modified two-step pyrolysis kinetic model, which was initially described in other work [136]. Such modification includes a dimensionless parameter to account for tar reactivity above 650 °C [135]. Moreover, the rate at which tar escapes the solid phase depends on the agitation of biomass inside the rotary kiln; and in general, higher rotation speeds are associated with higher tar contents.

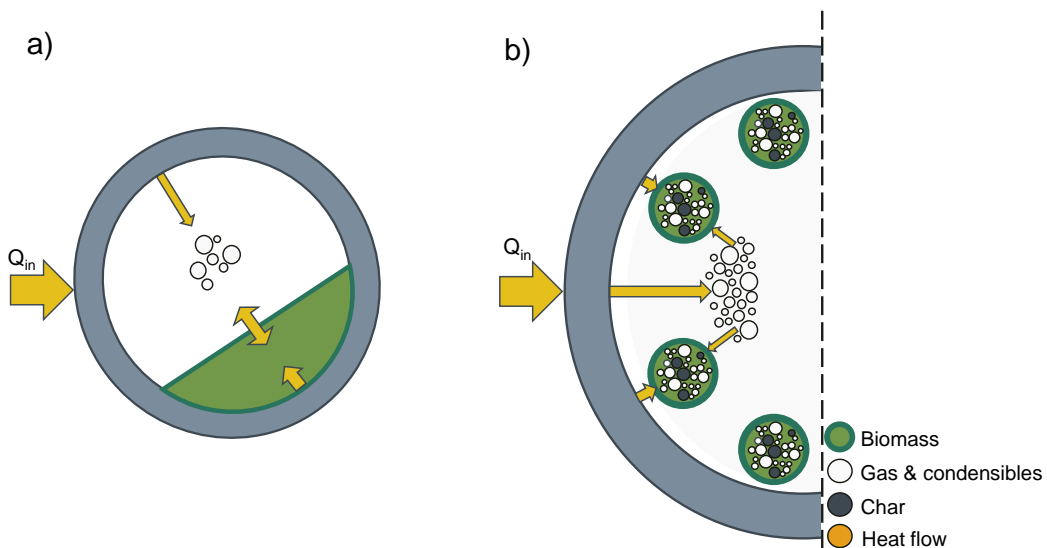


Figure 2.7: Approach for taking a rotary kiln a) as a reference for modelling an auger reactor b)

An auger reactor can also be modelled as a plug flow reactor with an extended residence time that accounts for the granular flow. Rotating screw conveyors allow the controlled flow of granular materials through different heating zones, which makes such conveyors particularly suited for biomass pyrolysis and torrefaction applications [137].

Granular flow

When coarse biomass is transported or processed in auger reactors, granular flow needs to be considered. The representation of the flow of solids inside a screw conveyor represents a complex problem, specially if particle's trajectories are required. However, coarse biomass transport inside conveyors could be simplified by assuming that the granular flow inside a conveyor resembles a plug flow reactor [137]. In such cases, the mean residence time of biomass in screw conveyors becomes relevant. The residence time in screw reactors can be predicted with empirical correlations, as a function of the rotational frequency and the volumetric throughput rate. A previous work [137] found that the the residence time of biomass in screw reactors depends on the screw reactor's geometry and not on the material being transported. In cases where particles do not move uniformly inside an auger reactor, axial dispersion appears [137].

Heat transfer in auger reactors

Heat transfer, both in screw reactors and in rotary kilns can be evaluated through heat pene-

tration theories for determining wall and solid heat transfer coefficients [85]. Heat transfer is one of the most relevant phenomena to consider in rotary kiln design and modelling because it conditions the kiln's performance. While rotary kilns have been studied extensively [138], there is limited information regarding the determination of heat transfer coefficients for pyrolysis auger reactors that consider a rotary kiln-based approach [85].

2.5 Concluding remarks

Within this context, the purpose of this work is to provide some insights on the use of particle models for describing pyrolysis, as an alternative to predict product distributions and temperature gradients; but also as a tool for providing early stage information on the effect of operating conditions over potential economic, environmental and energy outcomes. Such information is retrieved by combining a pyrolysis mechanistic modelling approach at a particle scale, with a boundary immobilization technique that has not been used yet in pyrolysis modelling, but has proved to be useful for modelling water evaporation from within porous media [66] and for describing transient two-phase diffusion [67].

Chapter 3

Single thermally-thick biomass particle pyrolysis model

This chapter presents a mechanistic model that describes pyrolysis for a single shrinking biomass particle with internal temperature gradients (thermally thick particle). This model is developed on the basis of mass, energy and momentum conservation. The changing properties on the surface of the particle constitute a moving boundary problem, which is addressed by reformulating the model using a one dimension spatial transformation. Such reformulation allows to predict temperature gradients and product distribution during pyrolysis within seconds. This chapter first describes the developed particle model and the approach taken for finding a numerical solution. Product distribution and temperature gradients resulting from the particle model are then presented in the results section. Potential applications of the particle model for assessing energy, economic and environmental outcomes are then described. Finally, the conclusions arising from the performed work are presented.

Publication from this work: Chico-Proano, Andres, George Manos, Lazaros G Papageorgiou, and Eric S Fraga. 2021. “Heating Strategies in Cellulose Pyrolysis as an Alternative For Targeting Energy Efficient Product Distribution.” Chemical Engineering Transactions 86: 61–66.

3.1 Introduction

Biomass pyrolysis is a complex thermochemical process that depends not only on the properties and morphology of each particular feedstock, but also on the operating conditions used in pyrolysis. As a result, different experimental and modelling strategies have been developed for unraveling pyrolysis’ complex kinetics and reaction mechanisms [45, 9, 59, 60]. Modelling approaches assist in the study of complex thermochemical processes such as biomass pyrolysis, which otherwise will require multiple experiments at

laboratory and at pilot scales for assessing the effect of biomass properties' variability, and the impact of changes in operating conditions, over pyrolysis outcomes.

Most pilot and industrial-scale pyrolysis applications require coarse biomass particles as feedstock. The mentioned coarse particles experience internal temperature gradients during pyrolysis and they are referred to as thermally thick particles [46]. Considering the poor thermal conductivity of biomass and the consequent influence of biomass size on pyrolysis yields and product distribution [47], the study of thermally thick biomass pyrolysis during pyrolysis is required for developing pilot and industrial pyrolysis applications. In spite of this, the majority of the available information regarding biomass pyrolysis considers the thermal behaviour of fine biomass particles ($< 1 \text{ mm}$) [43, 44]. Considering small particle sizes and consequently low masses, aims to avoid heat and mass transfer resistances during pyrolysis [45]. Nonetheless, even small biomass masses (0.3-3.0 mg) could experience such resistances whenever high heating rates are applied ($\geq 50^\circ\text{C min}^{-1}$). In such cases, neglecting heat and mass transfer resistances in pyrolysis results in a poor prediction of pyrolysis products distribution [9]. The inherent complexity of biomass pyrolysis, especially when coarse biomass is considered, makes pyrolysis modelling a challenging endeavour. Modelling approaches at a particle scale have been applied as an alternative to describe biomass pyrolysis behaviour and as an option to deal with pyrolysis inherent complexity. Previous works [25, 36, 26, 27, 39] have modelled pyrolysis at a particle scale to predict product distribution and temperature gradients for a biomass particle. The mentioned research has mainly addressed the pyrolysis of dry, thermally thick biomass particles. However, biomass moisture content should not be overlooked given its impact over product distribution, drying-associated energy requirements, and because it can reduce biomass milling energy consumption in pre-treatment stages [46].

Biomass pyrolysis kinetics and the different transfer phenomena that take place throughout pyrolysis add complexity to biomass pyrolysis models [39], and computational fluid dynamics (CFD) is usually applied to solve such complex systems [26, 41]. Moreover, when reliable models are required for biomass pyrolysis at a particle scale, the change in the particle's size over time needs to be considered [36, 27]. This creates an additional modelling challenge: the constantly changing dimension, composition and temperature at the surface

of the particle; which represents a moving boundary problem. Moving boundaries posses additional difficulties for finding numerical solutions, specially when traditional mesh methods are used in CFD [42]. As a result, increasingly complex models, high computational times and scaling-up difficulties would be expected in pyrolysis particle models [26]. The mentioned drawbacks and model-related complexities have hindered the application of particle models in process design as discussed previously in Chapter 2, and new alternatives to overcome such difficulties are required.

3.2 Model description

During pyrolysis, biomass components undergo thermal degradation in an inert atmosphere. Pyrolysis combines simultaneous heat transfer, mass transfer, chemical reactions and phase change processes. However, coupling the mentioned phenomena into modelling approaches remains a challenge [139]. In thermally thick particles, the low thermal conductivity of biomass generates internal temperature gradients [47]. Such gradients become then relevant for pyrolysis given the strong dependence of pyrolysis on both the reaction temperature and the heating rate. The thermal energy required for pyrolysis to take place is generally supplied as heat flux from the surroundings of the particle to its surface via radiation and convection, and whenever a solid surface is in contact with the biomass, also via conduction. The heat flow that reaches the surface of the biomass particle increases the particle's temperature. Moreover, the heat is transferred towards the inside of the particle where the regions with sufficient energy undergo pyrolysis. As a result, solid components react to form gases, condensable species in gaseous phase (tar or bio-oil) and solid char. While such reactions take place, the porosity of the biomass increases and the biomass particle shrinks. This behaviour is represented schematically in Figure 3.1, and a modelling approach for describing such behaviour is developed in this section.

3.2.1 Preliminary analysis

Due to the complexity of biomass pyrolysis, the dominating processes that take place at a particle scale need to be identified first so they can be included as part of the model [14, 39]. The controlling physical and chemical phenomena in pyrolysis can be initially explored by comparing conductive and convective heat transfer with kinetics. For this purpose, dimensionless numbers such as the thermal Biot number (Bi) and the pyrolysis number Py^I can

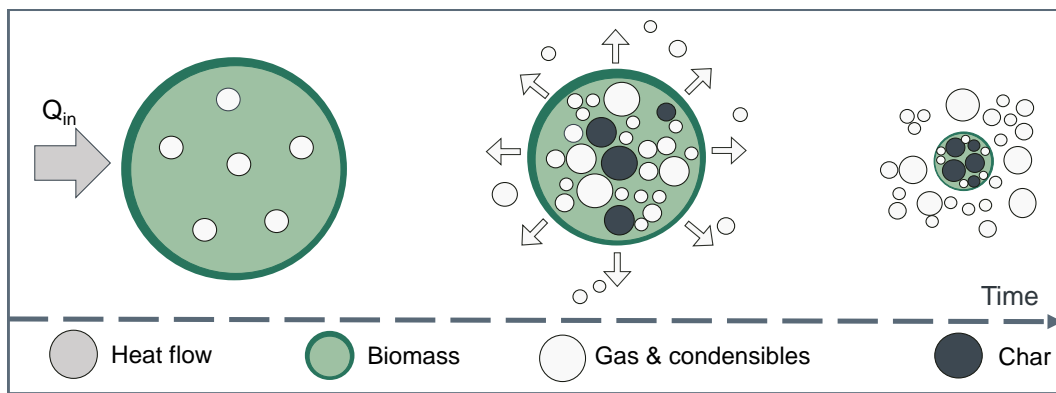


Figure 3.1: Representation of a shrinking biomass particle undergoing pyrolysis when a heat flux Q_{in} is supplied.

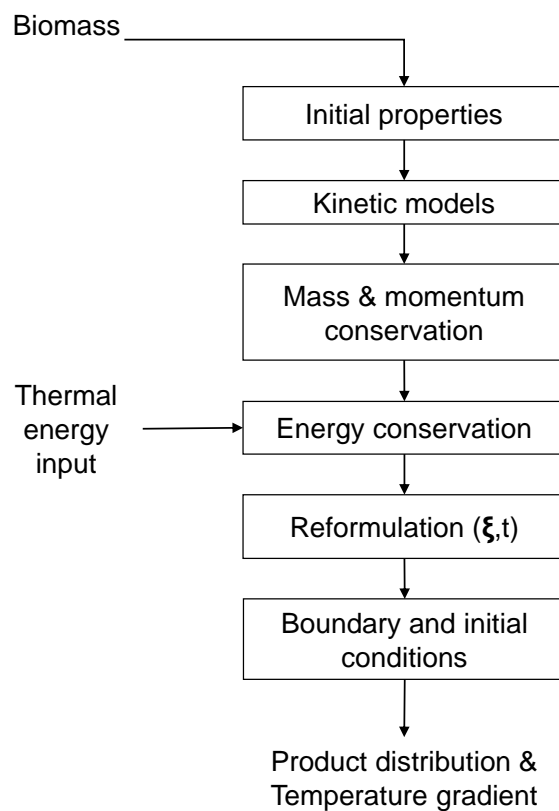


Figure 3.2: Schematic representation of the followed steps for developing the pyrolysis particle model.

be used [140]:

$$Py^I = \frac{\lambda}{k_{\text{apparent}} \rho_s C p_s L^2} \quad (3.1)$$

$$Bi = \frac{h_{\text{convection}} L}{\lambda} \quad (3.2)$$

The previous correlations for dimensionless numbers take into account the thermal conductivity of the particle, λ , the convective heat transfer coefficient between the surroundings of the particle and the surface of the particle, $h_{\text{convection}}$, the apparent kinetics for biomass pyrolysis, k_{apparent} , the solid phase density, ρ_s , the specific heat capacity of the solid phase, $C p_s$, and the characteristic length, L . Whereas the thermal Biot number allows to draw comparisons regarding the importance of the external convective heat transfer and the conductive intraparticle heat transfer; (Py^I) support comparisons between reaction timescales and conduction timescales. Consequently, such dimensionless numbers take into account operating parameters such as the heating rate during pyrolysis, the particle's external and internal temperatures [129]. Whereas the mentioned dimensionless numbers can provide some insights on the existence of intraparticle temperature gradients and pyrolysis controlling-phenomena; characteristic times add another layer of information towards a better understanding of the relevant phenomena that take place in pyrolysis [14]. Lower and upper limits for particle sizes ($d = 5.0 \cdot 10^{-3} \text{ m}$ to $2.0 \cdot 10^{-2} \text{ m}$), initial moisture contents (0 to 10 wt%), initial particle temperatures ($T_o = 80$ to 250°C) and external temperatures ($T_\infty = 260$ to 650°C) are considered for the calculation of characteristic times. Such lower and upper limits correspond with previous models and experimental studies addressing pyrolysis of thermally thick particles [140, 14, 52, 25]. The rates associated with reaction (apparent pyrolysis reaction rate), heat transfer (internal conduction and external convection) and mass transfer (gas phase molecular diffusion and intraparticle gaseous flow) are characteristic times used to describe pyrolysis [39].

Figure 3.3 shows that particles of $d \approx 20 \text{ mm}$, present Biot numbers ≥ 1 and Py^I numbers in the 10^{-6} order. In such cases, intraparticle temperature gradients occur and pyrolysis would be expected to be conduction-limited [76]. This is supported by the information presented in Table 3.1, where bigger particles experience higher conductive times when compared to external heating times; thus exhibiting temperature gradients [39]. In such conditions, parti-

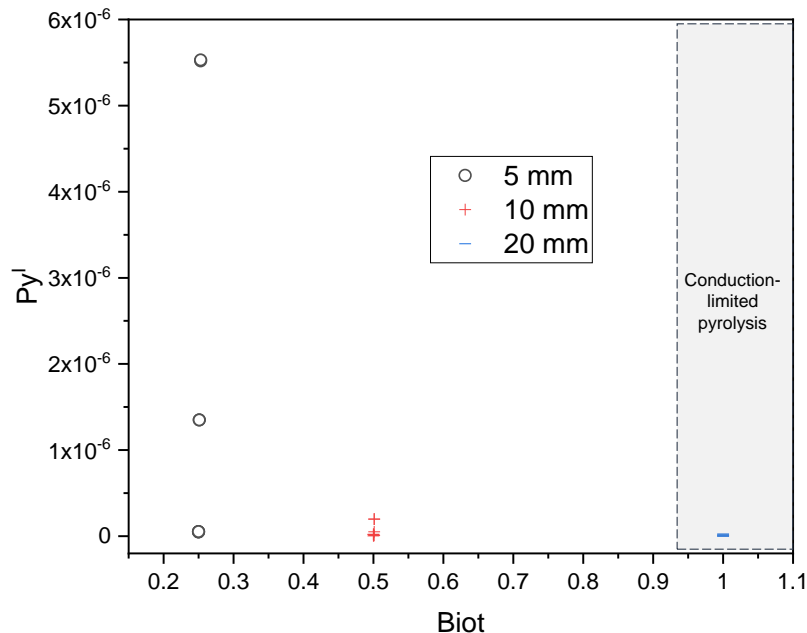


Figure 3.3: Biot numbers and corresponding \bar{P}_y^I numbers for different particle sizes and operating conditions. Conduction-limited pyrolysis lies in the shaded area of the plot

cles are thermally thick, which is of interest for this work. Similarly, shorter diffusion times and higher fluid flow times in centimetre-sized particles indicate diffusion-lead mass transfer in pyrolysis. Therefore, diffusion should be included when modelling centimetre-sized particles pyrolysis. For smaller particles, $d < 15$ mm, Figure 3.3 shows resulting $Bi < 1$ and \bar{P}_y^I in the 10^{-6} range. Hence, pyrolysis in such particles most likely is convection-limited [76]. This is supported by the information presented in Table 3.1, where bigger particles experience higher conductive times when compared to external heating times; thus exhibiting temperature gradients [39]. Similarly, shorter diffusion times and higher fluid flow times in centimetre-sized particles indicate diffusion-lead mass transfer in pyrolysis. Therefore, diffusion should be included when modelling centimetre-sized particles pyrolysis. Regarding particles with $d < 15$ mm, Figure 3.3 shows resulting $Bi < 1$ and \bar{P}_y^I in the 10^{-6} range. The following subsections explain in detail the developed modelling approach for describing pyrolysis in thermally thick biomass particles.

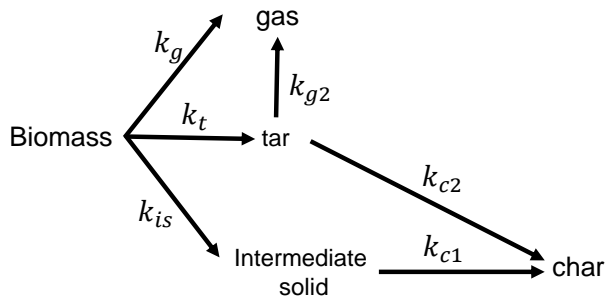
3.2.2 Kinetic models used in this work

This work considers two different lumped kinetic models and one detailed kinetic model for describing the reactions that take place during biomass pyrolysis. The considered lumped kinetic models include a tar cracking reaction and they group pyrolysis products under three categories: gases, tar and char [74, 36, 24]. The first lumped kinetic model (kinetic model

Table 3.1: Order of magnitude for the estimated characteristic times through pyrolysis for lower and upper limits

Diameter (mm)	T range (K)	Apparent kinetics ($\frac{1}{k_{\text{apparent}}}$)	Diffusion ($\frac{L^2}{D_{\text{eff}}}$)	Intraparticle fluid flow ($\frac{\mu L^2}{\Delta PK}$)	Conductive heat ($\frac{\rho_s C_p s L^2}{\lambda}$)	External heat ($\frac{\rho_s C_p s L^2}{h_{\text{convection}}}$)
5.0	525 – 650	$10^5 - 10^3$	1	10	1000	1 – 1000
20.0	525 – 650	$10^5 - 10^3$	10 – 1	10	$10^4 - 10^3$	1 – 1000

1) included in this work considers biomass as a single specie as shown below [136, 14].

**Figure 3.4:** Schematic of kinetic model 1 describing a lumped pyrolysis reaction scheme.

The second lumped kinetic model (kinetic model 2) included in this work takes into account biomass as a mixture of cellulose, hemicellulose and lignin. Moreover, such biomass components are considered to react without interactions between them and they undergo pyrolysis by forming intermediate (active) species as described in Figure 3.5 [141, 142]. The corresponding reactions, kinetic parameters and energy-related information are detailed in Table A.1.

The detailed reaction scheme developed by [25] and modified by [26] is also used in this section to describe pyrolysis reactions. This detailed kinetic model (kinetic model 3) contains pyrolysis reactions for biomass components and for intermediate species. Secondary charring reactions are also included in kinetic model 3 [25, 27] and the charring degree is

Table 3.2: Reactions, kinetic parameters and enthalpy of reaction for biomass pyrolysis considering a lumped kinetic model [26].

No. Reaction	Reaction	A (s^{-1})	Ea ($J \text{ mol}^{-1}$)	Δh ($J \text{ kg}^{-1}$)
1	Biomass \rightarrow Gas	$1.3 \cdot 10^8$	140300	150000
2	Biomass \rightarrow Char	$2.0 \cdot 10^8$	133100	150000
3	Biomass \rightarrow Tar	$1.1 \cdot 10^8$	121300	150000
4	Tar \rightarrow Gas	$4.3 \cdot 10^8$	108000	-50000

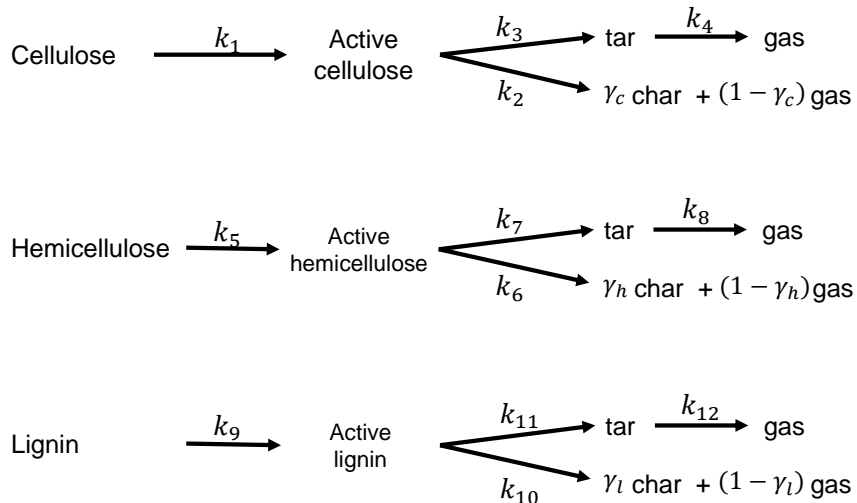


Figure 3.5: Schematic of kinetic model 2 describing pyrolysis for biomass components.

tuned depending on the operating conditions (fast, intermediate or slow pyrolysis) using the parameters x_{cell} , x_{hce} , x_{lig} , $x_{G\{ \cdot \}}$. The reactions, kinetic parameters and enthalpy of reaction associated with this detailed kinetic model are presented in Table A.3. The identification of the chemical species included in this kinetic model is included in the supporting information.

3.2.3 Moisture

In general, moisture can be found within biomass particles as bound water, as free water, or as water vapor [143]. Whereas bound water involves water absorption within cellular walls by hydrogen bonding with cellulose hydroxyl locations; free water refers to capillary water. Free water is only present for moisture contents below a threshold value, known as the fiber saturation point (FSP). Thus, the FSP represents the moisture content at which only bound water exists within cellular walls. If only bound water is present, the biomass moisture content is in equilibrium with the relative humidity of the surroundings [144]. Although the FSP needs to be determined for each particular type of biomass, woody materials usually present a FSP near 30 wt.% [144]. There is plenty of information regarding the FSP of wood and woody materials [145]; however, the information for other types of lignocellulosic biomass such as agricultural and agroindustry crops and waste biomass is scarce.

Wood drying had been studied previously using experiments and mathematical models [146, 143, 147, 148]. Moisture transport phenomena throughout drying is dependent on the heating rate. For slow drying conditions, temperatures reach values below the normal boiling point of water, liquid-phase flows are more relevant than vapor fluxes and water

transport is controlled by free water capillarity and by bound water diffusion [148]. For fast drying conditions, which also occur in the initial stages of pyrolysis or gasification, gas phase convective transport becomes relevant [148, 143].

In general, there are three modelling approaches for describing water evaporation in wood drying. The first approach, which is also the simplest one, is an equilibrium model that considers water evaporation to be described only by a Clausius-Clapeyron expression [149]. Such model is commonly applied for slow drying and it is unstable at high temperatures [146]. The second approach considers a thermal model, which is a complex model that includes moisture evaporation as a heat-rate-controlled process [143]. Such complex approach has been mainly used for describing drying processes in fluidized-bed and concurrent fixed-bed gasifiers and combustors, where drying and reaction characteristic times are of the same order of magnitude, meaning reaction and drying processes occur simultaneously [148]. Thermal models are useful whenever a detailed study of moisture evaporation is required. This model can describe with high accuracy moisture evaporation dynamics, at high temperatures, in wood drying and combustion applications [149, 150]. However, the complex mathematical formulations required for thermal models and their consequent high computational cost, have hindered its application in processes where moisture evaporation is not the main focus of study [148]. The third approach considers a kinetic model as a way to simplify the previously mentioned thermal model. Such kinetic model considers evaporation processes to be described by simple one-step Arrhenius-type chemical reactions. This simplified approach is particularly useful for describing bound water evaporation. Kinetic models are also an alternative to describe moisture evaporation in processes where drying occurs at faster rates than chemical reactions, such as pyrolysis or gasification. Whereas a kinetic model approach can reproduce moisture evaporation at high temperatures and it can be easily implemented in code, it might not be useful if capillarity is relevant for moisture evaporation and transport [28, 146, 148]. Similarly, a kinetic model approach is not useful if insights regarding mass transfer coefficients in moisture evaporation are required, nor if moisture contents close to the FSP are evaluated.

Water evaporation from biomass is incorporated in our model by considering both a kinetic model approach and a thermal model approach. The kinetic model approach use an Arrhenius-type correlation for describing biomass drying as presented in Table 3.5. Such approach lumps different physical phenomena into an Arrhenius-type expression; there-

fore, it represents a simplification of a water evaporation diffusion model [28, 29]. Within unreacted biomass regions, where lower temperatures are found, water recondensation is modelled by considering that water vapor is in supersaturated state. Moreover, condensation is considered to occur at a rate that is proportional to the ratio between the mass flowrate of water vapor and the biomass thickness. The developed model considers biomass with moisture contents below 10%wt., which is below the FSP for most woody materials. Given that the moisture contents evaluated with the model are below the fiber saturation point, and considering that only intermediate to fast pyrolysis conditions are taken into consideration; a kinetic law approach would provide a good representation of biomass drying [148].

3.2.4 Required physical properties

The specific heats, the enthalpies of formation and the composition of lumped species used in this section are determined using correlations and data found in literature for low pressure (0.1 MPa) and temperatures up to 1500 K [39, 25, 106]. The details on their calculation are included in the supporting information.

3.2.5 Estimation of thermophysical properties used in the model

The different components that take part in biomass pyrolysis either as reactants, intermediate species or products, make it necessary to have a set of thermophysical properties that can be used for modelling purposes. Whenever detailed kinetic models are chosen, up to 50 different chemical species are involved in pyrolysis; however, the thermophysical properties of all the involved species are usually not readily available in literature nor included in databases of commercial chemical process simulators [151, 124]. The required calculations and the procedure for estimating specific heats, density of gaseous mixtures and enthalpies of formation of the chemical species are presented in A.

3.2.6 Particle model development

The formulation of a particle model for describing biomass pyrolysis requires the combination of mass, energy and momentum conservation, and the corresponding pyrolysis kinetic models for solid and gaseous species. The developed model is based on the following considerations:

- Only gaseous species could be transferred across the solid particle [25].

The products from pyrolysis can be found either in solid phase (char) or in gaseous phase (gases and tar). When biomass pyrolysis occurs, the gaseous non-condensable and condens-

Table 3.3: Detailed reaction scheme and kinetic parameters for biomass pyrolysis [27, 25].

		Reaction	A (s^{-1})	E_a (J/mol)	Δh (kJ/kg)
R1	Cell	\rightarrow CellA	$4.0 \cdot 10^{13}$	188370	150
R2	CellA	\rightarrow $(1 - x_{cell}) \cdot (0.45\text{HAA} + 0.2\text{GLYOX} + 0.3\text{C}_3\text{H}_6\text{O} + 0.25\text{HMFU} + 0.05\text{H}_2 + 0.31\text{CO} + 0.41\text{CO}_2 + 0.4\text{CH}_2\text{O} + 0.83\text{H}_2\text{O} + 0.02\text{HCOOH} + 0.15\text{CH}_3\text{OH} + 0.1\text{CH}_3\text{CHO}) + 0.05\text{G}\{\text{H}_2\} + 0.2\text{G}\{\text{CH}_4 + 0.61\text{CHAR}\} + x_{cell} \cdot (5.5\text{CHAR} + 4\text{H}_2\text{O} + 0.5\text{CO}_2 + \text{H}_2)$	$2.0 \cdot 10^6$	80000	150
R3	CellA	\rightarrow $(1 - x_{cell}) \cdot (\text{LVG/same as R2}) + x_{cell} \cdot (5.5\text{CHAR} + 4\text{H}_2\text{O} + 0.5\text{CO}_2 + \text{H}_2)$	4.0 T	41860	150
R4	HCE	\rightarrow $0.4\text{AA(HW)}/0.1\text{AA(SW)} + 0.58\text{HCEA1} + 0.42\text{HCEA2}$	$1.0 \cdot 10^{10}$	129770	
R5	HCEA1	\rightarrow $(1 - x_{hce}) \cdot (0.5\text{CO} + 0.5\text{CO}_2 + 0.325\text{CH}_4 + 0.8\text{CH}_2\text{O} + 0.1\text{CH}_3\text{OH} + 0.25\text{C}_2\text{H}_4 + 0.125\text{ETOH} + 0.025\text{H}_2\text{O} + 0.025\text{HCOOH} + 0.275\text{G}\{\text{CO}_2\} + 0.4\text{G}\{\text{COH}_2\} + 0.125\text{G}\{\text{H}_2\} + 0.45\text{G}\{\text{CH}_3\text{OH}\} + 0.875\text{CHAR}) + x_{hce} \cdot (4.5\text{CHAR} + 3\text{H}_2\text{O} + 0.5\text{CO} + \text{H}_2)$	$1.2 \cdot 10^9$	125580	
R6	HCEA1	\rightarrow $(1 - x_{hce}) \cdot (0.1\text{CO} + 0.8\text{CO}_2 + 0.3\text{CH}_2\text{O} + 0.25\text{H}_2\text{O} + 0.05\text{HCOOH} + 0.15\text{G}\{\text{H}_2\} + 0.15\text{G}\{\text{CO}\} + 1.2\text{G}\{\text{COH}_2\} + 0.2\text{G}\{\text{H}_2\} + 0.625\text{G}\{\text{CH}_4\} + 0.375\text{G}\{\text{C}_2\text{H}_4\} + 0.875\text{CHAR}) + x_{hce} \cdot (4.5\text{CHAR} + 3\text{H}_2\text{O} + 0.5\text{CO}_2 + \text{H}_2)$	0.15 T	33500	
R7	HCEA1	\rightarrow $(1 - x_{hce}) \cdot (\text{XYL /same as R5}) + x_{hce} \cdot (4.5\text{CHAR} + 3\text{H}_2\text{O} + 0.5\text{CO}_2 + \text{H}_2)$	3.0 T	46050	
R8	HCEA2	\rightarrow $(1 - x_{hce}) \cdot (0.2\text{HAA} + 0.175\text{CO} + 0.275\text{CO}_2 + 0.5\text{CH}_2\text{O} + 0.1\text{ETOH} + 0.2\text{H}_2\text{O} + 0.025\text{HCOOH} + 0.4\text{G}\{\text{CO}_2\} + 0.925\text{G}\{\text{COH}_2\} + 0.25\text{G}\{\text{CH}_4\} + 0.3\text{G}\{\text{CH}_3\text{OH}\} + 0.275\text{G}\{\text{C}_2\text{H}_4\} + \text{CHAR}) + x_{hce} \cdot (4.5\text{CHAR} + 3\text{H}_2\text{O} + 0.5\text{CO}_2 + \text{H}_2)$	$0.5 \cdot 10^{10}$	138140	
R9	LIG-C	\rightarrow $0.35\text{LIG-CC} + 0.1\text{pCOUMARYL} + 0.08\text{PHENOL} + 0.32\text{CO} + 0.3\text{CH}_2\text{O} + \text{H}_2\text{O} + 0.7\text{G}\{\text{CH}_2\} + 0.495\text{G}\{\text{CH}_4\} + 0.41\text{G}\{\text{C}_2\text{H}_4\} + 5.735\text{CHAR}$	$1.33 \cdot 10^{15}$	203020	
R10	LIG-H	\rightarrow $\text{LIG-OH} + 0.25\text{HAA} + 0.5\text{C}_3\text{H}_6\text{O} + 0.5\text{G}\{\text{C}_2\text{H}_4\}$	$0.67 \cdot 10^{13}$	156970	
R11	LIG-O	\rightarrow $\text{LIG-O} + \text{CO}_2$	$0.33 \cdot 10^9$	106740	
R12	LIG-CC	\rightarrow $(1 - x_{lig}) \cdot (0.35\text{HAA} + 0.3\text{pCOUMARYL} + 0.2\text{PHENOL} + 0.4\text{CO} + 0.65\text{CH}_4 + 0.6\text{C}_2\text{H}_4 + 0.7\text{H}_2\text{O} + 0.4\text{G}\{\text{CO}\} + \text{G}\{\text{COH}_2\} + 6.75\text{CHAR}) + x_{lig} \cdot (15\text{CHAR} + 4\text{H}_2\text{O} + 3\text{H}_2)$	$3.0 \cdot 10^7$	131860	
R13	LIG-OH	\rightarrow $(1 - x_{lig}) \cdot (\text{LIG} + 0.55\text{CO} + 0.05\text{CO}_2 + 0.1\text{CH}_4 + 0.6\text{CH}_3\text{OH} + 0.9\text{H}_2\text{O} + 0.05\text{HCOH} + 0.6\text{G}\{\text{CO}\} + 0.85\text{G}\{\text{COH}_2\} + 0.1\text{G}\{\text{H}_2\} + 0.35\text{CH}_4 + 0.3\text{G}\{\text{CH}_3\text{OH}\} + 0.2\text{G}\{\text{C}_2\text{H}_4\} + 5.735\text{CHAR})$	$1.0 \cdot 10^8$	125580	
R14	LIG	\rightarrow $(1 - x_{lig}) \cdot (\text{Synapaldehyde} + x_{lig} \cdot (10.5\text{CHAR} + 3\text{H}_2\text{O} + 0.5\text{CO}_2 + 3\text{H}_2))$	4.0 T	50200	
R15	LIG	\rightarrow $(1 - x_{lig}) \cdot (\text{LIG} + 0.2\text{C}_3\text{H}_6\text{O} + \text{CO} + 0.2\text{CH}_4 + 0.2\text{CH}_2\text{O} + 0.4\text{CH}_3\text{OH} + 0.2\text{CH}_3\text{CHO} + 0.95\text{H}_2\text{O} + 0.05\text{HCOOH} + 0.45\text{G}\{\text{CO}\} + 0.5\text{G}\{\text{COH}_2\} + 0.4\{\text{CH}_4\} + 0.65\text{G}\{\text{C}_2\text{H}_4\} + 4.15\text{CHAR})$	$0.40 \cdot 10^9$	125580	
R16	LIG	\rightarrow $(1 - x_{lig}) \cdot (\text{LIG} + 0.4\text{CO} + 0.2\text{CH}_4 + 0.4\text{CH}_2\text{O} + 0.6\text{H}_2\text{O} + 0.2\text{G}\{\text{CO}\} + 2\text{G}\{\text{COH}_2\} + 0.4\{\text{CH}_4\} + 0.4\text{G}\{\text{CH}_3\text{OH}\} + 0.5\text{G}\{\text{C}_2\text{H}_4\} + 6\text{CHAR} + x_{lig} \cdot (10.5\text{CHAR} + 3\text{H}_2\text{O} + 0.5\text{CO}_2 + 3\text{H}_2))$	0.083 T	33500	
R17	G $\{\text{CO}_2\}$	\rightarrow CO_2	$1.0 \cdot 10^5$	100460	
R18	G $\{\text{CO}\}$	\rightarrow $(1 - x_{G\{\cdot\}}) \cdot \text{CO} + x_{G\{\cdot\}} \cdot (0.5\text{CHAR} + 0.5\text{CO}_2)$	$3.0 \cdot 10^{13}$	209300	
R19	G $\{\text{COH}_2\}$	\rightarrow $0.75\text{G2}\{\text{COH}_2\} + 0.25(\text{H}_2 + 0.5\text{CO} + 0.25\text{CO}_2 + 0.25\text{CHAR})$	$1.0 \cdot 10^6$	100460	
R20	G $\{\text{H}_2\}$	\rightarrow H_2	$1.0 \cdot 10^{12}$	313960	-50
R21	G $\{\text{CH}_4\}$	\rightarrow CH_4	$2.0 \cdot 10^{13}$	300000	-50
R22	G $\{\text{CH}_3\text{OH}\}$	\rightarrow $(1 - x_{G\{\cdot\}}) \cdot \text{CH}_3\text{OH} + x_{G\{\cdot\}} \cdot (\text{CHAR} + \text{H}_2\text{O} + \text{H}_2)$	$1.2 \cdot 10^{13}$	209300	
R23	G $\{\text{C}_2\text{H}_4\}$	\rightarrow $0.3\text{C}_2\text{H}_4 + 0.7(\text{CH}_4 + \text{CHAR})$	$1.0 \cdot 10^6$	100460	
R24	G2 $\{\text{COH}_2\}$	\rightarrow $0.2\text{G3}\{\text{COH}_2\} + 0.8(\text{CO} + \text{H}_2)$	$1.5 \cdot 10^9$	209300	

sible species that are released from the solid phase, have lower molecular weights than the solid species that remain in the solid phase (biomass and char). Therefore, gas molecules can move through the shrinking porous solid easier than bigger molecules corresponding to the solid components [4, 25]. The mentioned consideration influences the resulting particle model given that the mass balances and continuity equations will only consider gaseous moving species. Moreover, by neglecting the transport of solid species within the solid particle, changes in the pore size distribution associated to internal solid fragmentation cannot be evaluated. Although solid fragmentation had been found in coal and biomass combustion and pyrolysis, its consideration is relevant whenever biochar structure and shape needs to be determined. Moreover, solid fragmentation provides some insights regarding char surface area, which is an important property for assessing adsorption capabilities of a produced char [2]. As a consequence, by not considering moving solid species, the developed model would not be able to predict pore distribution or surface area changes in the resulting char.

- The gaseous species behave as ideal gases [26].

Existing particle models for describing combustion, pyrolysis or gasification, consider the gaseous products to have ideal behaviour [4, 39, 26]. The mentioned consideration is related to the low pressures at which conventional pyrolysis takes place (0.1 MPa), which allow to consider ideal behaviour in the 450-800 °C range where pyrolysis takes place [4]. The ideal gas consideration has an impact over the properties of the gaseous phase and also over the way momentum and heat transfer is described [39]. Consequently, the current model could only be used within pressure and temperature ranges that guarantee an ideal behaviour. Any other thermodynamic state that does not guarantee ideal behaviour on the gaseous products

Table 3.4: Parameters for biomass water evaporation [28, 29]

Process	A (s ⁻¹)	Ea (J mol ⁻¹)	Δh (J kg ⁻¹)
moisture → H ₂ O _{vapor}	5.13 · 10 ¹⁰	88000	-2440000
H ₂ O _{vapor} → moisture			

Table 3.5: Parameters for biomass water evaporation [28, 29]

Process	A (s ⁻¹)	Ea (J mol ⁻¹)	Δh (J kg ⁻¹)
moisture → H ₂ O _{vapor}	5.13 · 10 ¹⁰	88000	-2440000

from pyrolysis cannot be described.

- Reacting particles enter the process with moisture contents way below the fiber saturation point [24].

Moisture content in pyrolysis modelling represents a trade-off between adding complexity to the model and expanding the model to different types of feedstocks. When moisture is included, another phase (liquid) needs to be considered and a triphasic pyrolysis problem needs to be solved. In such circumstances, complexity arises from the estimation of transport properties and from considering water evaporation that takes place in a porous media [38, 66]. Because of this, previous works that modelled biomass pyrolysis did not include moisture content in their analysis [39, 25, 4, 26]. In spite of this, moisture content is an important component of lignocellulosic feedstocks. In some cases, moisture content could reach as much as 60 % and neglecting its analysis limits the application of the developed model [38].

- Biomass is considered to be constituted by cellulose, hemicellulose and lignin only [76].

As it was mentioned in the previous chapter, biomass is a mixture of cellulose, hemicellulose, lignin, extractives, ashes and moisture [25]. Therefore, by considering only the carbohydrates in the analysis, the model is limited to cellulose, hemicellulose and lignin-only applications. Moreover, when considering that during pyrolysis, cellulose, hemicellulose and lignin interact with each other and that they decompose through 24 different reactions, to simplify the analysis might provide some fundamental understanding of the physical and chemical phenomena that takes place during pyrolysis at a particle scale [39, 52]. In addition, information regarding cellulose, hemicellulose and, in some cases, lignin, can be retrieved from literature to compare predicted and experimental product and temperature distributions, ruling out underlying synergies between biomass components [76].

- The biomass particle is spherical [105] and it shrinks with time following an isometric behaviour [152, 26, 25].

Biomass particles shrink during pyrolysis. This behaviour had been captured in previous works [26, 4] by considering spherical particles. Moreover, by considering an isometric behaviour, properties are considered to vary online with time and in the radial direction. This

consideration implies that properties remain the same as long as they are at the same radial distance from the centre of the particle and avoids the complexity associated when two or three dimensions are considered during pyrolysis [26, 4]. However, such consideration also limits the applicability of the model, and only idealized spherical particles could be evaluated. Similarly, transfer phenomena can also be assessed in the radial direction. Indeed, other geometries typically found for biomass (cylinders and discs) cannot be represented by the developed model [39].

- Latent heats associated to phase change in reactants or products is negligible [95].

Some of the components of biomass, and some of the products from pyrolysis could be present in amorphous or crystalline forms. Cellulose for instance, has a crystalline and amorphous fractions. The phase change enthalpy in such components is not considered in this modelling approach. The products from pyrolysis are considered to be either in solid phase or in gaseous phase, whether if they are condensable or permanent gases [153]. Such considerations neglect the use of enthalpy of phase change in the energy conservation equation. This simplification could have an effect over the temperature profile determination whenever the energy associated with phase change is considerable.

- Solid fragmentation for biomass particles undergoing pyrolysis is neglected [26, 25].

Throughout pyrolysis, char can be subjected to cracking and shrinking, which change the shape of the particles and can alter pyrolysis intra-particle phenomena [4]. By neglecting solid fragmentation, changes in shape or volume will only be related to shrinking. If biochar's mechanical resistance is a property of interest after pyrolysis, solid fragmentation should be considered.

- There is local thermal equilibrium between solid and gaseous phases [39, 25, 4, 26].

Local thermal equilibrium among phases has been considered for biomass pyrolysis in previous works [39, 4, 25, 26]. The considered approach involves a shrinking particle and the reaction (pyrolysis) takes place in the whole volume of the evaluated particle. Moreover, as it was stated before in this section, gaseous species move across the porous particle. Under such conditions, assumptions of local mass equilibrium cannot hold and the assumption of local thermal equilibrium becomes necessary to have an approximation for describing pyrolysis [154].

Throughout pyrolysis, volatiles and gases are released; consequently, biomass particles shrink and their porosity increases over time [72]. To account for this, shrinking is considered to be proportional to biomass conversion (η), which includes the initial (m_{b0}) and instantaneous (m_b) mass of biomass. Moreover, the volume of the particle (V_p) is considered to be a function of the initial particle volume (V_{p0}) and a η dependent shrinking factor f_{shrink} , as presented in equations 3.3 to 3.5 [26].

$$\eta = \frac{m_b}{m_{b0}} \quad (3.3)$$

$$V_p = V_{p0} \cdot f_{\text{shrink}} \quad (3.4)$$

$$f_{\text{shrink}} = f_{\text{shrink}_{\min}} + \eta(1 - f_{\text{shrink}_{\min}}) \quad (3.5)$$

Throughout pyrolysis, solid and gaseous phases coexist; thus individual and phase mass balances are included. Lumped and detailed kinetic reaction schemes, their corresponding stoichiometry, heats of reaction and kinetic parameters, are considered in the particle model [27, 25]. In the following section, detailed kinetic models will consider biomass constituted by cellulose, hemicellulose and lignin only. The continuity equation is applied to develop mass balances, and instantaneous concentrations of solid and gaseous phases, as well as for the individual species i in each phase are expressed in terms of the density. The instantaneous density for the solid phase ρ_S and for each individual component of the solid phase $\rho_{S,i}$ are calculated using the porosity of the reacting solid particle (φ) from equations 3.6 and 3.7.

$$\frac{\partial [\rho_S(1 - \varphi)]}{\partial t} = \Gamma_S \quad (3.6)$$

$$\frac{\partial [\rho_{S,i}(1 - \varphi)]}{\partial t} = \Gamma_{S,i} \quad (3.7)$$

The density of the solid phase as a function of the particle volume (V_p) and the mass of the solid phase (m_s) is defined as $\rho_S = m_s / (V_p \cdot \varphi)$. Similarly, the bulk density $\tilde{\rho}_i$ for a given component i can be calculated as $\tilde{\rho}_i = m_i / V_p$. The modeled particles are spherical and V_p can be estimated with the particle radius (r). The porosity (φ) is calculated with Equation 3.8, considering the bulk densities of biomass (ρ_{biomass}) and biochar ($\tilde{\rho}_{\text{char}}$), and the initial density of cellulose ($\rho_{\text{cellulose}}$) and biochar (ρ_{char}), which are obtained from literature [52].

$$\varphi = \frac{(\tilde{\rho}_{\text{char}} + \tilde{\rho}_{\text{biomass}})^2}{(\rho_{\text{char}} \tilde{\rho}_{\text{char}} + \rho_{\text{biomass}} \tilde{\rho}_{\text{biomass}})} \quad (3.8)$$

The solid phase's net formation rate (Γ_S) is determined from the contribution of individual solid components ($\Gamma_{S,i}$), as presented in equations 3.9 and 5.43. Resulting individual rates (r_j) are calculated with the Arrhenius equation (Eq. 5.44) using the concentration $C_{i,j}$ of the component i in reaction j , and with the corresponding stoichiometric coefficients ($\gamma_{i,j}$).

$$\Gamma_S = \sum_{i=1}^{n_c} \Gamma_{S,i} \quad (3.9)$$

$$\Gamma_{S,i} = \sum_{j=1}^{n_r} \gamma_{i,j} r_j \quad (3.10)$$

$$r_j = A_j e^{-\left(\frac{E_a}{R_{ideal}T}\right)} C_{i,j} \quad (3.11)$$

The mass balance for the gaseous phase (G) is defined in terms of the density of the gas mixture (ρ_G), the porosity (φ), the velocity of the gaseous phase (\mathbf{u}) and the net formation at the gaseous phase (Γ_G). ρ_G is calculated by applying the continuity equation in the gaseous phase (Eq. 3.12). The Darcy equation (Eq. 3.13) is applied for describing momentum transfer inside the porous particle, considering that the gas mixture moves across the solid phase resembling a flow of gases through porous media [4, 26].

$$\frac{\partial (\rho_G \varphi)}{\partial t} = -\nabla \cdot (\rho_G \mathbf{u}) + \Gamma_G \quad (3.12)$$

$$\mathbf{u} = -\frac{K_S}{\varphi \mu_G} \nabla P \quad (3.13)$$

Whereas the dynamic viscosity (μ_G) is obtained from literature [74], the effective permeability of the solid phase (K_S) is estimated as a linear combination of the solid components (Eq. 3.14).

$$K_S = \eta K_{biomass} + (1 - \eta) K_{char} \quad (3.14)$$

Gases are considered to follow an ideal behaviour and the corresponding equation of state is applied. Mass balances for individual components in the gaseous phase (G,i) are calculated with Eq. 3.15, where the diffusive term ($\nabla \cdot \mathbf{j}_{Gi}$) and individual gas fluxes passing through the biomass particle (\mathbf{j}_{Gi}) are estimated with the effective diffusivity (D_{eff}) using Eq. 3.16.

$$\frac{\partial (\rho_G \varphi w_{G,i})}{\partial t} = -\nabla \cdot (\rho_{G,i} \varphi w_{G,i} \mathbf{u}) - \nabla \cdot \mathbf{j}_{Gi} + \Gamma_{G,i} \quad (3.15)$$

$$\mathbf{j}_{G,i} = -D_{\text{eff}} \nabla \rho_G \varphi w_{G,i} \quad (3.16)$$

For any two gaseous species, A and B, diffusivity coefficients are estimated considering binary gaseous diffusion applying the correlation described in Eq. 3.17 [155]. The diffusion volumes ($\sum v_{A,B}$) are calculated for each component as the sum of atomic diffusion volumes found in literature [156, 155]. The effective diffusivity of the gaseous phase is calculated using the Fairbanks and Wilke expression [26]:

$$D_{AB} = \frac{1.00 \cdot 10^{-3} T^{1.75} \left(\frac{1}{MW_A} + \frac{1}{MW_B} \right)^{1/2}}{P[(\sum v_A)^{1/3} + (\sum v_B)^{1/3}]^2} \quad (3.17)$$

The energy balance includes both solid and gaseous phases as presented in equations 3.18, 3.19 and 3.20. Average specific heats ($\langle Cp_S \rangle$), material derivatives ($\frac{DT}{Dt}, \frac{DP}{Dt}$), effective thermal conductivity (λ_{eff}), heats of reaction ($\Delta H_{rx,j}$) and the produced/consumed mass of components of interest in a reaction ($m_{j,i}$) are considered in the energy balance calculation.

$$(\rho_s \varphi \langle Cp_S \rangle + \rho_G (1 - \varphi) \langle Cp_G \rangle) \frac{DT}{Dt} = -\nabla \cdot \mathbf{q} - \left(\frac{\partial \ln \rho_G}{\partial T} \right)_P \frac{DP}{Dt} \quad (3.18)$$

$$\nabla \cdot \mathbf{q} = \nabla \cdot (\lambda_{\text{eff}} \nabla T) + Q_{rx} \quad (3.19)$$

$$Q_{rx} = \sum_{j=1}^{n_r} \Delta H_{rx,j} \cdot m_{j,i} \quad (3.20)$$

$\langle Cp_G \rangle$ is calculated considering ideal gas additive properties, including molar fractions and specific heats of individual gaseous species. The effective thermal conductivity λ_{eff} and the average specific heat of the solid phase $\langle Cp_S \rangle$, are calculated in terms of the biomass ratio η , using the following correlations [26]:

$$\lambda_{\text{eff}} = \eta \lambda_{\text{biomass}} + (1 - \eta) \lambda_{\text{char}} \quad (3.21)$$

$$\langle Cp_S \rangle = \eta Cp_{\text{biomass}} + (1 - \eta) Cp_{\text{char}} \quad (3.22)$$

The values of the properties described in this section that are retrieved from literature are presented in Table 3.6.

3.2.7 Initial and boundary conditions

Initially, there are no formed products; therefore, the densities of char, tar, gases and all the individual products that could be formed from pyrolysis are zero. Biomass particles have an initial temperature T_0 , which needs to be defined, and they are under atmospheric pressure

Table 3.6: Properties of the substances used by the model

Property	Value	Units	Observation
m_{b0}	$\rho_{biomass} \cdot V p_0$	kg	Initial mass of biomass
r_0	$5 \text{ to } 15 \cdot 10^{-3}$	m	Initial radius
$f_{shrink_{min}}$	0.50	-	[26]
φ_0	0.68	-	Initial porosity [25]
$\rho_{biomass}$	1656.00	kg m ⁻³	[157]
ρ_{char}	1600.00	kg m ⁻³	[26]
μ_G	$3.0 \cdot 10^{-5}$	kg m ⁻¹ s ⁻¹	[74]
$K_{biomass}$	$1.0 \cdot 10^{-14}$	m ²	[74]
K_{char}	$1.0 \cdot 10^{-14}$	m ²	[74]
$\lambda_{biomass}$	0.25	w m ⁻¹ s ⁻¹	[26]
λ_{char}	0.10	w m ⁻¹ s ⁻¹	[26]
P_∞, P_0	101325	Pa	-
$h_{convection}$	20.00	W m ⁻² K ⁻¹	[4]
σ	$5.67 \cdot 10^{-8}$	W m ⁻² K ⁻⁴	[26]

P_0 . Similarly, given that there are no products, the velocity of the gaseous species inside the particle is zero. The mentioned conditions can be summarized as:

$$\rho_{particle} = \rho_{biomass}; \rho_i = 0, \forall i \neq biomass \quad (3.23)$$

$$T = T_0; \mathbf{u} = 0 \text{ (m s}^{-1}\text{)}; P = P_0 \quad (3.24)$$

For the boundary conditions at the surface of the particle, the external pressure (P_∞) is considered. The heat flux in the boundary ($r=R$) is described in terms of convection and radiation. For the radiation term, the Stefan-Boltzmann constant (σ) and the surface emissivity (ε) are considered. The mentioned conditions are summarized as follows:

$$P_{r=R} = P_\infty \quad (3.25)$$

$$\nabla \cdot (\lambda_{eff} T) = h_{convection}(T_\infty - T_{r=R}) + \sigma \varepsilon (T_\infty^4 - T_{r=R}^4) \quad (3.26)$$

3.2.8 Numerical solution and validation

3.2.8.1 Numerical solution

The previously developed model could be potentially applied for a one, two or three dimensional system. Given that a spherical particle was considered, the previously developed model is applied for a radial domain. For avoiding repetition, only the application of the continuity equation for the gaseous phase (Eq. 3.12) for a radial domain will be presented in

this section. Considering spherical coordinates and assuming that any variation takes place only in the radial direction, Eq. 3.12 can be presented in terms of the radial coordinate r :

$$\frac{\partial(\rho_G \varphi)}{\partial t} = -\frac{1}{r^2} \frac{\partial(\rho_G \varphi r^2 v_{radial})}{\partial r} + \Gamma_G \quad (3.27)$$

To overcome the challenges associated with the moving boundary of the shrinking particle throughout pyrolysis, we reformulate the model by applying Landau's transformation for a one dimension problem. This method had been used before for describing water evaporation from shrinking particles [66] and for describing transient two-phase diffusion [67]; however, its application in biomass pyrolysis modelling is novel. This approach represents a boundary immobilisation technique and uses the following spatial transformation:

$$\xi = \frac{r}{R} \quad (3.28)$$

The mentioned transformation considers the radial position (r), the radius of the particle at a given time (R) and a new variable (ξ) that varies between 0 (centre of the particle) and 1 (boundary of the particle). This transformation fixes the moving boundary at $\xi=1$ in a new co-ordinate system that includes ξ and time; thus avoiding computationally expensive methods for dealing with moving boundaries and facilitating the resolution of the model. Similarly to what was performed for presenting the equations in a radial domain, equations 3.12 and 3.27 are reformulated as follows:

$$\frac{\partial(\rho_G \varphi)}{\partial t} + \frac{\xi}{R} \frac{\partial R}{\partial t} \frac{\partial(\varphi \rho_G)}{\partial \xi} = -\frac{1}{R} \frac{1}{\xi^2} \frac{\partial(\xi^2 \varphi \rho_G v_{radial})}{\partial \xi} + \Gamma_G \quad (3.29)$$

The reformulated particle model, consisting of a set of differential and algebraic equations (DAEs) in the (ξ, t) domain, is implemented and solved using gPROMS ModelBuilder® version 7.0.9.

3.2.8.2 Validation of the developed model

The developed model is validated against experimental data from the literature in terms of yield of relevant products from pyrolysis and of the temperature at the centre of the particle. Previous works have dealt with lumped kinetics and modelling approaches[14, 26, 39]. The present work includes detailed kinetics in the analysis. Due to the variety of products that arise from detailed kinetics, and because of the limited information available,

only levoglucosan (LVG) yields are validated with experimental results. This decision is also aligned with LVG's high market price and potential applications in pharmaceutical, polymer and fine chemicals industries [119]. A previous work [15] that determined LVG yields at different pyrolysis temperatures, using cellulose as feedstock, is employed for the comparison with the results from the developed model. Correspondingly, in this case, cellulose is the only constituent of biomass and product yields (Y_{LVG}) are calculated using the model-predicted LVG moles (n_{LVG}), the maximum theoretical LVG moles for a given temperature ($n_{LVG, \text{max}}$), and the porosity (ϕ), with equations 3.30 and 3.31.

$$Y_{LVG} = \frac{n_{LVG}}{n_{LVG, \text{max}}} \quad (3.30)$$

$$n_{LVG} = \frac{w_{LVG} \rho_G(\phi) V_p}{MW_{LVG}} \quad (3.31)$$

The particle's core temperature is validated compared experimental results from a previous work [14] that addressed the behavior of a high-moisture content spherical biomass piece, exposed to radiative heat during pyrolysis. In this case, woody biomass, lumped kinetics [26] and a defined incident heat flux distribution around the modelled particle [14] are considered. For assessing the performance of the model regarding LVG yields prediction, the mean deviation (MD) is calculated using Eq. 3.32; whereas for evaluating the particle's core temperature prediction, the MD is calculated using Eq. 3.33 [39].

$$MD = |Y_{LVG, \text{experiment}}(t_{\text{final}}) - Y_{LVG, \text{model}}(t_{\text{final}})| \quad (3.32)$$

$$MD = \frac{1}{n} \sum_{i=1}^n |T_{\text{experiment}}(t_i) - T_{\text{model}}(t_i)| \quad (3.33)$$

3.3 Results and discussion

In this section, model-predicted temperature gradients and product distribution are described at first; and results from the developed model are then compared with experimental data from literature. The application of the particle model for assessing early-stage economic, environmental and energy outcomes is also presented in this section.

3.3.1 Temperature and product distribution from the particle model

Figure 3.6 a) suggests that within the modelled particles, higher temperatures are found near the surface of the particle whereas lower temperatures are reached towards the centre of the particle. This behaviour describes a particle's thermal gradient and corresponds with previous pyrolysis experiments of thermally thick biomass particles [136]. The observed temperature gradient could be attributed, among other factors, to biomass' low thermal conductivity ($0.1\text{--}0.25 \text{ W m}^{-1} \text{ K}^{-1}$), the particle's size and porosity, and to the fast heating considered in this particular case[139, 26]. In such conditions, heat transfer via radiation and convection from the surroundings of the biomass particle to the particle's surface is faster than the heat being transferred inside the particle, which occurs mainly via conduction. Such behaviour corresponds with the higher conduction times, compared with the external heating times, from the preliminary analysis presented in Table 3.1. Similarly, Figure 3.6 b) shows an increase in temperature occurring at the centre of the particle while pyrolysis takes place. As seen in Figure 3.6 b), the temperature in the centre of the particle increases until an equilibrium is reached after 100 s, for the evaluated conditions. This behaviour resembles previous experiments of thermally thick biomass particles undergoing fast pyrolysis [14]. Consequently, the developed pyrolysis model predicts temperature gradients in thermally thick biomass particles. A good agreement between modelled and experimental temperatures ($\text{MD} \approx 0.6\text{--}3.6^\circ\text{C}$) is reached after 50 s of pyrolysis. However, if the model is applied to different heating conditions, particle sizes or feedstocks, particular attention needs to be placed on the incident heat flux distribution, pyrolysis kinetics and biomass properties[14].

The developed particle model can make use of both lumped and detailed kinetic models for predicting pyrolysis product distribution. Figure 3.7 shows that lumped kinetics provides a general understanding of the effect of changing operating conditions over pyrolysis product distribution. In this particular case, modifying the reaction temperature by 100°C , reduces the concentration of gases from pyrolysis in almost 6 wt. %. Complementary, Figure

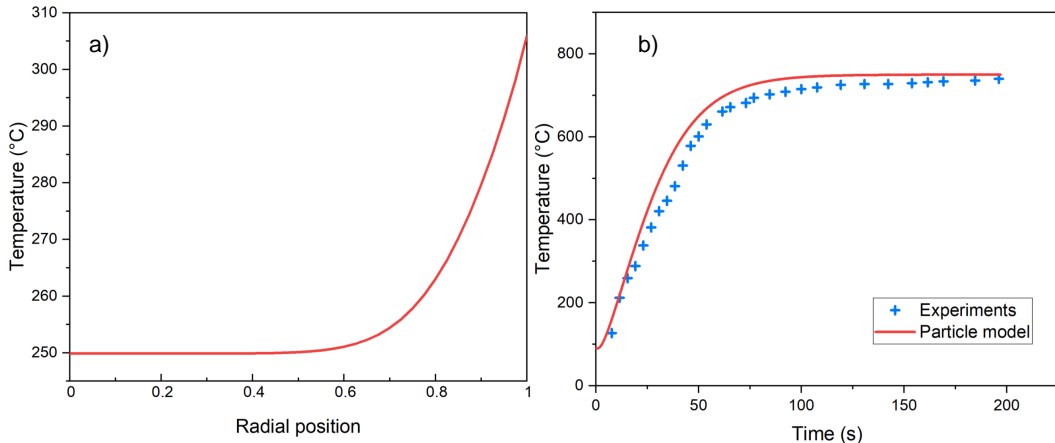


Figure 3.6: a) Temperature gradient, from the core (0.0) to the border (1.0), for 5 mm diameter particles undergoing fast pyrolysis with $T_0=250^\circ\text{C}$ and after 5 s. b) Predicted particle's core temperature for a 5 mm diameter particle, 9 wt. % initial moisture and 60 kW m^{-2} of incident heat flux; and corresponding experiments from literature [14].

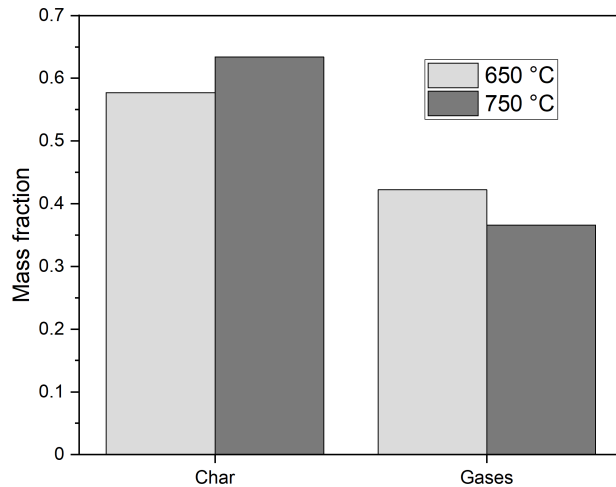


Figure 3.7: Product distribution at different temperatures using a cellulose particle model with a lumped kinetic model.

3.8 shows that if the same analysis is performed using detailed kinetics, at least 12 additional species could be identified, platform chemicals included. The presence of platform chemicals with high market value, such as levoglucosan (LVG) or hydroxymethylfurfural (HMFU), which could be orders of magnitude more expensive than energy-oriented gases from pyrolysis [119]; brings a new perspective of the potential applications for pyrolysis.

Figure 3.9 shows that the developed particle model can predict LVG yields from biomass fast pyrolysis, and that the predicted yields maintain correspondence with experimental data literature [15]. Considering that the MD at 500°C is 5.28 wt.%, and at 600°C is 1.04 wt.%; the model's LVG predictions are more accurate at higher temperatures (600°C). This be-

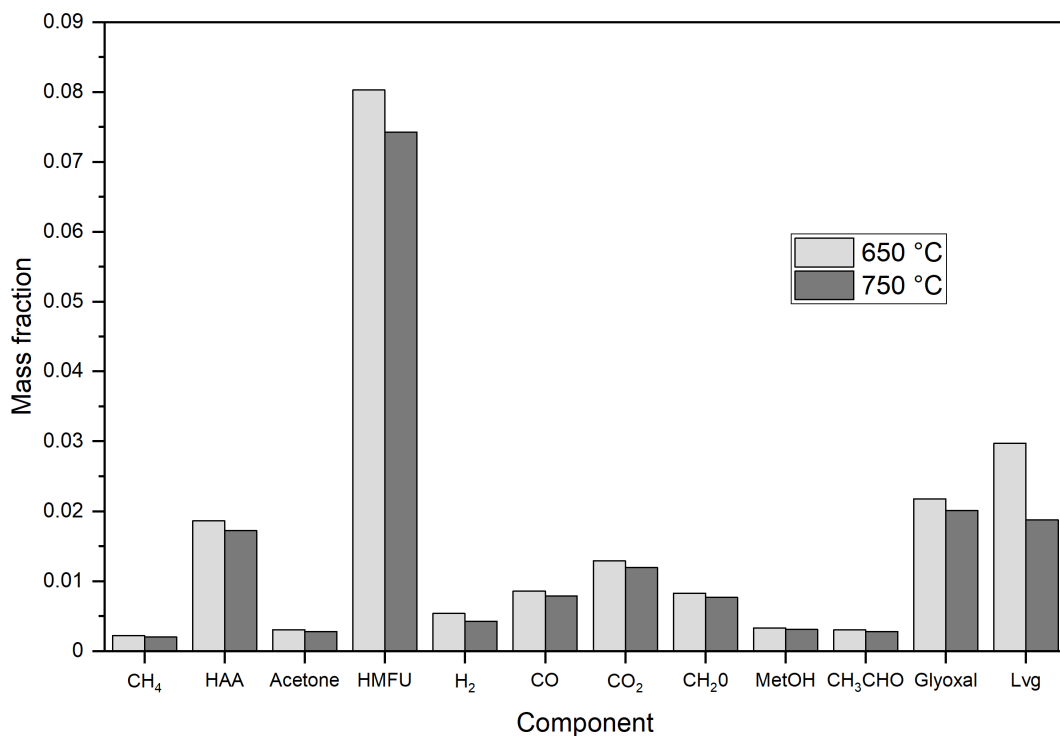


Figure 3.8: Product distribution for the gaseous phase using a cellulose particle model with detailed kinetics model.

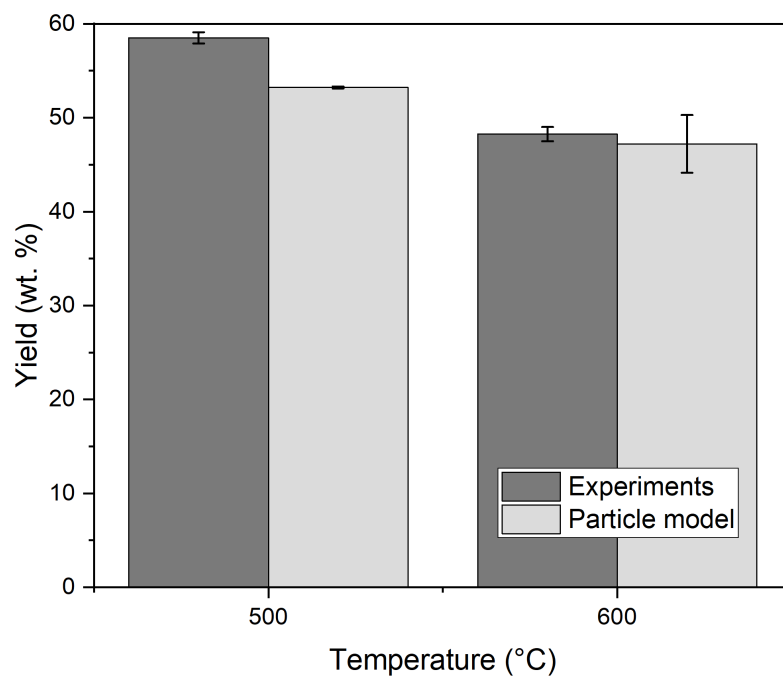


Figure 3.9: Levoglucosan yields from the developed model and from experiments [15]. Pyrolysis for cellulose particles with $r = 9 \cdot 10^{-3}$ m, $T_0 = 250$ °C and $T_\infty = 800$ °C. LVG yields obtained as average from different charring degrees: 0.025, 0.030 and 0.035.

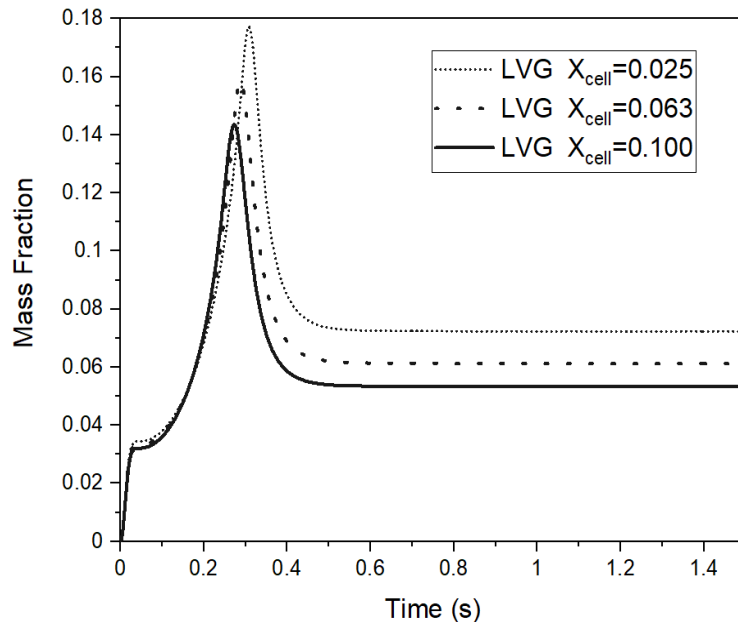


Figure 3.10: Mass fraction of LVG at different charring degrees (X_{cell}) for slow pyrolysis ($X_{cell} = 0.100$), intermediate pyrolysis ($X_{cell} = 0.063$) and fast pyrolysis ($X_{cell} = 0.025$).

haviour could be explained when considering that detailed kinetic models are particularly affected by both the reaction temperature and the heating rate [25, 24]. Pyrolysis, at either lower temperatures or lower heating rates presents different thermal decomposition than at higher temperatures and/or heating rates [14]. This different behaviour could potentially generate a more kinetically-driven pyrolysis and divergences between predicted yields and experimental data can arise as a result. The proposed model does not consider ashes nor extractives as biomass components. Moreover, diffusion and heat transfer coefficients, and particularly, the used kinetic models are potential sources of uncertainty [158, 36]. Consequently, the developed model could be further improved by including missing components and assessing model-related uncertainties.

Figure 3.10 shows that different heating regimes in pyrolysis, modify the mass fraction of LVG for a given temperature; and the LVG fraction could drop near 20 % when the process changes from fast (high heating rate) to slow (low heating rate) pyrolysis. Although using detailed kinetic models opens new possibilities in terms of identifying valuable platform chemicals, it also brings new challenges associated with kinetic-related uncertainties such as the charring factors, heats of reaction and stoichiometric coefficients[52].

3.3.2 Applications of the developed particle model

The previous results showed the behaviour of the particle model under different operating conditions. In this section however, the interest is to explore the use of the particle model for providing early stage information that could support future process design. For this purpose, thermal efficiency, economic and environmental applications for the model are presented.

3.3.2.1 Biomass heating strategies during pyrolysis

Four different heating alternatives were considered to evaluate the energy requirements throughout pyrolysis considering a reaction time of 60 seconds in each case. The mentioned heating alternatives are:

- **Alternative 1:** constant heating rate with a low heat flux \dot{Q}_1 for 60 seconds.
- **Alternative 2:** constant heating rate with a high heat flux \dot{Q}_2 for 60 seconds.
- **Alternative 3:** combination of heat fluxes in order $\dot{Q}_1 + \dot{Q}_2$, 30 seconds each.
- **Alternative 4:** combination of heat fluxes in order $\dot{Q}_2 + \dot{Q}_1$, 30 seconds each.

Results from the evaluation of heating alternatives

Product distribution dependence with heating rate is shown in Figure 3.11 a) and b). In general, the figure suggests that through the combination of heating strategies, it is possible to reduce the energy requirements during pyrolysis for attaining similar product distributions. Similarly, Figure 3.11 shows that using the same amount of energy but with different heating strategies (alternatives 3 and 4) can give similar product distributions. Moreover, it is evidenced that the initial heating rate determines the product distribution for lumped particle models. Heating alternatives 1 and 3, result into similar product distribution even if they have different energy requirements. Similarly, if a high tar content is needed, alternatives 2 and 4 could be used. In such case, combining heating strategies (alternative 4) has the potential to reduce the energy requirements associated to pyrolysis in approximately 10 %. The mentioned behaviour opens a future possibility for addressing process optimization, from a particle level scale, with views to minimize the associated energy requirements. The capability of the particle models for optimization strategies in terms of heating and product distribution has not been explored extensively yet in literature and it provides a future field of development.

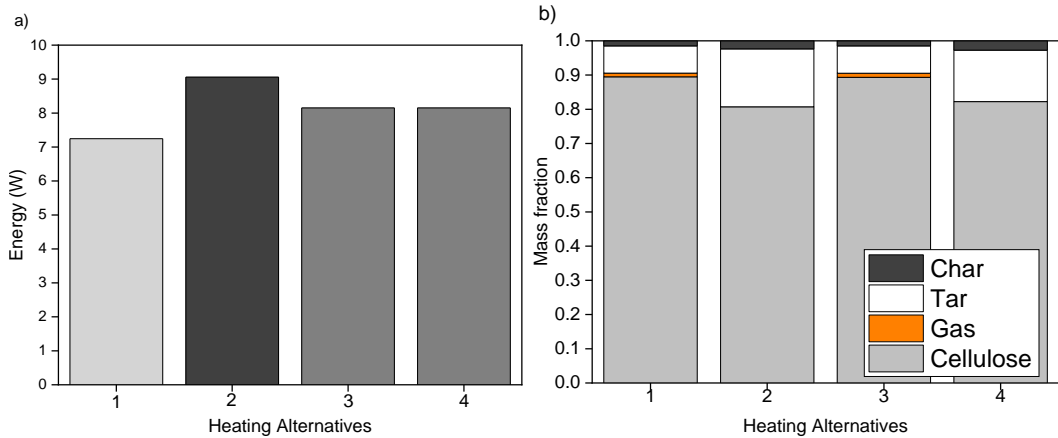


Figure 3.11: Energy consumption for different heating alternatives (a). Product distribution represented as mass fraction for different heating alternatives considering a lumped model for cellulose as feedstock (b).

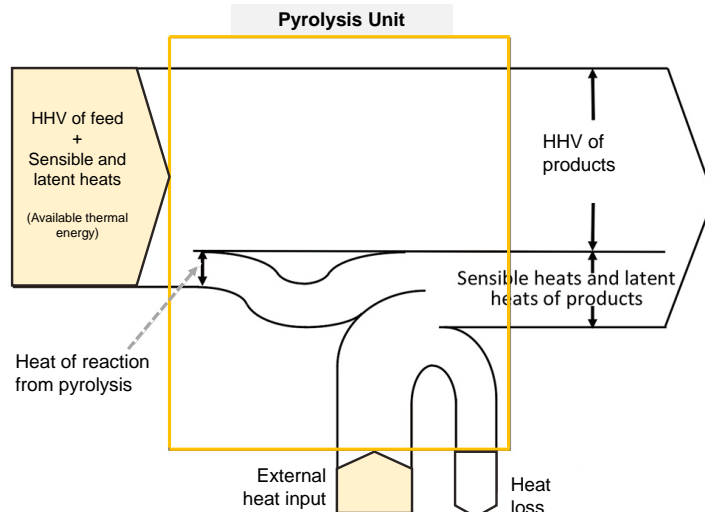


Figure 3.12: Diagram of the energy balance involved in the calculation of thermal efficiencies in the pyrolysis process. Adapted from Kodera & Kaiho (2016).

3.3.3 Thermal efficiency of the pyrolysis process

A previous work[125] addressed energy efficiency in torrefaction by comparing higher heating values (*HHV*) of products and reactants. Such comparison is made in terms of the energy yield (Y_{energy}), which is calculated with the mass (m) and higher calorific values (*HHV*) of products and feed, as presented in Eq. 3.34.

$$Y_{\text{energy}} = \frac{\sum_{i=1}^{n_c} m_{\text{product},i} \cdot HHV_{\text{product},i}}{\sum_{i=1}^{n_c} m_{\text{feed},i} \cdot HHV_{\text{feed},i}} \quad (3.34)$$

The previous equation provides a general understanding of the thermal efficiency in pyroly-

ysis; however, it does not include information about latent or sensible heats, heating rates, changes in operating conditions or energy losses. The present work includes an alternative to overcome such limitations by applying an energy balance that includes latent and sensible heats, heat inputs and energy losses besides *HHVs*. A schematic of the involved energy-related information is presented in Figure 3.12. Such approach calculates a so called pyrolysis thermal efficiency η_{th} (Eq. 3.35), which relates the useful thermal energy from the feed, external heat inputs and heat losses; with the useful thermal energy in the output. The calculation of η_{th} considers the biomass particle as the system and it includes the energy content from the feed (Q_{in}), the energy that goes into the system from the surroundings (Q_∞), the energy leaving the reacting particle (Q_{out}) and the lost energy in the process (Q_{lost}). Regarding the enthalpy leaving every differential volume of biomass reacting particle, the enthalpy was calculated for each solid and gaseous specie i considering the standard formation enthalpy and specific and latent heats as presented in 3.40.

$$\eta_{th} = \frac{Q_{in} + Q_\infty}{Q_{out} + Q_{lost}} \quad (3.35)$$

$$Q_{in} = \sum_{i=1}^{n_c} m_i ((h_{in,i}^\circ - h_{st,i}^\circ) + HHV_{feed,i}) \quad (3.36)$$

$$h_{in,i}^\circ = h_{st,i}^\circ + (T_{in} - 298) Cp_{solid,i}^\circ + (T_{evaporation,i}^\circ - 298) Cp_{liquid,i}^\circ + Lp_{evaporation,i} + (T_{in} - 298) Cp_{gas,i}^\circ \quad (3.37)$$

$$Q_{external} = A_{surface} (h_{convection}(T_\infty - T_{surface}) + \sigma \epsilon (T_\infty^4 - T_{surface}^4)) \quad (3.38)$$

$$Q_{out} = \sum_{i=1}^{n_c} m_i ((h_{out,i}^\circ - h_{st,i}^\circ) + HHV_{product,i}) \quad (3.39)$$

$$h_{out,i}^\circ = h_{st,i}^\circ + (T_{out} - 298) Cp_{solid,i}^\circ + (T_{evaporation}^\circ - 298) Cp_{liquid,i}^\circ + Lp_{evaporation,i} + (T_{out} - 298) Cp_{gas,i}^\circ \quad (3.40)$$

Given that enthalpy and *HHV* depends on the composition of pyrolysis products, correlations retrieved from literature, for estimating the value of *HHV* for a given C, H and O content, are used [30, 31]. Such correlations and the corresponding *HHV* for each pyrolysis product is presented in Table 3.7.

With the previously presented information, thermal efficiency could be defined for pyrolysis

Table 3.7: Pyrolysis products properties considered for the energy efficiency analysis [30, 31]

Component	Composition	Molecular formula	HHV [MJ kg ⁻¹]
Tar	78.00% C, 9.00 %H, 1.86% N, 10.60% O	CH _{1.38} O _{0.10} N _{0.02}	HHV = (338.2 * C + 1442.8 * (H - O/8)) * 0.001
Gas	30% CO, 30 %H ₂ , 40 %CH ₄		HHV = $\sum_{i=1}^{n_{\text{gases}}} w_i * i$
Char	71.20% C, 3.80 %H, 2.10% N, 5.70% O	CH _{0.64} O _{0.06} N _{0.03}	2.8·10 ⁷

as follows:

$$\eta_{th} = \frac{\text{Produced thermal energy}}{\text{Thermal energy going into the system}} \quad (3.41)$$

3.3.3.1 Economic and environmental outcomes from pyrolysis

The economic and environmental outcomes are determined as a function of the product distribution from pyrolysis. Since it is a preliminary evaluation, only market prices for the different products and feedstocks (p_i) are considered for estimating the economic outcome (EP) in £ per kg of initial biomass. Similarly, the global warming potential (GWP) associated to the pyrolysis products and feedstocks is considered as the environmental outcome and it is presented in kg CO₂ eq per kg of initial biomass. The economic and environmental outcomes are calculated with equations 3.42 and 3.43. The market prices for the feedstocks and products from pyrolysis, and their correspondent GWP are presented in Tables 3.8 and 3.8.

$$EP = \sum_{i=1}^{n_c} m_i p_i \quad (3.42)$$

$$ENV = \sum_{i=1}^{n_c} m_i GWP_i \quad (3.43)$$

Economic, environmental and energy efficiency outcomes from the applications of the particle model Biomass pyrolysis dependence on operating conditions: the external temperature that heat up biomass particles, biomass initial temperature and moisture content; is evidenced in Figure 3.13. This figure is a parallel coordinates plot, which considers each combination of moisture content, external and initial temperatures, as an individual observation that corresponds with the value of a normalized outcome or variable: Y_{energy}, η_{th} , EP and ENV . Moreover, to highlight the negative impact of increased CO₂ emissions, the negative ENV outcome ($-ENV$) is considered in the analysis. Figure 3.13 shows that for a single biomass particle undergoing pyrolysis, higher economic potentials (darker lines)

Table 3.8: Market prices for raw materials and products involved in pyrolysis

Component	(£ tonne ⁻¹)	Reference	Observation
Cellulose	37.23	[159]	Waste biomass
CellA	37.23	[159]	
HAA	23000.00	[160]	High purity
Glyox	2514.60	[160]	High purity
Acetone	739.79	[160]	Renewable product
HMFU	3000.00	[160]	High purity
H ₂	412.15	[161]	As syngas/mol CO
CO	412.15	[161]	As syngas/mol CO
CO ₂	412.15	[161]	As syngas/mol CO
CH ₄	165.00	[162]	
Formaldehyde	425.60	[160]	
Methanol	228.54	[160]	High purity
Acetaldehyde	17848.50	[160]	High purity
H ₂ O	0.00		No market value
Formic acid	42944.00	[160]	High purity
Biochar	76.91	[159]	
Levoglucosan	38700.00	[119]	Purification needed
Lumped species			
Gases	412.15	[161]	As syngas/mol CO
Bio-oil	630.00	[159]	

could be reached by combining high external temperatures, high biomass initial temperatures, and low moisture contents ($\leq 5\%$). However, the mentioned figure also shows that for the modelled particles, higher economic performances in pyrolysis are also associated with poorer environmental outcomes; therefore, evidencing conflicting economic and environmental outcomes in pyrolysis. Such behaviour could be explained when considering that some of most valuable products from pyrolysis are also the ones that exhibit higher global warming potentials [170, 171, 119, 159].

Regarding the energy associated to the process, Figure 3.13 shows that both Y_{energy} and η_{th} present similar tendencies for a set of operating conditions in pyrolysis. In general, better thermal performances (η_{th}) and better energy yields (Y_{energy}) are reached with combinations of high external temperatures and high biomass initial temperatures. It is also evidenced that for any combination of external and initial biomass temperatures, Y_{energy} cannot discriminate between different biomass moisture contents. On the contrary, η_{th} is sensible to changes in biomass moisture contents. This behaviour is illustrated in Figure 3.13, where 2 potential combination of parameters for achieving one of the highest *EP* (darker lines in the figure) can be identified: $T_\infty = 750^\circ\text{C}$, $T_0 = 260^\circ\text{C}$, moisture= 0.0 (w.t%); and

Table 3.9: Global warming potential (GWP) for a 100 years horizon for the products of cellulose pyrolysis.

Component	GWP $\left(\frac{\text{kg CO}_2\text{eq}}{\text{kg product}} \right)$	Reference
Cellulose	2.500	[163]
CellA	2.500	[163]
HAA	0.870	[164]
Acetone	4.600	[165]
HMFU	3.300	[163]
H ₂	0.295	[166]
CO	2.200	[167]
CO ₂	1.000	[167]
CH ₄	28.00	[167]
Methanol	2.970	[168]
Formic acid	1.500	[169]
Levoglucosan	2.190	[170]
Biochar	1.000	[171]

Component	GWP $\left(\frac{\text{kg CO}_2\text{eq}}{\text{MJ bio-oil}} \right)$	Reference
Formaldehyde*	0.035	[171]
Acetaldehyde*	0.035	[171]
Bio-oil	0.035	[171]

*Considered as bio-oil for calculation

$T_\infty = 750^\circ\text{C}$, $T_0 = 260^\circ\text{C}$, moisture = 5.0 (w.t%). The mentioned alternatives only differ in the moisture content; and whereas Y_{energy} is the same for both combination of parameters, η_{th} is 3-4% higher when a moisture content of 5.0 (w.t%) is considered. This difference between Y_{energy} and η_{th} could be explained by water sensible and latent heats, as well as by the enthalpies of the components which are not included in the Y_{energy} analysis. Considering that biomass drying is an expensive unit operation, and that moisture can significantly reduce biomass milling energy requirements [46], η_{th} could serve to develop metrics for establishing a future pyrolysis energy efficient framework, assessing existing trade-offs between biomass moisture content, size reduction-associated energy, required product distribution and overall energy requirements.

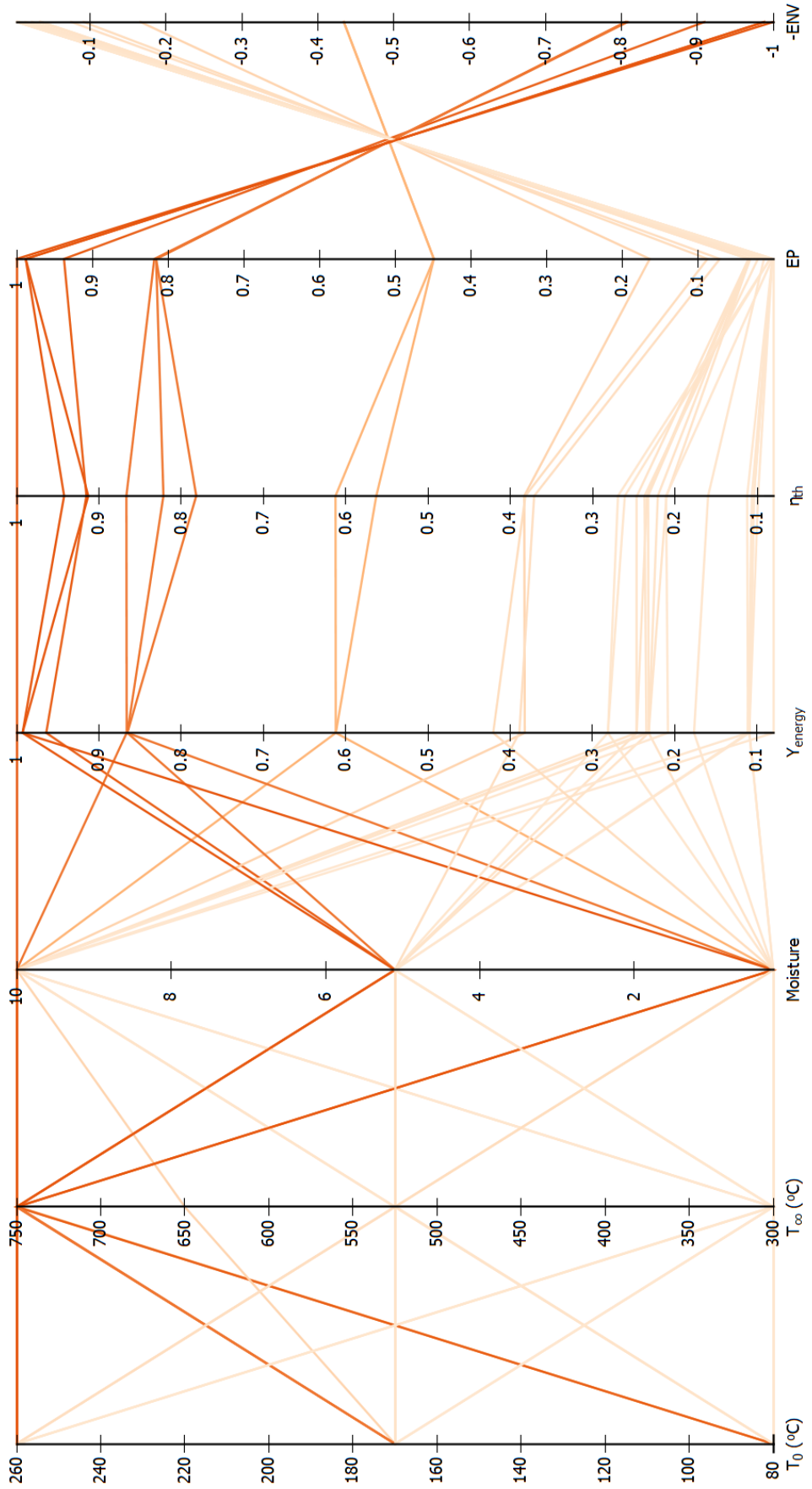


Figure 3.13: Outcomes for normalized Y_{energy} , η_{th} , EP and $-ENV$ for different conditions of initial biomass temperature (T_0), external temperature (T_∞) and percent-age of moisture content for pyrolysis, described by lumped model.

Regarding the economic and environmental outcomes, Figure 3.14 shows that in biomass pyrolysis, economic and environmental outcomes are in conflict. Moreover, the mentioned Figure evidences that higher pyrolysis temperatures could potentially favor As to provide an overview of the required conditions to maximize the economic potential (*EP*), minimize the associated CO₂ emissions (*ENV*) and to maximize pyrolysis' thermal efficiency (T_{eff}); a factorial regression was performed in each case, considering different T_o, T_∞ and moisture contents, and the resulting objective functions were optimized. As evidenced in Figure 3.14, environmental outcomes are in conflict with economic and thermal efficiency outcomes in pyrolysis. Moreover, it is shown that the maximized economic outcome correspond with the worst environmental performance in pyrolysis. This behaviour could be explained when considering that the products from pyrolysis with higher market value, such as HMFU (3000 £tonne⁻¹) or LVG (>30000 £tonne⁻¹), also present relatively high global warming potentials (3.30kgCO_{2eq}/kg HMFU and 2.19kgCO_{2eq}/kg LVG). Although it might seem counter-intuitive that higher thermal efficiencies correspond with poorer environmental outcomes; thermal efficiency in the present work is defined as a function of the energy generated from and provided to the biomass particle. As a result, some of the products that lead to higher values of η_{th} also present high associated GHG emissions. The previous results highlight how challenging having profitable and environmental-friendly biomass pyrolysis operations might be. At the same time, and given the observed trade-off between economic and environmental outcomes; process multi-objective optimization could help to unlock profitable and environmental-friendly pyrolysis.

3.4 Concluding remarks

A mechanistic model capable of predicting inner temperature gradients in thermally thick biomass particles with moisture content, undergoing pyrolysis, have been developed. This particle model can predict product distribution; and the model's predictions are more accurate at higher temperatures. The information provided by the model can serve as an early stage energy efficiency, economic and environmental source of information in situations where different operating conditions need to be evaluated. Pyrolysis profitable operations, at a particle-scale, benefit from the combination of high external temperatures (T_∞ = 750 °C), high biomass initial temperatures (T_o = 260 °C) and low moisture contents (≤ 5% wt.). On the contrary, better environmental performances at a particle scale arise from the combination of low external temperatures and low biomass initial temperatures. Findings highlight

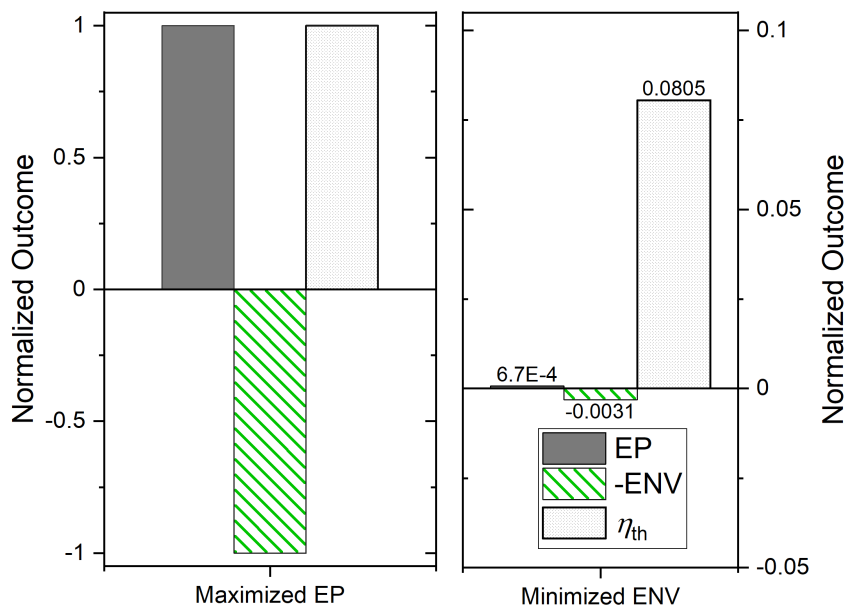


Figure 3.14: Differences in the resulting outcomes when the normalized economic potential (*EP*) is maximized and the normalized environmental outcome (*-ENV*) is minimized, considering a lumped model and varying T_{inlet} , T_∞ and biomass moisture content.

how challenging having profitable and environmental-friendly biomass pyrolysis operations could be; and in such situations, multi-objective optimization might unlock potential paths towards more profitable and more environmental friendly biomass pyrolysis operations.

Nomenclature	
Latin symbols	
A	pre-exponential constant (s^{-1})
A_{surface}	surface area (m^2)
C	concentration (mol m^{-3})
C_p	specific heat ($\text{J kg}^{-1} \text{K}^{-1}$)
D	diffusivity ($\text{m}^2 \text{s}^{-1}$)
d	particle diameter (m)
Ea	activation energy (J mol^{-1})
f_{shrink}	shrinking factor
$h_{\text{convection}}$	convection heat transfer coefficient ($\text{W m}^{-2} \text{K}^{-1}$)
h	specific enthalpy (J kg^{-1})
HHV	higher calorific value (J kg^{-1})
k	reaction rate (s^{-1})
K	effective permeability (m^2)
L	characteristic length (m)
L_p	latent heat ($\text{J kg}^{-1} \text{K}^{-1}$)
m	mass (kg)
MW	molecular weight (kg kmol^{-1})
n	number of moles (mol)
n_c	number of components
n_r	number of reactions
P	pressure (Pa)
Q	heat (J)
r	radius (m)
R_{ideal}	ideal gas constant ($\text{J K}^{-1} \text{mol}^{-1}$)
T	temperature (K)
t	time (s)
u	velocity of the gaseous phase (m s^{-1})
V	volume (m^3)
w	mass fraction
Greek symbols	
η	biomass conversion
ε	emissivity
Γ	net formation ($\text{mol s}^{-1} \text{m}^{-3}$)
γ	stoichiometric coefficient
φ	porosity
λ	thermal conductivity ($\text{W m}^{-1} \text{s}^{-1}$)
ρ	density (kg m^{-3})
μ	dynamic viscosity ($\text{kg m}^{-1} \text{s}^{-1}$)
σ	Stefan-Boltzmann constant ($\text{W m}^{-2} \text{K}^{-4}$)
Subscripts	
b	biomass
cell	cellulose
f	final
G	gaseous phase
i	component
j	reaction
0	initial value
p	particle
s	solid
st	standard conditions
∞	external value
min	minimum

Chapter 4

Characterization and pyrolysis kinetic modeling of lignin-rich biomass

In this chapter, the physico-chemical and thermal properties of palm kernel shells (PKS), a lignin-rich biomass, are determined experimentally. Moreover, pyrolysis of PKS and its main structural components is studied through thermogravimetric analysis (TGA). The main outputs are properties and kinetic parameters that are required to describe PKS pyrolysis at a reactor scale. Knowledge on the difference in pyrolysis between a particular type of biomass and its main components can underpin the development of models for describing biomass pyrolysis more accurately.

Publication from this work: Chico-Proano, Andres, Michelle Romero, A. Narváez C. Riccardo, Boris G. German, Daniel Rivadeneira, George Manos, Lazaros G. Papageorgiou, and Eric S. Fraga. 2022. “Combined Particle Model and Experimental Approach for Predicting Pyrolysis with Palm Kernel Shells.” Computer Aided Chemical Engineering 51: 343–48.

4.1 Introduction

Within biomass pyrolysis multi-scale modelling, feedstock’s particular characteristics and the utilized heating rates, are usually uncertain parameters that impact pyrolysis product distribution predictions. Such parameters need to be quantified in order to develop more accurate and scalable pyrolysis models [5]. The existing interactions between biomass components throughout pyrolysis, as well as the complex system of chemical reactions that takes place in pyrolysis, make it difficult to develop a generalized framework to describe biomass pyrolysis kinetics. Biomass pyrolysis is considered to follow a single step reaction kinetic model when thermal analysis experiments are performed [172]. However, when complex heterogeneous reactions are studied, a single kinetic model might not be sufficient to describe the reaction’s kinetics. In such circumstances, additional methods need to be

considered to evaluate changes at an structural and chemical level for describing complex reaction systems such as pyrolysis [50]. Kinetic parameters that are determined through thermal analysis experiments can only provide an approximation of the reaction rate for complex processes [173].

Previous pyrolysis models consider biomass as a cellulose, hemicellulose and lignin mixture [36, 141]. Moreover, lignocellulosic biomass had been represented as a linear combination of cellulose, hemicellulose and lignin [25]. However, biomass components interactions are not fully understood and they are difficult to quantify [54]; thus leading to poor agreement between predicted and experimental results. There are previous experimental works that have identified interactions between biomass components [55, 54]. However, this is not the case for modelling approaches, where there is little information regarding the effect of such interactions over pyrolysis modelling outcomes. The thermochemical decomposition of biomass in pyrolysis involves a complex system of primary and secondary chemical reactions. Hence, the determination of biomass pyrolysis reaction mechanisms and their associated kinetic parameters is a difficult task. This is particularly challenging for lignin because of the different composition and structures that lignin could present [49]. Moreover, information is still scarce regarding the effect of such interactions in residues with a complex morphology like PKS. There are previous studies that present a wide variety of biomass types, their properties and their use in pyrolysis [158, 174, 116, 18]. However, out of the 94 types of lignocellulosic biomass found in such studies, only 5 correspond with lignin-rich biomass ($> 40\%$ of lignin). Therefore, more research is required to characterize lignin-rich biomass and to evaluate its behaviour in pyrolysis.

Previous models have addressed pyrolysis complexity by considering biomass as a cellulose, hemicellulose and lignin only mixture [26, 141]. Other modelling approaches have included extractives by using additional lumped pyrolysis reactions [49, 36]. Inorganic components are not usually included in pyrolysis models; however, they could catalyze secondary reactions [36]. Existing interactions between cellulose, hemicellulose and lignin have been identified in pyrolysis [54, 55]; however the effect of such interactions over pyrolysis kinetics is not fully understood. Further work is needed to incorporate such interactions into biomass pyrolysis models, for improving the agreement between predicted and experimental results [54]. The combination of modelling and experimental approaches in complex thermochemical processes like pyrolysis, stands out as an opportunity to develop reliable

models for future process design and optimization. Whereas such properties and pyrolysis associated-kinetics are available for pure components [51, 9, 175, 45] and woody materials [176, 177, 97], they are scarce for residual biomass such as palm kernel shells [126]. This work aims to provide information on the properties of PKS with views to its later use for fuels and platform chemicals production via pyrolysis. In doing it so, this work explores a novel approach that includes biomass internal structure for estimating PKS pyrolysis kinetic parameters as a way to expand the understanding of the effect of biomass variability over pyrolysis kinetics, beyond compositional analysis.

4.2 Materials and experimental methods

4.2.1 Materials

This work considers two main materials: palm kernel shells (PKS) and a synthetic mixture of cellulose, hemicellulose and lignin that resembles PKS composition. The used PKS are from the *Elaeis guineensis* Jacq. variety and they are residues from a palm oil extracting company located in Ecuador. The synthetic mixture considers Alpha Chemika cellulose, D-xylose from LobaChemie as hemicellulose, and Sigma-Aldrich low sulfonate lignin. Cellulose, hemicellulose and lignin characteristics are detailed in the first section of Appendix B. Standard methods for the determination of palm kernel's physical, chemical and thermal properties, were applied when available. The mentioned methods are listed in Table 4.1. This section considers both a complete characterisation of palm kernel shells (PKS) and the development of a kinetic model for describing PKS and the synthetic mixture's pyrolysis using thermal analysis.

4.2.2 Experimental methods

4.2.2.1 Biomass sampling and preparation

Palm kernel shells (PKS) are sampled and quartered in accordance with the BS EN 18135:2017 standard. No size reduction is involved for determining the particle size distribution, particle's apparent density and bulk density. The other analyses presented in Table 4.1, require size reduction. Size reduction is undertaken using a UDY cyclone blade mill to obtain a particle size below 2 mm. PKS undergo size reduction as described in the BS EN 14780 standard before they are further characterized. Such characterization includes the proximal analysis (moisture, ash, volatiles and fixed carbon contents), cellulose, hemicellulose, lignin and extractives determination, the elemental or ultimate analysis, chemical

Table 4.1: Methods applied for palm kernel shell characterization

Property	Method of analysis
Physical characterization	
Bulk density	BS EN ISO 17828:2015
Apparent density	[178]
Particle size distribution	BS EN 17827-1:2016
Crystallographic structure	XRD analysis [179]
Morphology	Microscopy
Proximal Analysis	
Moisture content	BS EN 18134-1:2015
Ash content	BS EN 18122:2015
Volatiles	BS EN 18123:2015
Fixed carbon	Calculated by difference
Chemical characterization	
Extractives	NREL/TP-510-51619 method
Carbohydrates	NREL/TP-510-42618 method
Elemental analysis	BS EN 16948:2015
Functional groups analysis	FTIR analysis [180]
Energy content	
Higher heating value	BS EN 18125:2017

characterization through infrared spectroscopy and X-ray diffraction; and finally, the energy content is determined by measuring the higher heating value (HHV).

The moisture, ash and volatiles contents are determined by gravimetry in accordance with BS EN 18134-1:2015, BS EN 18122:2015 and BS EN 18123:2015 standards, correspondingly. The content of fixed carbon is determined by weight difference. Extractives are recovered from PKS using solid-liquid extraction with ethanol USP grade and water as solvents. Additional information regarding sampling and size reduction can be found in Appendix B.

4.2.3 Determination of physical properties of palm kernel shells

4.2.3.1 Bulk density

Biomass pyrolysis requires the analysis of particles' flow or granular flow, which dependent on the density of the biomass. The bulk density represents the volume occupied by the biomass as received or dry, including all the free spaces that might exist between particles; and it is required to predict the volumetric flow inside pyrolysis reactors. The apparent den-

sity in the other hand, represents the volume occupied by one particle of biomass is useful for determining particle-to-particle and particle-to-wall interactions [181]. Density determination is of particular interest for predicting transportation and storing costs [179]. PKS bulk density is determined by gravimetry in accordance with the BS EN 17828:2015 standard. A suitable cylindrical container of known volume is used to collect PKS. Moreover, the PKS inside the container are weighted, and such analysis is repeated three times.

4.2.3.2 Apparent density

The apparent density of PKS is determined considering the Archimedes' principle by suspending the PKS from a rigid support into a liquid of known density [178]. For this purpose, a Mettler Toledo XS1003S scale of 1 kg of capacity and 0.001 g precision was coupled with a density kit provided by the manufacturer as presented in Figure 4.1. Distilled water of density ρ_L is used as reference fluid and PKS density is calculated considering the PKS weight in air, $m_{PKS,air}$, and submerged in the liquid, $m_{PKS,L}$, as well as the air density ρ_{air} as shown in Eq. 4.1. Further details on the taken measurements and densities for the liquid and gas are presented in the corresponding section of Appendix B.

$$\rho_{PKS} = \frac{m_{PKS,air}}{m_{PKS,air} - m_{PKS,L}} (\rho_{air} - \rho_L) + \rho_L \quad (4.1)$$

4.2.3.3 Particle size distribution

Biomass is an abundant yet variable resource. Such variability is not only related to seasonability or sources for biomass, but to the actual physical and chemical properties which can very much vary, even within the same type of biomass [68]. The particle size is also a variable property, specially for biomass that has not been densified or pelletized previously, for instance, PKS. In such conditions, a size distribution would be expected among the biomass particles. Particle's size is not only important because of its effect over pyrolysis overall conversion and heat transfer [5], but because it is one of the most relevant parameters for studying biomass transportation and flow patterns [137, 181]. The particle size distribution of the sampled PKS is studied in accordance with the BS EN 17827-1:2016 standard. A rifle sampler is used to reduce the sample size near to 550 g, in order for the sample to fit inside a FRITSCH analysette 3 Spartan vibratory sieve shaker. Sieves of 12.50, 9.50, 6.68, 4.75, 3.35, 2.36 and 2.00 mm are used to study PKS particle size distribution. Three samples of

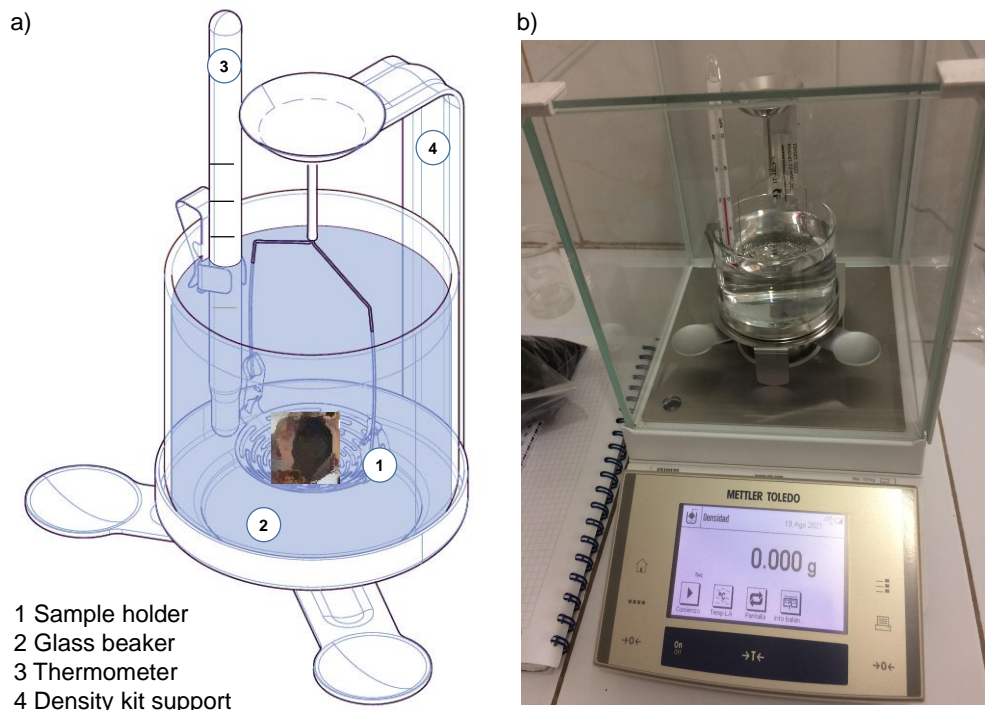


Figure 4.1: a) Density kit scheme using distilled water and b) assembled in the laboratory scale. Scheme modified from [16].

550 g are characterized, making sure the repeatability and reproducibility limits of the BS EN 17827-1:2016 standard are complied. The shaking time required for the separation is 20 minutes and the shaking speed is adjusted to maintain an amplitude of 1.5 mm. The median value of the size distribution of the PKS, d_{50} , is determined with the following equation:

$$d_{50} = C_{(n-2)} + (50 - S_{(n-2)}) \cdot \left(\frac{C_{(n-1)} + C_{(n-2)}}{S_{(n-1)} - S_{(n-2)}} \right) \quad (4.2)$$

Where:

d_{50} = size in mm corresponding to the 50% (wt.) of cumulative mass passed in sieves.

$C_{(n-2)}$ = diameter in mm of the hole for the sieve two sizes below d_{50} .

$C_{(n-1)}$ = diameter in mm of the hole for the sieve one size below d_{50} .

$S_{(n-2)}$ = cumulative mass in % passed two sizes below d_{50} .

$S_{(n-1)}$ = cumulative mass in % passed one size below d_{50} .

The sieves, sieve shaker equipment, and the characterization of PKS particle size distribution are presented in detail in Appendix B.

4.2.3.4 Proximal analysis

The proximal analysis considers the determination of moisture, ash, volatiles and fixed carbon contents in biomass.

4.2.3.5 Moisture content

The moisture content is determined in a drying oven at a temperature of $105 \pm 2^\circ\text{C}$ in accordance with the BS EN ISO 18134-3:2015 Standard. For this purpose, the PKS are extended in trays making sure not to exceed 0.2 grams of material per cm^2 . A balance capable of reading to the nearest 0.1 mg is required for the weight determinations. For the moisture content determination, a Memmert drying oven with programmable temperature, a desiccator and an Ohaus Pioneer Analytical balance are considered. The empty trays with their lids are weighted to the nearest 0.1 mg and 300 grams of PKS are added. The samples are left in the drying oven until constant weight, for at least 3 hours. A reference tray without sample is also used and weighted. The taken measurements are detailed in the Appendix B. The analysis is undertaken by triplicate and the moisture content is determined as follows:

$$\text{Moisture} = \frac{(m_2 - m_3) - (m_4 - m_5)}{(m_2 - m_1)} \cdot 100 \quad (4.3)$$

Where:

m_1 = mass of the empty tray for the sample in g.

m_2 = mass of the tray and sample before drying in g.

m_3 = mass of the tray and sample after drying in g.

m_4 = mass of the reference tray before drying in g.

m_5 = mass of the reference tray after drying in g.

4.2.3.6 Volatile matter content

For determining the content of volatile matter in PKS, the biomass is taken to $900 \pm 10^\circ\text{C}$ for 7 minutes using a F48018 Thermo Scientific digital furnace, in accordance with the BS EN 15148:2009 Standard. The loss in mass experienced by the PKS is weighted to the closest 0.1 mg using an Ohaus Pioneer Analytical balance. The moisture of the sample is previously determined as described in the previous procedures. Crucibles with lids are taken into the furnace at $900 \pm 10^\circ\text{C}$ for 7 minutes. The empty crucibles with lids are removed from the furnace and allow to cool to room temperature on a thermo-resistant plate and then they are stored in a desiccator and weighted. Approximately 1 g of sample, with a

size ≤ 1 mm is placed in the crucibles, which are then taken to the furnace for 7 minutes. After this time, the crucibles are left to cool on a thermo-resistant plate down to $30\text{--}50$ °C above room temperature, and then they are cooled in a desiccator. Finally, the crucibles are weighted to the nearest 0.1 mg. The analysis is performed by triplicate. The detail of the measurements are presented in the corresponding section of Appendix B. The volatile matter is then determined as follows:

$$\text{Volatile matter} = \left[\frac{100(m_2 - m_3)}{m_2 - m_1} - \text{Moisture} \right] \cdot \left(\frac{100}{100 - \text{Moisture}} \right) \quad (4.4)$$

Where:

m_1 = mass of the empty crucible and lid in g.

m_2 = mass of the crucible, lid and sample before heating in g.

m_3 = mass of the crucible, lid and sample after heating in g.

Moisture = sample's moisture content in wt.%.

4.2.3.7 Ash content

For determining the content of ashes in PKS, the biomass is taken to 550 ± 10 °C using a F48018 Thermo Scientific digital furnace, in accordance with the BS EN 18122:2015 Standard. The remaining residue after the thermal treatment is weighted to the closest 0.1 mg using an Ohaus Pioneer Analytical balance. Porcelain dishes are used to contain the sample, making sure that the load remains ≤ 0.1 g cm $^{-2}$. The sample for the ash content analysis needs to be dried beforehand. This means that the ash analysis could follow the moisture content analysis, if the sample is kept dry in a desiccator. For ashing the sample, the PKS-containing porcelain dish is placed in the furnace using a temperature program:

- Raise the furnace's temperature to 250°C within a period of 30-50 min.
- Maintain the temperature at 250°C for 60 min.
- Raise the furnace's temperature to 550 ± 10 °C within a period of 30 min.
- Maintain the temperature at 550 ± 10 °C for 120 min or more.
- Remove the dish from the furnace, cooled it down in a plate that is heat resistant for 5 to 10 min and place it into a desiccator for weighting.

The ash content analysis is performed by triplicate. The detail of the measurements are

presented in the corresponding section of Appendix B. The ash content is determined as follows:

$$\text{Ash content} = \frac{(m_3 - m_1)}{(m_2 - m_1)} \cdot 100 \cdot \frac{100}{100 - \text{Moisture}} \quad (4.5)$$

Where:

m_1 = mass of the empty dish in g.

m_2 = mass of the dish and sample in g.

m_3 = mass of the dish and ash in g.

Moisture = sample's moisture content in wt.%.

4.2.3.8 Fixed carbon content

The percentage of fixed carbon in PKS is calculated by difference, considering the previously determined components of biomass as follows:

$$\text{Fixed carbon} = 100 - (\text{Moisture} + \text{Ash content} + \text{Volatile matter}) \quad (4.6)$$

4.2.3.9 Crystallographic structure

Biomass components can form different crystalline and amorphous structures. Such structures and their identification could provide a deeper understanding of the way cellulose, hemicellulose and lignin interact with each other when forming different types of biomass. Both the PKS and the synthetic mixture are characterized using XRD. For this purpose, an AERIS Malvern Panalytical diffractometer is used with a Cu anode and $\text{k}\alpha 1$ filter radiation ($\lambda = 1.5406\text{\AA}$) working at 40 kV and 15 mA. The samples are analyzed using a 2° min^{-1} scanning rate and 2θ values ranging from 5° to 50° . The data is analyzed in OriginPro 2020b and Intensity versus 2θ plots are obtained. The equipment used for the XRD analysis and the obtained measurements are detailed in the corresponding section in Appendix B.

4.2.3.10 Microscopy

PKS samples need to be prepared before their analysis in the microscope. Such preparation involved an initial dehydration in ethanol series. This dehydration uses ascending concentrations of ethanol in water. Initially, the sample is washed with type 1 water. The sample is then washed with consecutive 50 % v/v, 75 % v/v, 95 % v/v and 100 % ethanol/type 1 water solutions, for 10 minutes in each case and with continuous stirring [182]. The washed



Figure 4.2: PKS sample preparation and analysis with a precision cutter a), polisher b), microscope c), using PKS cross sectional samples of 1.00 mm thick d) and e).

sample is then placed in a cylindrical container with epoxy resin and left to be hardened for 24 hours. Transverse sections of 1.00 mm are cut at 300 RPM using a Mekton MICRA-CUT 152 Precision cutter, and they are later polish in a Leco PX300 polisher using 9 µm and 0.5 µm polishing solutions. The samples are evaluated with and without toluidine blue as dyeing agent. The morphology of the PKS samples is analysed with a polarized light Zeiss Primotech microscope. The samples are divided in 3 zones for the analysis and the morphology of each zone considers between 8 to 10 different photographs with 20X and 50X magnification. The taken photographs are then compiled using the ZEISS Labscope software and one photo is obtain per analyzed zone. The equipment used in this section is presented in Figure 4.2. The registry of the taken photographs per section is detailed in the corresponding section in Appendix B.

4.2.4 Chemical characterization of PKS

The chemical characterization of PKS involves the determination of cellulose, hemicellulose and lignin content. PKS size is kept below 2 mm as mentioned at the beginning of this section, using a blade mill and following the BS EN 18135:2017 standard. Given that biomass extractives could interfere in the determination of carbohydrates, they need to be removed before the determination of cellulose, hemicellulose and lignin. Similarly, if biomass moisture content exceeds 10% wt., water should be removed from the sample.

4.2.4.1 Extractives removal and quantification

Extractives can interfere with the determination of biomass structural components. Their removal follows the NREL/TP-510-42619 Technical Procedure [183], which includes a two-step extraction process that uses water extraction followed by an ethanol extraction. Previous to the extraction process, the moisture content of the milled PKS sample is determined using an HB43-S Halogen Mettler Toledo Moisture Balance with a 1 mg precision and a moisture content repeatability of $\pm 0.3\%$. Each determination requires 1 g of sample and it is performed by triplicate. The analysis starts at room temperature and goes up to 105 °C. Given that the moisture content of the milled PKS used in this study is $7.26 \pm 0.16\% (< 10\%)$, the milled PKS did not require additional drying. The results of such determination can be found in Table B.15 of Appendix B.

The two-step extraction process initially requires to assemble a glass Soxhlet extraction unit. Such unit consists in a heating mantle, a 500 ml round bottom flask for collection of the solvent/extractives mixture, a 250 ml glass evaporator trap, a 125 ml glass Soxhlet tube with cotton cellulose thimbles and a condenser on the top for circulating cold water. Two extraction units are assembled to run simultaneously and their components are presented in Figure 4.3 a). The round bottom flasks, or boiling flasks, need to be previously dried. They are dried in a SN55 Memmert oven at 105°C for 12 hours and then placed in a dessicator until they reach room temperature. Once they are cooled down to room temperature, they are weighted in an Ohaus Pioneer Analytical balance, to the nearest 0.1 mg [183]. This weight is known as the oven dry weight or ODW. Approximately 10 g of milled PKS are placed inside each timble before the Soxhlet extraction.

The first stage of the extraction process involves the analysis of water-related extractives. In this case, approximately 190 ml of HPLC grade water are added into the round bottom flasks and the heating level is adjusted to have at least 4 to 5 siphon cycles each hour. The system operates in reflux for 8 hours and as time passes by, the extractives are transferred to the round bottom flasks as evidenced in Figure 4.3 b) and c). The heating is then turned off and the glassware is left to cool down until it reaches room temperature. The round bottom flasks, containing water-related extractives, are removed and kept aside for further solvent evaporation. The PKS sample is left in the cellulose timbles for the second extraction stage. The second stage analyses ethanol-related extractives in the sample. For this purpose, 190 ml of 190 proof USP ethanol are added to previously dried and weighted round bottom

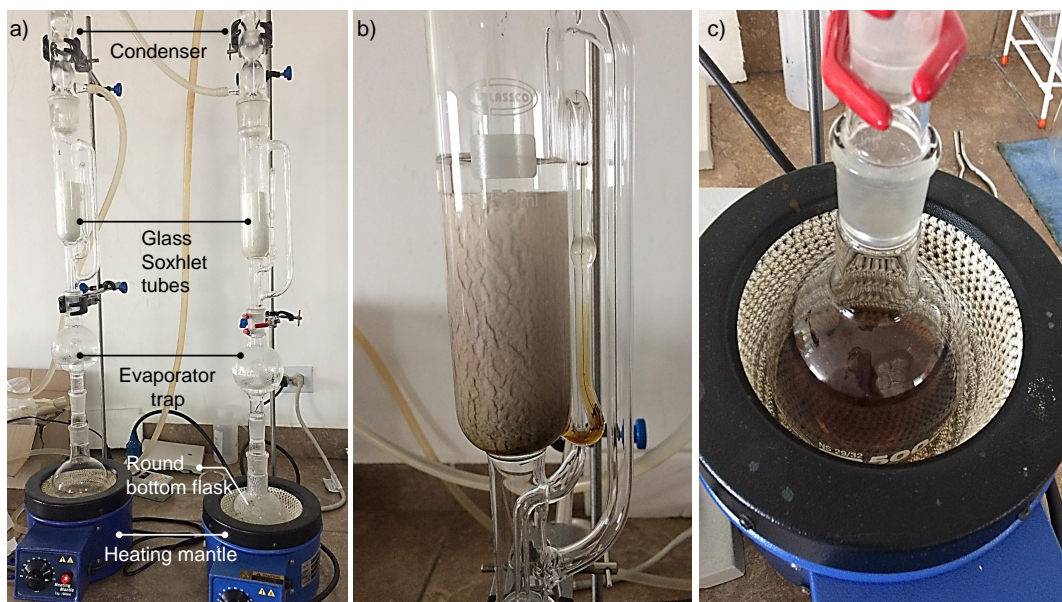


Figure 4.3: Soxhlet extraction unit with its components for extractives analysis a), extraction process after 4 hours b) and after 24 hours of extraction c).

flasks. The heating is set to reach between 6 to 10 siphon cycles each hour and the system operates in reflux for 24 hours. Similarly to the previous stage, the system is turned off and left to cool down until it reaches room temperature. The round flask containing ethanol-related extractives are kept aside for solvent evaporation. The timble containing now extractives-free biomass is removed and the solid biomass is placed in a cellulose filter inside a Buchner funnel. The solids are washed with 100 ml of new 190 proof USP ethanol under vacuum and let dry. This solid sample is used later on for quantifying cellulose, hemicellulose and lignin contents.

The solvent (water or ethanol) is removed from the round flasks using a vacuum rotary evaporator with a water bath kept at $40 \pm 5^\circ\text{C}$. The mentioned equipment is presented in detail in Figure 4.4. The round flasks that now contains only water soluble or ethanol soluble extractives without solvents, are placed in an oven at $40 \pm 2^\circ\text{C}$ for 24 hours. Finally, the round flasks are weighted and the amount of extractives is determined as weight percentage on a dry basis, taking into account the oven dry weight of the sample (ODW) as explained in Eq. 4.7 and Eq. 4.8. The calculation involve in the determination of extractives are presented in detail in the corresponding section of Appendix B.

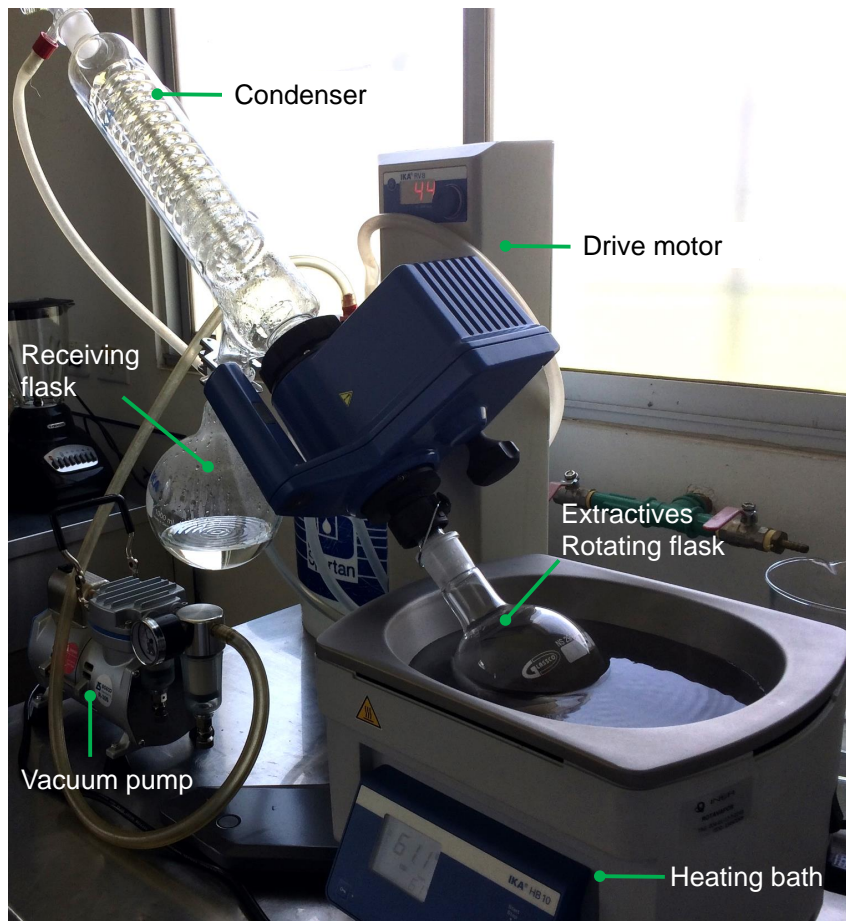


Figure 4.4: Soxhlet extraction unit with its components for extractives analysis a), extraction process after 4 hours b) and after 24 hours of extraction c).

$$ODW_{sample} = \frac{(Weight_{thimble+sample} - Weight_{thimble}) \cdot \%Total\ solids}{100} \quad (4.7)$$

$$\%Extractives = \frac{Weight_{flask+extractives} - Weight_{flask}}{ODW_{sample}} \cdot 100 \quad (4.8)$$

Where:

$Weight_{thimble+sample}$ = weight of the cellulose thimble containing the sample in [g].

$Weight_{thimble}$ = weight of the empty cellulose thimble in [g].

$\%Total\ solids$ = percentage of solids in the sample.

$\%Extractives$ = percentage of extractives in the sample.

$Weight_{flask+extractives}$ = weight of the round bottom flasks with the extractives in [g].

$Weight_{flask}$ = weight of the empty round bottom flasks in [g].

4.2.4.2 Determination of cellulose, hemicellulose and lignin content

The NREL/TP-510-42618 laboratory analytical procedure is used for determining structural carbohydrates (cellulose and hemicellulose) and lignin in biomass. The mentioned procedure requires an extractives-free biomass which undergoes a two-step acid hydrolysis to obtain carbohydrate monomers. Cellulose, hemicellulose and lignin contents are determined with high performance liquid chromatography (HPLC) and UV-Visible spectrophotometry. Cellulose and hemicellulose contents are quantified using HPLC with an Agilent 1260 Infinity chromatographer equipped with a RezexROA Organic Acid H⁺ column, using sulfuric acid 0.005 N as mobile phase, with a 0.5 mL min⁻¹ flowrate, operating at 30 °C, with an infrared detector working at 30 °C. The injection volume is 10 µL and the retention time is of approximately 3.6 minutes. Whereas acid-insoluble lignin is measured by gravimetry, acid-soluble lignin is measured by UV-Vis spectrophotometry in a DR6000 UV-VIS Hach spectrophotometer [184, 185, 186]. The detail of the measurements, used equipment and calculations for determining the cellulose, hemicellulose and lignin content in PKS is presented in Appendix B.

4.2.4.3 Elemental analysis

The ultimate or elemental analysis is determined in accordance with the BS EN 16948:2015 standard "Solid biofuels-Determination of total content of carbon, hydrogen and nitrogen" using a Perkin Elmer 2400 series II CHNS/O analyzer equipped with a thermal conductivity detector (TCD). Helium is used as carrier gas and Oxygen is used as combustion gas. Benzoic acid is used for calibration. The analyzed samples have a nominal size of 1 mm or less and the moisture content is determined previous the elemental analysis using an HB43-S Halogen Mettler Toledo Moisture Balance with a 1 mg precision and a moisture content repeatability of ±0.3%. Each moisture determination requires 1 g of sample and it is performed by triplicate. For the elemental analysis, 500 mg of the moist PKS or 500 mg of the moist synthetic mixture are weighted in a Perkin Elmer AD 6000 Autobalance, as it is presented in Figure 4.5. Analysis are conducted by triplicate. The content of carbon, hydrogen, nitrogen and sulphur are reported as weight percentages on a dry basis, whereas the oxygen content is calculated by difference. The elemental composition of PKS is also presented using a Van Krevelen diagram, which allows an easier comparison between different types of biomass. The detail of the measurements of the elemental analysis and of the calculations for determining the O:C and H:C ratios required in the Van Krevelen diagram,

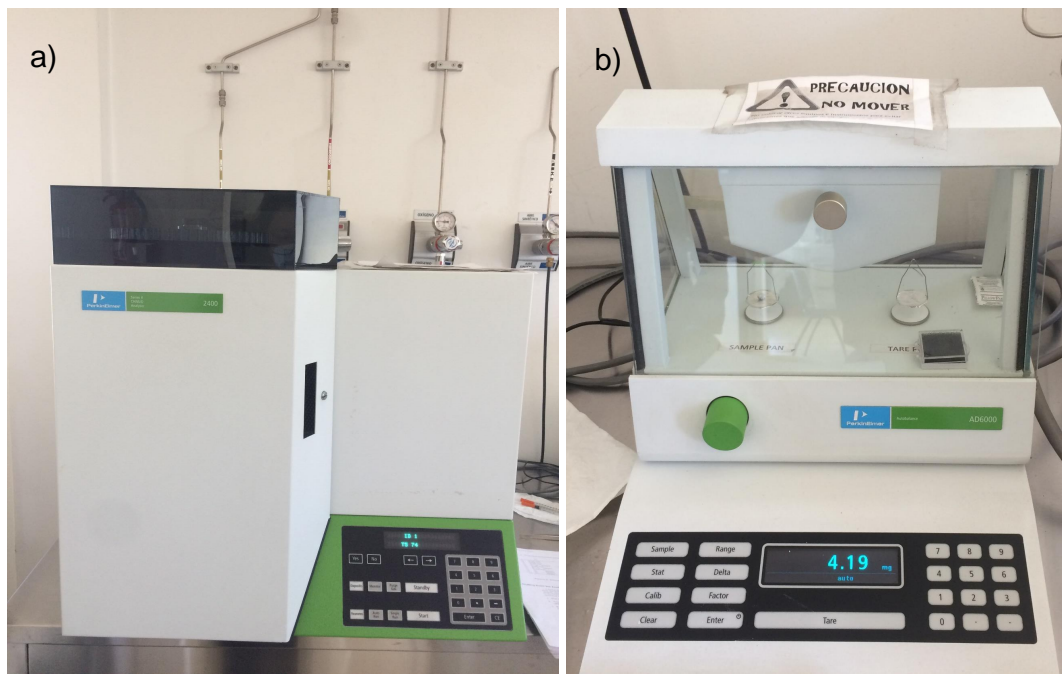


Figure 4.5: Elemental analyzer a) and micro balance b) used in the determination of the elemental composition in PKS.

are presented in the corresponding section of Appendix B.

4.2.4.4 FTIR functional group analysis

Infrared spectroscopy is particularly relevant for identifying characteristic functional groups that might be present in complex samples such as biomass. Moreover, this technique can provide information on the types of lignin that might be part of palm oil waste biomass [187]. The functional groups found in PKS and in the synthetic mixture resembling PKS are studied using Fourier transform infrared spectroscopy (FTIR). For this purpose, a JASCO FT/IR 4600 series is used for the measurements between 400 and 4000 cm^{-1} . The Spectra Manager CFR software is used for processing the data and the measurements are taken in the equipment presented in Figure 4.6.

4.2.5 Energy content analysis

The analysis of the energy content for PKS and for the synthetic mixture considers two sections. Whereas the first section deals with the measurement of the high heating value, HHV, the second section aims to develop an empirical correlation to predict the HHV of a lignin-rich biomass from its composition.



Figure 4.6: JASCO FT/IR 4600 series infrared spectrometer used for analyzing PKS and the synthetic mixture.

4.2.5.1 Higher heating value determination

Both the PKS and the prepared synthetic mixture are characterized in terms of the HHV in accordance with the BS EN 18125:2017 standard using an IKA® C2000 calorimeter that operates at constant volume. The test samples for determining the HHV need to be previously ground and passed through a 1.0 mm sieve. The moisture content of the sample is determined before the analysis, following the procedure explained in the previous subsections. The biomass density makes it necessary to pelletize the biomass samples before their HHV determination. For this purpose, approximately 500 mg of sample are weighted in an analytical balance with a 0.01 mg resolution. A pellet of the sample is then formed using an IKA C21 pelleting manual press. The pellet is placed inside a flat based nickel-chromium crucible that complies with the dimensions indicated in the BS EN 18125:2017 standard. The manual press, crucible and calorimeter used in this work is presented in Figure 4.7. A calibration procedure is performed before the HHV determination with benzoic acid as standard. Cotton is used as fuse in every determination and analysis are undertaken by triplicate. The determined HHV is reported on a dry and sulphur-free basis using equations 4.9 and 4.10. For this purpose. The detail of the measurements are presented in the corresponding section of Appendix B.

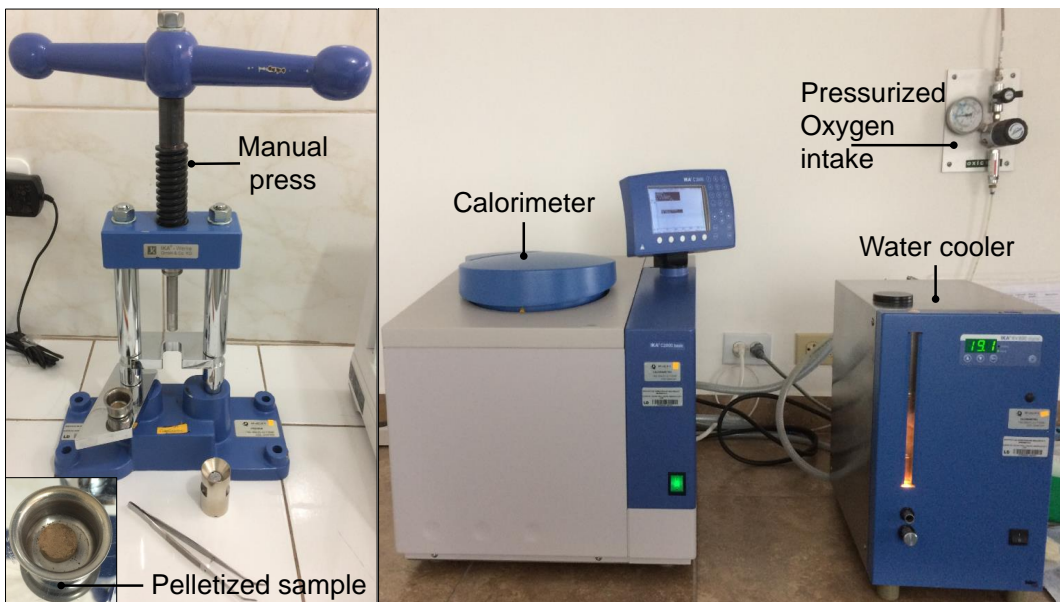


Figure 4.7: Calorimeter used for the determination of HHV in biomass, manual press and crucible with PKS pellet.

$$HHV_{\text{dry}} = HHV_{\text{moist}} \left(\frac{100}{100 - M_{\text{biomass}}} \right) \quad (4.9)$$

$$Q_s = 94.1 \cdot w(S) \cdot m_1 \quad (4.10)$$

Where:

HHV_{dry} = higher calorific value at constant volume of the dry sample in $[J \text{ g}^{-1}]$.

HHV_{moist} = higher calorific value at constant volume of the moist sample in $[J \text{ g}^{-1}]$.

M_{biomass} = moisture content in the sample [wt.%].

m_1 = mass of the sampled biomass [g].

Q_s = correction to be removed from the HHV due to sulfur content [J].

$w(S)$ = sulfur content in the sample [wt.%].

4.2.5.2 Development of an empirical correlation for predicting higher heating values of lignin-rich biomass

A relationship between the composition and the HHV is proposed on the basis of the properties of lignin-rich biomass found in literature and on the results from the characterization of lignin-rich biomass in this work. Given the little information regarding lignin-rich biomass in literature, an additional sample of biomass, coffee husk, was also characterized experimentally following the same methodology and considering the same standards as for the

Table 4.2: Correlations used for comparison purposes for predicting HHV in MJ kg⁻¹ for lignocellulosic biomass.

Correlation	Input for prediction	Reference
HHV = 0.0877(L)+16.4951	L = lignin content in wt.%	[20]
HHV = 0.3856(C+H)-1.6938	(C+H) = carbon + hydrogen in wt.%	[21]
HHV = 0.0979(L)+16.292	L = lignin content in wt.%	[22]

PKS characterization. The characterization of this lignin-rich biomass is presented in Table B.23 in the Appendix B. The correlation for the prediction of the HHV considered measured data in this work for PKS, coffee husk and the synthetic mixture resembling PKS composition; and it also considered data retrieved from literature for olive husk, walnut shell and hazelnut shell [19]. The develop correlation for predicting the HHV of lignin-rich biomass is developed using a linear regression and it is validated against the experimental and literature retrieved data. Moreover, three different correlations found in literature for predicting HHV in lignocellulosic biomass from its composition are used for comparison purposes. The mentioned correlations from literature are presented in Table 4.2. The comparison of the performance of the different correlations for predicting HHV in lignin-rich biomass is performed on the basis of the coefficient of determination, R^2 , and the root mean square error, $RMSE$.

The coefficient of determination, R^2 , provides information regarding the percentage of variability in the response variable, HHV , that can be explained or captured by the developed linear correlation. The closer R^2 gets to 1, the more variability in the response variable can be explained by the linear correlation. This coefficient gives a general idea of tendencies between predicted and measured quantities and it is calculated in terms of the experimental HHV for biomass, $HHV_{\text{experimental},i}$, the predicted HHV for biomass with each correlation, $HHV_{\text{predicted}}$ and the average of experimental values $HHV_{\text{experimental}}^{\text{average}}$, for a population size n as follows:

$$R^2 = 1 - \frac{\sum_{i=1}^n (HHV_{\text{experimental},i} - HHV_{\text{predicted},i})^2}{\sum_{i=1}^n (HHV_{\text{experimental},i} - HHV_{\text{experimental}}^{\text{average}})^2} \quad (4.11)$$

The $RSME$ indicates the deviation that exists between predicted and experimental values, and it constitutes the residuals' standard deviation. The $RSME$ is calculated as follows:

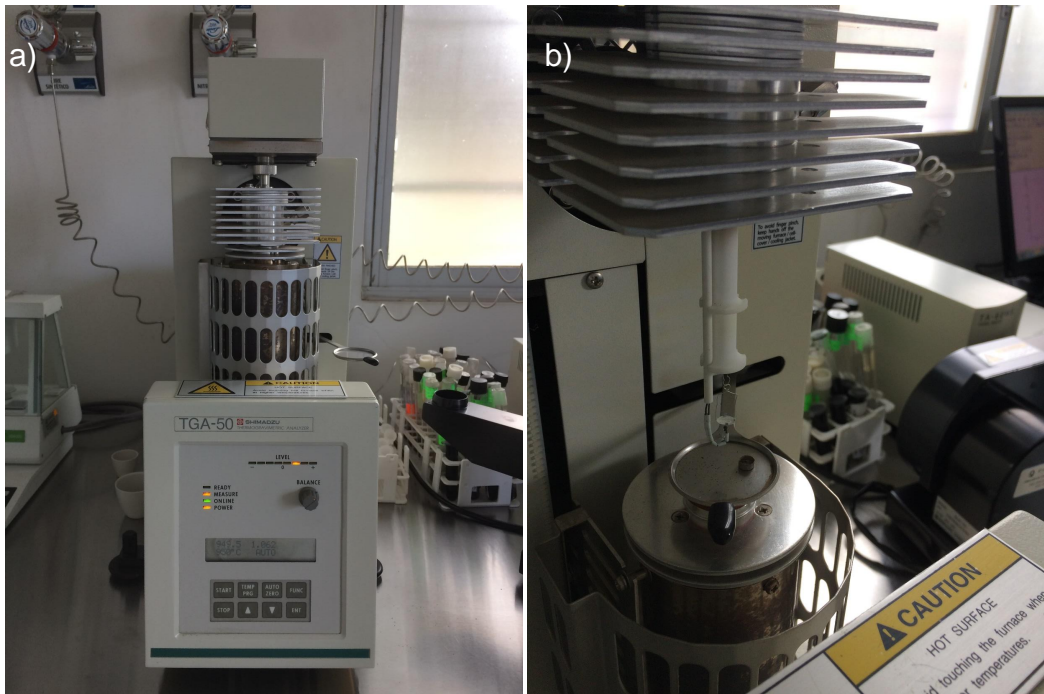


Figure 4.8: TGA equipment in operation a), and before the operation with the sample-containing platinum crucible.

$$RSME = \sqrt{\frac{\sum_{i=1}^n (HHV_{\text{predicted}, i} - HHV_{\text{experimental}, i})^2}{n}} \quad (4.12)$$

4.2.6 Thermal analysis and kinetic model determination

4.2.6.1 Thermogravimetric analysis (TGA)

Thermogravimetric analysis (TGA) is employed for evaluating the thermal decomposition of biomass throughout pyrolysis. Such analysis also allows to determine the kinetic parameters associated with palm kernel pyrolysis [188, 51, 189]. The behavior of PKS and of the synthetic mixture that resembles PKS composition throughout pyrolysis is assessed using thermogravimetric analysis [50]. Such analysis involves biomass thermal decomposition and it provides information for estimating pyrolysis kinetic parameters [188]. A Shimadzu TGA-5 thermogravimetric analyzer is employed for assessing palm kernel shells thermal degradation through pyrolysis, using 50 mL min^{-1} of N_2 [126, 190]. The mentioned equipment is presented in Figure 4.8.

In order to estimate palm kernel shell pyrolysis kinetic parameters, the analysis temperatures considered a range between room temperature and a maximum analysis temperature of 800°C , which corresponds with the maximum operating temperature in the pyrolysis pi-

lot plant that will be described in the next chapter ($750\text{ }^{\circ}\text{C}$) + $50\text{ }^{\circ}\text{C}$ [101]. Four heating rates (5, 20, 35 and $50\text{ }^{\circ}\text{C min}^{-1}$) are examined; and thermal lag throughout the TGA analysis is avoided by considering particles with sizes between 38 and $180\text{ }\mu\text{m}$, and samples of approximately 4 mg [101]. The sample is placed in a previously tared platinum crucible. Additionally, a mixture of cellulose, hemicellulose and lignin is prepared with similar concentrations of those found in the characterized palm kernel shells. The thermal decomposition of the prepared mixture is evaluated through TG analysis, under the same analysis conditions as the palm kernel shells. The control of the equipment and the collection and analysis of data were performed using the TA-60WS Thermal Analysis Workstation Software. The proposed TGA analysis corresponds with a multilevel factorial design of experiments, with 2 levels of biomass type (PKS and synthetic mixture), 4 levels of heating rate (5, 20, 35 and $50\text{ }^{\circ}\text{C min}^{-1}$) and 3 repetitions; which constitutes 24 determinations. In addition and for comparison purposes only, pure cellulose, hemicellulose and lignin samples are also evaluated. A cleaning cycle is run every 2 to 3 determinations to prevent fouling. The detail of the experiments as well as the measurements for the TGA analysis for both the PKS and the prepared synthetic mixture are detailed in the corresponding section of the Appendix B.

4.2.6.2 Kinetic model for PKS pyrolysis

The kinetic analysis is made in terms of the degree of conversion (α), which is a dimensionless value calculated from the initial (w_0) and final (w_f) mass of solid in the thermal analysis, as well as from the solid mass present at any time (w_t) in the analysis, as shown in Eq. 4.13. Considering that the pressure remained constant throughout the thermal analysis, the rate of pyrolysis is defined in terms of temperature (T) and α (Eq. 4.14). The temperature-dependent pyrolysis rate constant, $k(T)$, is described in terms of the activation energy, E_a , and the pre-exponential factor, A , using the Arrhenius equation (Eq. 4.15). In general, model-free or model-based approaches could be taken for defining $f(\alpha)$ and for finding the required kinetic parameters.

$$\alpha = \frac{w_0 - w_t}{w_0 - w_f} \quad (4.13)$$

$$\frac{d\alpha}{dt} = k(T)f(\alpha) \quad (4.14)$$

$$k(T) = A \exp\left(-\frac{E_a}{RT}\right) \quad (4.15)$$

Model-free approaches, also referred to as isoconversional methods, require the definition of

values of α and different reaction orders (n) could be evaluated. Similarly, the conversion function, $f(\alpha)$, follows a simple reaction-order model of n order (Eq. 4.16) [191]. The variation of the conversion with temperature can be defined as presented in Eq. 4.17.

$$f(\alpha) = (1 - \alpha)^n \quad (4.16)$$

$$\frac{d\alpha}{dT} = \frac{d\alpha}{dt} \frac{dt}{dT} \quad (4.17)$$

By considering a first order reaction ($n = 1$), and by combining Eq. 4.15, Eq. 4.16 and Eq. 4.17 in Eq. 4.14, the rate of pyrolysis is now defined by Eq. 4.18, and its integral expression is presented in Eq. 4.19.

$$\frac{d\alpha}{dT} = \frac{A}{\beta} \exp\left(-\frac{E_a}{RT}\right) (1 - \alpha) \quad (4.18)$$

$$\int_0^\alpha \frac{d\alpha}{(1 - \alpha)} = \frac{A}{\beta} \int_{T_0}^T \exp\left(-\frac{E_a}{RT}\right) dT \quad (4.19)$$

The right hand side term of Eq. 4.19 is known as the temperature integral and it is usually represented as $p\left(\frac{E_a}{RT}\right)$. The previous equations consider a constant heating rate (β). Given that Eq. 4.19 does not have an analytical solution, the Flynn-Wall-Ozawa (FWO) approximation is applied. The FWO approximation is an isoconversional method that considers a constant value for α and consequently, it assumes that the reaction rate depends only on the reaction temperature [50]. Moreover, the FWO method considers an apparent activation energy that remains constant while the reaction takes place between T_0 and T , which is the temperature at a given value of α . Similarly, for a constant value of conversion (α), the integral on the left hand side of Eq. 4.19 is a constant represented by $g(\alpha)$. With the mentioned considerations, Eq. 4.19 could be rewritten as:

$$g(\alpha) = \frac{A}{\beta} \int_{T_0}^T \exp\left(-\frac{E_a}{RT}\right) dT = \frac{A}{\beta} \frac{E_a}{R} p\left(\frac{E_a}{RT}\right) \quad (4.20)$$

Given that the temperature integral in the previous equation does not have an exact analytical solution, the Doyle's approximation could be used as follows [192, 50]:

$$\log p\left(\frac{E_a}{RT}\right) \cong -2.315 - 0.4567\left(\frac{E_a}{RT}\right), \quad \text{for } 20 \leq \left(\frac{E_a}{RT}\right) \leq 60 \quad (4.21)$$

Eq. 4.20 can be rearranged, logarithms at both sides of the equation can be taken and

Doyle's approximation for the temperature integral (Eq. 4.21) could be included as follows:

$$\log(\beta) = \log\left(\frac{A E_a}{R g(\alpha)}\right) - 2.315 - 0.4567 \frac{E_a}{RT} \quad (4.22)$$

For applying the FWO method, a value of α is fixed and the $\log(\beta)$ is plotted against $1/T$ for different heating rates ($20, 30$ and 50 $^{\circ}\text{C min}^{-1}$). This is repeated for different values of α and parallel lines are obtained. The slope of each one of the obtained lines is equivalent to $-0.4567\left(\frac{E_a}{R}\right)$, and the activation energy can be calculated accordingly. Similarly, the intercept of the mentioned lines with the y-axis determines the value of $\log(A)$, and consequently, the value of A can be calculated. Given that for each value of α , there is a corresponding value for E_a and A ; average values of these two kinetic parameters are reported.

For comparison purposes, the Kissenger-Akahira-Sunose (KAS) method for determining E_a and A is applied. In such case, $g(\alpha) = n^{-1}[(1 - \alpha)^{-n} - 1]$. The KAS method also considers an approximate solution of the heat integral given by Eq. 4.23 and Eq. 4.24. When the KAS method is applied for a defined conversion (α), a straight line is obtained when plotting $\ln\left(\frac{\beta}{T^2}\right)$ vs. $1/T$. Moreover, the slope in such plot corresponds to $-E_a/R$ and the value of E_a can be obtained accordingly.

$$p\left(\frac{E_a}{RT}\right) \cong \left(\frac{E_a}{RT}\right)^{-2} \exp^{-\left(\frac{E_a}{RT}\right)} \quad (4.23)$$

$$\ln\left(\frac{\beta}{T^2}\right) = \ln\left(\frac{AE_a}{Rg(\alpha)}\right) - \frac{E_a}{RT} \quad (4.24)$$

4.3 Results

4.3.1 Physical, chemical and thermal characterization: general findings

The general results from the physical, chemical and thermal characterization of the palm kernel shells are presented in Table 5.2. The information in this table shows that PKS have a bulk density of 536.54 kg m^{-3} , which is 2 to 7 times higher than other common types of residual biomass like loose or briquetted corn stover, making PKS bulk density comparable to densified biomass such as wood pellets ($520 - 640 \text{ kg m}^{-3}$) [193]. PKS density, in combination with a resulting HHV of 19.32 MJ kg^{-1} , make PKS a suitable feedstock for energy applications. Moreover, such properties highlight the fact that PKS do not re-

Table 4.3: Results from the palm kernel shell characterization

Property	Value
Size and density	
Bulk density [kg m ⁻³]	536.54 ± 2.13
Apparent density [kg m ⁻³]	1286.67 ± 11.77
d ₅₀ [mm]	4.74 ± 0.010
d ₈₀ [mm]	6.51 ± 0.007
Proximal analysis	
Moisture content [wt.%]	10.62 ± 0.07
Ash content [wt.%]	2.31 ± 0.17
Volatiles [wt.%]	77.18 ± 0.08
Fixed carbon ^a [wt.%]	9.88 ± 0.19
Elemental analysis ^b	
C [wt.%]	51.81 ± 0.20
H [wt.%]	7.14 ± 1.75
N [wt.%]	0.59 ± 0.04
S [wt.%]	0.25 ± 0.19
O ^a [wt.%]	40.19 ± 1.33
Biomass composition ^c	
Cellulose [wt.%]	17.52 ± 2.32
Hemicellulose [wt.%]	26.36 ± 0.28
Lignin [wt.%]	56.12 ± 1.19
Extractives	
Water soluble extractives [wt.%]	2.51 ± 0.50
Ethanol soluble extractives [wt.%]	3.27 ± 0.18
Energy content ^b	
Higher heating value [MJ kg ⁻¹]	20.77 ± 0.07

^a Calculated by difference.

^b Calculated on dry basis.

^c Calculated on dry and extractives free basis.

quire a densification process prior to their use as energy source in applications that are similar to those of pelletized or densified biomass. On the contrary, in cases where higher energy density is required, PKS should undergo pyrolysis to obtain biochar, a solid product with increased energy content. Indeed, PKS biochar has shown to reach a HHV near 27.50 MJ kg⁻¹, which represents an increment of nearly 40 % in the energy content, when compared to unpyrolyzed PKS [126].

Regarding the results from the proximal analysis presented in Table 5.2, the low moisture and ash content, and the high volatiles content found in the PKS, show that PKS are suitable for thermochemical processing via pyrolysis. Given that PKS particle size is in average 4.74 [mm] and that 80% of the particles reach a diameter of 6.51 [mm] or below, thermally thick

particles would be expected [44]. In such circumstances, the moisture content found in PKS (10.62 %) shows that intermediate and high heating rates could be used in PKS pyrolysis without a previous drying process, which would represent a less energy-intensive overall process. The moisture content found in PKS reaches the upper limit (11.00%) at which pyrolysis could be delayed by moisture but without affecting the products distribution [74]. Moreover, moisture contents of nearly 10.00%, or less, are preferred in pyrolysis processes where bio-oil is the product of interest [5]. On the contrary, if slow pyrolysis and slow heating rates are required, water evaporation within PKS could further delay pyrolysis and the overall char production could be reduced in the vicinity of the particle's centre [74]. Regarding the other parameters of the proximal analysis, and comparing them to other types of lignocellulosic biomass, such as the ones presented in Table 4.4; PKS show potential for energy applications and thermochemical processes, like pyrolysis, might be the more suitable technologies for processing PKS.

The resulting PKS ash content of 2.31 % is an average value when compared with other types of lignin-rich biomass and a low value when compared with other residual biomass with higher cellulose or hemicellulose content such as rice husk, wheat straw or barley straw. However, when comparing PKS properties with some of the specifications for type A and B non-woody pellets for commercial and residential applications, the ash content in PKS is below the 6.0% and 10.0% required in type A and type B pellets, correspondingly. This facilitates the use of PKS as an energy source and it makes its thermochemical processing easier given that higher ash contents translates into operational problems, shorter cleaning and maintenance times, and higher overall handling and production costs [116]. The high content of volatiles in PKS (77%) favors a thermochemical conversion for PKS in which most of the products will be either gases or condensable species. Similarly, the low fixed carbon content (9.88%) shows that thermochemical processes such as pyrolysis or gasification would be preferable for processing PKS [116]. The cellulose, hemicellulose and lignin content in PKS will be discussed in further detail later on, when the chemical composition of PKS is studied. At this stage it is only worth mentioning that the particularly high lignin content (56.12%) makes PKS a different type of biomass when considering previous biomass-related research [194, 116, 195, 3]. Moreover, PKS high lignin content limits its biodegradability. Thus, biochemical processing routes such as anaerobic digestion, might not be suitable with this feedstock [116]. Finally, the low extractives content (< 6.0 wt.%)

Table 4.4: Proximal analysis comparison between different types of lignocellulosic feedstock

Biomass	Moisture [%]	Volatiles [%]	Fixed carbon [%]	Ash [%]	Reference
Lignin-rich biomass					
PKS	10.62	77.18	9.88	2.31	This work
Dry PKS	-	86.36	11.06	2.58	This work
Olive husk	-	63.90	32.80	3.30	[19]
Walnut shell	-	59.3	37.9	2.8	[19]
Hazelnut shell	-	70.3	28.3	1.4	[19]
Lignin	9.00	73.5	1.5	16	[17]
Cellulose or hemicellulose-rich biomass					
Rice husk	9.40	74.00	13.20	12.80	[17]
Sugarcane bagasse	10.40	76.70	14.70	2.20	[17]
Rice straw	7.30	60.84	16.61	22.55	[196]
Wheat straw	16.00	59.00	21.00	4.00	[116]
Barley straw	30.00	46.00	18.00	6.00	[116]
Danish pine	8.00	71.60	19.00	1.60	[116]

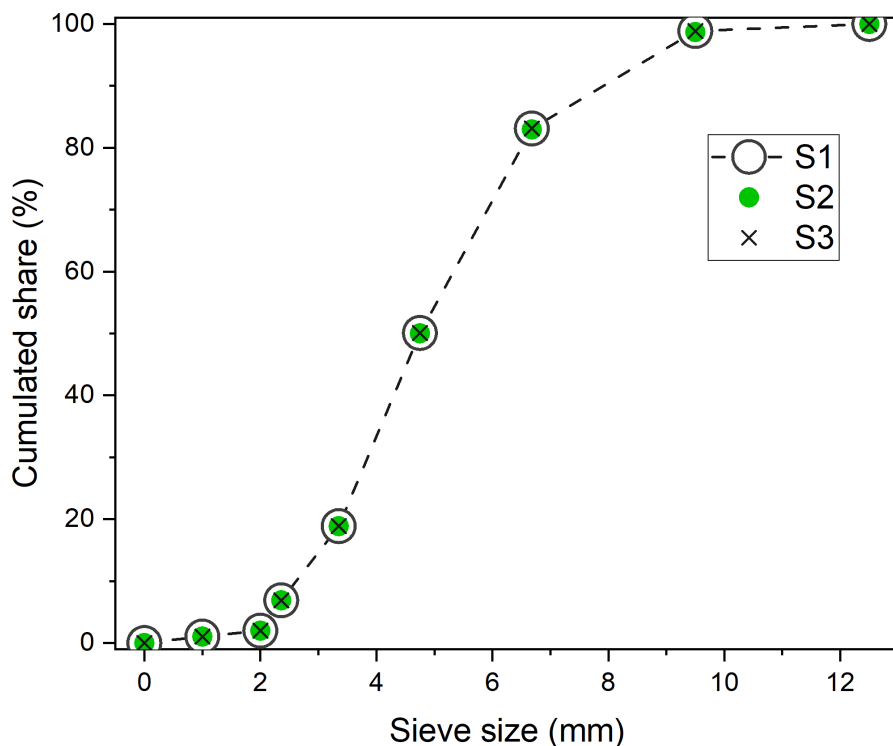
found in PKS, indicates that there is no need of a previous extraction process for removing components that might affect pyrolysis. In conclusion, the results corresponding to the characterization of PKS suggest that PKS could be either used as a solid fuel as is, without any previous processing stage or any previous densification process; or it can also undergo pyrolysis without the need of pretreatment stages for obtaining bio-oil, biochar, gases or platform chemicals.

4.3.2 PKS size and density

Table 5.1 and Figure 5.1 show that PKS particles are in the order of millimetres. Indeed, 50% of the PKS particles are approximately 5 millimetres or bigger and 30% of the PKS particles are between 5 y 7 millimetres approximately. The size distribution on Table 5.1 also shows that there are not many fine particles, having near 10% of the PKS particles with sizes of 2.36 millimetres or smaller. Considering that particle sizes of 1 millimetre or smaller behave as thermally-thin particles in slow pyrolysis conditions [139], it would be expected that PKS behave mostly like thermally-thick particles in slow pyrolysis conditions. Similarly, for fast pyrolysis conditions, particles 2 to 3 orders of magnitude smaller than a millimetre behave as isothermal or thermally thin particles in pyrolysis [76]. Therefore, PKS particles will most likely behave as thermally-thick particles regardless of the heating rate selected for pyrolysis. In such circumstances, modelling PKS pyrolysis requires the

Table 4.5: Average results of particle size distribution for PKS

Size	Share [%]	Cumulative share [%]	d_{50} [mm]	d_{80} [mm]
<2.00	1.03 ±0.01	1.03 ±0.01		
2.00	0.96 ±0.00	2.00 ±0.01		
2.36	4.89 ±0.02	6.89 ±0.03		
3.35	12.03 ±0.09	18.92 ±0.06		
4.75	31.27 ±0.17	50.19 ±0.23	4.74 ±0.010	
6.68	32.78 ±0.35	82.97 ±0.14		6.51 ±0.007
9.5	15.80 ±0.10	98.77 ±0.09		
12.5	1.23 ±0.09	100.00 ±0.00		

**Figure 4.9:** Cumulative share for different particle sizes for 3 different PKS samples.

consideration of internal temperature gradients and the analysis of thermally-thick particles becomes relevant.

4.3.3 PKS chemical composition and its relationship with the energy content

Table 4.4 showed lignin as the main structural component of palm kernel shells, followed by hemicellulose and cellulose. The lignin content found in this work corresponds with previously studied PKS [126]; however, the content of hemicellulose and cellulose differs. Whereas in the present study, hemicellulose and cellulose were found to represent 26.36%

and 17.52% of PKS structural components correspondingly, it has been reported that hemicellulose and cellulose could reach 14.20% and 27.51% in PKS [126]. Such variation could be explained by the different varieties of palm tree used in each study and by the differences in environmental factors and growing and harvesting practices. Such results highlight the need to study each particular feedstock, and they show the limitations of assuming a generalized composition for PKS.

The results from the elemental analysis are organized in the Van Krevelen diagram of Figure 4.10, which also includes other lignin-rich and cellulose-rich types of biomass retrieved from literature [17, 18, 19]. The Van Krevelen diagram shows that the studied types of lignin-rich biomass have a similar behaviour in terms of presenting low O/C atomic ratios, compared to cellulose-rich biomass, which present higher O/C ratios. Lower oxygen contents are associated with higher energy contents. Moreover, it is possible to divide the Van Krevelen plot with a diagonal that separates the plot in two zones: a lignin-rich biomass zone (colored zone) and a cellulose or hemicellulose-rich biomass zone (uncolored zone). The identified lignin-rich zone in the Van Krevelen plot allows to infer a pattern regarding the energy content of lignin-rich biomass. Indeed, when comparing Figure 4.10 with the value of HHV reported in Figure 4.11, it is evidenced that, for lignin-rich biomass, lower O/C ratios are related with higher heating values in biomass. This also means that as we move towards the left hand side of the Van Krevelen plot into the lignin-rich biomass zone, smaller O/C ratios are related to higher HHV. Such behaviour could be explained when considering that lower amounts of oxygen and higher amounts of carbon (low O/C ratios) are associated to better fuels in general and higher quality of liquid fuels in pyrolysis [179]. The behaviour observed in the Van Krevelen plot and in the HHV content of biomass also points out a potential correlation between the amount of C in a lignin-rich biomass and its energy content. This behaviour is not evidenced in the cellulose or hemicellulose-rich zone.

4.3.3.1 Correlation between lignin-rich biomass composition and its HHV

The high heating value for different types of biomass, presented in Figure 4.11 shows that, out of the studied biomass in this work, walnut shell is the one with the highest energy content, reaching 21.6 MJ kg^{-1} . The studied PKS, also presents a high HHV of 20.77 MJ kg^{-1} . Moreover the existing relationship between O/C atomic ratios and higher HHV is highlighted. It is worth noticing that even though the synthetic mixture is formulated with the same cellulose, hemicellulose and lignin content as the PKS; their HHV differ in

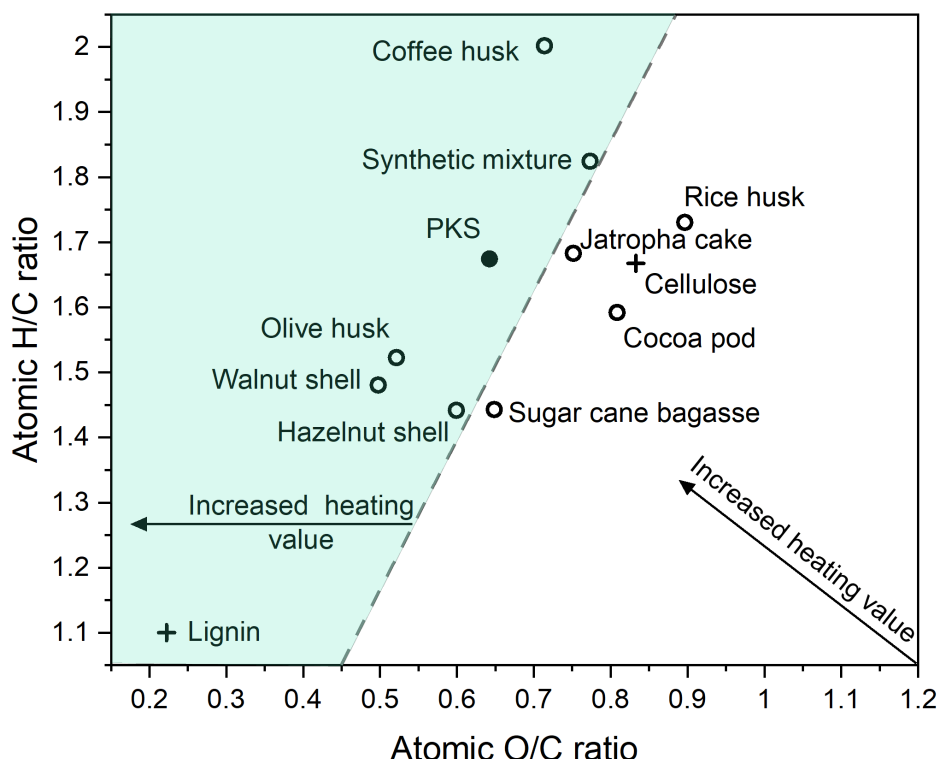


Figure 4.10: Van Krevelen diagram for the PKS from this work and for other types of biomass from literature [17, 18, 19]; with a lignin-rich biomass zone identified and coloured (> 43.9 wt.% of lignin).

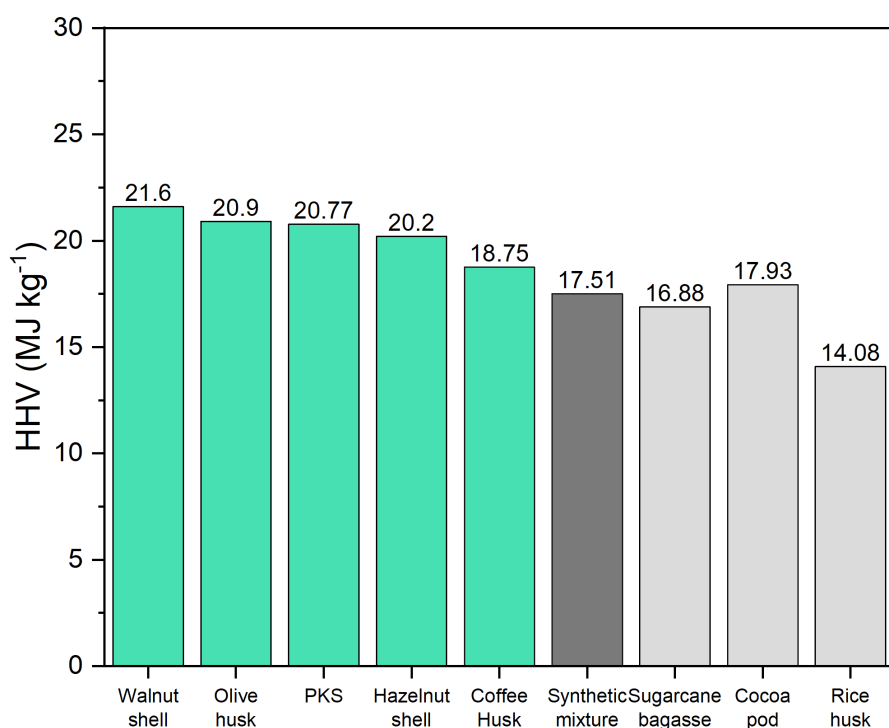


Figure 4.11: Higher heating values determined for PKS and retrieved from literature [17, 18, 19].

approximately 16 %. Such results could be explained when considering that biomass is a complex mixture of cellulose, hemicellulose, lignin, extractives and inorganic components. Moreover, even if the same concentration of cellulose, hemicellulose and lignin is present in the synthetic mixture, only one type of hemicellulose (D-xylose) and one type of lignin (low sulfur lignin) were considered in the synthetic mixture. However, PKS, as most types of biomass, are formed by combinations of heteropolysaccharides that make out hemicellulose and by different types of lignins which could generate the difference in energy content [6]. Moreover, in the synthetic mixture, all the components are loose since they are powders; whereas in the PKS, the components are arranged forming different structures that could also have an impact over the HHV. Lignin-cellulose and lignin-hemicellulose interactions have been found previously in biomass [54, 95], and such interactions or simply the morphology of the structures that biomass' main three components form in PKS will not be present in the synthetic mixture.

In spite of the mentioned contrast among the different types of lignin-rich biomass considered in this work, the previously presented Van Krevelen plot (Figure 4.10) and the HHV presented in Figure 4.11 show a tendency for increasing the HHV whenever the C content also increases in lignin-rich feedstocks. As a result, when the HHV is plotted against the C content for such type of biomass, a linear correlation could be obtained, as presented in Figure 4.12. The HHV of lignin-rich biomass can then be expressed in MJ kg^{-1} , as a function of the wt.% of carbon, C , as follows:

$$\text{HHV} = 0.35124(C) + 2.4639 \quad (4.25)$$

The developed correlation for predicting HHV from the wt.% of C from this work is compared to other correlations found in literature in order to understand potential differences or similarities when different empirical correlations are applied. Table 4.6 shows that

In order to identify the model that better predicts the HHV for lignin-rich biomass, a comparison regarding the differences between predicted and measured HHVs is initially presented in Table 4.6. The information presented in this table suggests that HHV prediction models that are based on the lignin content are not suitable for lignin-rich biomass. Similarly, the mentioned Table shows that both the synthetic mixture and the coffee husk are the two types of biomass whose HHV is more difficult to predict with a linear correlation. Moreover, the correlations that use the mass concentration of carbon or carbon and hydro-

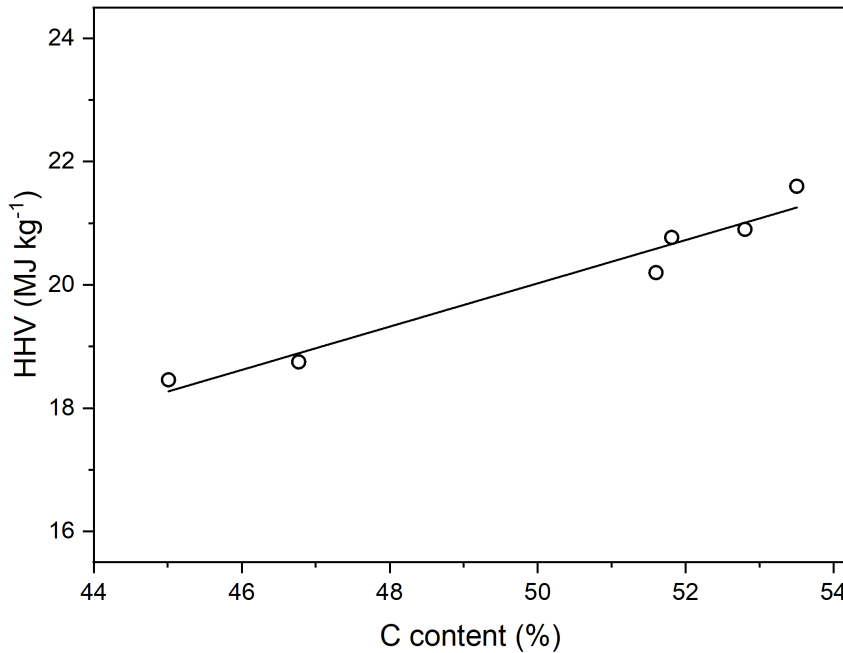


Figure 4.12: Higher heating values for dry lignin-rich for different carbon contents.

Table 4.6: Comparison between experimental results, the correlation developed in this work and correlations from previous works.

Biomass	HHV [MJ kg⁻¹] Measured	This work		[20]		[21]		[22]	
		HHV [MJ kg⁻¹] Predicted	Difference [MJ kg⁻¹] wt.% C based	HHV [MJ kg⁻¹] Predicted	Difference [MJ kg⁻¹] Lignin based	HHV [MJ kg⁻¹] Predicted	Difference [MJ kg⁻¹] wt.% C-H based	HHV [MJ kg⁻¹] Predicted	Difference [MJ kg⁻¹] Lignin based
PKS	20.77	20.66	-0.11	21.42	+0.65	21.04	+0.27	21.79	+1.02
Synthetic mixture	18.46	18.27	-0.19	21.42	+2.96	18.30	-0.16	21.79	+3.33
Olive husk	20.90	21.01	+0.11	20.74	-0.16	21.25	+0.35	21.03	+0.13
Walnut shell	21.60	21.26	-0.34	21.08	-0.52	21.48	-0.12	21.41	-0.19
Hazelnut shell	20.20	20.59	+0.39	20.26	+0.06	20.59	+0.39	20.49	+0.29
Coffee husk	18.75	18.89	+0.14	20.35	+1.60	19.35	+0.60	20.59	+1.84

gen have a better opportunity to predict the HHV in lignin-rich biomass. Such behaviour is corroborated by the statistical parameters presented in Table 4.7. The summary of the results for the regression model for predicting HHV from wt.% of C are presented in Table 4.7. The correlation proposed with this work for predicting HHV in lignin-rich biomass presented the minimum value of RMSE (0.288) and the value of R-Square (COD) closest to one (0.955). The mentioned table also points out that the correlation proposed by [21], which is based on the percentage of C and H in the biomass, can also be applied for lignin-rich biomass. Unlike cellulose-rich or hemicellulose-rich biomass, for lignin-rich biomass, the lignin content is not relevant for predicting the HHV. This behaviour could be explained

Table 4.7: Comparison of statistical parameters between correlations for predicting HHV from composition of biomass.

Parameter	This work	[20]	[21]	[22]
Residual sum of Sq	0.33249	1.2965	0.44467	1.61561
Pearson's r	0.97762	0.10281	0.97117	0.10281
R-Square (COD)	0.95574	0.01057	0.94318	0.01057
Adj. R-Square	0.94467	-0.2368	0.92897	-0.23679
RMSE [MJ kg ⁻¹]	0.28831	0.56932	0.33342	0.63553

by the type of biomass used to build HHV prediction correlations. Moreover, it is also clear that the proposed model still needs to be improved by considering more types of lignin-rich biomass, which could help to develop more robust correlations for predicting energy content in terms of easily measurable properties such as the carbon content.

4.3.4 Crystallographic structure

The results from the XRD analysis presented in Figure 4.13 a) and b) show that despite having the same content of cellulose, hemicellulose and lignin, the PKS and the synthetic mixture do not have the same internal structures nor the same type of carbohydrates. Such results suggest that mimicking PKS with a synthetic mixture has its limitations and it might not be the most accurate way to represent the disposition of carbohydrates in lignin-rich biomass. Regarding the XRD analysis for PKS, the results presented in Figure 4.13 a) show peaks that correspond to cellulose 1 β in the proximity of 21.90° and 16.00° [90, 91]. Cellulose peaks are the only ones that are easily identifiable in the XRD analysis of PKS. The presence of such peaks could be explained when considering that cellulose has crystalline and amorphous zones, and for the PKS samples, cellulose forms some crystalline structures [92]. Regarding the cellulose peaks in the synthetic mixture, the same angles are identified; however, the cellulose peaks in the synthetic mixture are more defined, which is an indication of the fewer interactions that cellulose has with other components in the synthetic mixture, compare to the PKS sample. Another difference that is present when comparing the XRD from the PKS and from the synthetic mixture, is the number and definition of hemicellulose peaks. Whereas in the PKS, hemicellulose appears as shoulders in the 12.45°, 18.16° and 34.64°; the synthetic mixture shows quite a variety of well defined peaks corresponding to D-xylose, the carbohydrate that was used to mimic hemicellulose.

Such difference in the hemicellulose-related peaks highlights the differences in terms of internal structures that both, the PKS and the synthetic mixture have. Indeed, in the PKS, hemicellulose forms some sort of amorphous structure together with the other carbohydrates, whereas in the synthetic mixture, D-xylose is not interacting or forming other types of compounds with the other carbohydrates. Finally, lignin being an amorphous polymer and being the most plentiful in both samples, is not present in the XRD as well defined peaks, but as a molecule that covers a broad range in the XRD analysis. Moreover, lignin most likely interacts with cellulose and hemicellulose to form amorphous structures in PKS [93].

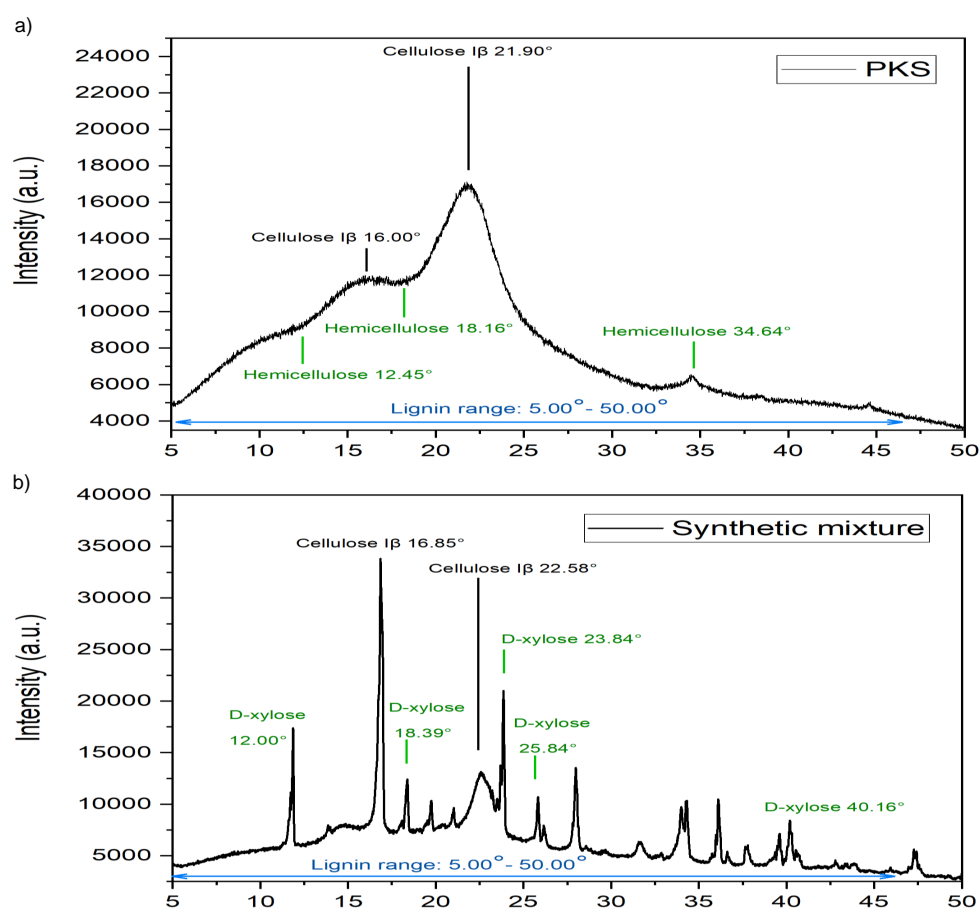


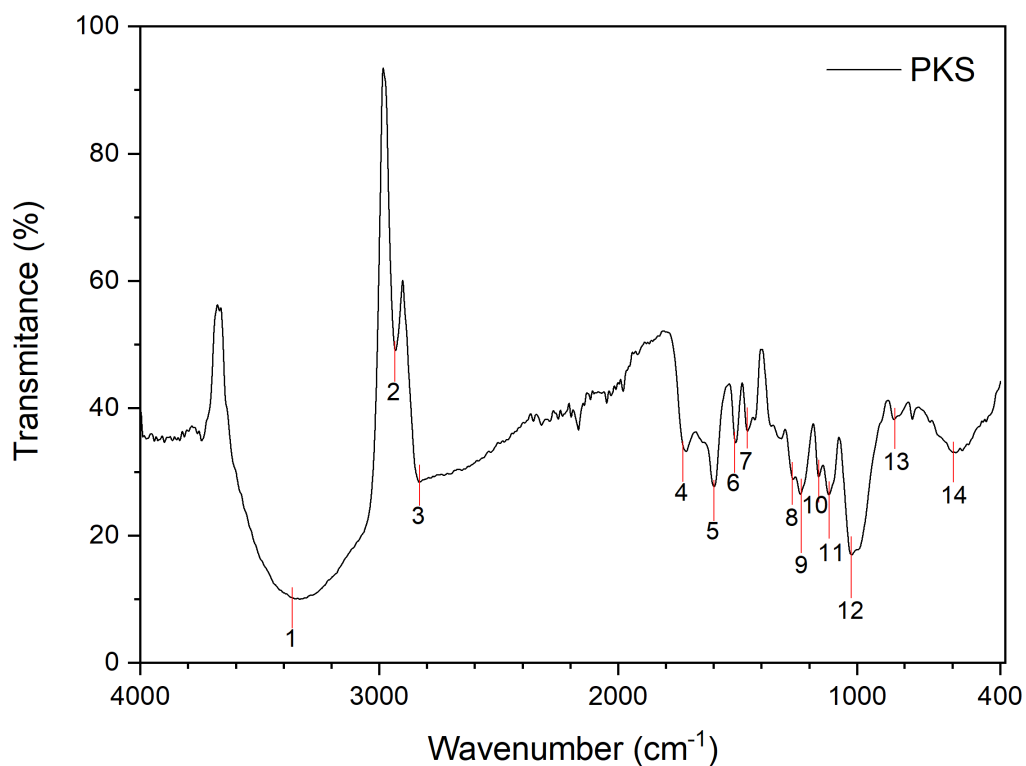
Figure 4.13: XRD analysis for a) palm kernel shells and b) the synthetic mixture.

4.3.5 Functional groups and FTIR analysis

The results presented previously in Table 5.2 showed that the most abundant component found in PKS is lignin, followed by hemicellulose and cellulose. However, unlike cellulose, hemicellulose and specially lignin, can be present in different forms, types and structures

[197]. Figure 4.14 shows the results from the FTIR analysis for PKS. The first peak at 3332 cm^{-1} evidences -OH stretching from phenyl alcohol or from a diol [198]. The 2933 cm^{-1} peak represents a -C-H stretching and the 1727 cm^{-1} indicates non conjugated -C=O stretching; both peaks are an indication of the presence of hemicellulose [198, 199]. The peak found in the proximity of 2832 cm^{-1} corresponds with a -CH stretching found in cellulose molecules [199]. The presence of carbonyl groups is confirmed close to the 1727 cm^{-1} where a non-conjugated C=O stretching suggests the presence of hemicellulose [199, 200]. The peak found at the 1599 cm^{-1} corresponds with the aromatic skeletal vibrations in -C=C- groups from Syringil and Guayacil [199, 201]. Phenyl alcohols can also be identified by the -OH deformation in the peak corresponding to 1508 cm^{-1} . The 1458 cm^{-1} peak is related with C-C ring stretching and vibration from aromatic methyl groups, corresponding to cellulose and hemicellulose [179, 202]. Lignin, mainly in the Guayacil structure, is identified in the 1274 cm^{-1} peak due to -CH, -CO-H and -C-O bend from phenyl alcohol. The presence of Syringil is also possible in the mentioned peak [199, 201, 187]. The presence of Guayacil is once again evidenced in the 1238 cm^{-1} as -OH deformation from a phenyl alcohol or as the presence of aryl groups from lignin [201, 179]. The peaks found at 1167 cm^{-1} corresponds to aromatic -CH deformation, which reveals the presence of HGS-type lignin [201, 202]. The footprint region for PKS, going from 500 to 1500 cm^{-1} , is dominated by the presence of lignin in its Syringil and Guayacil form [201, 202, 179]. However, due to the importance of such region for distinguishing between lignin-rich types of biomass, this section will be further addressed by considering Figure 4.16. A summary of the identified functional groups and their ban location in the infrared spectra is presented in Table 4.8. The mentioned table represents a guideline in identifying lignin-rich biomass and it is a helpful tool for distinguishing the existing types of lignin in a given feedstock.

For comparison purposes, the FTIR analysis of the synthetic mixture is also presented in this section. Figure 4.15 presents the FTIR analysis of the mentioned sample. When comparing the FTIR from the PKS and from the synthetic mixture, it is evidenced that both samples share the first three peaks at 3332 , 2933 and 2832 cm^{-1} . The first common peak, located in the 3332 cm^{-1} is an indication of the presence of aromatics, phenyl alcohol and diols [198]. The second common peak located in the 2933 cm^{-1} highlights the presence of hemicellulose, corresponding to -C-H stretching in -CH₂ and -CH₃ groups [198, 199]. Whereas the third common peak, which evidences -CH stretching in the 2832 cm^{-1} region, is related to

**Figure 4.14:** FTIR spectra of PKS.**Table 4.8:** Identification of characteristic groups in PKS using FTIR spectra.

No.	Location [cm ⁻¹]	Type of bond	Group	Reference
1	3332	-OH stretching	Phenyl alcohol	[198]
		-OH stretching	HO-R-OH alcohol	
2	2933	-C-H stretching in -CH ₂ and -CH ₃ groups	Hemicellulose	[198, 199]
3	2832	-C-H stretching	Cellulose	[199]
4	1727	Non-conjugated C=O stretching	Hemicellulose	[200, 199]
5	1599	Aromatic skeletal -C=C- vibrations	Lignin: Syringil/Guayacil	[199, 201]
6	1508	-OH deformation	Phenyl alcohol	
7	1458	C-C ring stretching and methoxyl C-H bending	Aromatic group	[202]
8	1274	-CH,-CO-H bend, C-O from phenyl alcohol/ether	Lignin: predominantly Guayacil, possible Syringil	[199, 201, 187]
9	1238	-OH deformation from phenyl alcohol	Lignin: Guayacil	[201]
10	1167	Aromatic -CH deformation	Lignin: HGS. hydroxy phenylpropane H-lignin	[187, 202]
11	1118	-COC- symmetric stretch in glycosidic group -CH from an aromatic in plane deformation	Cellulose Lignin: Syringil	[199] [201]
12	1022	-CO stretching from phenyl alcohol	Lignin: Guayacil	[201]
13	843	-C-H bend out of plane	Lignin: Syringil/Guayacil	[201, 202]

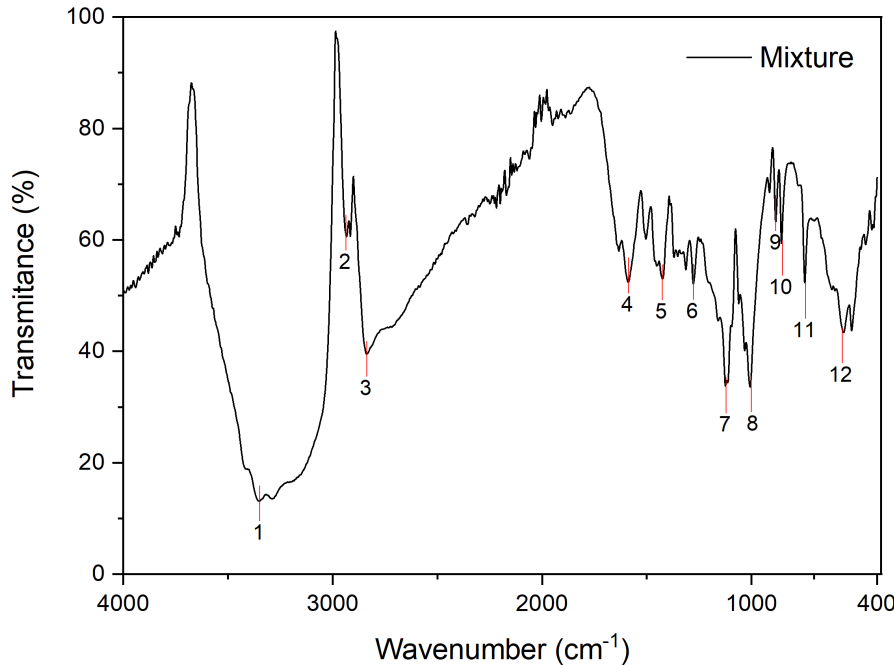


Figure 4.15: FTIR spectra of the synthetic mixture resembling PKS composition.

the presence of Cellulose [199]. In spite of these similarities in FTIR analysis between PKS and the synthetic mixture, the region between 1400 and 400 cm⁻¹ show some differences. In order to explore such differences, a comparative plot between OKS and the synthetic mixture, in the 1400-400 cm⁻¹ section, is presented in Figure 4.16. As it is evidenced in the mentioned figure, the main difference between the PKS and the synthetic mixture appears to be the type of lignin that each of the samples have. Considering that lignin could usually be found in Syringil (S), Guayacil (G) or p-hydroxyphenil (H) form [201], Figure 4.16 shows that the main difference between PKS and the synthetic mixture is that the synthetic mixture lacks lignin in the Guayacil form nearby the 1238 cm⁻¹. Considering that Guayacil presents a more stable structure than Syringil [65], it would be expected that the PKS and the synthetic mixture present differences in their behaviour when subjected to thermal stress such as in pyrolysis.

4.3.6 Microscopy

The microscopy analysis and the results presented in this subsection aim to have a better understanding of the morphology of the PKS. Figure 4.17 shows that PKS are formed by an intricate network of cell-like structures that are reinforced by thick walls. Moreover, it is not possible to visualize free spaces or air pockets/cavities within PKS structure. Such distribution could be one of the reasons of PKS high density. A closer look into the mor-

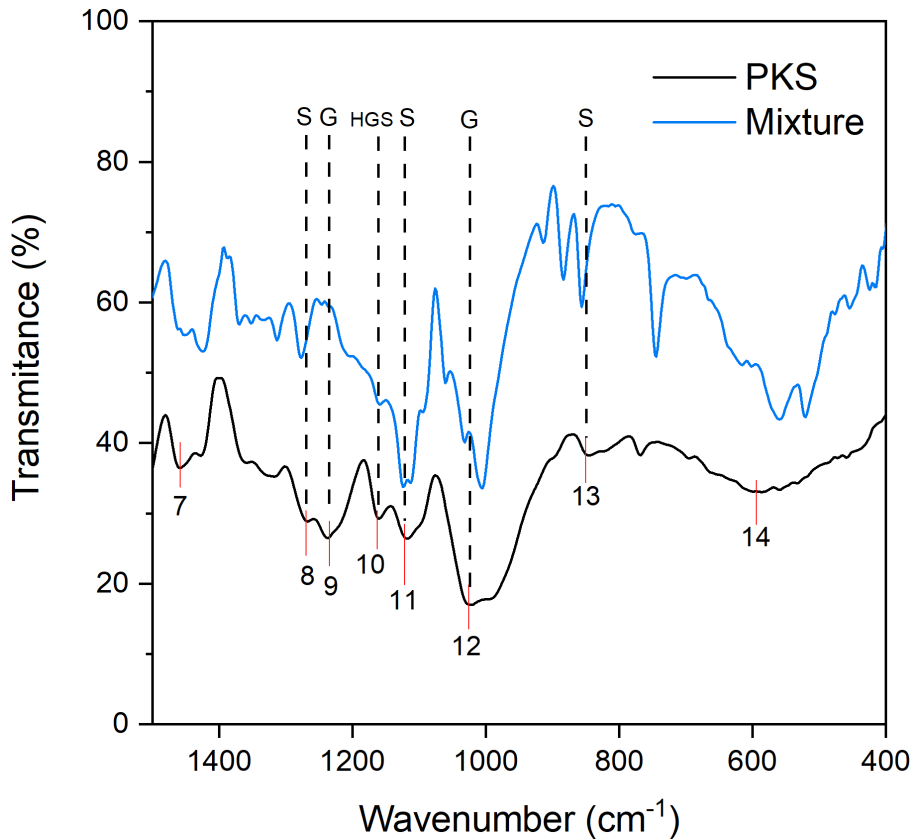


Figure 4.16: Section of the 1400–400 cm^{−1} of the FTIR spectra of PKS.

phology of PKS is shown in Figure 4.18, where it is possible to observe arrangements of potential cellulose group of fibres within what would be expected to be a lignin and hemicellulose matrix. Moreover, the walls surrounding these cell-like structures are also evident in this Figure. Given that lignin is the main component of PKS and to have a rough idea of lignin's distribution within PKS, the dyeing agent (Toluidine blue) used in Figure 4.19 reveals that lignin is in principle as one of the components of the wall of the cell-like structures, but also as a component of the matrix that holds the previously identified fibre arrangements. The analysis used for understanding PKS morphology should be complemented with fluorescence microscopy to effectively identify cellulose, hemicellulose and lignin. However, the distribution of lignin for PKS found in this work is similar to what other authors have found using fluorescence microscopy [203].

4.4 Thermal analysis and kinetic model determination

In this section, the results regarding the thermal behaviour of both palm kernel shells and the synthetic mixture are first described for different heating rates. Moreover, the pyrolysis

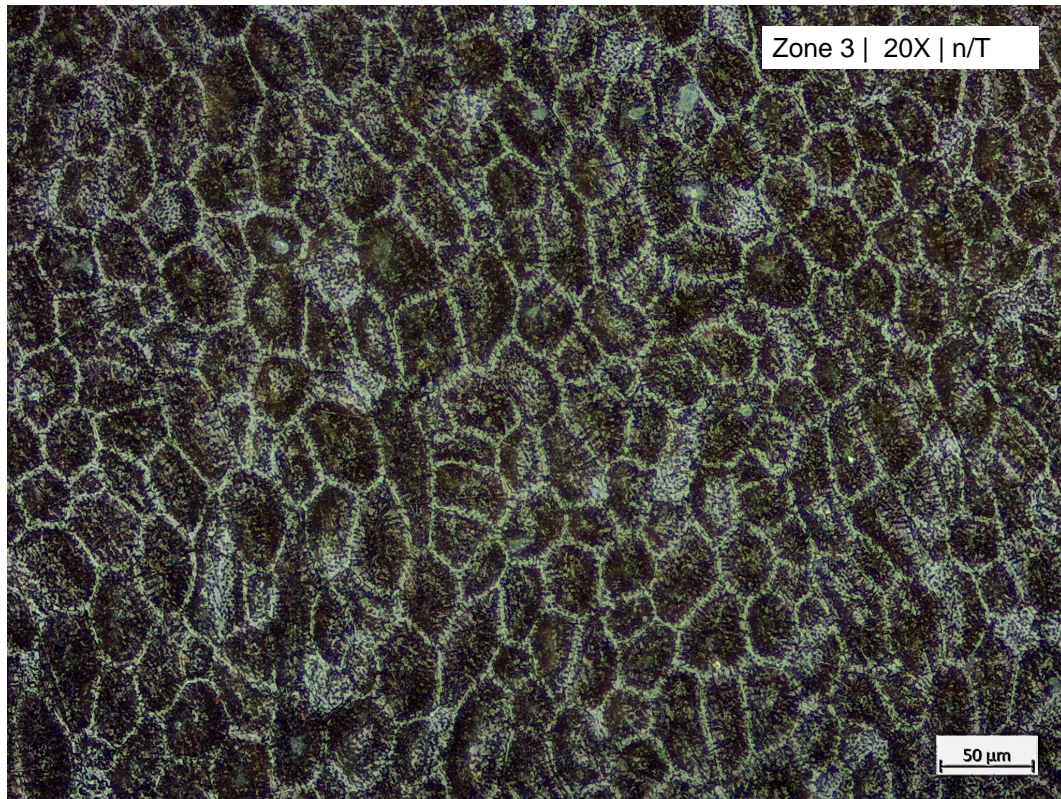


Figure 4.17: Morphology of the PKS in the polarized light microscope, zone 3 with 20X magnification and without Toluidine (n/T).

stages are identified for both types of biomass. Later in this section, pyrolysis kinetics are studied for the PKS and the corresponding kinetic parameters are found and compared with the available literature.

4.4.1 Thermal analysis and behaviour throughout pyrolysis

4.4.1.1 Heating rates and remaining mass after pyrolysis

Figures 4.20 and 4.21 show the thermal decomposition of PKS undergoing pyrolysis for different heating rates between 5 and 50 $^{\circ}\text{C min}^{-1}$. It could be inferred from such results, that whereas the heating rates of 20, 30 and 50 $^{\circ}\text{C min}^{-1}$ behave in a similar way throughout pyrolysis, the PKS that is pyrolyzed at a heating rate of 5 $^{\circ}\text{C min}^{-1}$ behave differently. Such difference in behaviour could be indicating that whereas at 5 $^{\circ}\text{C min}^{-1}$, PKS are still in a slow pyrolysis regime, the PKS that are pyrolyzed at 20, 35 and 50 $^{\circ}\text{C min}^{-1}$ could be undergoing an intermediate pyrolysis regime. When contrasting the heating rates from the analysis with the values available in literature, slow pyrolysis would be expected below the 20 $^{\circ}\text{C min}^{-1}$ [23]. Figure 4.21 also suggests that PKS gets consumed almost completely throughout pyrolysis, given that pyrolysis lasts 4 times more than when other heating rates

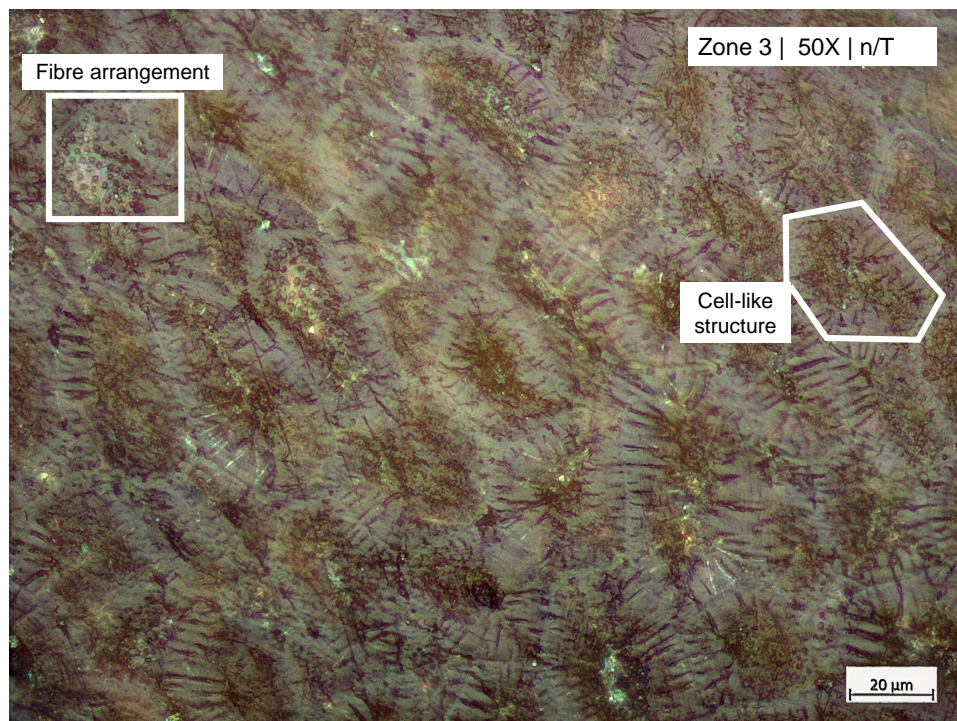


Figure 4.18: Morphology of the PKS in the polarized light microscope, zone 3 with 50X magnification and without Toluidine (n/T).

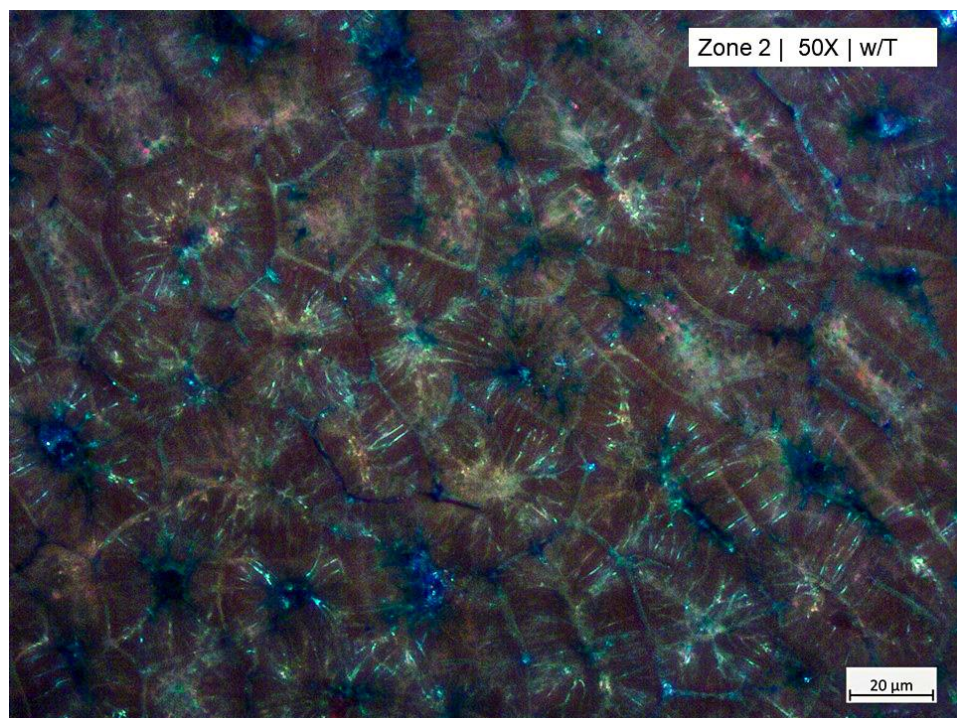


Figure 4.19: Potential location of lignin and morphology of the PKS in the polarized light microscope, zone 2 with 50X magnification and with Toluidine blue as dyeing agent (w/T).

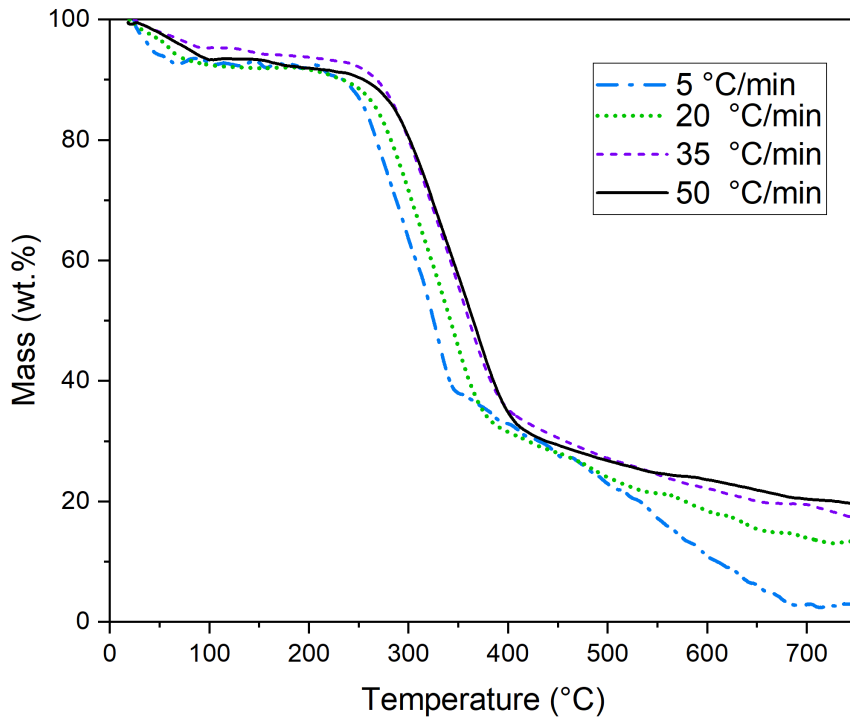


Figure 4.20: Average remaining mass determined through a TG analysis of palm kernel shells undergoing pyrolysis at different heating rates

are applied. This difference in pyrolysis behaviour and the time-scales in which pyrolysis takes place at $5\text{ }^{\circ}\text{C min}^{-1}$, compared to the other heating rates, might favor secondary reactions and charring reactions that have a different reaction mechanism than those of intermediate pyrolysis conditions [52]. Consequently, for the determination of pyrolysis kinetics only $20, 30$ and $50\text{ }^{\circ}\text{C min}^{-1}$ are considered. Such heating rates are also in agreement with a minimum difference of $15\text{ }^{\circ}\text{C}$ between heating rates, which is necessary to obtain reproducible kinetic results [204].

The results presented in Figure 4.22 show that for a given heating rate, PKS and the synthetic mixture reach different values of remaining mass at the end of pyrolysis. Indeed, after the synthetic mixture is pyrolyzed, the remaining solid fraction (ashes, char and unreacted biomass) is higher than the remaining mass for the PKS. This could be explained when considering the difference in composition between PKS and the synthetic mixture. Moreover, components such as sulfur are also higher in the synthetic mixture and this could cause more remaining solids after pyrolysis [197].

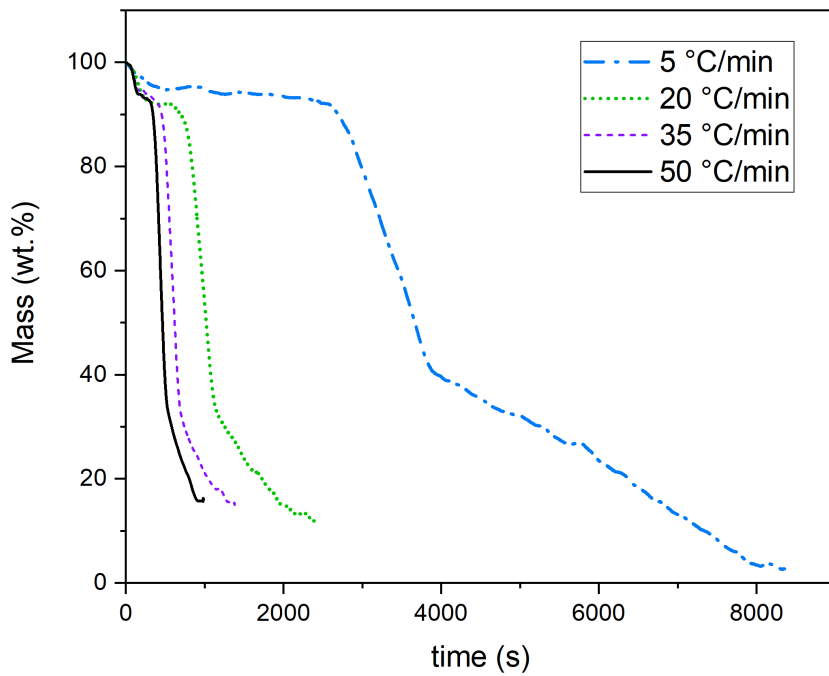


Figure 4.21: Comparison of average remaining mass from a TGA for palm kernel shells, undergoing pyrolysis at 5, 20, 35 and 50°C.

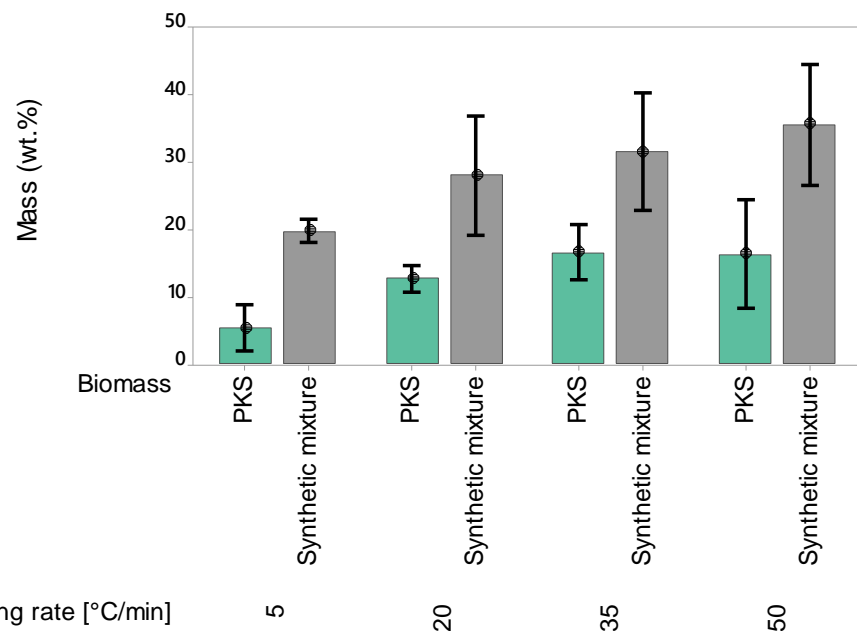


Figure 4.22: Remaining mass at the end of pyrolysis with palm kernel shells and the synthetic mixture, for heating rates of 5, 20, 35 and 50°C presented as an interval plot considering 95% CI for the mean. Individual standard deviations are used to calculate the intervals.

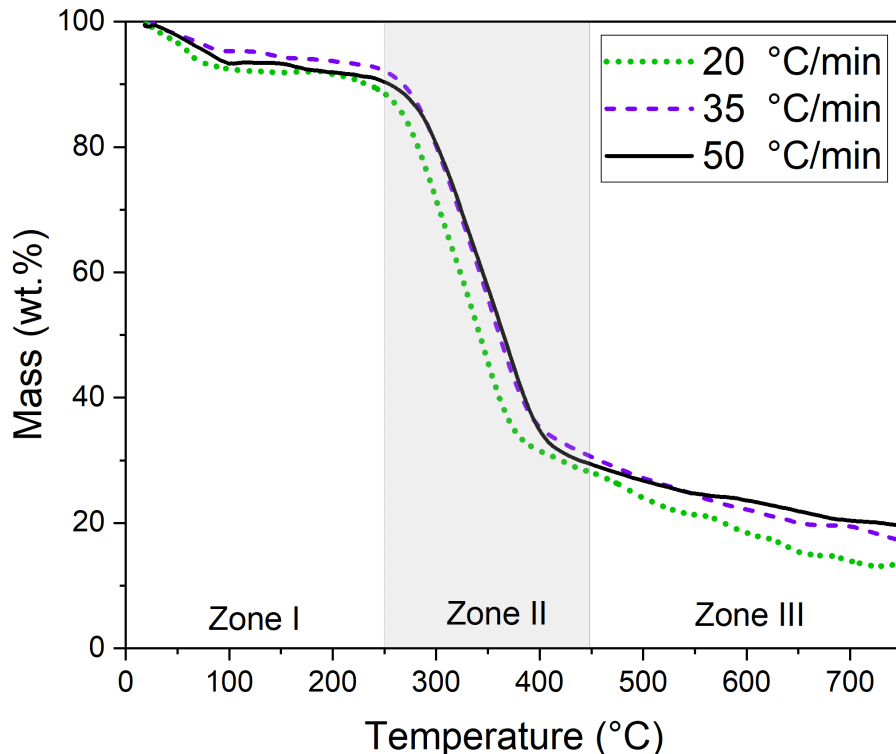


Figure 4.23: Thermal analysis of PKS pyrolysis at different heating rates considering TGA.

4.4.1.2 Pyrolysis behaviour for PKS and for the synthetic mixture

The results presented in Figures 4.23 and 4.24 show the weight loss evolution for PKS in pyrolysis. Results suggest that the thermal degradation of PKS could be considered to occur in three zones. Zone I occurs at $T < 250$ °C, and it involves the heating of the biomass and the evaporation of water. Approximately a 10% mass loss is observed in this first zone, which corresponds with the moisture content of PKS from Table 5.2. A second zone is observed between 250 – 400 °C, which is the region with highest mass loss in PKS pyrolysis. Such mass loss evidences the release of volatiles from PKS and the formation of char [205]. A final zone is observed at $T > 450$ °C, where the mass loss take place at a much lower rate. Figures 4.25 and 4.26 highlight the effect of the heating rate over PKS pyrolysis; and in general, higher heating rates are associated with faster devolatilization. The differential analysis presented in Figure 4.24 shows overlapping peaks throughout pyrolysis in the 250–450 °C range. Such overlapping suggests that cellulose, hemicellulose and lignin pyrolysis occurs simultaneously within PKS.

Figure 4.25 shows that the pyrolysis of the synthetic mixture occurs through the same previously identified 3 zones. However, there are some differences when both the PKS and

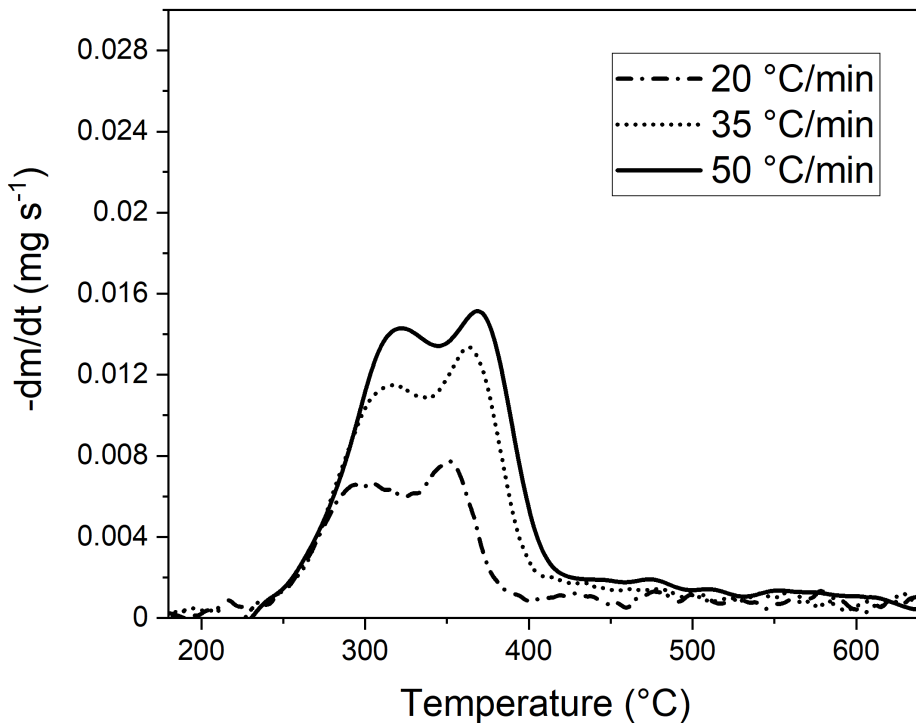


Figure 4.24: Differential thermal analysis of PKS pyrolysis at different heating rates.

the synthetic mixture undergo pyrolysis. Figures 4.25 and 4.26 show that for the synthetic mixture, pyrolysis occurs between 150 – 450 °C, which differs from the 250 – 450 °C range for zone II observed in PKS. Figure 4.25 also shows a peak in the 150 – 250 °C region that was not present in the PKS analysis. Such differences could be explained with the information presented in Figure 4.27. This figure shows that the difference in behavior between PKS and the prepared synthetic mixture, could be attributed to an earlier hemicellulose pyrolysis, as well as to a continuous pyrolysis of lignin in the synthetic mixture. Figure 4.27 also shows that PKS present a presumably more stable structure in pyrolysis as compared to the mixture. The mentioned behavior suggests that in the synthetic mixture, hemicellulose, cellulose and lignin are free to react if the required activation energy is reached. Considering that hemicellulose (xylan) and lignin present lower activation energies than cellulose in the 260 – 340 °C range, it would be expected that hemicellulose and lignin react first, as presented in Figure 4.27. On the contrary, the behavior presented by the PKS suggest that in this particular case, hemicellulose and lignin might not react independently and as easy as in the synthetic mixture. This could be explained when considering that PKS are a complex mixture of interacting components in a convoluted morphology, which involves a packed and resistant surface with a fibrous interior. This would suggest that the representation of

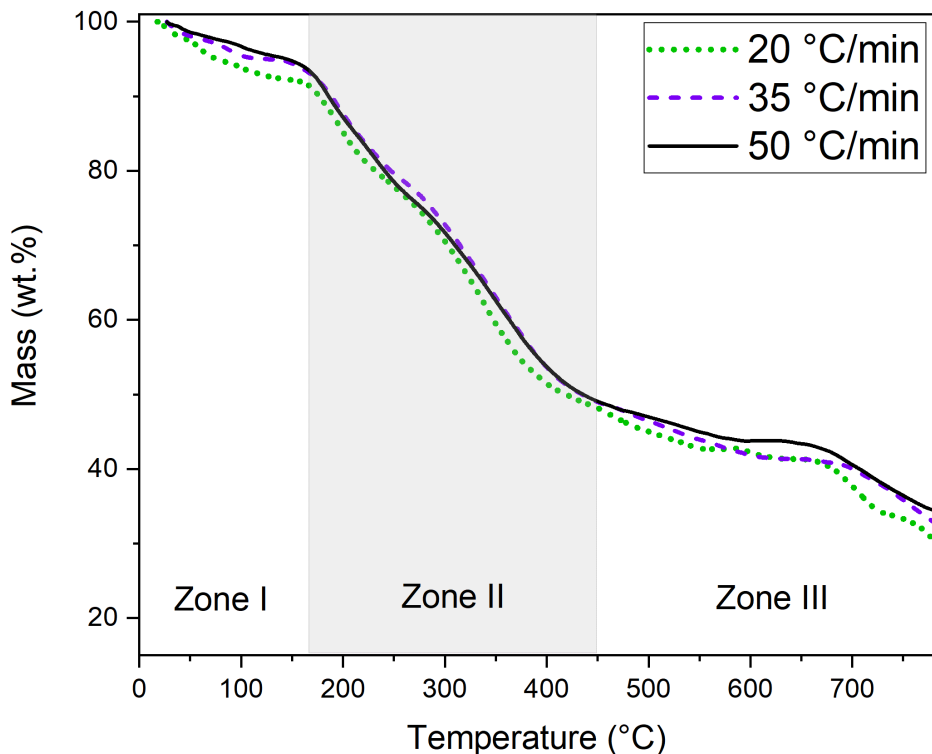


Figure 4.25: Thermal analysis of the synthetic mixture under pyrolysis at different heating rates considering TGA.

PKS as a combination of their main components might not be sufficient for describing pyrolysis. Moreover, Zone II and Zone III from PKS pyrolysis might be related to the different structures that lignin might form within PKS. As evidenced both in the FTIR analysis and in the microscopy analysis from the previous sections, lignin is present mainly as Syringil and Guayacil in PKS, and morphologically, lignin is part of a matrix and a wall in PKS micro-structure. It is therefore possible, that during pyrolysis, an easy to access lignin or lignin/carbohydrate complex and a more difficult to access lignin or lignin/complex co-exist. This possibility however needs to be further investigated since secondary reactions and charring reactions might be more important during pyrolysis than interactions between biomass components or carbohydrates accessibility [52, 206]. Considering the differences during pyrolysis and in the composition, between PKS and the synthetic mixture, the study of the kinetic model in the next section will only consider palm kernel shells.

4.4.2 Kinetic model for the pyrolysis of palm kernel shells

In this section, the kinetic parameters for PKS pyrolysis are determined using two isoconversional approaches: the Flynn-Wall-Ozawa method (FWO) and the Kissinger-Akahira-

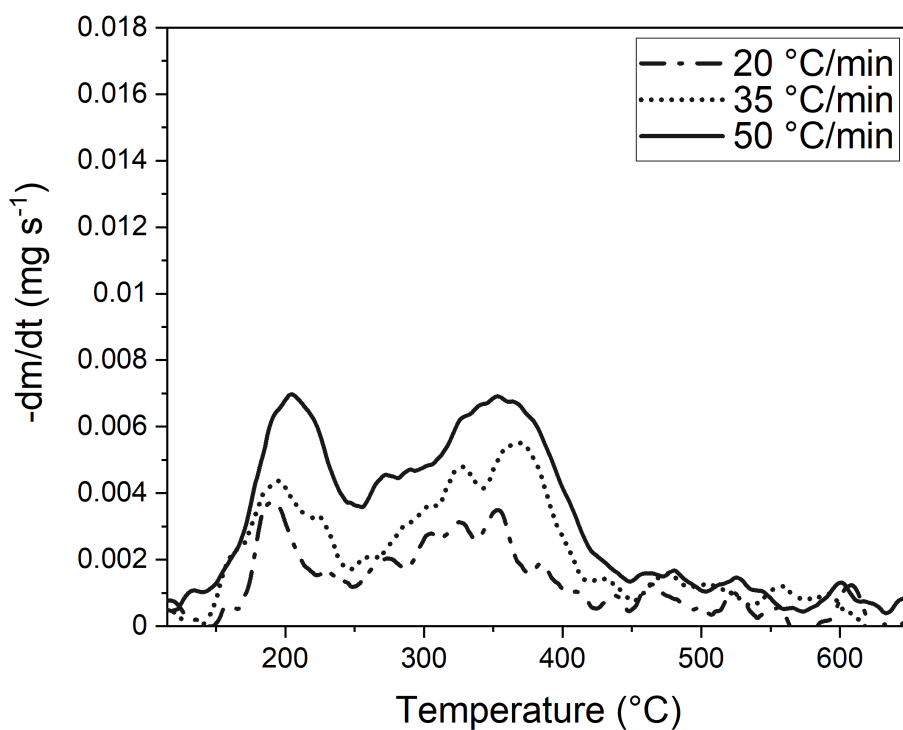


Figure 4.26: Differential thermal analysis of the synthetic mixture under pyrolysis at different heating rates.

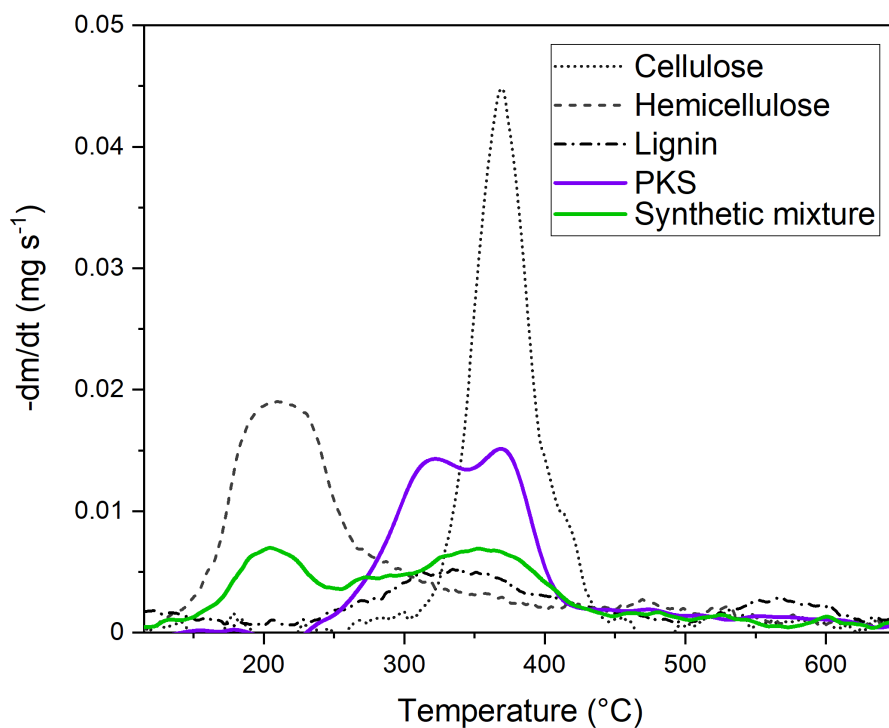


Figure 4.27: Mass loss rate for different samples undergoing pyrolysis at $50\text{ }^{\circ}\text{min}^{-1}$ obtained from TGA.

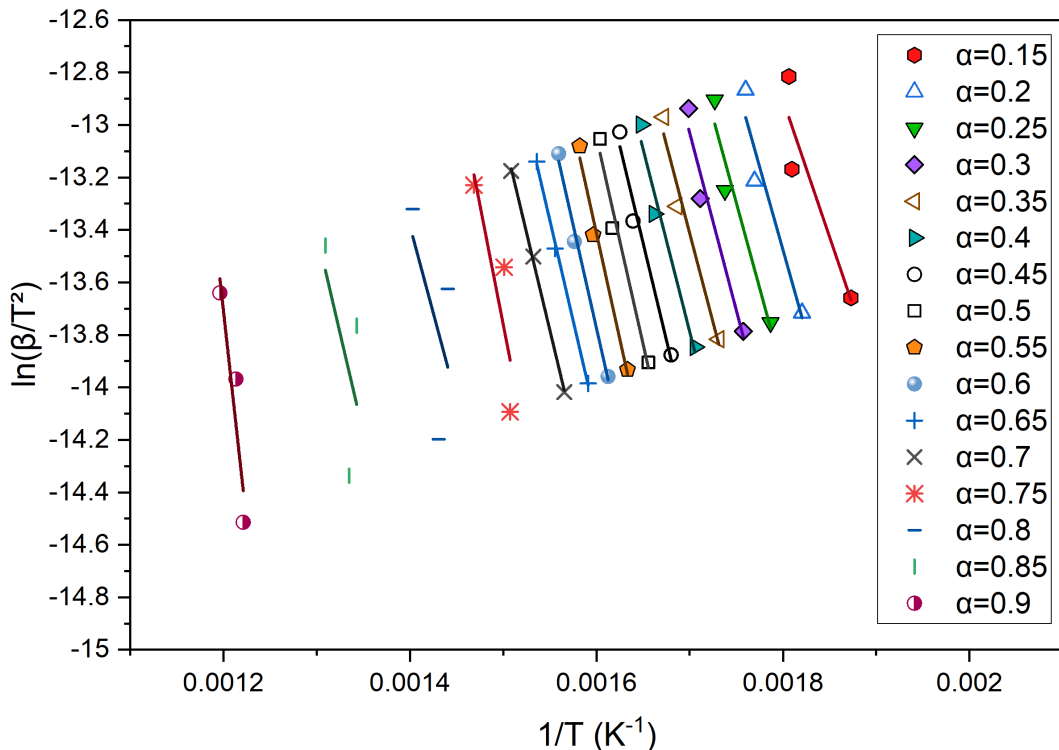


Figure 4.28: Linear regression for different conversions resulting from the TGA PKS analysis using the KAS method

Sunose method (KAS). Figure 4.28 and Table 4.10 show the obtained kinetic parameters when the KAS method is applied. The mentioned table and figure suggest that the KAS method is more suitable for conversion values, α , between 0.2 and 0.7, where coefficients of determination, R^2 are expected to reach values between 0.93 and 1.00. For conversion values lower than 0.20 or higher than 0.7, the KAS method is not appropriate and it could lead to mistakes in the determination of kinetic parameters. Such limitation could be related either to the method itself, given that it uses an approximation to solve the heat integral [207], or to the fact that PKS pyrolysis experience different reactions at higher conversions. The later is also a possibility when we consider the 3 zones that were previously identified for PKS pyrolysis in Figure 4.23. Indeed, when we reach the zone nearby 400 °C, which corresponds to Zone III of PKS pyrolysis, we are approaching conversions (α) of 0.7. This conversion, as presented in Table 4.9 is the upper limit for applying the KAS method for determining PKS pyrolysis kinetic parameters. Beyond such conversion value, the KAS method is not appropriate due to lack of linearity.

The results from Figure 4.29 and Table 4.10 show, as they did for the application of the KAS method, that the FWO method is more suitable for conversion, α , values between 0.2 and

Table 4.9: Activation energy for palm kernel shell pyrolysis, for $0.2 \leq \alpha \leq 0.7$, using the KAS method

α	Slope	Intercept	E_a (kJ mol $^{-1}$)	$\log A^*$	R 2
0.20	-12631.30	9.26	105.02	7.52	0.93
0.25	-13000.93	9.45	108.09	7.74	0.94
0.30	-13515.92	9.95	112.37	8.08	0.96
0.35	-13549.26	9.62	112.65	8.04	0.97
0.40	-13922.94	9.88	115.76	8.26	0.97
0.45	-14793.27	10.96	122.99	8.84	0.98
0.50	-15744.64	12.14	130.90	9.47	0.98
0.55	-16093.16	12.33	133.80	9.65	0.98
0.60	-15722.02	11.38	130.71	9.31	0.99
0.65	-15289.06	10.34	127.11	8.94	1.00
0.70	-14864.20	9.26	123.58	8.56	1.00

* A units in s $^{-1}$

0.7 which correspond to coefficients of determination, R 2 between 0.93 and 1.00. Given that the FWO method uses a different approximation than the KAS method for solving the heat integral, it would be expected that the limitations arising from both methods at high pyrolysis conversions ($\alpha \geq 0.7$) are more related to the complexity of pyrolysis and to the presence of additional reactions, than to the application of the FWO or KAS method itself. Indeed, previous authors [27, 36, 179] define Zone III in pyrolysis as a complex region with charring and char formation reactions. The variation experienced by the activation energy in Figure 4.30 is an indication that during PKS pyrolysis, a complex reaction system takes place, which reflects as increasing and decreasing stages of the activation energy with different conversion values [208].

The obtained average activation energies E_a and pre-exponential factors when the FWO and KAS methods are applied, are presented in Table 4.11. The average activation energy presented in Table 4.11 (124.68 KJ mol $^{-1}$) is lower than the 130-235 KJ mol $^{-1}$ range for PKS pyrolysis reported in literature [126]. This could be explained when considering that the PKS used in the present work consisted of 56.12% lignin, 26.36% hemicellulose and 17.52% cellulose, as compared to the 58.3% lignin, 14.20% hemicellulose and 27.51% of cellulose found in literature [126]. Considering that for temperatures between 260-340 °C,

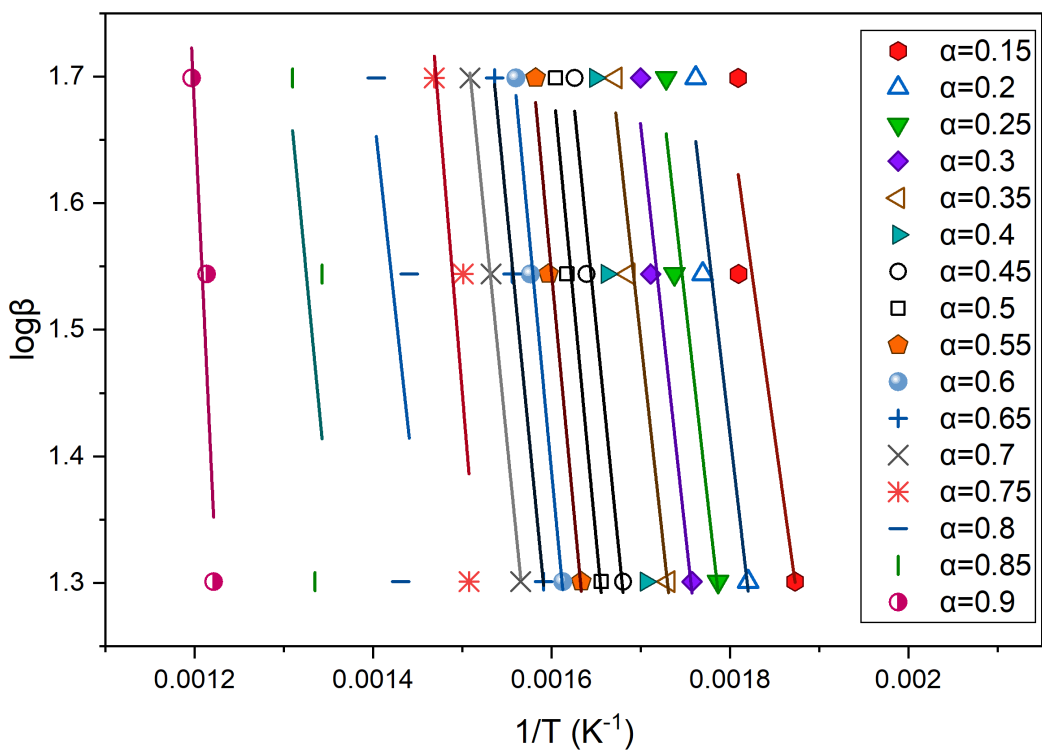


Figure 4.29: Linear regression for different conversions resulting from the TGA PKS analysis using the FWO method.

Table 4.10: Activation energy for palm kernel shell pyrolysis, for $0.2 \leq \alpha \leq 0.7$, using the FWO method

α	Slope	Intercept	E_a (kJ mol ⁻¹)	$\log A^*$	R ²
0.20	-6039.66	12.29	109.96	9.83	0.93
0.25	-6222.87	12.41	113.29	10.05	0.94
0.30	-6421.57	12.58	116.91	10.30	0.96
0.35	-6394.36	12.36	116.41	10.17	0.97
0.40	-6616.94	12.58	120.47	10.44	0.97
0.45	-7006.81	13.06	127.56	10.97	0.98
0.50	-7436.63	13.60	135.39	11.55	0.98
0.55	-7529.01	13.59	137.07	11.59	0.99
0.60	-7448.14	13.30	135.60	11.37	0.99
0.65	-7195.13	12.75	130.99	10.88	1.00
0.70	-7020.36	12.29	127.81	10.50	1.00

* A units in s⁻¹

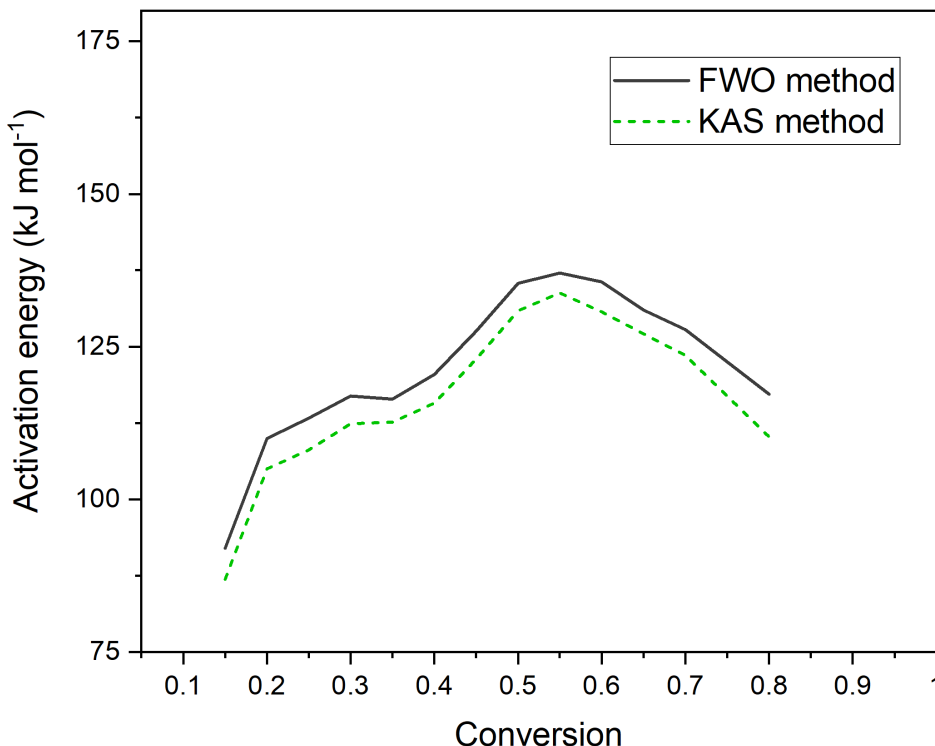


Figure 4.30: Tendency of the activation energy E_a for different values of conversion α calculated using the FWO and KAS methods

Table 4.11: Comparison of the activation energy (E_a) and pre-exponential factor A for palm kernel shell pyrolysis

Parameter	FWO method	KAS method	Literature [126]
E_a (kJ mol ⁻¹)	124.68 ± 9.69	120.27 ± 9.96	$130.04 - 235.59$
$\log A^*$	10.70 ± 0.62	8.58 ± 0.72	-

* A units in s⁻¹

cellulose present higher activation energies than hemicellulose, lower activation energies for pyrolysis would be expected for the feedstock used in this work. These results highlight that the variability in composition and properties also translate into different kinetic parameters in pyrolysis. Finally, the variability in the properties of similar feedstocks is evidenced in Table 4.11, where PKS originated in different countries have different composition, different cellulose, hemicellulose and lignin. Moreover, the activation energy and pre-exponential factor also vary from study to study. Such variation highlights one again the necessity to analyze every feedstock and to determine relevant properties when lignin-rich biomass is intended for modelling or process design applications.

Table 4.12: Composition of palms kernel shells and kinetic parameters for pyrolysis

Origin	HHV [MJ kg ⁻¹]	Cellulose [wt.%]	Hemicellulose [wt.%]	Lignin [wt.%]	C [wt.%]	H [wt.%]	N [wt.%]	O [wt.%]	S [wt.%]	Heating rate [°C min ⁻¹]	E _a [kJ mol ⁻¹]	T [°C]	Method	Author
Cameroon	19.50	-	-	53.7	6.3	0.3	38.2	-	5	65.4	213-368	Coats-Redfern	[209]	
India	-	-	-	-	-	-	-	-	10	56.9	175-410	Coats-Redfern	[210]	
									20	50.0	205-460			
									30	54.1	180-525			
									40	47.8	196-630			
									50	52.5	196-400			
Malaysia	19.72	27.5	14.2	58.3	55.89	-	-	41.15	-	10,20,40	205.3	30-900	FWO	[126]
										205.7	30-900	KAS		
Colombia	18.87	14.64	27.06	58.30	46.05	5.14	0.62	45.40	0.14	-	-	-	-	[203]
Ecuador	20.77	17.52	26.36	56.12	51.81	7.14	0.59	40.19	0.25	20,35,50	124.7	25-800	FWO	This work
										120.3	25-800	KAS		

4.5 Concluding remarks

In this chapter, lignin-rich biomass is initially characterized and studied. Furthermore, lignin-rich biomass pyrolysis is also evaluated at laboratory scale. Palm kernel shells (PKS) an abundant residue from the palm oil extracting industry is the main focus of this chapter's analysis. However, due to the lack of information regarding the properties of lignin-rich biomass, another feedstock, coffee husk, was also evaluated. Moreover, a synthetic mixture of cellulose, hemicellulose and lignin was prepared to mimic PKS composition with the purpose of identifying potential differences or similarities that contribute with the understanding of pyrolysis when lignin-rich biomass is considered. PKS stands out as an energy source due to its high bulk density (536.54kg m^{-3}) and higher heating value of 20.77 MJ kg^{-1} . Moreover, PKS low moisture content (10.62%), low ash content (2.31%), high volatiles content (77.18%) and low sulfur content (0.25%) make PKS suitable for pyrolysis or for other thermochemical processes. The particle size of PKS make it necessary to consider PKS as thermally-thick particles if their pyrolysis needs to be modeled. The analysis of the Van Krevelen diagram and of the higher heating value revealed that it is possible to develop a correlation for predicting the energy content in lignin-rich biomass from its carbon content. The developed correlation for predicting HHV is promising given that there are no correlations dedicated to biomass with high lignin content. The PKS showed different properties than the synthetic mixture mimicking PKS. PKS was found to have 3 types of lignin and its morphology revealed that in PKS, ligin is present as part of cell-like structures and as part of a matrix that contains cellulose fibers.

Regarding the thermal behaviour of biomass throughout pyrolysis, PKS and the synthetic mixture to mimic PKS are found to pass through 3 different zones in pyrolysis. In spite of this, the synthetic mixture decomposes differently than PKS, evidencing the influence of the morphology and the effect of the interactions between biomass components in pyrolysis. The FWO and KAS methods for finding pyrolysis kinetic parameters were suitable for conversions between 0.2 and 0.7. For higher or lower conversions than the one mentioned, such methods are not appropriate and a different alternative is required for estimating pyrolysis kinetic parameters. The average activation energy for PKS was found to be 124.68 (KJ mol^{-1}) when using the FWO method and 120.27 when the KAS method is applied. The results from this chapter highlights the importance of having real data and experimental kinetic parameters if potential modelling or scaling-up applications are to be considered.

The next chapter shows an alternative to integrate laboratory measured properties with modelling approaches for describing pyrolysis at a reactor scale.

Chapter 5

Pyrolysis of coarse biomass in a single screw auger reactor

This chapter initially explores the development of a granular flow model from both Eulerian and Lagrangian perspectives. The granular flow model is developed for an auger pyrolyzer of a single screw that used PKS as feedstock. The first granular flow approach develops an empirical correlation using operational data from the reactor; and the second one implements a discrete element method (DEM) simulation to predict the biomass residence time in the reactor. The auger reactor operates with palm kernel shells, which behave like thermally thick particles. The auger reactor is characterized in terms of its geometry and by measuring the mass flow rate for different screw speeds. Relevant coefficients for developing the DEM are determined by combination of experiments and simulations. Finally, this chapter explores the combination of the previously developed particle model from Chapter 3 with a granular flow model that defines the residence time of the biomass inside the reactor.

Publication from this work: Romero, Michelle, Boris German, Daniel Rivadeneira, Diego Chulde, Andres Chico-Proano, Ricardo A.C. Narváez, and Javier Martínez Gómez. 2022. “Assessment of Pilot Scale Pyrolysis Gas Production as Fuel for Cogeneration.” *Chemical Engineering Transactions* 92 (January): 211–16.

5.1 Introduction

The development of reactor models for describing biomass pyrolysis is still limited and most of the available information is directed towards the development of fluidized bed and packed bed reactors [5]. There are particle models that had been used before to describe biomass pyrolysis [25, 4, 24, 113, 39]. There are also existing models to describe pyrolysis in auger reactors and rotary kilns [132]; however, there is little information regarding the combination of a particle model with an auger reactor model to describe biomass pyrolysis. There are also particle models that had been used as part of multi-scale modeling strategies

for fluidized beds, moving grates and fixed bed pyrolysis reactors [25, 4, 24, 113, 39]. Similarly, a previous work, coupled heat and mass transfer with a distributed activation energy kinetic model (DAEM) for modeling steady state biomass pyrolysis inside an auger reactor, in the axial direction [132]. The mentioned work models a pyrolysis auger reactor as a rotary kiln. Nonetheless, the mentioned model neglects interactions between biomass particles, it does not consider the existing granular flow inside the reactor and it does not include a temperature profile inside the particles.

The complexity of the model for describing the pyrolysis of coarse particles in a biomass-heated auger reactor, requires three sub-models: a heat transfer model that represents the energy flow from the reactor to the biomass, a granular flow model that predicts biomass residence times in the auger reactor, and a kinetic model for coarse biomass particles. This combination is particularly challenging whenever coarse biomass particles are considered. Perhaps the area that requires more attention is the development of granular flows.

5.1.1 Granular flow in auger reactors

The complexity for modelling coarse biomass particles inside an auger reactor is related to the residence time that such particles require for abandoning the reactor. Similarly, to have the residence time makes auger reactor much more easier because once the residence time is known, the auger reactor can be modelled as a simple PFR reactor. There are mainly two ways for determining the residence time in auger reactors, using experimental data to build empirical correlations; or to model the granular flow particle by particle so average residence times could be obtained [137, 211]. In spite of such alternatives, palm kernel shells and lignin-rich biomass still have not expanded their use or application in granular flow systems.

5.1.1.1 Empirical determinations of residence time

Rotating screw conveyors allow the controlled flow of granular materials through different heating zones, which makes such conveyors particularly suited for biomass pyrolysis and torrefaction applications [137]. The representation of the flow of solids inside a screw conveyor represents a complex problem, specially if particle's trajectories are required. However, coarse biomass transport inside conveyors could be simplified by assuming that the granular flow inside a conveyor resembles a plug flow reactor [137]. In such cases, the mean residence time of biomass in screw conveyors becomes relevant. The residence time in screw reactors can be predicted with empirical correlations, as a function of the rotational

frequency and the volumetric throughput rate. The residence time of biomass in screw reactors depends on the screw reactor's geometry and not on the material being transported. In cases where particles do not move uniformly inside an auger reactor, axial dispersion appears [137]. Such empirical approach has not been applied yet for describing palm kernel shells granular flow. Indeed, it has mostly been used for regular and small regular raw materials. Therefore, there is still the need to characterize complex biomass with such empirical methods. This approach considers the analysis of the group of particles and represents an Eulerian approach to describing granular flow.

5.1.1.2 Determination of the granular flow using discrete element methods

The characterization of granular flow can also consider a discrete elements method approach, a numerical method that evaluates interactions between discrete particles that are in contact. Each particle is studied separately and each particle needs its own equations to be defined in terms of rotation and translation at a given time. The amount of interactions in such cases require the use of specialized software that integrates Newton's law of motion with particle-particle collisions and wall-particle collision using a soft sphere approach [212]. The simulation usually considers the Hertz-Mindlin contact model coupled with the elastic-plastic spring dashpot for adding an extra frictional force that constraints rolling in particles that are not spherical such as PKS. Finally, the rigor of the DEM demands a series of coefficients that are specific of the feed material and of the processing conditions. DEM approaches are usually complex and for palm kernel shells, there are missing properties that cannot be found in literature. This work also aims to provide some of such information so future works can be developed. The DEM approach considers a Lagrangian perspective for describing granular flow, which is a completely different approach than the empirical correlation described before.

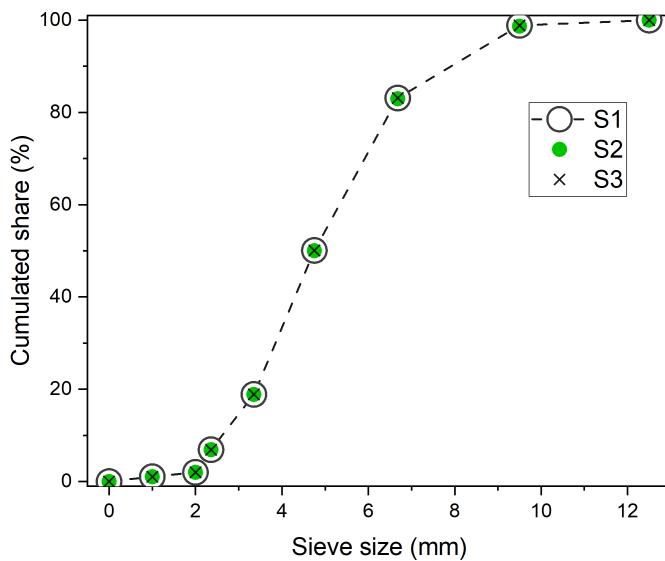
5.2 Description of the feed material and the reaction system

5.2.1 Feed material

The only material fed to the auger reactor is palm kernel shells, PKS. This material was extensively characterized in the previous chapter. However, for its use in the auger reactor certain properties need to be recalled. Table 5.1 and Figure 5.1 show that most PKS are 6.68 mm or bigger. Regarding the bulk density for PKS, it reaches in average 536.54 kg m^{-3} .

Table 5.1: Average results of particle size distribution for PKS

Size [mm]	Share [%]	Cumulative share [%]	d_{50} [mm]	d_{80} [mm]
<2.00	1.03 ± 0.01	1.03 ± 0.01		
2.00	0.96 ± 0.00	2.00 ± 0.01		
2.36	4.89 ± 0.02	6.89 ± 0.03		
3.35	12.03 ± 0.09	18.92 ± 0.06		
4.75	31.27 ± 0.17	50.19 ± 0.23	4.74 ± 0.010	
6.68	32.78 ± 0.35	82.97 ± 0.14		6.51 ± 0.007
9.5	15.80 ± 0.10	98.77 ± 0.09		
12.5	1.23 ± 0.09	100.00 ± 0.00		

**Figure 5.1:** Cumulative share for different particle sizes for 3 different PKS samples.**Table 5.2:** Results from the palm kernel shell characterization

Property	Value
Size and density	
Bulk density [kg m ⁻³]	536.54 ± 2.13
Apparent density [kg m ⁻³]	1286.67 ± 11.77
d_{50} [mm]	4.74 ± 0.010
d_{80} [mm]	6.51 ± 0.007

5.2.2 Description of the reactor system

The auger pyrolyzer used in this research is a 4.80 [kg min⁻¹] capacity reactor. The reactor is made of AISI 304 stainless steel of 8 [mm] of thickness. The PKS is fed through a hopper and a feed screw moved by an electric motor. During normal operations, both the feed motor and the discharge are kept at the same velocities and only the pyrolyzer motor that controls

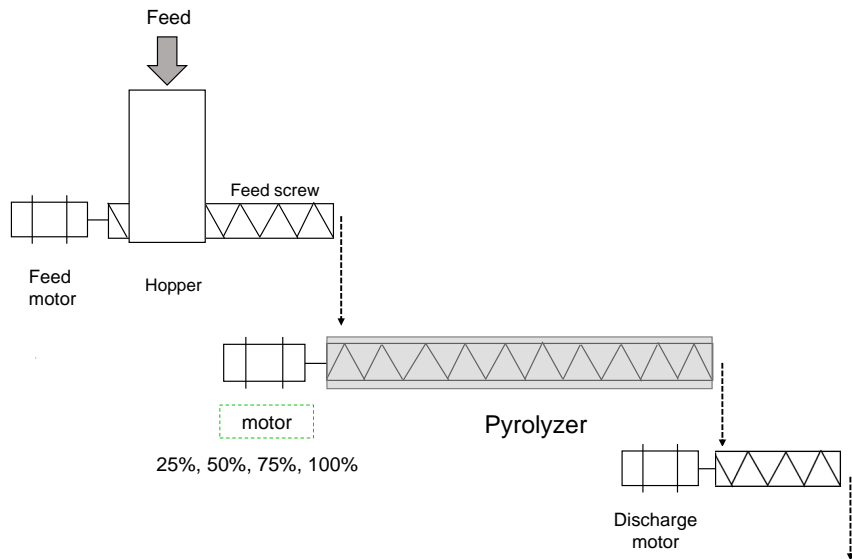


Figure 5.2: Configuration of the auger reactor used for PKS pyrolysis.

Table 5.3: Relevant dimensions from the auger reactor

Parameter	Units	Value
Length (from inlet to outlet)	mm	2950
Shell diameter	mm	525
Screw diameter	mm	497
Radial clearance	mm	28
Shaft diameter	mm	25
Pitch	mm	400
Flight thickness	mm	5
Maximum rotational velocity	rpm	5.6

the speed of the auger screw could vary considering 25%, 50%, 75% and 100% of the maximum rotational velocity (5.6 rpm) as presented in Figure 5.2. The pyrolyzer is heated externally with flue gas from a biomass burner that guarantees a constant temperature. The pyrolyzer is a hollow cylinder which contains one screw for moving biomass. The plan of the pyrolyzer with its measurements is presented in Figure 5.3. The complete measurements of the reactor are presented in Table 5.3. Once that the geometry and dimensions of the auger reactor have been defined, the flow within the auger reactor needs to be described.

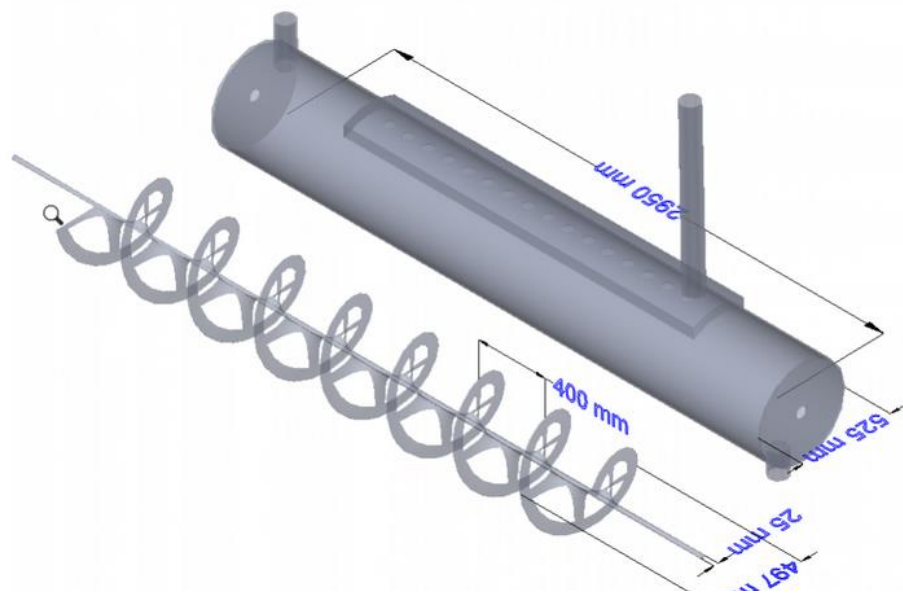


Figure 5.3: Plan of the auger reactor and the internal screw.

5.3 Determination of residence time distributions with an empirical mathematical model

5.3.1 Data collection

5.3.1.1 Mass flow rates in the equilibrium

Initially the mass flow rates \dot{m} corresponding to 25, 50, 75 and 100% of the maximum rotational velocity in the screw, were measured using a Bonvoisin YP-D Series Precision Balance with 0.1 g resolution. Measurements were taken every 10 s for a total of 50 s in each case. The measurements were performed by triplicate.

5.3.1.2 Mass flow rates for determining the residence time distribution

For measuring the mass flow rate in this conditions, the feed screw and the discharge screw and motors remained at their 100% capacity, only the motor of the screw from the pyrolyzer varied. The system was initially run at steady state conditions for 25, 50, 75 and 100% of the maximum rotational velocity in the screw. Once the steady-state was reached, a negative step change was set in place, the feed motor was turned off, cutting the feed to the pyrolyzer. This initial time without feed is called t_0 and from this time, the discharge from the pyrolyzer was weighted every 10 s with a Bonvoisin YP-D Series Precision Balance with 0.1 g resolution, until no more biomass could be collected. All the experiments were performed by triplicate.

5.3.1.3 Calculation procedure for the residence time distribution

The residence time that is obtained experimentally could be used for calculating the mean residence time and even the axial dispersion [137]. The negative step-change has an effect over the mass flow rate at the outlet of the screw. The cumulative mass or mass inventory that existed in the screw reactor at t_0 can be calculated using the mass flow measured at the screw conveyor outlet rate $\dot{m}(t)$ at time t :

$$m = \int_{t_0}^{\infty} \dot{m}(t) dt \quad (5.1)$$

The volume of the auger reactor (V) can be calculated from its geometry, and the volume of material can be calculated from (m) and the bulk density of palm kernel shells. In such circumstances, the volume V in the auger reactor that is occupied by the solid, using the fractional degree of filling α using[137]:

$$\alpha = \frac{m}{\rho_m \cdot V} \quad (5.2)$$

The theoretical ideal residence time τ_{ideal} can be determined using the screw geometry, the distance between the conveyor's inlet and outlet, l , the pitch , p , and the rotational frequency of the screw (v) as follows:

$$\tau_{ideal} = \frac{l}{p \cdot v} \quad (5.3)$$

The function $F(t)$ for the cumulative residence time distribution whenever there is a step change can be determined when the mass flow rate change $\dot{m}_0 - \dot{m}(t)$ is divided by the size of the step change:

$$F(t) = \frac{\dot{m}_0 - \dot{m}(t)}{\dot{m}_0} \quad (5.4)$$

In such circumstances, the mean residence time τ is expressed as follows [137]:

$$\tau = \int_0^1 t dF \quad (5.5)$$

Finally, one of the forms of the mathematical model for estimating residence time can be calculated a follows [137]:

$$\tau_{model} = \frac{1}{p \cdot v_{screw}} \cdot \left(k_0 + k_1 \frac{Q}{v_{screw}} \right) \quad (5.6)$$

Where:

τ_{model} = estimated mean residence time.

Q = volumetric flow rate in the auger reactor.

v_{screw} = frequency of the screw conveyor.

k_0, k_1 = model coefficients.

The previously described approach does not follow every PKS involved. On the contrary, it analyzes bulk properties and the mass flow rate is also a result of bulk properties. Because of this, such approach represents an Eulerian approach to granular flow of PKS.

5.4 Determination of residence times distributions from a DEM approach

The DEM approach, studies the granular flow problem from a different perspective than the empirical correlation proposed in the previous section. Indeed, the DEM follows every particle involved in the system and studies the interactions between individual particles. This approach is also known as a Lagrangian approach. In this section, a DEM Lagrangian approach will be described initially for finding residence times in an auger reactor. Moreover, the empirical correlation used in the previous section is applied again but to the simulated data. As a result, the lagrangian perspective transforms into an Eulerian perspective which can be integrated easier into other type of models for describing biomass pyrolysis.

5.4.1 Materials and methods

5.4.1.1 Palm kernel shells

The DEM approach considers palm kernel shells, PKS, as the subject of analysis. The PKS maintain the same properties that have considered in this Chapter and that were determined experimentally in the previous Chapter.

5.4.2 PKS characterization

There are four categories of properties of PKS that are required for the DEM analysis. The first one involves gravimetric properties, whereas the second one considers the particle's size distribution of PKS. The third category involves mechanical properties associated to PKS and the final category considers interaction properties between particles.

Table 5.4: PKS size distribution considered for the DEM approach

Particle diameter [mm]	Percentage %
4.75	39.45
6.68	40.59
9.50	19.96

5.4.2.1 Gravimetric properties

The properties required in this section for the DEM approach involve the bulk density (536.54 kg m^{-3}) and the apparent density of PKS ($1286.67 \text{ kg m}^{-3}$).

5.4.2.2 Particle size distribution

The size distribution of PKS is required for the DEM approach. The size distribution of PKS is the same as the one presented in 5.1 in this chapter. PKS have a variety of sizes and for the purpose of reducing computational times, only 3 different particle diameters will be considered, based on the results from the experimental size distribution. The PKS size distribution for the DEM approach is presented in Table 5.4.

5.4.2.3 Mechanical properties of PKS

The mechanical properties required for the DEM approach are the Young modulus and the Poisson's ratio. These properties are retrieved mainly from the work of Raji & Favier (2004), and from Spanoudakis et al., (2021). The Young modulus used for PKS is 70 MPa , and the Young modulus for the walls of the auger reactor is 200 GPa. So as to reduce the computational time, the mentioned values could be reduced even in three orders of magnitude without affecting the shearing effect of moving particles. The considered Poisson's ratio for PKS is 0.30 and for the reactor's wall is 0.29.

5.4.2.4 Interaction properties

Regarding the restitution coefficients, the particle-particle interaction coefficient is defined as 0.13, whereas for the wall-particle interaction, it is defined in 0.45 [213].

The particle-wall sliding friction coefficient is determined experimentally using a 65 mm diameter open cylinder with 40 mm height, The cylinder was placed over a 300x350 mm AISI 304 stainless steel plaque, making sure there is no inclination and then it was filled with PKS. The steel plaque rests over a tilting platform with a screw. The cylinder is rose near 5.0 mm to avoid contact with the steel surface and the platform is tilted until sliding is



Figure 5.4: Tilting surface and configuration for measuring the coefficient of friction.

detected. At this point the inclination angle α is measured.

A similar configuration is used for determining the sliding coefficient of friction μ . The open ended cylinder and the tilting platform are used again. The cylinder rests over the 300x350 mm AISI 304 stainless steel plaque, making sure there is no inclination and then it was filled with PKS. The cylinder is removed completely so PKS form a cone. The platform is tilted until the first particles of PKS start rolling. The inclination angle α at which PKS start rolling is measured [214]. The coefficient of friction μ is calculated using the tilting angle α as follows:

$$\mu = \tan(\alpha) \quad (5.7)$$

The tilting platform used in this determination is presented in Figure 5.4. The particle-particle friction coefficients are calculated later during the calibration of the simulation. In order to verify that the number of observations in each case is enough, two statistical estimators are used for evaluating convergence of the α angle with respect to its mean and standard deviation. In a previous work, Nguyen et al., (2021) defined such estimators as

follows :

$$\text{Convergence}_{mean} = \frac{1}{n} \sum_{i=1}^n K_i \quad (5.8)$$

$$\text{Convergence}_{std} = \sqrt{\frac{\sum_1^n (K_i - \bar{K})}{n}} \quad (5.9)$$

Where:

$\text{Convergence}_{mean}$ = mean-associated convergence estimator.

Convergence_{std} = deviation-associated convergence estimator.

K_i = observation i of variable K .

\bar{K} = mean value of the variable K .

n = number of observations.

5.4.3 Discrete element model approach

Discrete element modelling constitutes a numerical approach that is useful whenever interactions between particles are present. There are several works that apply DEM to describe granular materials [215, 216]. The amount of interactions that could exist between particles make it necessary to use a specialized software in granular flow. LIGGGHTS is an open source software for modeling granular materials through DEM. This software simulates macroscopic granular systems by integrating Newton's second law with particle-to-particle and particle-to-wall collisions. For developing a granular flow model, LIGGGHTS software was used considering the Hertz-Mindlin contact model along with the elastic plastic spring dashpot "EPSD2" model, which constraints the rolling for particles that are not spherical.

The Herzt-Mindlin model indicates that the amount of normal δ_n and tangential δ_t overlap is a measure of the repulsive force that results from a collision between particles. In the case of the frictional force between two granular particles, when two particles are separated a distance r , and such distance is smaller than their contact distance $d = R_i + R_j$, which is a sum of the particles' radii; If $r > d$, there is no force between the particles, in which case:

$$F = (k_n \delta_{nij} - \gamma_n v n_{ij}) + (k_t \delta_{tij} - \gamma_t v t_{ij}) \quad (5.10)$$

Where:

k_n = elastic constant for normal contact.

k_t = elastic constant for tangential contact.

δn_{ij} = normal overlap distance between the two particles.

δt_{ij} = tangential overlap distance between the two particles.

γ_n = viscoelastic damping constant for normal constant.

γ_t = viscoelastic damping constant for tangential constant.

$v n_{ij}$ =normal relative velocity, normal component of relative velocity of particles.

$v t_{ij}$ =tangential relative velocity, tangential component of relative velocity of particles.

The left hand side of Eq. 5.10 is also known as the normal force F_n , whereas the right hand side is known as the tangential force F_t . The magnitude of δt_{ij} is truncated as much as necessary to comply with a local Coulomb yield Criterion where $F_t \leq \mu F_n$, where μ is the grain-grain friction coefficient. Surfaces are referred to as slipping when the Coulomb yield criterion is satisfied [217]. The shear modulus (G) can be determined from the Poisson's ratio and Young's module. The Hertz-Mindlin contact model depends on the coefficient of restitution (e), Young's modulus (Y), Poisson's (ν), the coefficient of static friction (μ_s), and the coefficient of rolling fiction (μ_r). Typical and average values of overlaps are between 0.1-0.5%.

The selected Hertz-Mindlin model requires the calculation of certain coefficients: k_n , k_t , γ_n and γ_t . Their calculation can be perform with:

$$k_n = \frac{4}{3} Y^* \sqrt{R^* \delta_n} \quad (5.11)$$

$$\gamma_n = -2\sqrt{5/6}\beta \sqrt{S_n m^*} \geq 0 \quad (5.12)$$

$$k_t = 8G^* \sqrt{R^* \delta_n} \quad (5.13)$$

$$\gamma_t = -2\sqrt{5/6}\beta \sqrt{S_t m^*} \geq 0 \quad (5.14)$$

Whenever two granular particles are in contact, the following relationships apply:

$$S_n = 2Y^* \sqrt{R^* \delta_n} \quad (5.15)$$

$$S_t = 8GY^* \sqrt{R^* \delta_n} \quad (5.16)$$

$$\beta = \frac{\ln(e)}{\sqrt{\ln^2(e) + \pi^2}} \quad (5.17)$$

$$\frac{1}{Y^*} = \frac{1 - v_1^2}{Y_1} + \frac{1 - v_1^2}{Y_2} \quad (5.18)$$

$$\frac{1}{G^*} = \frac{2(2 + v_1)(1 - v_1)}{Y_1} + \frac{2(2 + v_2)(1 - v_2)}{Y_2} \quad (5.19)$$

$$\frac{1}{R^*} = \frac{1}{R_1} + \frac{1}{R_2} \quad (5.20)$$

$$\frac{1}{m^*} = \frac{1}{m_1} + \frac{1}{m_2} \quad (5.21)$$

In the previous set of equations, Y represents the Young's modulus, G the shear modulus, v is the Poisson ratio, e is the coefficient of restitution, m is the mass and R is the particle's radius. The subscripts 1 or 2 make reference to the particle in contact [215, 216]. Once that the model has been described, the model needs to be calibrated.

5.4.4 DEM calibration: procedure and experiments

The physical characteristics for PKS such as size, density, bulk density, coefficient of sliding friction for particle-wall were determined experimentally. The mechanical properties of PKS are retrieved from literature. The previously presented DEM model considers spheres as the particles that interact. PKS particles however, are not completely spherical and so, the bulk density of PKS needs to be calibrated using a simulation in LIGGGHTS software. Similarly, particle-particle interactions were not possible to be determined experimentally and their value needs to be found using a simulation.

The parameters that will serve as a base for the calculation of other parameters that are presented in Table 5.8.

To determine the particle-particle friction coefficients a particle flow experiment is applied. Such experiment is a particle discharge test in which the repose angle is measured. This experiment was numerically reproduced by DEM so particle-particle friction coefficients can be determined. The test for discharging particles is explained in detail in the next subsection.

Table 5.5: Parameters used for the DEM

DEM Parameter	Symbol	Value	Reference
Poisson's ratio	ν_p	0.30	[218]
Young's Modulus [MPa]	Y_p	7.00	[218]
Wall Poisson's ratio	ν_w	0.29	[218]
Wall Young's Modulus [MPa]	Y_w	200	[218]
Coefficient of restitution particle-particle	e_{pp}	0.130	[213]
Coefficient of restitution particle-wall	e_{pw}	0.45	[213]

5.4.4.1 Test for discharging particles

The test for evaluating particle's discharge required to build a box that had a division made of stainless steel with flaps on the side. The dimensions of the testing device are taken from literature and presented in Figure 5.6. The system is made with a wooden box with an upper and lower compartment, as presented in Figure 5.6. A stainless steel plaque is placed in the back wall of the device and on the support with flaps, making sure that PKS are only in contact with the steel, as if it was inside the auger reactor. The upper compartment is filled with 3 kg of PKS and the side flaps collapse letting the PKS fall into the lower compartment. A transparent window is also put in place in the front of the device to make sure the involved angles can be determine. The height of filling in the upper compartment for the 3 kg of PKS was used as a reference to calibrate the density in the DEM model.

5.4.4.2 Simulation set-up

The simulations for the calibration of the model and for determining the granular flow were undertaken in LIGGGHTS 3.8.0 software, using 24 parallel processors in a computer with Intel® Xeon® CPU E5-2650 v4 of 2.2 Ghz.

The time step determination considered Rayleigh's critical time T_R as follows:

$$T_R = \frac{\pi R \left(\frac{\rho}{G} \right)^{0.5}}{0.1631\nu + 0.8766} \quad (5.22)$$

Where:

G = shear modulus.

ρ = particle's density.

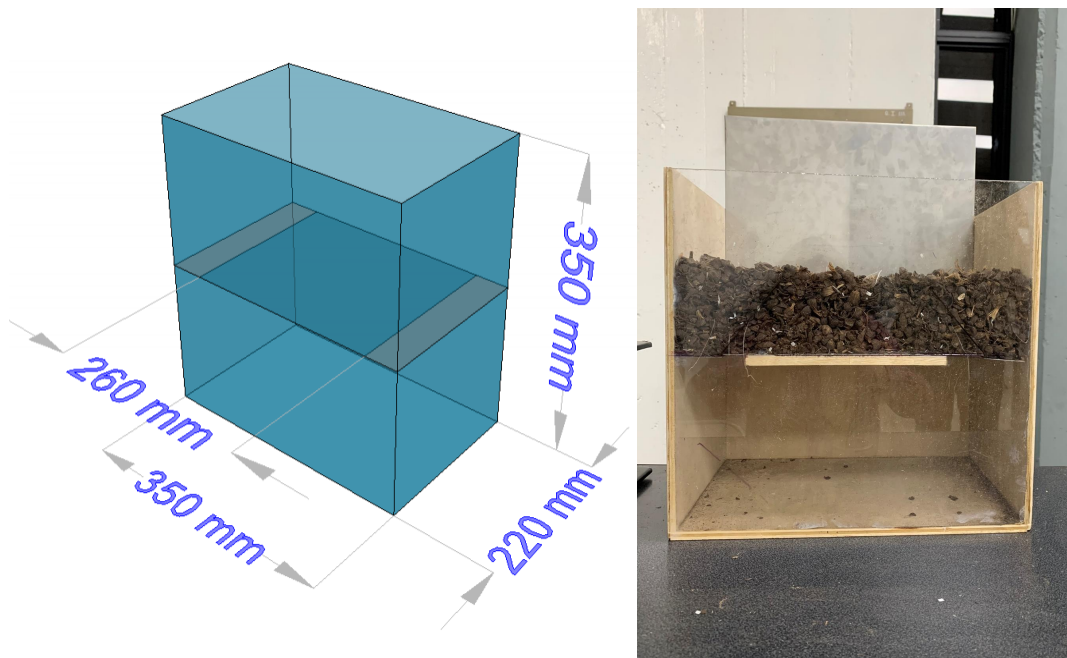


Figure 5.5: Device for evaluating particle's discharge.



Figure 5.6: Evaluation of discharge for PKS particles.

ν = Poisson's ratio.

R = radius of the smallest particle.

For estimating the simulation time, a value between 0.2-0.4 times T_R could be taken [219].

5.4.5 Residence time using a DEM approach

For determining the residence time using a DEM approach, two different alternatives are evaluated: a simulated residence time and an empirical correlation built with simulated data.

5.4.5.1 Simulated residence time

The first alternative considers an average residence of all the particles that manage to pass through the auger reactor. Because of the structure and the geometry of the auger reactor, some particles will not leave the reactor as they will be allocated in places of difficult access. Such particles are not considered in the determination of the residence time. The rest of the particles are tracked independently, and each particle i has a time to entry the auger reactor $t_{in,i}$ and a registered time at which each particle leaves the reactor $t_{out,i}$ and each particle's residence time τ_i can be calculated as follows:

$$\tau_i = (t_{out,i} - t_{in,i}) \quad (5.23)$$

The limits defined as inlet and outlet in the auger reactor correspond with the feed and discharge nozzles in the reactor. The mean residence time is finally calculated as the mean of the residence time distributions generated in the analysis. The particles that due to the geometry of the auger reactor remain inside the reactor, are not taken into consideration for the residence time analysis.

5.4.5.2 Empirical correlation for residence times distribution using simulated flow rates

In this section, simulated mass flow rates are used to determine residence time distributions. For this purpose, the same procedure presented earlier in this chapter for building a mathematical model for estimating mean residence times from experimentally-measured flow rates is applied.

The function $F(t)$ for the cumulative residence time distribution is determined first considering a simulated step change in the feed, which generates a change in the mass flow rate

calculated as $\dot{m}_0 - \dot{m}(t)$ and then divided by the size of the step change [220]:

$$F(t) = \frac{\dot{m}_0 - \dot{m}(t)}{\dot{m}_0} \quad (5.24)$$

The mean residence time τ is determined as the integral with respect of time of the $F(t)$ function[137]:

$$\tau = \int_0^1 t dF \quad (5.25)$$

Finally, one of the forms of the mathematical model for estimating residence time can be calculated as a function of the mass flow \dot{m} , the pitch p and the velocity of the screw v_{screw} [137]:

$$\tau_{model} = \frac{1}{p \cdot v_{screw}} \cdot \left(k_0 + k_1 \frac{\dot{m}}{v_{screw}} \right) \quad (5.26)$$

Where:

τ_{model} = estimated mean residence time.

\dot{m} = mass flow rate in the auger reactor.

v_{screw} = rotational speed of the screw conveyor.

k_0, k_1 = model coefficients.

p = pitch of the screw.

Equation 5.26 is an alternative representation of the original equation proposed by Nache-nius et. al., (2015), that considered a correlation that included the volumetric flow rate instead of the mass flow rate. As a result, the units of k_1 in this work are different from the ones in the original equation.

5.4.5.3 Comparison between the alternatives for estimating granular flow rates in auger reactors

The comparison of the performance of the different alternatives to determine the residence time, τ , is made on the basis of the coefficient of determination, R^2 and the root mean square error $RMSE$.

$$R^2 = 1 - \frac{\sum_{i=1}^n (\tau_{experimental,i} - \tau_{predicted,i})^2}{\sum_{i=1}^n (\tau_{experimental,i} - \tau_{average})^2} \quad (5.27)$$

The $RSME$ indicates the deviation that exists between predicted and experimental values, and it constitutes the residuals' standard deviation. The $RSME$ is calculated as follows:

$$RSME = \sqrt{\frac{\sum_{i=1}^n (\tau_{\text{predicted}, i} - \tau_{\text{experimental}, i})^2}{n}} \quad (5.28)$$

5.5 Results

5.5.1 Determination of residence time distributions with an empirical mathematical model

5.5.1.1 Mass flow rates in the equilibrium

The results for the mass flow rates in steady state show in Figure 5.7 that the mass flow rate is stable after 20 seconds in each case. Similarly, the variation in the mass flow rate increases for the lower flow rates. The mentioned figure also indicates that a linear increment in the frequency of the screw do not correspond with a linear increment in the mass flow rate of PKS in the studied auger reactor. Indeed, Figure 5.7 shows that when the velocity of the screw increases from 25% to 50% of the maximum rotational velocity, the mass flow rate nearly doubles; whereas increments from 50% to 75% or from 50% to 100% of the maximum rotational speed, generate maximum a 10% increase in the mass flow rate. This behaviour has been identified before in the operation of screw conveyors [221] and it is related to the void fraction inside the screw and to a threshold height of biomass inside the conveyor. While the void volume of the screw conveyor is high, as in the 25% velocity condition, any increase in the screw speed represents higher mass flow rate. However, after certain volume is reached and certain height inside the screw has been reached, back-flow phenomena start to appear. This means that some of the particles are sent back as a result of the movement of the screw. Thus generating a lower increment in the mass flow rate for increasing screw velocities.

5.5.1.2 Mass flow rates for determining the residence time distribution

The effect of the negative step-change over the mass flow rates are evidenced in Figure 5.8. The mentioned Figure shows that in every case, the negative step-change has a delay effect before the mass flow rate starts to decrease, which in the case of the mass flow rates with 25% of the maximum rotational velocity, corresponds to 325 s. Even when the feed has stopped, the system remains in steady state for a certain time and then there is an abrupt fall of the mass flow rate. It is also evident that the higher the RPMs, the fastest the system reaches steady state and the mass flow rate falls sooner.

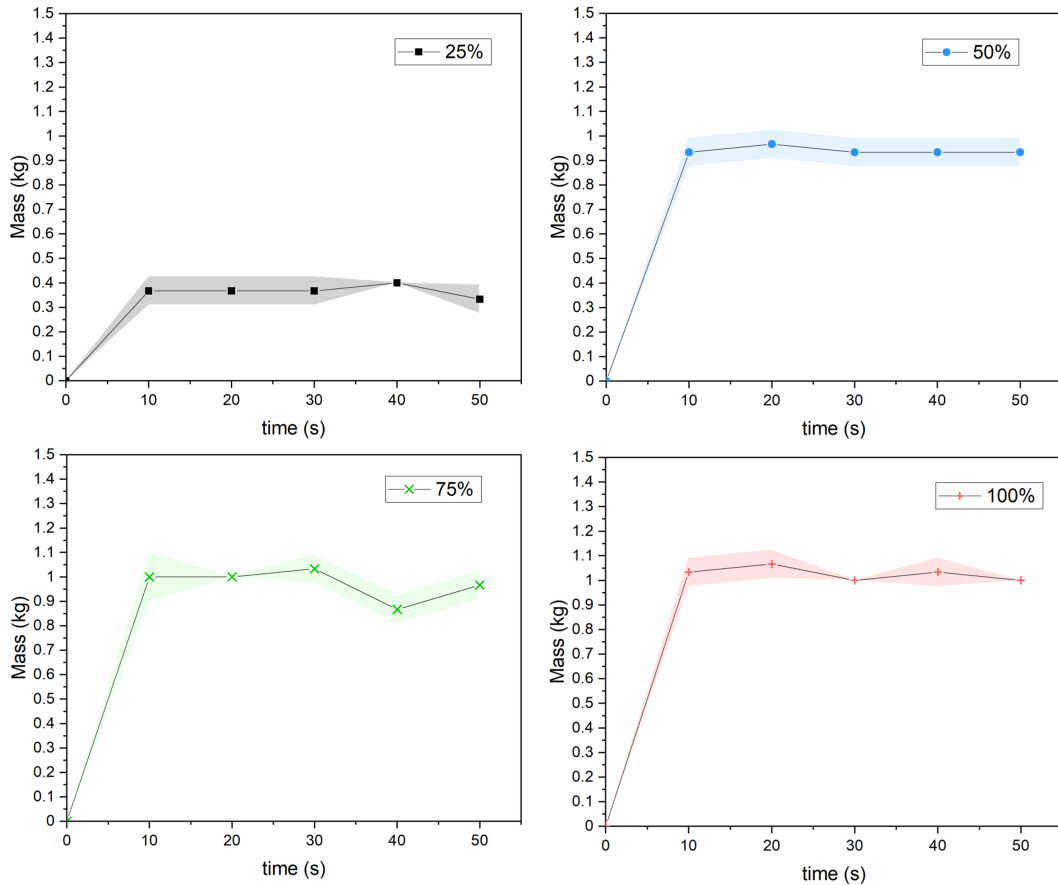


Figure 5.7: Mass flow rate in steady state for 25%, 50%, 75% and 100% of the maximum rotational velocity. Average of three measurements.

5.5.1.3 Results for the residence time distributions

The results for estimating the mean residence time required the analysis between experimental and modeled residence times. The adjusted parameters for the mean residence time equation are presented in Table 5.6. The obtained results show that a linear correlation is enough to determine a mean residence time when the geometry of the auger reactor and the frequency of the screw are known. Moreover, the applied methodology generates a simple equation that could be incorporated in any other reactor models without over complicating the calculation. There is however a downside to this method, and that is that experimental data in sufficient amount and quality needs to be considered for the calculations. This is not always possible, and it is quite usual to face situation where data is not available [222]. In such circumstances the proposed methodology for finding the mean residence time might not work. Moreover, the followed methodology considers a constant size distribution and if it is going to be integrated into a shrinking particle model for describing pyrolysis, the

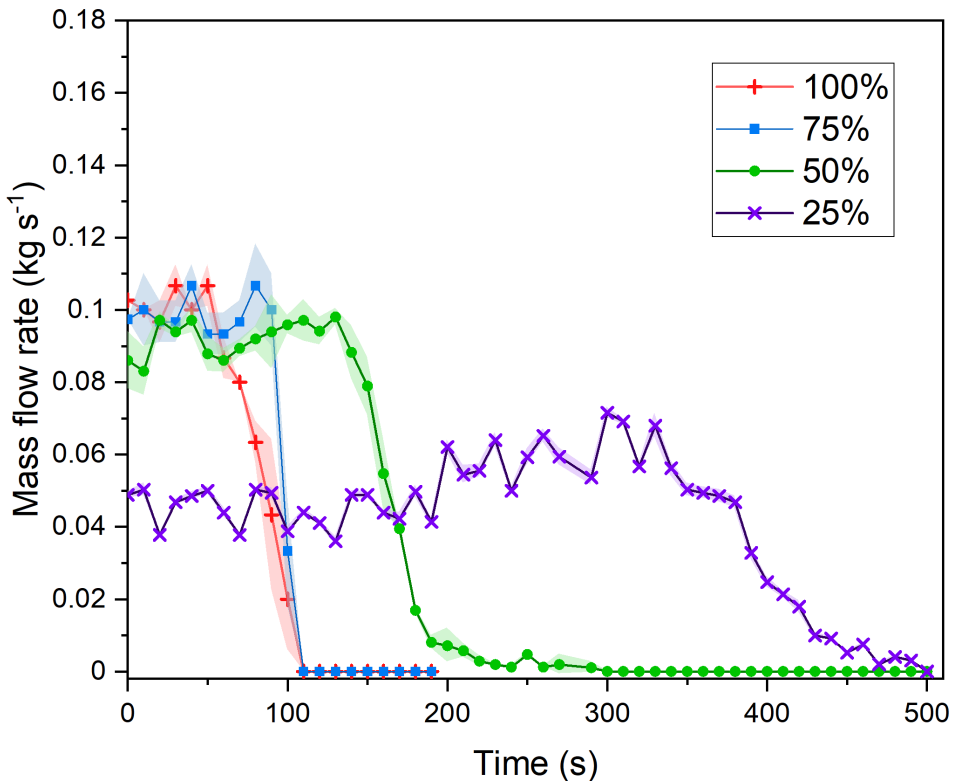


Figure 5.8: Negative step-change effect over the mass flow rate of the pyrolysis screw operating at different percentages of the maximum rotational velocity. Average for three measurements.

mean residence time might increase as the biomass particles react and shrink [36].

The model for describing residence times as a function of operating conditions, and specifically k_0 and k_1 , is determined using a linear regression with all the experimental data collected in the negative-step experiments. The obtained values of k_0 and k_1 involved a R^2 value close to 1, which only indicates that the developed empirical model captures the granular flow occurring in the auger reactor up to a certain degree.

5.5.2 Determination of residence time distributions using a DEM approach

5.5.2.1 Interaction properties for PKS

There are several works dealing with granular flow in screw conveyors, and in applications of DEM for simple shapes, usually completely spherical [223]. The results from the tilting surface for determining inclination angles are presented in this section. Only one type of surface (AISI 304 stainless steel) is used and only palm kernel shells are evaluated and 10 observations were performed in each case. The results of the statistic estimators evaluating the number of observations are presented in figures C.1 and C.2 of the corresponding section

Table 5.6: Parameters found for the mean residence time mathematical equation

Parameter	Value
Equation	$\tau = \frac{1}{p \cdot v_{screw}} \cdot \left(k_0 + k_1 \frac{\dot{m}}{v_{screw}} \right)$
k_0	140.94539 ± 46.71413
k_1	2.37474 ± 1.24136
p [m]	0.40000
Reduced Chi-S	297.05052
R-Square (COD)	0.99173
Adj. R-Square	0.98760

Table 5.7: Values of the particle-wall coefficients determined experimentally

Coefficient	Selected value	Range
particle-wall sliding coefficient	0.39	0.39-1.00
particle-wall rolling coefficient	0.65	0.47-1.00

of Appendix C. The analysis of the convergence shows that the performed measurements are enough to have an approximate idea of the sliding friction and rolling friction coefficients. Nonetheless, it would be useful to have more observations to verify that the trend towards more reliable measurements is kept.

The results of the calculated friction coefficients are presented in Table 5.7. The determined values for the particle-wall interactions are similar to other coefficients available in literature for similar types of biomass [224].

5.5.2.2 DEM calibration results

Palm kernel shells have an irregular surface and they are not completely spherical. Given that the particle-wall coefficients measured previously are in the 0.39-0.47 range, it would be expected that particle-particle coefficients reach values between 1.00 and the particle-wall sliding coefficient. To compare the repose angles in PKS between the DEM simulation and the experiments, different combinations of particle-wall sliding friction and rolling friction are evaluated. The evaluated combinations and their correspondent angle of repose are presented in Figure 5.10. This Figure suggest that, in general, the increase of the friction coefficients also increments the response angle. Moreover, the mentioned Figure shows that the particle-particle sliding friction coefficient has a higher impact over the repose angle. The selected combination of particle-particle sliding and rolling friction coefficients is 0.39



Figure 5.9: Comparison between experimental setup and DAE simulation for determining friction coefficients.

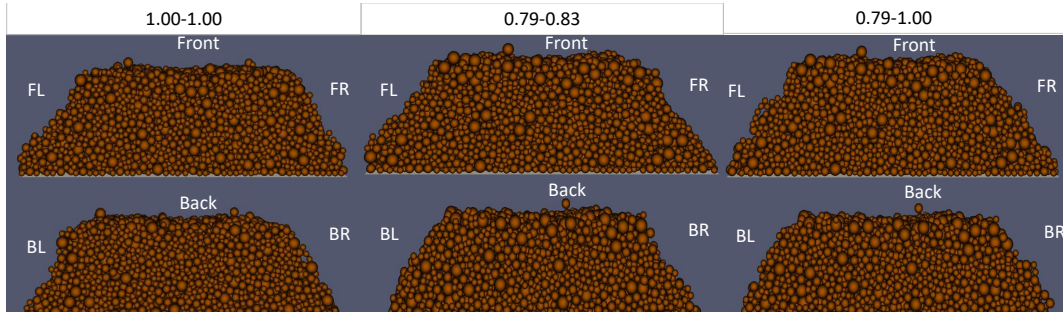


Figure 5.10: Part of the results considering front and back repose angles using a DEM simulation in LIGGGHTS. Sliding coefficient-Rolling coefficient. F=front, B=back, L=left, R=right.

and 0.47. These values are the closest to the experimental value.

Figures 5.9 and 5.10 highlight the importance of considering a distribution of sizes in the DEM model and also they show that slight modifications of even just one of the particle-particle friction coefficients can modify completely the outcome of the simulation. The DEM approach is sensible to such changes. The complete set of images regarding the results of the simulation in LIGGGHTS are in Appendix C.

To analyze the individual effect of each one of the particle-particle friction coefficients over the repose angle, initially the rolling friction coefficient was kept constant, whereas the sliding friction coefficient varied. Then, the sliding friction coefficient was kept constant while the rolling coefficient varied. Figure 5.11 a) shows that for a constant rolling friction coeffi-

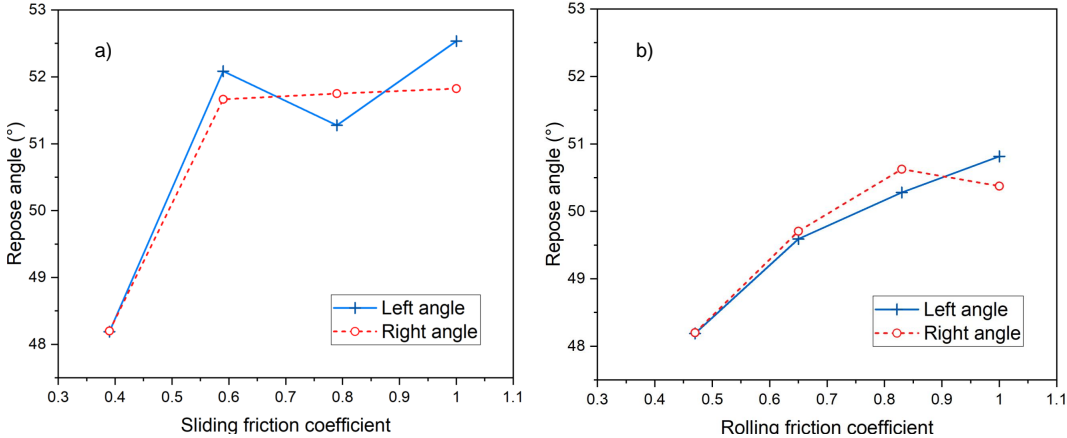


Figure 5.11: Effect over the repose angle of varying the sliding coefficient for a) constant rolling coefficient $\mu_{rolling} = 0.47$, and of varying the rolling coefficient for b) constant sliding coefficient $\mu_{sliding} = 0.39$.

cient, an increment on the sliding friction coefficient increases the repose angle. Moreover, this increment in the repose angle is more intense between values of 0.4-0.6 for the sliding friction coefficient. After the threshold of 0.6, changes in the repose angle are negligible. This behaviour indicates that large sliding friction coefficients tolerate more elastic deformation in tangential directions. As a result, the pile of PKS will be more stable [225]. Regarding the effect of the rolling friction coefficients over the repose angle, Figure 5.11 b) shows that an increase of the rolling friction coefficient increases also the repose angle; nonetheless, such effect is more important for rolling friction coefficients between 0.5-0.8. From the previous analysis and for the reached repose angles, sliding friction coefficients have a bigger effect over the angle of repose than the rolling friction coefficient, up to a threshold value where sliding friction coefficients do not modify the angle of repose.

Figure 5.12 summarizes the previous findings regarding the combination of rolling and sliding friction coefficients. The mentioned figure evidences the effect of sliding friction coefficients over the angle of repose, but it also indicates that combinations of low sliding coefficients and low rolling coefficients have a better chance to resemble experiments.

5.5.2.3 DEM model validation

As it was mentioned before in this chapter, it is possible to determine a residence time by introducing a negative-step in the feed once that steady-state has been reached. It is also possible to include the negative step in the simulation with LIGGGHTS. Similarly, the mass flow rate is monitored constantly until no more particles abandon the reactor. As presented in Figures 5.13 and 5.14, the mas flow rate of equilibrium in every case corresponds approx-

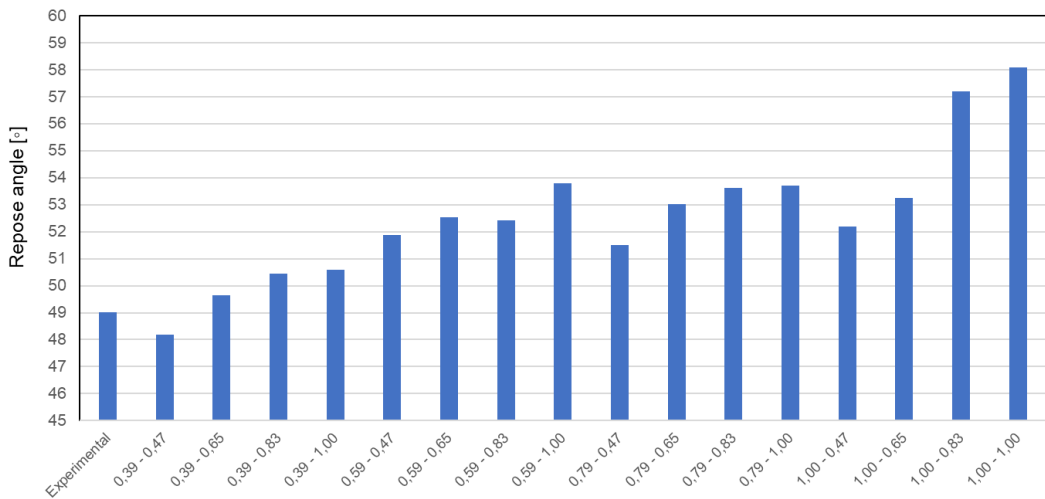


Figure 5.12: Average repose angle for different combinations of particle-particle sliding friction and rolling friction coefficients.

imately with the mean value of the mass flow rate from the DEM simulations. Similarly, the negative step-change introduced both experimentally and in the DEM simulation, causes a reduction in the mass flow rate at approximately the same time. For instance, in the results for 50% of the rotational velocity, both the experimental and simulated mass flow rate start descending at approximately 100 s after introduced the negative step change. The

The simulations behave in a similar way than the experiments; nonetheless, the variation of the mass flow rate of the DEM model is considerably higher than the one observed in experiments. Such behaviour could respond to a variety of causes. One of them could be the difference in the time steps where mass is measured. Regarding this, the granular flow pattern inside an auger reactor could involve having emptier or fuller sections of the screw and by having small time steps, some measurements will contain almost no mass. This behaviour was also visualized during the experimental analysis when collecting the mass for determining the residence time. Indeed in the span of 10 seconds, there were occasions in which mass will not come out until the last second. The time step for the DEM simulation is $5.00 \cdot 10^{-5}$, which corresponds with the 32.00% of Rayleigh's critical time. Because the time step is bigger in the experimental analysis, variations or irregularities in the feed will not be as evident. On the other hand, the time step for the DEM simulation was established on terms of Rayleigh, as it is broadly the case [226]; nonetheless, such approach for selecting simulation times had been found to generate variations in the model [224]. Another of the potential causes of the pulse-like flow rate is an indication that solids might

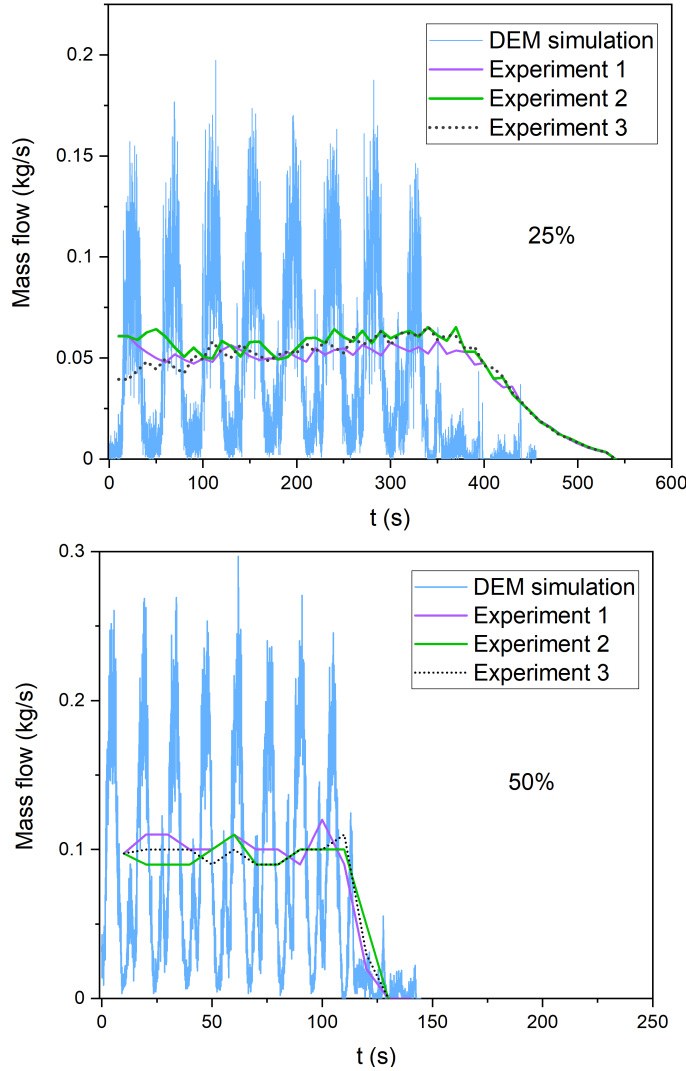


Figure 5.13: Comparison of mass flow rates at the outlet of the reactor from the DEM simulation and the experimental results for 25% and 50% of the maximum rotational velocity.

not have been uniformly distributed [227].

Despite the differences that were found in the behaviour of the modelled auger reactor, the simulations captured qualitatively the behaviour of the granular flow of PKS. The calibrated parameters that are used in the DEM model are presented in Table 5.8.

5.5.2.4 Comparison of mass flow rate determination from experimental and simulation approaches

As mentioned before in this chapter, there are three different alternatives for estimating residence time distributions that are covered in this work. The first one being an empirical correlation for residence time in terms of experimental measurements. A second alternative considers the simulation of the granular flow using a DEM approach in which particles are

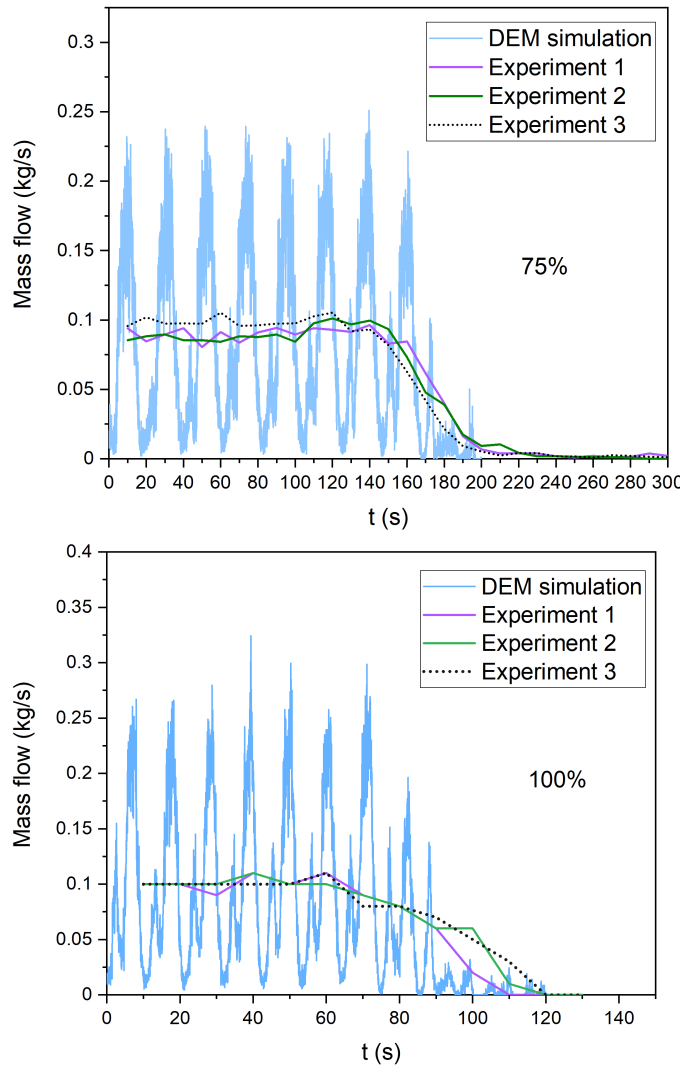


Figure 5.14: Comparison of mass flow rates at the outlet of the reactor from the DEM simulation and the experimental results for 75% and 100% of the maximum rotational velocity.

tracked and an average residence time is obtained from the particles going in and out of the reactor. Finally, the empirical correlation for predicting residence times is applied to a DEM simulation recreating the experimental procedure.

The values from the previous tables were compared using R^2 to have an idea on which approach might be more appropriate to use.

The results from Table 5.13 show that although the mathematical correlation for describing the mean residence time adjusts to the experimental results, the empirical correlation developed does not explain completely the behaviour of the granular flow. Such behaviour reflects on the relatively high values of RSME. The model could be too simple and although it predicts residence time fairly good, it cannot explain behaviour or attribute-related pre-

Table 5.8: Parameters used in the DEM simulation

DEM Parameter	Symbol	Value
Particle's Poisson ratio	ν_p	0.3
Young Modulus (MPa)	Y_p	7
Wall Poisson's ratio	ν_w	0.29
Coefficient of restitution (particle-particle)	e_{pp}	0.13
Coefficient of restitution (particle-wall)	e_{pw}	0.45
Coefficient of sliding friction (particle-particle)	μ_{pp}	0.39
Coefficient of sliding friction (particle-wall)	μ_{pw}	0.47
Coefficient of rolling friction (particle-particle)	μ_{pp}^r	0.39
Coefficient of rolling friction (particle-wall)	μ_{pw}^r	0.65

Table 5.9: Mean residence time determined from experiments.

% of maximum rotational velocity.	Mean residence time $\tau_{experiments}$ [s]
25	431.00 ± 19.84
50	175.38 ± 3.15
75	120.96 ± 2.39
100	91.62 ± 3.11

Table 5.10: Mean residence time determined from empirical correlation using experiments.

% of maximum rotational velocity.	Mean residence time $\tau_{correlation}$ [s]
25	424.27 ± 1.56
50	196.45 ± 12.02
75	116.39 ± 3.78
100	82.46 ± 10.00

Table 5.11: Mean residence time determined from DEM simulations followed by an empirical correlation.

% of maximum rotational velocity.	Mean residence time $\tau_{simulated}$ [s]
25	306.50 ± 29.80
50	160.75 ± 13.83
75	110.17 ± 9.77
100	81.41 ± 4.27

Table 5.12: Mean residence time determined from DEM simulations tracking particles.

% of maximum rotational velocity.	Mean residence time $\tau_{tracker}$ [s]
25	343.13 ± 36.41
50	172.24 ± 20.91
75	117.64 ± 18.10
100	90.06 ± 15.79

dictions. Therefore, the information that the model provides might not be complete and some other metric will be required. The previous results highlight the fact that both Eulerian and Lagrangian approaches could be used for characterizing the granular flow inside an auger reactor. Moreover, even if Eulerian and Lagrangian approaches could predict residence times with the same precision, the Lagrangian approaches are capable of capturing additional information besides mass flow rate to describe there residence times. Moreover, results show that a DEM approaches (Lagrangian $\tau_{tracker}$) could be tranformed in to Eulerian approaches (Lagrangian-to-Eulerian $\tau_{simulated}$) so it can be implemented easier in other multi-scale modelling alternatives. Such opportunities represent different possibilities to face diverse types of problems or applications involving biomass transportation and pro-

Table 5.13: Comparison of statistical parameters between correlations for predicting residence time.

Parameter	$\tau_{correlation}$	$\tau_{simulated}$	$\tau_{tracker}$
Approach	Eulerian	Lagrangian transformed into Eulerian	Lagrangian
Pearson's r	0.99532	0.99978	0.99979
R^2	0.99067	0.99955	0.99958
Adj. R-Square	0.98974	0.99933	0.99938
RSME [s]	14.106	2.93513	2.49916

Table 5.14: Comparison between simulations using the DEM

Parameter	Percentage of the maximum rotational speed			
	25%	50%	75%	100%
Computational time	573h 57min	268h 53min	163h 42min	84h 57min
Particles simulated	201077	188069	146100	124932
Particles tracked	169737	169990	130710	82895
Computational specifications	Intel® Xeon® CPU E5-2650 v4 @ 2.2 GHz 2.2 GHz (2 physical processors - 24 cores per processor 48 logic processors) Simulation run: mpi 24 logical processors			

cessing. For instance, if the operating data from an auger reactor is available, an Eulerian approach could be used to characterize the granular flow. On the contrary, if no operational data is available, a DEM approach could be used to generate the required data and this could be transformed again into an empirical, easy-to-implement correlation that represents an Eulerian approach.

Another metric that could be compared in the cases of DEM simulations is the computational time. The previous results showed that the DEM model is capable of capture the behaviour of PKS granular flow; however, this comes with a cost and for what is shown in Table 5.14, the computational cost of simulation for the DEM approach might be too high. Despite the accuracy of the DEM model, the computational cost is too high for evaluating different applications and it should not be a regular procedure for evaluating changes in the DEM parameters or for even trying some optimization alternatives with process design views. In such circumstances, it is possible to look for a different alternative to solve the problem. It is possible to try to find ways to reduce the computational time. The first step would be to optimize the parameters used in the simulation in order to reduce computational times [228].

Another one of these alternatives could be the reformulation of the problem in a simpler way, so less particles are needed. To use a different approach such as the combination of Eulerian and Lagrangian approaches could also be useful. Other types of software or even black-box models could also be an alternative for reducing computational times and to avoid the use of super computers, which are not available for the average process engineering practitioner [228].

Table 5.15: Activation energy (E_a) and pre-exponential factor A in s^{-1} , for palm kernel shell pyrolysis

Parameter	Value
E_a (kJ mol $^{-1}$)	124.68 ± 9.69
$\log A^*$	10.70 ± 0.62

5.6 Multi-scale modelling approach for describing an auger reactor

In this section an alternatives is proposed for continuing with the multi-scale strategy for biomass pyrolysis in the future. The lack of data for validation of this strategy hinders further developments regarding biomass pyrolysis.

This approach takes a volume control in the auger reactor and place round PKS particles, similar to the ones developed in Chapter 3, within this control volume. For modelling the auger reactor, three components are required: the first one is the granular flow model which describes the residence time, the second one is the kinetic model which describes the reactions that take place throughout pyrolysis and the third component is a heat transfer model, which basically defines the way energy goes in and out of the particle. A simple multi-scale strategy is proposed. This strategy couples the shrinking biomass particle model developed in Chapter 3, with the kinetic model for pyrolysis developed in Chapter 6 and the residence time distribution developed in the current chapter. The initial idea is to group a finite number of PKS particles in a defined control volume, similar in length to the particle's outer diameter, and follow this control volume throughout the residence time. No interactions are considered between solid particles in different control volumes. Such approach is schematically presented in Figure 5.15.

Kinetic modelling

The pyrolysis reaction considered for the particle model includes the properties and the kinetic parameters measured in Chapter 6. The pyrolysis reaction fro PKS is:

The kinetic parameters considered are summarized in Table 5.15.

5.6.1 Issues arising from using a different kinetic model

Throughout the last chapter, it became clear that PKS do not behave as a mixture of cellulose, hemicellulose and lignin would behave. Nonetheless, most of the applications of particle models and reactor models for pyrolysis consider biomass as such mixture [4, 27, 49].

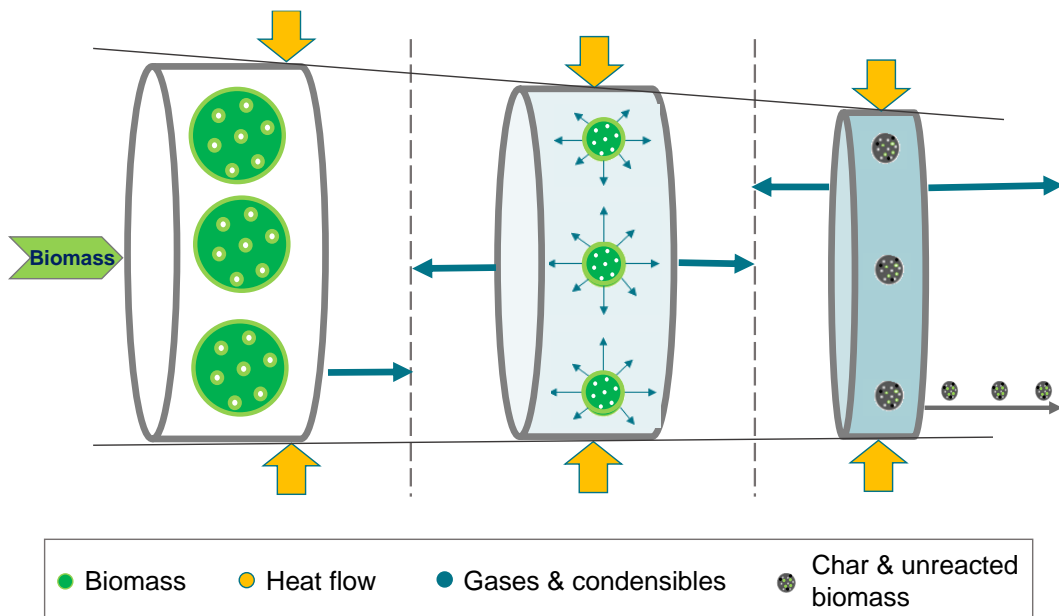


Figure 5.15: Multi-scale modeling strategy for describing biomass pyrolysis inside and auger reactor



Figure 5.16: Devolatilization reaction for palm kernel shells undergoing pyrolysis.

This usually works into a certain extent for woody materials where cellulose or hemicellulose are the main components. However, in the case of lignin-rich biomass as the palm kernel shells, using kinetics of the main components can compromise the results of the reactor model. For understanding the limitations of conventional kinetic approaches using a linear combination of cellulose, hemicellulose and lignin; such combination is modelled and compared against the results of TGA for PKS. Figure 5.17 considered experimental data and a particle model, just like the developed for Chapter 2. The properties and kinetic models for the modelled PKS can be found in a previous work [229]. The synthetic mixture and the PKS experiments are the same used for the TGA analysis from the previous chapter. As it is evidenced in the mentioned Figure, when the kinetics of PKS pyrolysis are not the experimental ones, changes will be expected. This only reassures us the importance of using real, laboratory determined kinetics for high-lignin biomass.

Granular flow model

The granular flow model used in the multi-scale model considers the empirical correlation

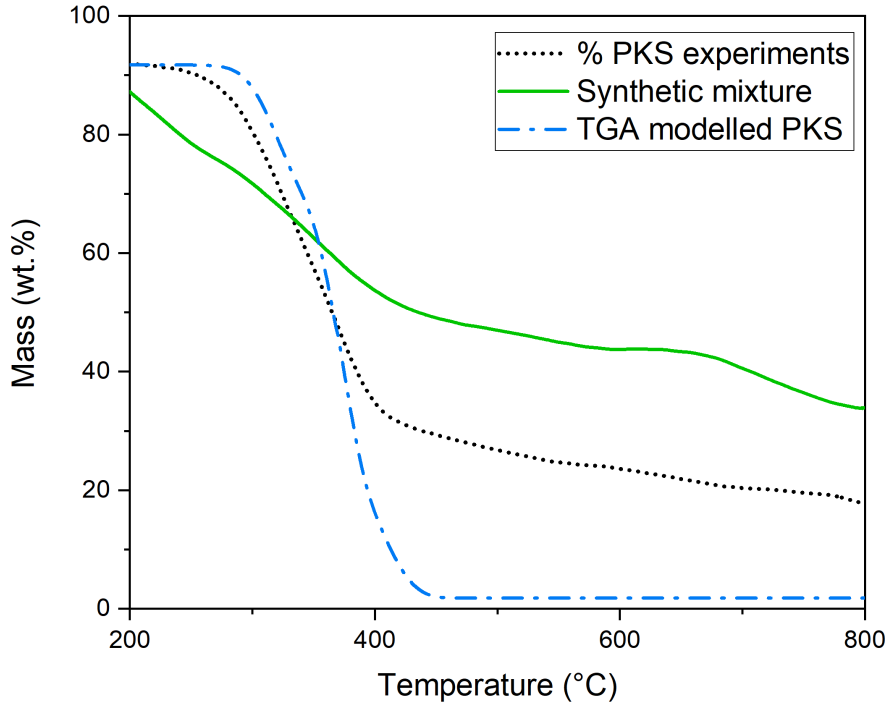


Figure 5.17: Comparison thermal decomposition during pyrolysis.

Table 5.16: Parameters for the mean residence time mathematical equation

Parameter	Value
Equation	$\tau = \frac{1}{p \cdot v_{screw}} \cdot \left(k_0 + k_1 \frac{\dot{m}}{v_{screw}} \right)$
k_0	140.94539 ± 46.71413
k_1	2.37474 ± 1.24136
p [m]	0.40000

obtained from the operation of the pilot plant, and the relevant information is presented in Table 5.16.

Heat transfer considerations

The geometry of the auger reactor and the movement of the palm kernel shells inside the reactor makes it necessary to consider different heat transfer processes that occur simultaneously while pyrolysis takes place. In order to understand the different processes that take place in an auger reactor involving heat transfer, a similar approach to study heat transfer in rotary kilns could be useful [85]. Inside the reactor there is a PKS covered wall (*cw*), an exposed wall or uncovered inner surface (*ew*) and a biomass bed (*cb*). The exposed

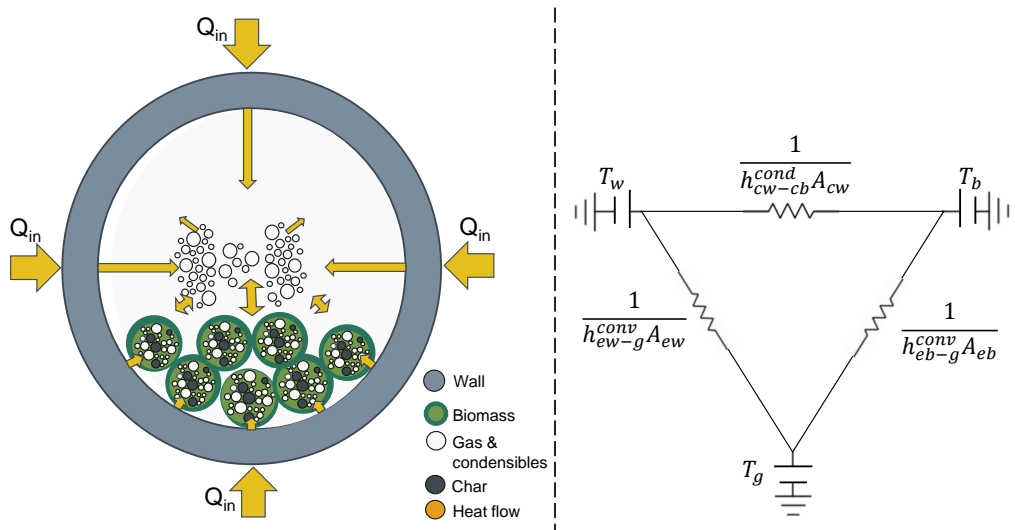


Figure 5.18: Scheme of the heat transfer phenomena involved in the auger reactor, considering the wall temperature T_w , the biomass bed temperature T_b and the gas temperature T_g .

metallic surface is heated through convection and radiation. The PKS covered surface is heated mainly via conduction, and the interactions between the PKS bed and the gas inside the reactor (g) occur via convection. A representation of the mentioned interactions is available in Figure 5.18, which has also been described in a previous work [85]. Radiative heat transfer is not presented in the mentioned diagram; however, the equations required for its calculation will be presented in this section.

The heat transfer analysis for developing the multi-scale strategy is of vital importance to make sure the model is robust and that can accurately represent the operation of an auger reactor. The heat transfer can be evaluated as energy added per unit of length (\dot{q}_{a-lu}) or as

energy exchanged per unit of length (\dot{q}_{e-lu}) using the following equations:

$$\dot{q}_{a-lu,s} = (h_{cw-cb}^{cond} A_{cw} + h_{ew-eb}^r A_{eb})(T_w - T_s) \quad (5.29)$$

$$\dot{q}_{e-lu} = (h_{eb-g}^{conv} + h_{eb-g}^r A_{eb})(T_w - T_g) \quad (5.30)$$

$$\dot{q}_{a-lu,g} = (h_{ew-g} + h_{ew-g}^r A_{ew})(T_w - T_g) \quad (5.31)$$

$$h_{cw-cb}^{cond} = 1/\left(x \frac{Dp}{kg}\right) + \left(2 \sqrt{\frac{[(1-y)k_b \rho_b C p_b + y k_c \rho_c C p_c] \cdot n \cdot \sin(\alpha) \cos(\alpha)}{pitch}}\right)^{-1} \quad (5.32)$$

$$h_{ew-g}^{conv} = (1.54 \cdot Re_g^{0.575} Re_s^{-0.292}) \frac{kg}{De} \quad (5.33)$$

$$h_{eb-g}^{conv} = (0.46 \cdot Re_g^{0.535} \cdot Re_s^{0.341} \eta^{-0.341}) \frac{kg}{De} \quad (5.34)$$

$$h_{eb-g}^r = \frac{(J_w - J_s)(\tau_g F_{eb-ew})}{T_w - T_s} \quad (5.35)$$

$$h_{ew-eb}^r = \frac{(J_s - E_g)(\epsilon_g F_{eb-g})}{T_s - T_g} \quad (5.36)$$

$$h_{ew-g}^r = \frac{(J_w - E_g)(\epsilon_g F_{ew-g})}{T_w - T_g} \quad (5.37)$$

The mentioned approach for estimating the heat transfer in an auger reactor is complete and surely can support the development of complete multi-level pyrolysis models. However, the associated heat transfer coefficients need to be determined experimentally, or at least validated with experiments. In this work, it was not possible to perform more analysis to validate heat transfer coefficients and this hindered the development of such component. However, with views on combining, even at a preliminary stage, the components of a multi-scale modelling approach for describing pyrolysis; a simple multi-scale model is applied. One of the simplest alternatives is to model the auger reactor as if it was a plug flow reactor. Moreover, each one of the differential volumes of the PFR also contains a number of biomass particles N_p which react throughout a given residence time τ . To simplify the analysis, the model considers a high enough axial Peclet number Pe_{axial} , so local thermal equilibrium between solid and gaseous phases in the continuous process is achieved. Pe_{axial} was estimated, as indicated in Eq. 5.38, in terms of the axial diffusion D , the velocity v , the characteristic distance L_c and the thermal diffusion α . Moreover, radial diffusion is considered to be negligible [85, 4].

$$Pe_{axial} \equiv \frac{L_c v}{D} \equiv \frac{L_c v}{\alpha} \quad (5.38)$$

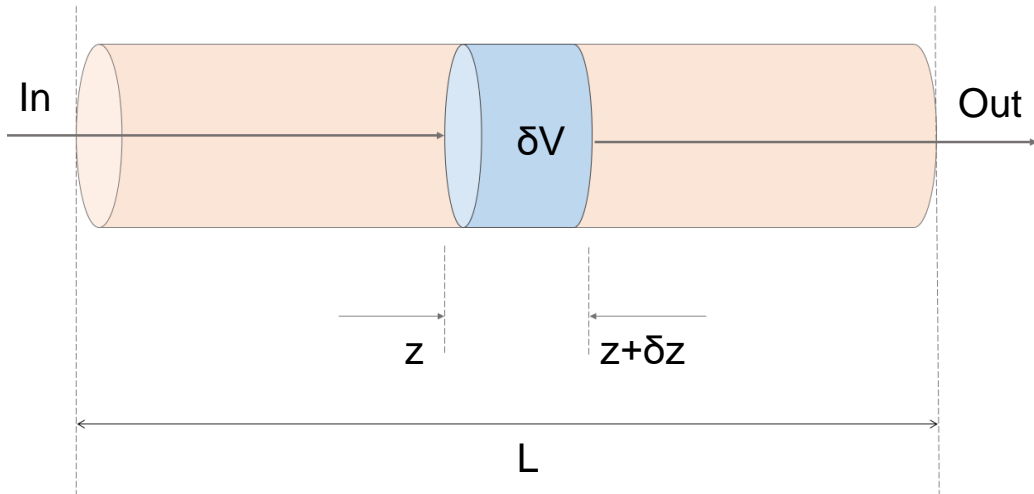


Figure 5.19: Definition of the differential volume in the PFR to perform mass and energy balances

The mass and energy balances are performed over a differential volume δV and over the whole reactor length L , which is represented in Figure 5.19. The mass and energy balance equations for the PFR reactor model are presented in this section. In order to simplify as much as possible the reactor model, so initial insights could be retrieved regarding product distribution for a defined temperature, axial dispersion and radial dispersion were neglected. The PFR model considered the gas and solid mixture form a one phase bulk mixture, whose properties can be determined in terms of average values [230]. For each individual component i , concentration C_i is considered to be distance dependent and given in (mol m^{-3}) . Furthermore, for a lumped or detail kinetic model, the mass balance of each one of the components considers the velocity of the mixture inside the reactor v in (m s^{-1}) . The mentioned mass balance is defined by Equation 5.39.

$$\frac{\partial (C_i)}{\partial t} = -v \frac{\partial (C_i)}{\partial z} + \Gamma_i \quad (5.39)$$

The velocity was calculated in terms of the volumetric flowrate \dot{V} in $(\text{m}^3 \text{s}^{-1})$, required residence time τ in (s) and the reactor volume V in (m^3) . Moreover the reactor volume was calculated in terms of the radius (r) and length (L) for a cylindrical reactor, as presented in

the next lines.

$$\dot{V} = v \cdot \pi r^2 \quad (5.40)$$

$$\tau = V/\dot{V} \quad (5.41)$$

$$V = \pi r^2 L \quad (5.42)$$

The generation term Γ_i , which includes the moles being consumed or generated due to the pyrolysis reaction is calculated with similar equations to the ones developed in the particle model, as first order reactions and with reaction rates that can be described with the Arrhenius equation. Due to the variety of reactions that take place during pyrolysis and the numerous components interacting, Γ_i is determined particularly for each component i involved in a reaction j . Moreover, molecular weights are used to get concentration in (kg m⁻³ s⁻¹). The values for the kinetic constants $k_{i,j}$ are obtained from A_j and Ea_j presented in the first section of this chapter. With these premises, the applied equations are presented in the following lines:

$$\Gamma_i = \sum_{j=1}^{n \text{ reactions}} v_{i,j} \dot{r}_j \quad (5.43)$$

$$\dot{r}_j = k_j C_{i,j} \quad (5.44)$$

$$k_j = A_j e^{-\frac{Ea_j}{RT}} \quad (5.45)$$

Where:

i = component

j = reaction

$v_{i,j}$ = stoichiometric coefficient for component i in reaction j

\dot{r}_j = reaction rate (kg m⁻³ s⁻¹)

k_j = rate constant j (s⁻¹)

$C_{i,j}$ = concentration of component i in reaction j (kg m⁻³)

A_j = pre-exponential factor for reaction j (s⁻¹)

Ea_j = activation energy for reaction j (J mol⁻¹)

5.6.2 Initial and boundary conditions

The initial conditions and the boundary conditions for the PFR model are described in the following lines. The preliminary model considers a fixed amount of heat being transferred

to the reactor and consequently, into in the boundary ($r=R$) of each one of the particles in the volume control, is described in terms of convection and radiation. For the radiation term, the Stefan-Boltzmann constant (σ) and the surface emissivity (ε) are considered. Initially, the reactor is fed only with palm kernel shells and nitrogen as carrier gas. Therefore, the concentration of all the components, except biomass, is zero. The initial pressure of the system is P_0 and the initial temperature T_0 . For the initial conditions, it was considered that $\rho_{PKS} = \rho_{PKS,0}$; $\rho_i = 0$; $P = P_0$.

The mentioned simplification do not consider the complex heat transfer phenomena that undergoes inside an auger reactor. Indeed, a more realistic and accurate way to define the energy that ends up being taken by the conglomerate of particles inside the reactor, require the analysis of the different zones (zones with solids, zones with gases, etc.) where heat is potentially exchanged. One alternative to this comes from the heat transfer equations proposed by Codignole et al., (2018) to asses an auger reactor as a rotary kiln. Moreover, as boundary conditions, it was considered that the temperature and concentration do not change in the boundaries of the system. This consideration implies that the reactor is sufficiently large so equilibrium can be reached. Correspondingly, the boundary conditions are:

$$\frac{\partial T}{\partial z} \Big|_{z=L} = 0 \quad (5.46)$$

$$\frac{\partial C_i}{\partial z} \Big|_{z=L} = 0 \quad (5.47)$$

5.6.3 Numerical solution

The mentioned mass, momentum and energy balances, that represent the simplified PFR reactor model, consist of a set of ODEs, DEs and algebraic equations, that were implemented and solved using gPROMS ModelBuilder® version 7.0.9.

5.6.4 Preliminary results

As previously discussed, the development of a multi-level model for describing biomass pyrolysis in an auger reactor still requires further work for coupling and validating the heat transfer mechanisms involved in this process. Similarly, real data regarding the operation of the auger pyrolyzer are necessary for validating any modelling approach. In spite of such limitations, Figure 5.20 shows that initially, it is possible to couple a kinetic model, with a particle model and in this case, within a PFR reactor framework. Furthermore, the effect

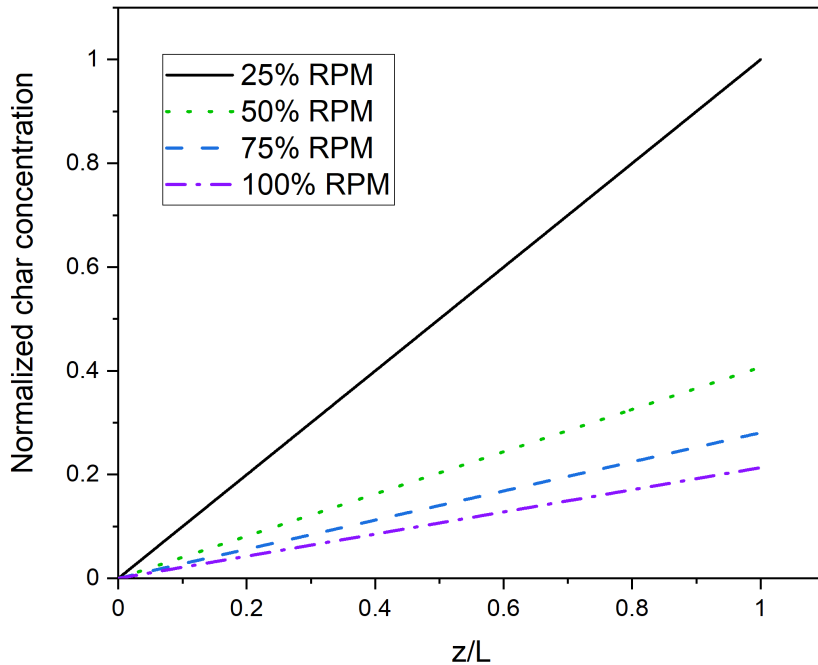


Figure 5.20: Normalized char production for different screw velocities.

of using different velocities in the auger reactor also modifies the char production. For the studied velocities and residence times, lower screw velocities are associated with higher char concentrations in the product side. Nonetheless, the adequate coupling of the different scales (micro, particle and reactor) still needs to be further developed and researched. Regarding the computational times, all of the performed calculations required under 70 s to be performed, using a computer equipped with an Intel®Core™i7-10610U CPU@ 1.80GHz 2.30 GHz and 16 GB of installed RAM.

5.7 Concluding remarks

This chapter considers the development of some of the required inputs for transforming a particle-scale model into a reactor-scale application for addressing lignin-rich biomass pyrolysis. The determination of residence times is key for any reaction, even more so for complex chemical processes such as pyrolysis. Both Eulerian and Lagrangian approaches were studied as a way for determining residence times and to evaluate any potential differences. With information regarding the operation of an auger pyrolyzer it was possible to build a correlation for predicting the residence time as a function of the speed of the screw and the mass flow rate. A DEM approach was also implemented and it was found to be capable of predicting flow rates, although at high computational costs. Finally the

combination of a particle model, kinetics, and granular flow considerations can support the development of reactor models.

Chapter 6

Conclusions and future research

The main findings and contributions from this work are presented in this chapter. In addition, potential directions for future research are included in the end of this chapter.

This work addresses lignin-rich biomass pyrolysis at different scales, as an alternative to break down pyrolysis complexity, so relevant information could be obtained at every scale of biomass pyrolysis. The development of models is complemented by inputs from experiments at laboratory and pilot scales. This study initially describes pyrolysis for thermally-thick biomass particles in general; later it focus in finding properties and kinetics for lignin-rich biomass and finally, it evaluates alternatives for describing granular flow in auger pyrolysis reactors.

In general, there are several novelties in this work that set it apart from other studies available in literature regarding biomass pyrolysis experiments and modelling. Such novel features include: the reformulation of a pyrolysis particle model for simplifying its resolution, the inclusion of early-stage economic, environmental and energy-related indicators in pyrolysis particle models; a correlation for predicting the energy content in lignin-rich biomass pyrolysis, a set of properties for palm kernel shells that include their pyrolysis kinetics, a correlation for estimating the residence time in an auger reactor, values for rolling and sliding friction coefficients that could be used for simulation purposes, models for describing granular flow of palm kernel shells inside a single-screw auger reactor.

Throughout this research, a mechanistic particle model for thermally-thick biomass pyrolysis is developed and some of its applications discussed (Chapter 3). Since most of the available models and properties for biomass consider woody materials, a lignin-rich type of

biomass was characterized and its pyrolysis kinetic model presented (Chapter 4), granular flow models that describe a pilot plant pyrolysis operation in an auger reactor were defined (Chapter 5). The next lines highlight the main findings and contributions of this work.

6.1 Single thermally-thick biomass particle pyrolysis model

The initial contribution presented in this work corresponds to a particle model, based on energy, mass and momentum conservation, which includes a boundary immobilisation technique to describe thermally thick biomass pyrolysis at a particle scale for different combinations of moisture contents and initial and heating temperatures. Temperature gradients and pyrolysis product distribution are determined with the model, which can be easily resolved with the support of gPROMS ModelBuilder®.

The existing nexus between pyrolysis operating conditions and the resulting energy, environmental and economic outcomes can be investigated fairly easily with the developed model. Findings highlight the challenges of having profitable and environmental-friendly biomass pyrolysis operations at the same time. For the studied temperatures and moisture contents, results suggest that a combination of high biomass initial temperatures, high external heating temperatures and low moisture contents are associated with higher economic outcomes but also with poorer environmental performances.

Perhaps one of the most interesting features of the particle model and the reformulation for accounting for the changing boundary, is the computational time for solving such a complex model. For a particle model with 11 components and 13 reactions, 6 to 12 differential control elements and a reaction time of 600 seconds, the required computational time is in average between 3.0 to 3.5 seconds; whereas for the usual approach that requires CFD for solving the pyrolysis particle model, typical computational times are between the order of tenths of minutes, when simplifications are made, to up to several hours [231]. The developed approach reduced computational times by orders of magnitude and this opens the opportunity for new applications or for incorporating the particle model in different multi-scale approaches.

6.2 Characterization and pyrolysis kinetic modelling of lignin-rich biomass

The main contribution of the work performed in this chapter is related with the understanding of the interactions between biomass main components and the effect of different structures and morphology of biomass over properties such as energy content. Moreover, the results from this chapter draw a line in terms of behaviour between conventional types of biomass and lignin-rich biomass.

Palm kernel shells not only showed interesting properties as a fuel, but also its composition, particularly the content of lignin, proved to be key in understanding why their thermal decomposition varies from other cellulose-rich or hemicellulose-rich biomass. A correlation for determining the high heating value of lignin-rich biomass was developed as a function of the carbon content. The particle size of PKS make it necessary to consider PKS as thermally-thick particles if their pyrolysis needs to be modeled.

PKS pyrolysis takes place at higher temperatures and in a narrower temperature range than PKS pure components. Pyrolysis kinetics can be obtained relatively easy from TGA data. However, most of the methods for estimating PKS pyrolysis kinetic parameters are only suitable for conversions between 0.2 and 0.7. The average activation energy of pyrolysis for the studied PKS is $124.68 \text{ KJ mol}^{-1}$. Different composition and properties in PKS translate into different pyrolysis kinetic parameters, and kinetics should be assessed carefully if pyrolysis modelling and scaling-up is required.

6.3 Pyrolysis of coarse biomass in a single screw auger reactor

This chapter initially explores the development of a granular flow model from both Eulerian and Lagrangian perspectives. The granular flow model is developed for an auger pyrolyzer of a single screw that used PKS as feedstock. The first granular flow approach develops an empirical correlation using data collected from the operation of a reactor; and the second one implements a discrete element method (DEM) simulation to predict the biomass residence time in the reactor. The auger reactor operates with palm kernel shells, which behave like thermally thick particles and have internal temperature gradients.

A DEM approach was developed and implemented in this chapter, which is capable of

predicting flow rates, although at high computational costs. Friction rolling and sliding coefficients between particle-particle and particle-wall were determined, providing useful information for future DEM simulations that might required to consider PKS. The DEM approach was found to be precise but the computational cost hinders any potential application for process design and optimization. Finally the combination of a particle model, kinetics, and granular flow considerations can support the development of reactor models and multi-scale pyrolysis.

6.4 Summary of the most relevant contributions from this work

The most relevant contributions from this work are listed in the following lines:

- A mechanistic model capable of predicting products and internal temperatures considering one particle of biomass that experiences shrinking. The availability of single particle models support the development of technologies for waste-to-value and waste-to-energy.
- A reformulated particle model that make it possible to have a fast solution, dropping the computational cost in orders of magnitude compared to CFD approaches. At the same time, such advantage for solving otherwise complex systems, allowed to include information regarding economic, environmental and energy efficiency.
- Physical, chemical and thermal properties for PKS in case it is necessary to evaluate its use in. A linear correlation for predicting the energy content in lignin-rich biomass was also developed. Finally, the kinetic parameters for PKS pyrolysis were calculated.
- An empirical correlation to characterize granular flow inside a single screw auger reactor was developed.
- A model that can predict the behaviour of the PKS particle inside an auger reactor is developed using a Lagrangian approach through DEM modelling, that can be transformed into an equally precise model for predicting residence times.

6.5 Future research

This section propose particular recommendations for continuing with the research that has been developed so far.

6.5.1 Extending the applicability of the developed particle model

In this work, the developed particle model captured pyrolysis behaviour in terms of particle's internal temperature and product composition when compared with experimental data from literature. However, to extend the application of the model to other types of biomass or for other initial conditions, certain improvements could be done to the particle model:

The particle model presented in Chapter 3 was developed for biomass with moisture contents of $\simeq 10$ wt.% or less; however, if other types of biomass with higher moisture contents are to be considered, the particle model needs to be modified. Such modification depends also on the moisture content. For biomass with moisture contents below the fiber saturation point (near 30 wt.%) [232], a thermal model might be more adequate for describing water evaporation given that drying and reaction characteristic times would be of the same order [233]. In cases where moisture content surpasses the FSP, an evaporation model for capillary water might be more suitable for the particle model.

Similarly, the model could be expanded to include biomass with a high content of extractives. The particle model developed in Chapter 3 did not consider extractives as part of biomass components. The content of extractives could be addressed by considering a separate pyrolysis reaction for hydrophobic or hydrophilic extractives [49].

6.5.2 To associate the characteristics of more types of lignin-rich biomass undergoing pyrolysis to establish a general behaviour for lignin-rich biomass.

In Chapter 4, palm kernel shells and coffee husk were characterized in terms of elemental analysis, higher heating value, moisture and carbohydrates content. Only these few properties allowed to identify a correlation for HHV from the carbon content in biomass. Similarly, the analysis could be complemented with proximal analy-

sis and pyrolysis analysis for many other types of lignin-rich biomass.

The characterization properties and the pyrolysis behaviour of lignin-rich biomass can be used to establish correlations between easy-to-measure properties such as moisture content, fixed carbon, volatile matter and ashes, to predict pyrolysis kinetics in lignin-rich biomass. The determination of cellulose, hemicellulose and lignin content is also an equipment-intensive characterization procedure and to find a way to predict cellulose, hemicellulose and lignin from other properties will be particularly useful. Artificial Neural Networks could be one of the first alternatives for trying to find such correlations.

On the basis of the findings of the behaviour of PKS in pyrolysis, it would be useful to define a new kinetic model and mechanism of reaction for lignin-rich biomass given that traditional mechanisms do not represent the behaviour of this particular type of biomass.

6.5.3 Further work at a reactor level and multi-scale strategy

The validation of the multi-scale model is the first task to address in the future. Such validation would require a previous design of experiments to understand how the granular flow, the kinetic model and the heat transfer are operating simultaneously. In Chapter 5 it was possible to validate the granular flow and the kinetic model separately. However, more data need to be developed for the auger reactor in continuous operation and maybe even with other types of biomass besides PKS, so as to confirm that the proposed multi-scale modelling strategy could be applied for different types of biomass.

The next step will be to develop a multi-objective and multi-scale optimization strategy for pyrolysis. Most of the information available in literature related to economic or environmental outcomes from pyrolysis uses information from lumped models. Consequently, they could be limited in terms of estimating the true potential of pyrolysis as an alternative for providing energy, fuels and bulk chemicals in a profitable and environmental-friendly way. The information regarding multi-objective optimization strategies when particle and reactor levels are developed during pyrolysis modelling is limited. However, there are some previous works that consider input-output analysis for optimizing economic and environmental objectives. The in-

formation regarding improving social objectives during thermochemical processes is also limited [234, 235]. This will be the first step towards incorporating the developed high-lignin biomass pyrolysis into biorefineries.

6.5.4 Incorporation of the developed approach into the context of biorefineries

For incorporating the developed multi-scale model for lignin-rich pyrolysis into biorefineries, pre-treatment and refining stages need to be considered. The utilized feedstock needs to be treated so as to control the moisture content and the particle size [236]. Moreover, the products from pyrolysis need to be separated and upgraded, even considering catalytic processes, to produce high added-value chemicals.

In order to evaluate pyrolysis as one of the potential building blocks of a biorefinery, the developed pyrolysis process will be combined with pretreatment stages (drying, size reduction), competing technologies (transesterification, combustion, gasification, hydrothermal carbonization) and separation units for recovering products of interest.

The current work provides a glimpse of the capabilities of the particle model to include economic and environmental information. Therefore, further indicators need to be quantified. The estimation of the costs and revenue streams, as well as the environmental outcomes, associated with the operation of each unit, including pyrolysis, needs to be defined.

Publications that resulted from this work

The detail of the publications related with the content of this work are presented in the next lines.

Chico-Proano, Andres, Michelle Romero, A. Narváez C. Ricardo, Boris G. German, Daniel Rivadeneira, George Manos, Lazaros G. Papageorgiou, and Eric S. Fraga. 2022. “Combined Particle Model and Experimental Approach for Predicting Pyrolysis with Palm Kernel Shells.” *Computer Aided Chemical Engineering* 51: 343–48.

Chico-Proano, Andres, George Manos, Lazaros G Papageorgiou, and Eric S Fraga. 2021. “Heating Strategies in Cellulose Pyrolysis as an Alternative For Targeting Energy Efficient Product Distribution.” *Chemical Engineering Transactions* 86: 61–66.

Romero, Michelle, Boris German, Daniel Rivadeneira, Diego Chulde, Andres Chico Proano, Ricardo A.C. Narváez, and Javier Martínez Gómez. 2022. “Assessment of Pilot Scale Pyrolysis Gas Production as Fuel for Cogeneration.” *Chemical Engineering Transactions* 92 (January): 211–16.

Participation in conferences

WCCE11-11th World Congress of Chemical Engineering. 2023. Buenos Aires, Argentina. Oral presentation: Understanding the differences in behaviour between palm kernel shells and their structural components under pyrolysis conditions.

Congress on pyrolysis and co-generation. 2021. Quito, Ecuador (Online). Oral presentation: Pyrolysis mathematical modelling and applications focused on efficient product generation.

The 15th International Conference on Chemical and Process Engineering. 2021. Naples, Italy (Online). Oral presentation: Heating strategies in cellulose pyrolysis as an alternative for targeting energy efficient product distribution.

The 32nd European Symposium on Computer-Aided Process Engineering (ESCAPE-32). 2022. Toulouse, France. Combined particle model and experimental approach for predicting pyrolysis with palm kernel shells.

ChemEngDayUK2021. 2021. Bradford, UK (Online). Poster Presentation. Enhanced flexibility in biomass pyrolysis through heating strategies.

CPSE Annual Industrial Consortium Meeting. 2020. London, UK (Online). Poster presentation. Modelling cellulose pyrolysis at a particle scale for platform chemicals and fuels production.

UCL 3MT three minute thesis competition. 2019. London, UK. Flexible biomass pyrolysis through modelling and optimization.

Research stay

Visiting researcher at National Institute of Research in Energy and Geology of Ecuador, Quito, Ecuador (April 2021-June 2021). Advisor: Dr. Ricardo Narvaez Cueva.

Appendix A

Single thermally-thick biomass particle

A.1 Determination of temperature ranges for applying the ideal gas equation of state for the considered components in the model

A.1.1 Kinetic models used for describing pyrolysis

Two different kinetic models from literature are used to describe pyrolysis. The first one, also referred as lumped model, groups all the products under three categories: solid (char), condensibles (tar) and gases. The second one, also referred to as detailed reaction scheme, predicts the yield of each individual product associated to pyrolysis [25, 74].

A.1.1.1 Estimation of the specific heat at constant pressure

The variety of reactants, intermediate and final products involved in pyrolysis, requires different correlations for gaseous, liquid and solid species. Low pressure (0.1 MPa) and a working temperature between 200 and 1500 K are considered for estimating the required thermophysical properties. Such conditions guarantee an ideal behaviour in gaseous species. Such consideration is supported on the basis of the obtained values of the compressibility factor Z . The value of Z is determined from the generalized compressibility charts [156] using reduced properties. The reduced temperature T_r determined as $T_r = T/T_c$, the reduce volume V_r , determined as $V_r = V/V_c$ and the reduce pressure P_r defined as $P_r = P/P_c$, are calculated using critical properties T_c, V_c and P_c from literature [156]. The detail of the calculations of

A.1. Determination of temperature ranges for applying the ideal gas equation of state for the considered components

Z and the obtained values for the gaseous species involved in pyrolysis is presented in Appendix A.

For ideal gases, the specific heat is determined using correlations and data found in literature. The specific heat at constant pressure $Cp_{G,i}$ is determined with a temperature-dependent polynomial correlation defined by [237, 156]:

$$\frac{Cp_{G,i}}{R} = a_0 + a_1 T + a_2 T^2 + a_3 T^3 + a_4 T^4 \quad (\text{A.1})$$

In the previous equation, $Cp_{G,i}$ for a particular gas i considers the ideal gas constant R , empirical coefficients a and temperature T . Whenever the previously mentioned coefficients a_1, a_2, a_3, a_4 , are not found in literature, data from previous works for specific heat at different temperatures, within the pyrolysis temperature range (450-800 °C), were used to build a temperature-dependent polynomial function using nonlinear regression. The Minitab 19 statistical software was used to find a correlation between specific heat and temperature, as well as to determine the corresponding variance and residual plots. Finally, for substances whose specific heat is not available in literature for the pyrolysis temperature range, the Benson group additivity method is used and the contributions to the specific heat from each group, k_{add} of atoms were determined in accordance with Eq. A.2 [238, 156]. For this purpose, the number of k groups in the molecule, N_k , and the specific heat of each k group for a given T and Cp_k are used.

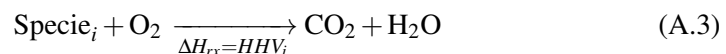
$$Cp_{G,i}(T) = \sum_{k=1}^{n \text{ groups}} N_k Cp_k(T) \quad (\text{A.2})$$

The mentioned additivity method gives a Cp value for each temperature. For this reason, a polynomial correlation for Cp_G and T was obtained through nonlinear regression. Whenever empirical coefficients were not available in literature, tabulated data of specific heat for different temperatures were used. Moreover, in such cases, nonlinear regression was employed to obtain a specific heat and temperature relationship. In the case of solid species (cellulose, hemicellulose, lignin and char), empirical correlations for determining the specific heat were retrieved from literature. The resulting correlations for Cp and T , for each one of the species involved in pyrolysis are presented in Table A.5 in Appendix A.

A.1. Determination of temperature ranges for applying the ideal gas equation of state for the considered components

A.1.1.2 Enthalpy of formation

The enthalpy of formation for pure species is retrieved from literature if available [156]. Whenever the enthalpy of formation of a particular pure or lumped species i is not available in the literature, the higher heating value HHV and the corresponding complete combustion reaction presented in Eq. A.3 are considered. The Hess law is applied then to determine the heat of formation of a particular species at standard conditions following Eq. A.4.



$$HHV_i = \sum_{i=1}^n (\hat{H}_{i,st}^0)_{\text{products}} - \sum_{i=1}^n (\hat{H}_{i,st}^0)_{\text{reactants}} \quad (\text{A.4})$$

The boiling temperature of tar from cellulose varies within a range. This is a result of the many components that could be found in tar. A previous work that assessed tar evaporation during pyrolysis from cellulose identified two different kinetic regimes: one corresponding with fast pyrolysis (high heating rates) and one corresponding with slow pyrolysis (low heating rates). Previous works have identified that the volatility of tars from pyrolysis are similar to the volatility of levoglucosan, one of the main components found in tar from cellulose pyrolysis [239]. Under such circumstances, the latent heat for tar vaporization could be considered to be 141 kJ mol⁻¹. For low heating rates (6°C min⁻¹), tar evaporation takes place in the 310-370 °C. The mentioned temperature range is a result of existing mass transfer limitations for tar evaporation during pyrolysis. A fraction of the produced tar remains in the solid phase and tar recovery in the gaseous phase can reach 76% at the mentioned temperature range. In general, for cellulose pyrolysis, char yields remain low (below 8%) [239]. The boiling points for cellulose ($T_{\text{Tar cell}}$) and levoglucosan-derived tars ($T_{\text{Tar levo}}$), in °C, can be estimated from pressure measurements in torr, using the empirical correlations detailed in equations A.5 and A.6.

$$\ln P_{\text{Tar cell}} = 40.289 - \frac{16948}{T_{\text{Tar cell}}} \quad (\text{A.5})$$

$$\ln P_{\text{Tar levo}} = 32.391 - \frac{14452}{T_{\text{Tar levo}}} \quad (\text{A.6})$$

A.1. Determination of temperature ranges for applying the ideal gas equation of state for the considered components

Within the lumped model, secondary reactions are included by considering tar cracking reactions. The lumped model reactions, kinetic parameters and energy-related information are detailed in Table A.1. The detailed kinetic reaction scheme developed by Ranzi et al. (2014) and modified by Anca-Couce (2012), also referred to as the RAC reaction scheme, is used in this work to describe pyrolysis from a detailed-component perspective. The mentioned RAC reaction scheme considers biomass as a mixture of cellulose, hemicellulose and lignin. Moreover, it includes intermediate species such as active cellulose (CELLA), active hemicellulose (HCEA) and different types of lignin. Secondary reactions and heating rates are taken into account by including heating rate-dependent charring factors for cellulose (X_{cell}), hemicellulose (X_{hcell}) and lignin (X_{lig}) [24, 25]. Moreover, intermediate gaseous species that remain trapped in the solid phase when formed are identified in this work as $G\{\}$. The mentioned species are summarized in Table A.2. The reactions considered in the RAC scheme are detailed in Table A.4. The present work incorporates water evaporation from biomass during pyrolysis by considering that such evaporation follows a first-order reaction [28, 29], as presented in Table 3.5.

Table A.1: Reactions, kinetic parameters and enthalpy of reaction for biomass pyrolysis considering lumped kinetic models [26].

No. Reaction	Reaction	A (s^{-1})	Ea ($J mol^{-1}$)	Δh ($J kg^{-1}$)
1	Biomass → Gas	$1.3 \cdot 10^8$	140300	150000
2	Biomass → Char	$2.0 \cdot 10^8$	133100	150000
3	Biomass → Tar	$1.1 \cdot 10^8$	121300	150000
4	Tar → Gas	$4.3 \cdot 10^8$	108000	-50000

Table A.2: Particular species considered for the stoichiometry of detailed reaction schemes [24, 25].

Identification	Specie	Observation
CELL	Cellulose	
CELLA	Active cellulose	
HAA	Hydroxyacetaldehyde	
GLYOX	Glyoxal	
HMFU	Hydroxymethylfurfural	

A.2. Detailed reaction scheme, RAC scheme, with the complete the reactions and compounds involved in pyrolysis.

Table A.2: (Continued.)

Identification	Specie	Observation
G{H2}	Hydrogen	Trapped in solid phase
G{H4}	Methane	Trapped in solid phase
LVG	Levoglucosan	
HCE	Hemicellulose	
AA (HW)	Acetic acid	For high molecular weight HCE
AA (SW)	Acetic acid	For low molecular weight HCE
HCEA1	Active cellulose	Type 1, intermediate
G{CO2}	Carbon dioxide	Trapped in solid phase
G{COH2}	Formaldehyde	Trapped in solid phase
G{CH3OH}	Methanol	Trapped in solid phase
G{CO}	Carbon monoxide	Trapped in solid phase
G{C2H4}	Ethylene	Trapped in solid phase
XYL	Xylan	
HCEA2	Active cellulose	Type 2, intermediate
LIG-C	Lignin	Lignin with -C radicals
LIG-CC	Active lignin	Intermediate from LIG-C
pCOUMARYL	p-coumaryl alcohol	
LIG-H	Lignin	Lignin with -H radicals
LIG-OH	Lignin	Lignin with -OH radicals
LIG	Lignin	
G{H2}	Hydrogen	Trapped in solid phase

A.2 Detailed reaction scheme, RAC scheme, with the complete the reactions and compounds involved in pyrolysis.

A.2. Detailed reaction scheme, RAC scheme, with the complete the reactions and compounds involved in pyrolysis

Table A.3: Detailed reaction scheme and kinetic parameters for biomass pyrolysis [27, 25].

		Reaction	A (s ⁻¹)	E_a (J/mol)	Δh (kJ/kg)
R1	Cell	\rightarrow CellA	$4.0 \cdot 10^{13}$	188370	150
R2	CellA	\rightarrow $(1 - x_{cell}) \cdot (0.45\text{HAA} + 0.2\text{GLYOX} + 0.3\text{C}_3\text{H}_6\text{O} + 0.25\text{HMFU} + 0.05\text{H}_2 + 0.31\text{CO} + 0.41\text{CO}_2 + 0.4\text{CH}_2\text{O} + 0.83\text{H}_2\text{O} + 0.02\text{HCOOH} + 0.15\text{CH}_3\text{OH} + 0.1\text{CH}_3\text{CHO}) + 0.05\text{G}\{\text{H}_2\} + 0.2\text{G}\{\text{CH}_4 + 0.61\text{CHAR}\} + x_{cell} \cdot (5.5\text{CHAR} + 4\text{H}_2\text{O} + 0.5\text{CO}_2 + \text{H}_2)$	$2.0 \cdot 10^6$	80000	150
R3	CellA	\rightarrow $(1 - x_{cell}) \cdot (\text{LVG/same as R2}) + x_{cell} \cdot (5.5\text{CHAR} + 4\text{H}_2\text{O} + 0.5\text{CO}_2, + \text{H}_2)$	4.0 T	41860	150
R4	HCE	\rightarrow $0.4\text{AA(HW)}/0.1\text{AA(SW)} + 0.58\text{HCEA1} + 0.42\text{HCEA2}$	$1.0 \cdot 10^{10}$	129770	
R5	HCEA1	\rightarrow $(1 - x_{hce}) \cdot (0.5\text{CO} + 0.5\text{CO}_2 + 0.325\text{CH}_4 + 0.8\text{CH}_2\text{O} + 0.1\text{CH}_3\text{OH} + 0.25\text{C}_2\text{H}_4 + 0.125\text{ETOH} + 0.025\text{H}_2\text{O} + 0.025\text{HCOOH} + 0.275\text{G}\{\text{CO}_2\} + 0.4\text{G}\{\text{COH}_2\} + 0.125\text{G}\{\text{H}_2\} + 0.45\text{G}\{\text{CH}_3\text{OH}\} + 0.875\text{CHAR}) + x_{hce} \cdot (4.5\text{CHAR} + 3\text{H}_2\text{O} + 0.5\text{CO} + \text{H}_2)$	$1.2 \cdot 10^9$	125580	
R6	HCEA1	\rightarrow $(1 - x_{hce}) \cdot (0.1\text{CO} + 0.8\text{CO}_2 + 0.3\text{CH}_2\text{O} + 0.25\text{H}_2\text{O} + 0.05\text{HCOOH} + 0.15\text{G}\{\text{H}_2\} + 0.15\text{G}\{\text{CO}\} + 1.2\text{G}\{\text{COH}_2\} + 0.2\text{G}\{\text{H}_2\} + 0.625\text{G}\{\text{CH}_4\} + 0.375\text{G}\{\text{C}_2\text{H}_4\} + 0.875\text{CHAR}) + x_{hce} \cdot (4.5\text{CHAR} + 3\text{H}_2\text{O} + 0.5\text{CO}_2 + \text{H}_2)$	0.15 T	33500	
R7	HCEA1	\rightarrow $(1 - x_{hce}) \cdot (\text{XYL /same as R5}) + x_{hce} \cdot (4.5\text{CHAR} + 3\text{H}_2\text{O} + 0.5\text{CO}_2 + \text{H}_2)$	3.0 T	46050	
R8	HCEA2	\rightarrow $(1 - x_{hce}) \cdot (0.2\text{HAA} + 0.175\text{CO} + 0.275\text{CO}_2 + 0.5\text{CH}_2\text{O} + 0.1\text{ETOH} + 0.2\text{H}_2\text{O} + 0.025\text{HCOOH} + 0.4\text{G}\{\text{CO}_2\} + 0.925\text{G}\{\text{COH}_2\} + 0.25\text{G}\{\text{CH}_4\} + 0.3\text{G}\{\text{CH}_3\text{OH}\} + 0.275\text{G}\{\text{C}_2\text{H}_4\} + \text{CHAR}) + x_{hce} \cdot (4.5\text{CHAR} + 3\text{H}_2\text{O} + 0.5\text{CO}_2 + \text{H}_2)$	$0.5 \cdot 10^{10}$	138140	
R9	LIG-C	\rightarrow $0.35\text{LIG-CC} + 0.1\text{pCOUMARYL} + 0.08\text{PHENOL} + 0.32\text{CO} + 0.3\text{CH}_2\text{O} + \text{H}_2\text{O} + 0.7\text{G}\{\text{CH}_2\} + 0.495\text{G}\{\text{CH}_4\} + 0.41\text{G}\{\text{C}_2\text{H}_4\} + 5.735\text{CHAR}$	$1.33 \cdot 10^{15}$	203020	
R10	LIG-H	\rightarrow $\text{LIG-OH} + 0.25\text{HAA} + 0.5\text{C}_3\text{H}_6\text{O} + 0.5\text{G}\{\text{C}_2\text{H}_4\}$	$0.67 \cdot 10^{13}$	156970	
R11	LIG-O	\rightarrow $\text{LIG-O} + \text{CO}_2$	$0.33 \cdot 10^9$	106740	
R12	LIG-CC	\rightarrow $(1 - x_{lig}) \cdot (0.35\text{HAA} + 0.3\text{pCOUMARYL} + 0.2\text{PHENOL} + 0.4\text{CO} + 0.65\text{CH}_4 + 0.6\text{C}_2\text{H}_4 + 0.7\text{H}_2\text{O} + 0.4\text{G}\{\text{CO}\} + \text{G}\{\text{COH}_2\} + 6.75\text{CHAR}) + x_{lig} \cdot (15\text{CHAR} + 4\text{H}_2\text{O} + 3\text{H}_2)$	$3.0 \cdot 10^7$	131860	
R13	LIG-OH	\rightarrow $(1 - x_{lig}) \cdot (\text{LIG} + 0.55\text{CO} + 0.05\text{CO}_2 + 0.1\text{CH}_4 + 0.6\text{CH}_3\text{OH} + 0.9\text{H}_2\text{O} + 0.05\text{HCOH} + 0.6\text{G}\{\text{CO}\} + 0.85\text{G}\{\text{COH}_2\} + 0.1\text{G}\{\text{H}_2\} + 0.35\text{CH}_4 + 0.3\text{G}\{\text{CH}_3\text{OH}\} + 0.2\text{G}\{\text{C}_2\text{H}_4\} + 5.735\text{CHAR})$	$1.0 \cdot 10^8$	125580	
R14	LIG	\rightarrow $(1 - x_{lig}) \cdot (\text{Synapaldehyde} + x_{lig} \cdot (10.5\text{CHAR} + 3\text{H}_2\text{O} + 0.5\text{CO}_2 + 3\text{H}_2))$	4.0 T	50200	
R15	LIG	\rightarrow $(1 - x_{lig}) \cdot (\text{LIG} + 0.55\text{CO} + 0.05\text{CO}_2 + 0.1\text{CH}_4 + 0.6\text{CH}_3\text{OH} + 0.9\text{H}_2\text{O} + 0.05\text{HCOH} + 0.6\text{G}\{\text{CO}\} + 0.45\text{G}\{\text{COH}_2\} + 0.5\text{G}\{\text{CH}_4\} + 0.4\text{G}\{\text{C}_2\text{H}_4\} + 4.15\text{CHAR})$	$0.40 \cdot 10^9$	125580	
R16	LIG	\rightarrow $(1 - x_{lig}) \cdot (\text{LIG} + 0.55\text{CO} + 0.05\text{CO}_2 + 0.1\text{CH}_4 + 0.6\text{CH}_3\text{OH} + 0.9\text{H}_2\text{O} + 0.05\text{HCOH} + 0.6\text{G}\{\text{CO}\} + 0.45\text{G}\{\text{COH}_2\} + 0.5\text{G}\{\text{CH}_4\} + 0.4\text{G}\{\text{C}_2\text{H}_4\} + 6\text{CHAR} + x_{lig} \cdot (10.5\text{CHAR} + 3\text{H}_2\text{O} + 0.5\text{CO}_2 + 3\text{H}_2)$	0.083 T	33500	
R17	G{CO ₂ }	\rightarrow CO_2	$1.0 \cdot 10^5$	100460	
R18	G{CO}	\rightarrow $(1 - x_{G\{\cdot\}}) \cdot \text{CO} + x_{G\{\cdot\}} \cdot (0.5\text{CHAR} + 0.5\text{CO}_2)$	$3.0 \cdot 10^{13}$	209300	
R19	G{COH ₂ }	\rightarrow $0.75\text{G2}\{\text{COH}_2\} + 0.25(\text{H}_2 + 0.5\text{CO} + 0.25\text{CO}_2 + 0.25\text{CHAR})$	$1.0 \cdot 10^6$	100460	
R20	G{H ₂ }	\rightarrow H_2	$1.0 \cdot 10^{12}$	313960	-50
R21	G{CH ₄ }	\rightarrow CH_4	$2.0 \cdot 10^{13}$	300000	-50
R22	G{CH ₃ OH}	\rightarrow $(1 - x_{G\{\cdot\}}) \cdot \text{CH}_3\text{OH} + x_{G\{\cdot\}} \cdot (\text{CHAR} + \text{H}_2\text{O} + \text{H}_2)$	$1.2 \cdot 10^{13}$	209300	
R23	G{C ₂ H ₄ }	\rightarrow $0.3\text{C}_2\text{H}_4 + 0.7(\text{CH}_4 + \text{CHAR})$	$1.0 \cdot 10^6$	100460	
R24	G2{COH ₂ }	\rightarrow $0.2\text{G3}\{\text{COH}_2\} + 0.8(\text{CO} + \text{H}_2)$	$1.5 \cdot 10^9$	209300	

A.2. Detailed reaction scheme, RAC scheme, with the complete the reactions and compounds involved in pyrolysis

Table A.4: Reactions for softwood biomass pyrolysis corresponding to the RAC reaction scheme [24, 25].

No.	Description
Reaction	
R1	CELL → CELLA
R2	CELLA → $(1 - gx_{cell}) \cdot (0.45\text{HAA} + 0.2\text{GLYOX}$ $+ 0.3\text{C}_3\text{H}_6\text{O} + 0.25\text{HMFU} + 0.05\text{H}_2 + 0.31\text{CO}$ $+ 0.41\text{CO}_2 + 0.4\text{CH}_2\text{O} + 0.15\text{CH}_3\text{OH} + 0.1\text{CH}_3\text{CHO}$ $+ 0.83\text{H}_2\text{O} + 0.02\text{HCOOH} + 0.05\text{G}\{\text{H}_2\} + 0.2\text{G}\{\text{CH}_4\}$ $+ 0.61\text{CHAR}) + gx_{cell} \cdot (5.5\text{CHAR} + 4\text{H}_2\text{O} + 0.5\text{CO}_2 + \text{H}_2)$
R3	CELLA → $(1 - gx_{cell}) \cdot (\text{LVG/same products R2})$ $+ gx_{cell} \cdot (5.5\text{CHAR} + 4\text{H}_2\text{O} + 0.5\text{CO}_2 + \text{H}_2)$
R4	HCE → $0.4\text{AA(HW)}/0.1\text{AA(SW)} + 0.58\text{HCEA1}$ $+ 0.42\text{HCEA2}$
R5	HCEA1 → $(1 - gx_{hce}) \cdot (0.5\text{CO} + 0.5\text{CO}_2 + 0.325\text{CH}_4$ $+ 0.8\text{CH}_2\text{O} + 0.1\text{CH}_3\text{OH} + 0.25\text{C}_2\text{H}_4 + 0.125\text{ETOH}$ $+ 0.025\text{H}_2\text{O} + 0.025\text{HCOOH} + 0.275\text{G}\{\text{CO}_2\}$ $+ 0.4\text{G}\{\text{COH}_2\} + 0.125\text{G}\{\text{H}_2\} + 0.45\text{G}\{\text{CH}_3\text{OH}\}$ $+ 0.875\text{CHAR}) + gx_{hce} \cdot (4.5\text{CHAR} + 3\text{H}_2\text{O} + 0.5\text{CO}_2 + \text{H}_2)$
R6	HCEA1 → $(1 - gx_{HCE}) \cdot (0.1\text{CO} + 0.8\text{CO}_2 + 0.3\text{CH}_2\text{O}$ $+ 0.25\text{H}_2\text{O} + 0.05\text{HCOOH} + 0.15\text{G}\{\text{H}_2\} + 0.15\text{G}\{\text{CO}\}$ $+ 1.2\text{G}\{\text{COH}_2\} + 0.2\text{G}\{\text{H}_2\} + 0.625\text{G}\{\text{CH}_4\}$ $+ 0.375\text{G}\{\text{C}_2\text{H}_4\} + 0.875\text{CHAR})$ $+ gx_{HCE} \cdot (4.5\text{CHAR} + 3\text{H}_2\text{O} + 0.5\text{CO}_2 + \text{H}_2)$
R7	HCEA1 → $(1 - gx_{HCE}) \cdot (\text{XYL /same as R5})$ $+ gx_{HCE} \cdot (4.5\text{CHAR} + 3\text{H}_2\text{O} + 0.5\text{CO}_2 + \text{H}_2)$

A.2. Detailed reaction scheme, RAC scheme, with the complete the reactions and compounds involved in pyrolysis

Table A.4: (Continued.)

No.	Description
Reaction	
R8	$\mathbf{HCEA2} \rightarrow (1 - gx_{HCE}) \cdot (0.2\text{HAA} + 0.175\text{CO}$ $+ 0.275\text{CO}_2 + 0.5\text{CH}_2\text{O} + 0.1\text{ETOH} + 0.2\text{H}_2\text{O}$ $+ 0.025\text{HCOOH} + 0.4\text{G}\{\text{CO}_2\} + 0.925\text{G}\{\text{COH}_2\}$ $+ 0.25\text{G}\{\text{CH}_4\} + 0.3\text{G}\{\text{CH}_3\text{OH}\} + 0.275\text{G}\{\text{C}_2\text{H}_4\}$ $+ \text{CHAR}) + gx_{HCE} \cdot (4.5\text{CHAR} + 3\text{H}_2\text{O} + 0.5\text{CO}_2 + \text{H}_2)$
R9	$\mathbf{LIG-C} \rightarrow 0.35\text{LIG-CC} + 0.1\text{pCOUMARYL}$ $+ 0.08\text{PHENOL} + 0.32\text{CO} + 0.3\text{CH}_2\text{O} + \text{H}_2\text{O} + 0.7\text{G}\{\text{CH}_2\}$ $+ 0.495\text{G}\{\text{CH}_4\} + 0.41\text{G}\{\text{C}_2\text{H}_4\} + 5.735\text{CHAR}$
R10	$\mathbf{LIG-H} \rightarrow \text{LIG-OH} + 0.25\text{HAA} + 0.5\text{C}_3\text{H}_6\text{O}$ $+ 0.5\text{G}\{\text{C}_2\text{H}_4\}$
R11	$\mathbf{LIG-O} \rightarrow \text{LIG-O} + \text{CO}_2$
R12	$\mathbf{LIG-CC} \rightarrow (1 - gx_{LIG}) \cdot (0.35\text{HAA} + 0.3\text{pCOUMARYL}$ $+ 0.2\text{PHENOL} + 0.4\text{CO} + 0.65\text{CH}_4 + 0.6\text{C}_2\text{H}_4$ $+ 0.7\text{H}_2\text{O} + 0.4\text{G}\{\text{CO}\} + \text{G}\{\text{COH}_2\} + 6.75\text{CHAR})$ $+ gx_{LIG} \cdot (15\text{CHAR} + 4\text{H}_2\text{O} + 3\text{H}_2)$
R13	$\mathbf{LIG-OH} \rightarrow \text{LIG} + 0.55\text{CO} + 0.05\text{CO}_2 + 0.1\text{CH}_4$ $+ 0.6\text{CH}_3\text{OH} + 0.9\text{H}_2\text{O} + 0.05\text{HCOH} + 0.6\text{G}\{\text{CO}\}$ $+ 0.85\text{G}\{\text{COH}_2\} + 0.1\text{G}\{\text{H}_2\} + 0.35\text{CH}_4$ $+ 0.3\text{G}\{\text{CH}_3\text{OH}\} + 0.2\text{G}\{\text{C}_2\text{H}_4\} + 5.735\text{CHAR}$
R14	$\mathbf{LIG} \rightarrow (1 - x_{LIG}) \cdot \text{Synapaldehyde}$ $+ x_{LIG} \cdot (10.5\text{CHAR} + 3\text{H}_2\text{O} + 0.5\text{CO}_2 + 3\text{H}_2)$

A.2. Detailed reaction scheme, RAC scheme, with the complete the reactions and compounds involved in pyrolysis

Table A.4: (Continued.)

No.	Description
Reaction	
R15	LIG $\rightarrow (1 - x_{LIG}) \cdot (0.2\text{C}_3\text{H}_6\text{O} + \text{CO} + 0.2\text{CH}_4 + 0.2\text{CH}_2\text{O} + 0.4\text{CH}_3\text{OH} + 0.2\text{CH}_3\text{CHO} + 0.95\text{H}_2\text{O} + 0.05\text{HCOOH} + 0.45\text{G}\{\text{CO}\} + 0.5\text{G}\{\text{COH}_2\} + 0.4\{\text{CH}_4\} + 0.65\text{G}\{\text{C}_2\text{H}_4\} + 4.15\text{CHAR})$
R16	LIG $\rightarrow (1 - x_{LIG}) \cdot (0.4\text{CO} + 0.2\text{CH}_4 + 0.4\text{CH}_2\text{O} + 0.6\text{H}_2\text{O} + 0.2\text{G}\{\text{CO}\} + 2\text{G}\{\text{COH}_2\} + 0.4\{\text{CH}_4\} + 0.4\{\text{CH}_3\text{OH}\} + 0.5\text{G}\{\text{C}_2\text{H}_4\} + 6\text{CHAR} + x_{LIG} \cdot (10.5\text{CHAR} + 3\text{H}_2\text{O} + 0.5\text{CO}_2 + 3\text{H}_2)$
R17	G{CO₂} $\rightarrow \text{CO}_2$
R18	G{CO} $\rightarrow (1 - x_{G\{\}}) \cdot \text{CO} + x_{G\{\}} \cdot (0.5\text{CHAR} + 0.5\text{CO}_2)$
R19	G{COH₂} $\rightarrow 0.75\text{G2}\{\text{COH}_2\} + 0.25(\text{H}_2 + 0.5\text{CO} + 0.25\text{CO}_2 + 0.25\text{CHAR})$
R20	G{H₂} $\rightarrow \text{H}_2$
R21	G{CH₄} $\rightarrow \text{CH}_4$
R22	G{CH₃OH} $\rightarrow (1 - x_{G\{\}}) \cdot \text{CH}_3\text{OH} + x_{G\{\}} \cdot (\text{CHAR} + \text{H}_2\text{O} + \text{H}_2)$
R23	G{C₂H₄} $\rightarrow 0.3\text{C}_2\text{H}_4 + 0.7(\text{CH}_4 + \text{CHAR})$
R24	G{COH₂} $\rightarrow 0.2\text{G3}\{\text{COH}_2\} + 0.8(\text{CO} + \text{H}_2)$

A.3 Estimation of specific heat at constant pressure for developing the particle model

Table A.5: Correlations for estimating specific heat for different species involved in pyrolysis in $\text{J K}^{-1} \text{kg}^{-1}$.

Component	Detailed species		Source
	Correlation		
Cellulose	$C_p = 970 + 5.13(T - 273)$		[240]
Active cellulose	$C_p = 970 + 5.13(T - 273)$		[240]
HAA	$C_p = -2.3025 \cdot 10^{-5}T^2 + 0.06266T + 29.3647$		[156]
GLYOX	$C_p = 2 \cdot 10^{-8}T^3 + 1 \cdot 10^{-4}T^2 + 0.1811T + 16.564$		[241]
Acetone	$C_p = -9 \cdot 10^{-5}T^2 + 0.2923T + 40.961$		[242]
HMFU	$C_p = -2.3025 \cdot 10^{-4}T^2 + 0.5374T - 5.2093$		[156]
Hydrogen	$C_p = 2 \cdot 10^{-6}T^2 - 0.0014T + 29.358$		[243]
Carbon monoxide	$C_p = (31.258 - 0.0168T + 4 \cdot 10^{-5}T^2 - 3 \cdot 10^{-8}T^3 + 7 \cdot 10^{-12}T^4)R$		[243]
Carbon dioxide	$C_p = (3.259 + 1.356 \cdot 10^{-3}T + 1.502 \cdot 10^{-5}T^2 - 2.374 \cdot 10^{-8}T^3 + 1.056 \cdot 10^{-11}T^4)R$		[243]
Formaldehyde	$C_p = (4.174 - 6.986 \cdot 10^{-3}T + 4.211 \cdot 10^{-3}T^2 - 4.443 \cdot 10^{-8}T^3 + 1.535 \cdot 10^{-11}T^4)R$		[243]
Methanol	$C_p = (4.174 - 6.986 \cdot 10^{-3}T + 4.211 \cdot 10^{-5}T^2 - 4.443 \cdot 10^{-8}T^3 + 1.535 \cdot 10^{-11}T^4)R$		[243]

Table A.5: (Continued.)

Component	Correlation	Source
Acetaldehyde	$C_p = (4.174 - 6.986 \cdot 10^{-3}T + 4.211 \cdot 10^{-5}T^2 - 4.443 \cdot 10^{-8}T^3 + 1.535 \cdot 10^{-11}T^4)R$	[243]
Water	$C_p = (4.395 - 4.186 \cdot 10^{-3}T + 1.405 \cdot 10^{-5}T^2 - 1.564 \cdot 10^8T^3 + 0.632 \cdot 10^{-11}T^4)R$	[243]
Formic acid	$C_p = (3.809 + 1.568 \cdot 10^{-3}T + 3.587 \cdot 10^{-5}T^2 - 4.410 \cdot 10^{-8}T^3 + 1.672 \cdot 10^{-11}T^4)R$	[243]
$G\{H_2\}$	$C_p = 2 \cdot 10^{-6}T^2 - 0.0014T + 29.358$	[243]
$G\{CH_4\}$	$C_p = (4.568 - 8.975 \cdot 10^{-3}T + 3.631 \cdot 10^{-5}T^2 - 3.407 \cdot 10^8T^3 + 1.091 \cdot 10^{-11}T^4)R$	[243]
Char	$C_p = 0.91 + 3.49 \cdot 10^3T - 1.24 \cdot 10^6T^2 - 4.43 \cdot 10^9T^3 + 2.63 \cdot 10^{-12}T^4$	[243]
LVG	$C_p = 2.796 + 0.766(T) - 4.9 \cdot 10^{-4}T^2 + 1 \cdot 10^7T^3$	[244]
Lumped species		
Component	Correlation	Source
Biomass	$C_p = 1500 + T$	[26]
Gas	$C_p = 770 + 0.629T - 1.91 \cdot 10^{-4}T^2$	[26]
Tar	$C_p = -100 + 4.4T - 1.57 \cdot 10^{-3}T^2$	[26]

Char	$C_p = 808.9 + 0.93T$	[26]
------	-----------------------	------

Appendix B

Characterization and pyrolysis kinetic modeling of lignin-rich biomass

B.1 Materials

The properties of the cellulose, hemicellulose and lignin used in this work to prepare a synthetic mixture that resembles PKS are presented in Figure B.1 and tables B.1, B.2 and B.3.

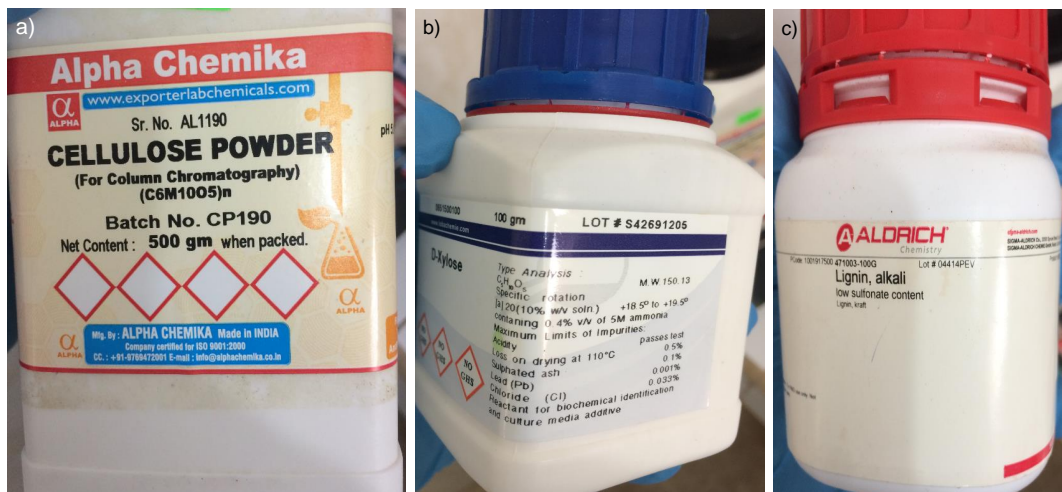


Figure B.1: Cellulose a), D-xylose b) and Lignin c) used for preparing the synthetic mixture to resemble PKS.

B.1.1 Sample preparation

The palm kernel shells (PKS) used for this study were collected, sampled and quartered following the BS EN 18135:2017 standard. Figure B.2 show, in a general way, the followed sampling and quartering procedure. When size reduction was required, the

Table B.1: Cellulose properties provided by the manufacturer [32].

Property	Specification
Type	For Column Chromatography
Presentation	Crystalline powder
pH	5.0-7.0
CAS Number	9004-34-6
Manufacturer	Alpha Chemika

Table B.2: D-Xylose properties provided by the manufacturer [33].

Property	Specification
Molecular weight [g/mol]	150.13
Presentation	Crystalline powder
Loss on drying [%]	<0.5
Sulphated ash [%]	<0.1
CAS Number	58-86-6
Manufacturer	LOBA Chemie

PKS were processed with the blade mill presented in Figure B.3.

B.1.2 PKS bulk and apparent density

PKS bulk density of the PKS as received (wet basis) is determined in accordance with the BS EN 17828:2015 standard. For this purpose, a cylindrical container of constant transversal area is used. Moreover, the volume of the container is measured by filling the container with water from a graduated beaker and the weight of the PKS was determined by gravimetry, using a 3 kg capacity scale with a precision of 0.01 g. The bulk density of the PKS as received is calculated following Eq. B.1. The detail of the measurements for the determination of the bulk density are presented in Table B.4.

Table B.3: Lignin properties provided by the manufacturer [34].

Property	Specification
Color	Brown to black
Presentation	Powder/crystals
Carbon content [%]	47.0-51.0
Sulfur content [%]	<3.6
pH	10.0-11.0
CAS Number	8068-05-1
Manufacturer	SIGMA-ALDRICH



Figure B.2: Palm kernel shells sampling before characterization and thermal analysis.



Figure B.3: Cyclone blade mill used for palm kernel shells size reduction.

$$\rho_{\text{bulk}} = m_2 - m_1 V_{\text{container}} \quad (\text{B.1})$$

Where:

Table B.4: Bulk density measurements for PKS

Measurement	$(m_2 - m_1)$ [kg]	Volume [m ³]	Density [kg m ⁻³]
M1	1.964	$3.642 \cdot 10^{-3}$	539.303
M2	1.958	$3.645 \cdot 10^{-3}$	537.114
M3	1.947	$3.642 \cdot 10^{-3}$	534.739
M4	1.950	$3.645 \cdot 10^{-3}$	534.988
		Average	536.536
		STD	2.130

Table B.5: Density for distilled water in g cm³ at different temperatures [16].

T [°C]	0	0.1	0.2	0.3	0.4	0.5	0.6	0.7	0.8	0.9
18	0.99859	0.99858	0.99856	0.99854	0.99852	0.99850	0.99848	0.99846	0.99844	0.99842
19	0.99840	0.99838	0.99836	0.99835	0.99833	0.99831	0.99828	0.99826	0.99824	0.99822
20	0.99820	0.99818	0.99816	0.99814	0.99812	0.99810	0.99808	0.99806	0.99803	0.99801
21	0.99799	0.99797	0.99795	0.99793	0.99790	0.99788	0.99786	0.99784	0.99781	0.99779
22	0.99777	0.99775	0.99772	0.99770	0.99768	0.99765	0.99763	0.99761	0.99758	0.99756

ρ_{bulk} = bulk density in kg m⁻³.

m_2 = mass of the filled container in kg.

m_1 = mass of the empty container in kg.

$V_{\text{container}}$ = mass of the filled container in kg.

The determination of the apparent density of PKS, ρ_{PKS} , considers three different samples for its determination. Distilled water is used as reference fluid. The temperature of the distilled water (T) is measured in each analysis with an alcohol thermometer. The density of the distilled water for each registered temperature, ρ_L , is obtained from Table B.5. Similarly, for a given analysis temperature (T), the air density (ρ_{air}) is calculated assuming ideal behaviour. The registered weights for PKS in air, $m_{PKS, \text{air}}$, and in the water $m_{PKS, L}$, are presented in Table B.6. As previously mentioned in Chapter 4, the apparent density of the PKS is determined with Eq. B.2.

$$\rho_{PKS} = \frac{m_{PKS, \text{air}}}{m_{PKS, \text{air}} - m_{PKS, L}} (\rho_{\text{air}} - \rho_L) + \rho_L \quad (\text{B.2})$$

Table B.6: Measurements and calculationS of PKS apparent density

	$m_{PKS,air}$ [kg]	$m_{PKS,L}$ [kg]	T [°C]	ρ_L [kg m ⁻³]	ρ_{air} [kg m ⁻³]	ρ_{PKS} [kg m ⁻³]
Sample 1	$1.047 \cdot 10^{-3}$	$0.232 \cdot 10^{-3}$	20.6	998.110	2.476	1281.530
Sample 2	$0.855 \cdot 10^{-3}$	$0.199 \cdot 10^{-3}$	20.6	998.110	2.476	1300.139
Sample 3	$0.947 \cdot 10^{-3}$	$0.208 \cdot 10^{-3}$	20.6	998.11	2.476	1278.343
					Average	1286.671
					STD	11.773

B.1.3 Particle size distribution

B.1.3.1 Measurements

The measurements for the weight % of particles that are retained in each sieve, as well as the cumulative weight % for each sieve seize, are reported in this section, in accordance with the BS EN 17827-1:2016 standard. Each one of the three samples' particle distributions are characterized, and an average particle size d_{50} is also computed among these samples. The share of retained mass at every sieve size is determined with Eq. B.3, whereas the cumulative share is determined following Eq. B.4.

$$\text{share}_i = \left(\frac{w_{\text{fraction}, i}}{w_{\text{total}}} \right) \cdot 100 \quad (\text{B.3})$$

$$\text{cumulative share}_i = \sum_{n=1}^i \text{share}_i \quad (\text{B.4})$$

Where:

$w_{\text{fraction}, i}$ = percentage of retained weight in fraction/size i [%].

$w_{\text{fraction}, i}$ = weight retained in fraction/size i [kg].

w_{total} = total sample weight used in the analysis [kg].

cumulative share $_i$ = cumulative retained shares up to sieve size/fraction i .

i = size fraction or sieve size.

n = number of size fraction or sieve size.

The equipment and sieves used for the particle size distribution characterization



Figure B.4: Vibratory sieve shaker and sieves of different size used for PKS size distribution determination.

Table B.7: Results of the particle size distribution for sample 1 of PKS

Fraction	Sieve [mm] [mm]	Sample mass $\cdot 10^{-3}$ [kg]	Share [%]	Cumulative share [%]
1	<2.00	5.60	1.02	1.02
2	2.00	5.30	0.96	1.98
3	2.36	26.80	4.87	6.86
4	3.35	66.70	12.13	18.99
5	4.75	173.00	31.47	50.46
6	6.68	178.00	32.38	82.83
7	9.5	87.50	15.91	98.75
8	12.5	6.90	1.26	100.00
Total mass		549.80		

are presented in Figure B.4. The measurements for the three analyzed samples are presented in tables B.7, B.8 and B.9.

B.1.3.2 Calculations

The particle size calculation corresponding to the 50%(*wt.*) and 80%(*wt.*) of cumulative mass passed in the sieves was performed following Eq. 4.2, and the results are presented in Table B.10 and Table B.11.

Table B.8: Results of the particle size distribution for sample 2 of PKS

Fraction	Sieve [mm]	Sample mass $\cdot 10^{-3}$ [kg]	Share [%]	Cumulative share [%]
1	<2.00	5.70	1.04	1.04
2	2.00	5.30	0.96	2.00
3	2.36	26.90	4.90	6.90
4	3.35	65.90	11.99	18.89
5	4.75	171.10	31.14	50.03
6	6.68	181.00	32.94	82.97
7	9.5	86.40	15.72	98.69
8	12.5	7.20	1.31	100.00
Total mass		549.50		

Table B.9: Results of the particle size distribution for sample 3 of PKS

Fraction	Sieve [mm]	Sample mass $\cdot 10^{-3}$ [kg]	Share [%]	Cumulative share [%]
1	<2.00	5.70	1.04	1.04
2	2.00	5.30	0.96	2.00
3	2.36	27.00	4.91	6.92
4	3.35	65.80	11.98	18.89
5	4.75	171.40	31.20	50.09
6	6.68	181.40	33.02	83.11
7	9.5	86.60	15.76	98.87
8	12.5	6.20	1.13	100.00
Total mass		549.40		

Table B.10: Results of calculation of d_{50} for three samples of PKS

Sample	C3 [mm]	C4 [mm]	S3 [%]	S4 [%]	d_{50} [mm]
1	3.35	4.75	18.99	54.46	4.73
2	3.35	4.75	18.89	50.03	4.75
3	3.35	4.75	18.89	50.09	4.75
			Average	4.74	
			STD	0.01	

Table B.11: Results of calculation of d_{80} for three samples of PKS

Sample	C3 [mm]	C4 [mm]	S3 [%]	S4 [%]	d_{80} [mm]
1	3.35	4.75	18.99	54.46	4.73
2	3.35	4.75	18.89	50.03	4.75
3	3.35	4.75	18.89	50.09	4.75
			Average	4.74	
			STD	0.01	

**Figure B.5:** Digital dry oven used for moisture content determination.

B.1.4 Proximal analysis

B.1.4.1 Moisture content

The moisture content analysis is undertaken in a Memmert digital dry oven, as presented in Figure B.5. The details of the measurements are presented in Table B.12.

B.1.4.2 Volatile matter content

The volatile matter content analysis is undertaken in a F48018 Thermo Scientific digital furnace, as presented in Figure B.6. The details of the measurements are presented in Table B.13.

Table B.12: Moisture measurements

	m₁ Empty tray [g]	m₂ Cold tray+sample [g]	m₃ Hot tray+sample [g]	m₄ Cold reference tray [g]	m₅ Hot reference tray [g]	Moisture wt.%
Sample 1	7.92	308.02	276.09	7.94	7.91	10.63
Sample 2	8.07	308.36	276.63	7.94	7.91	10.56
Sample 3	8.00	308.12	276.01	7.94	7.91	10.69
						Average 10.63 ± 0.07

**Figure B.6:** Furnace used for volatile matter determination.

B.1.4.3 Ash content

The ash content analysis is undertaken in a F48018 Thermo Scientific digital furnace, similar to the one described previously for volatile matter determination. The details of the measurements are presented in Table B.14.

B.1.5 X-Ray Diffraction characterization

The PANalytical AERIS XRD analyzer, its sampler and sample holder are presented in Figure B.7. The scanning in the XRD analysis provided 4141 data points,

Table B.13: Volatile matter determination measurements

	m₁ Empty crucible [g]	m₂ Cold sample+crucible [g]	m₃ Hot sample+crucible [g]	Moisture [%]	Volatile [%]
Sample 1	7.92	308.02	276.09	7.94	7.91
Sample 2	8.07	308.36	276.63	7.94	7.91
Sample 3	8.00	308.12	276.01	7.94	7.91
Average 77.18±0.08					

Table B.14: Ash content determination measurements

	m₁ Empty dish [g]	m₂ Dish+sample [g]	m₃ Dish+ashes [g]	Moisture [%]	Ash content [%]
Sample 1	25.12	26.12	25.14	7.42	2.40
Sample 2	23.87	24.87	23.89	7.42	2.12
Sample 3	24.09	25.09	24.12	7.42	2.42
Average					2.31 ± 0.17

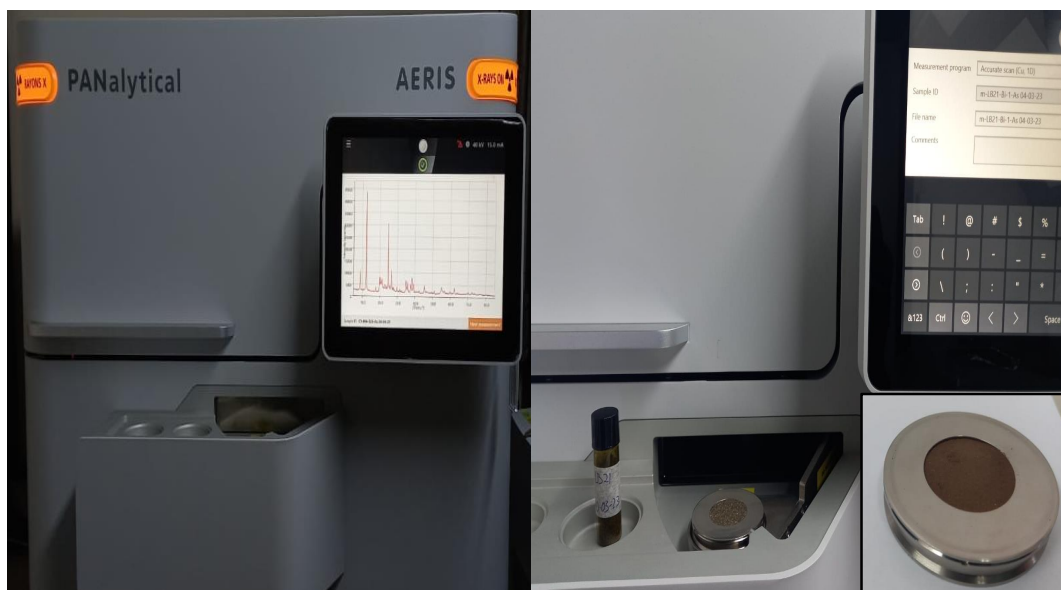
both for the PKS and for the synthetic mixture; therefore, the measurements are uploaded in a repository.

- PKS XRD data:

https://github.com/AndresCh2018/PhD_combined_multi_scale_modelling_biomass/blob/main/XRD_palm_kernel_shells.csv

- Synthetic mixture XRD data:

https://github.com/AndresCh2018/PhD_combined_multi_scale_modelling_biomass/blob/main/XRD_synthetic_mixture.csv

**Figure B.7:** XRD equipment, sampler and sample holder.

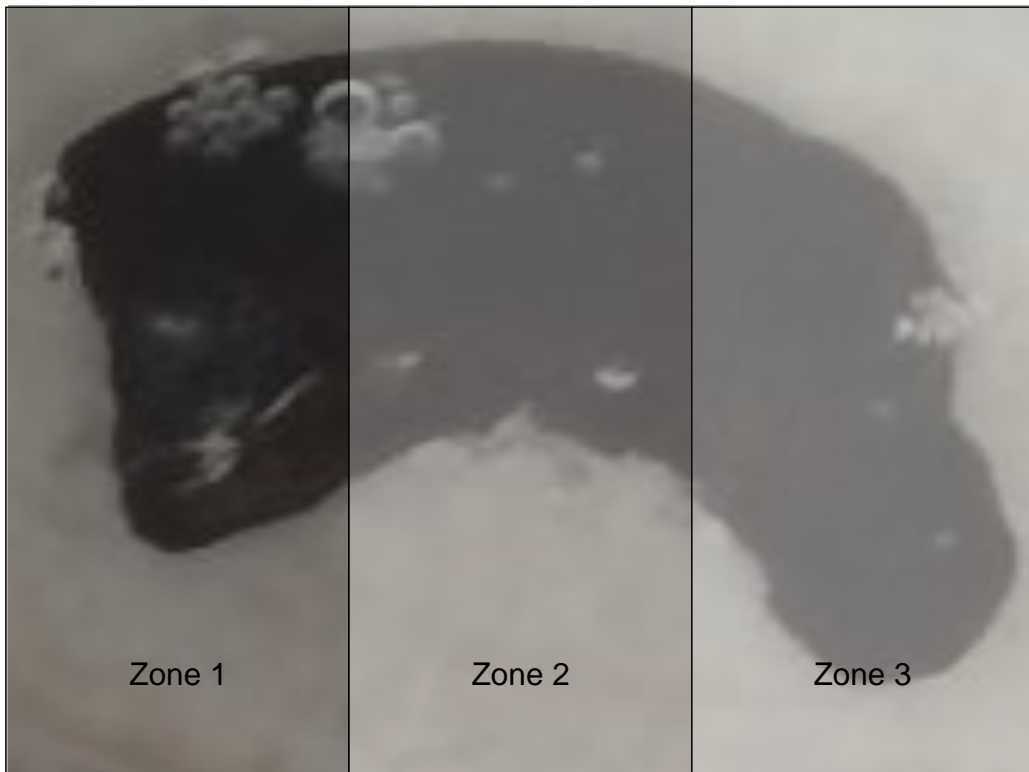


Figure B.8: PKS zones studied in the microscopy analysis.

B.1.6 Microscopy

The zones in which PKS samples are devided for their analysis under the microscope is presented in Figure B.8. The compiled photographs for each zone, with and without Toluidine blue are presented in this section.

B.1.7 Extractives determination and quantification

The equipment used for the determination of moisture content in milled PKS is presented in Figure B.21. Similarly, the results from the determination of moisture content in the milled PKS are presented in Table B.15. The measurements and calculations for determining water-soluble and ethanol-soluble extractives in PKS samples are detailed in Tables B.16 and B.17. The relative percent difference (RPD), the root mean square deviation (RMS) and the standard deviation (σ) between the two analyzed samples (X_1 and X_2) is determined in accordance with the NREL/TP-510-42619 technical procedure, as presented in equations B.5, B.6 and B.7. For this purpose, the mean value of the mentioned samples (X_{mean}), the number of samples (n) and each individual measurement (X_i) are considered. The corresponding measurements and

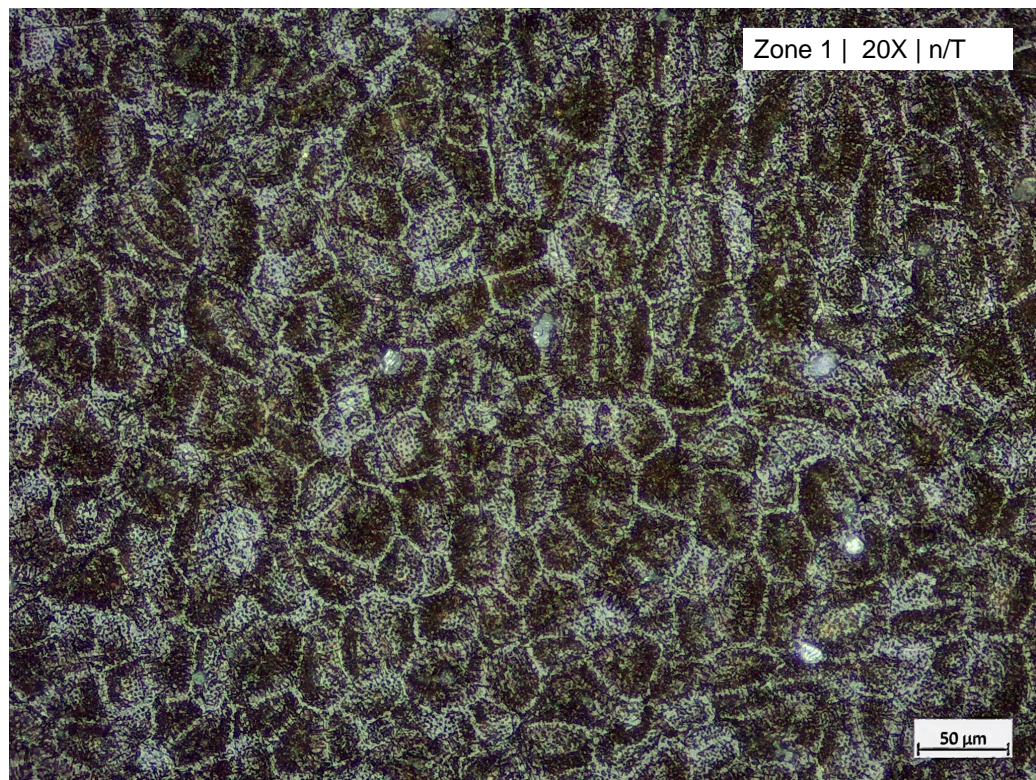


Figure B.9: Compiled microscopy of PKS, zone 1 without Toluidine.

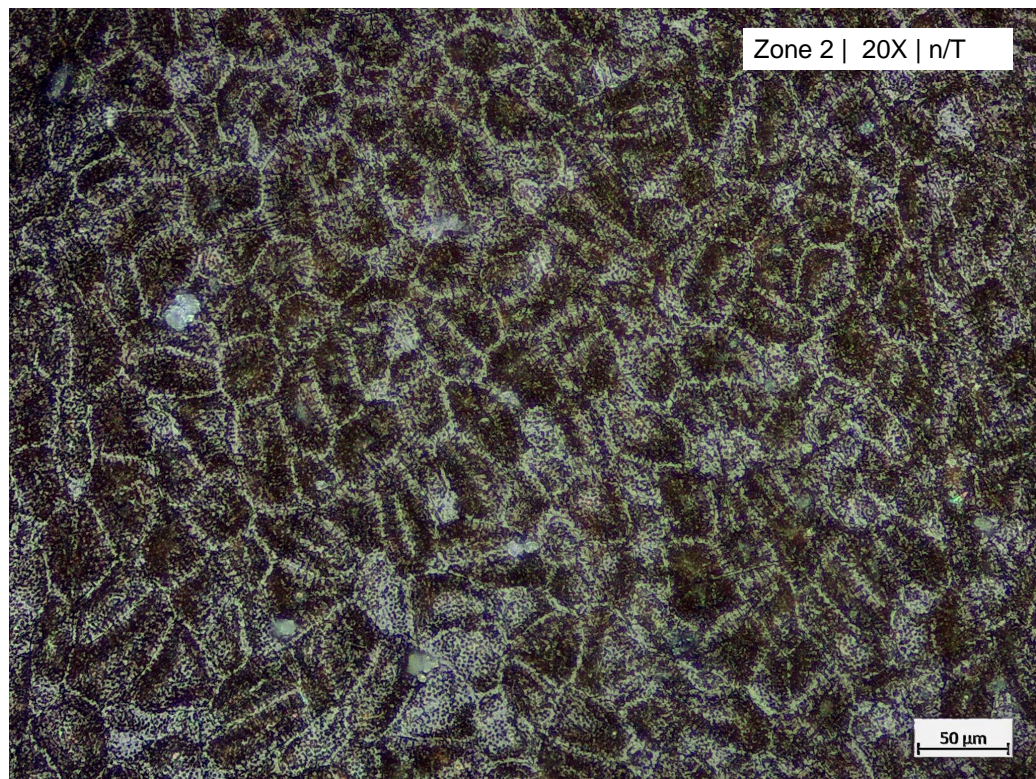


Figure B.10: Compiled microscopy of PKS, zone 2 without Toluidine.

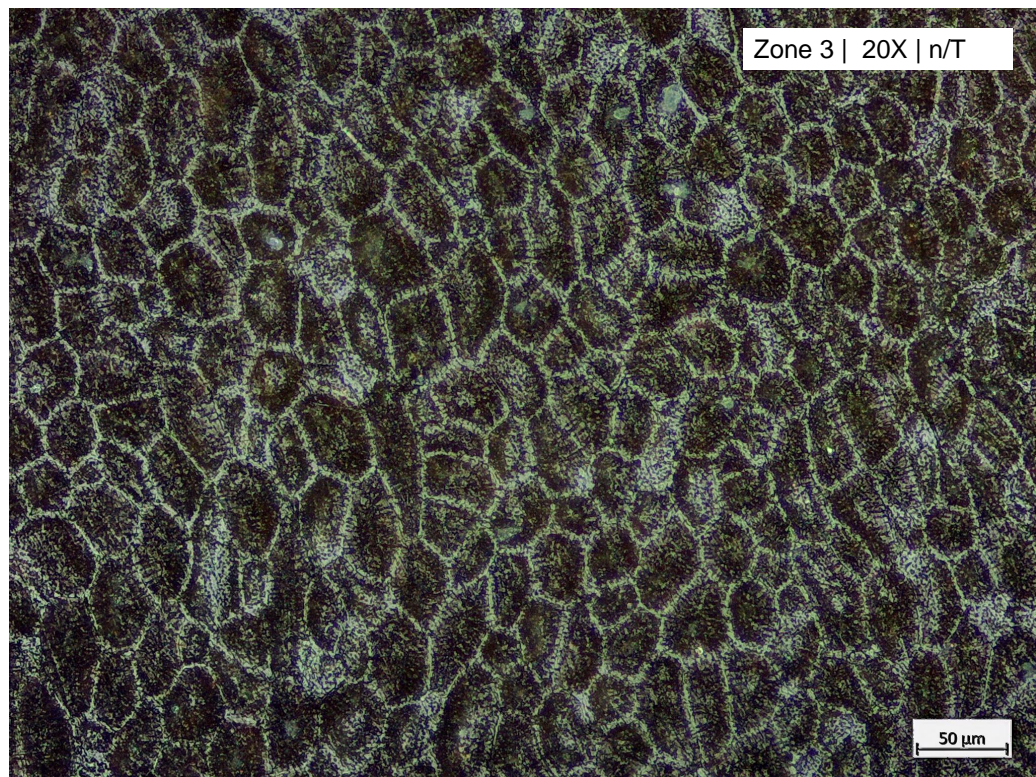


Figure B.11: Compiled microscopy of PKS, zone 3 without Toluidine.

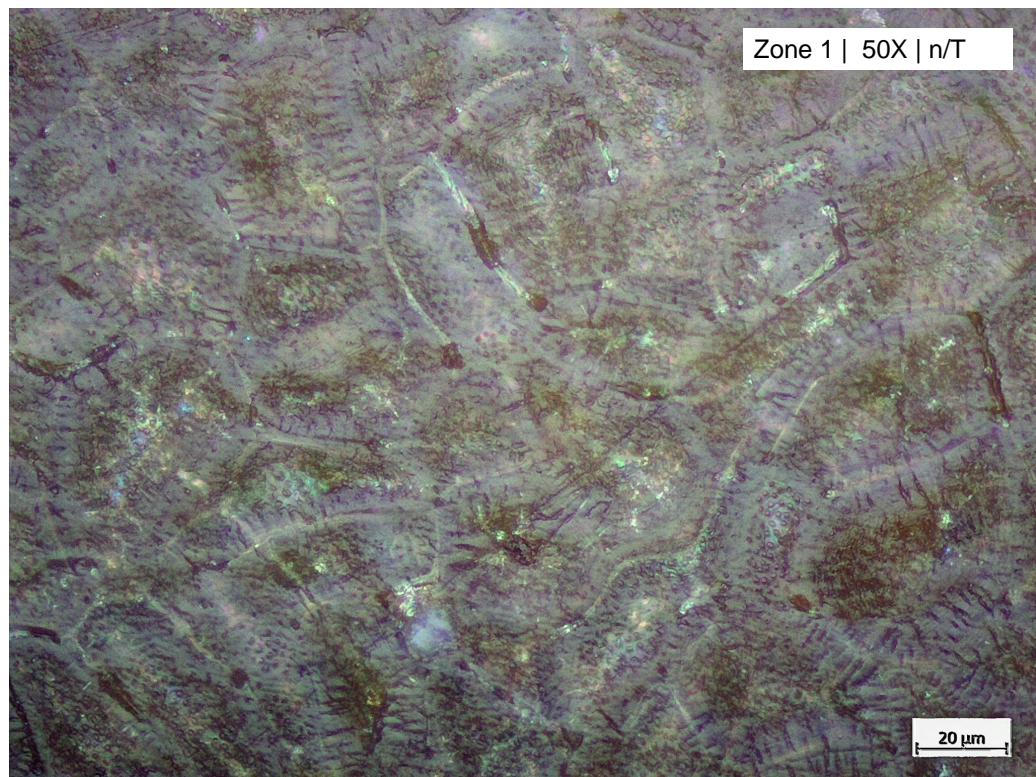


Figure B.12: Compiled microscopy of PKS, zone 1 without Toluidine.

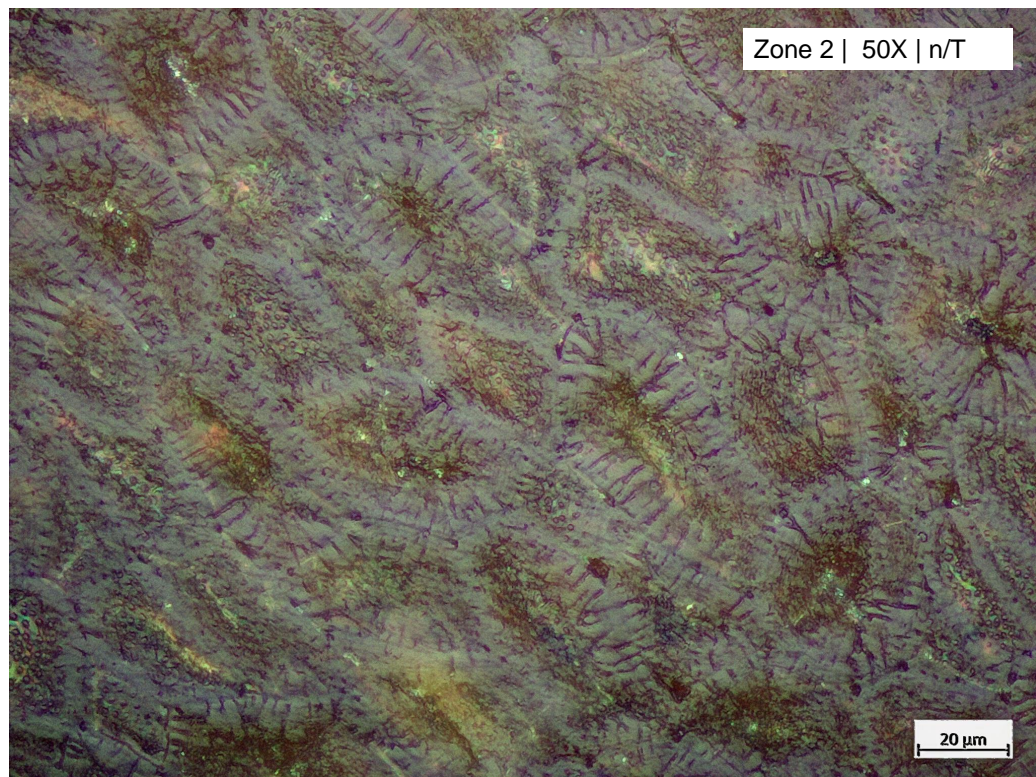


Figure B.13: Compiled microscopy of PKS, zone 2 without Toluidine.

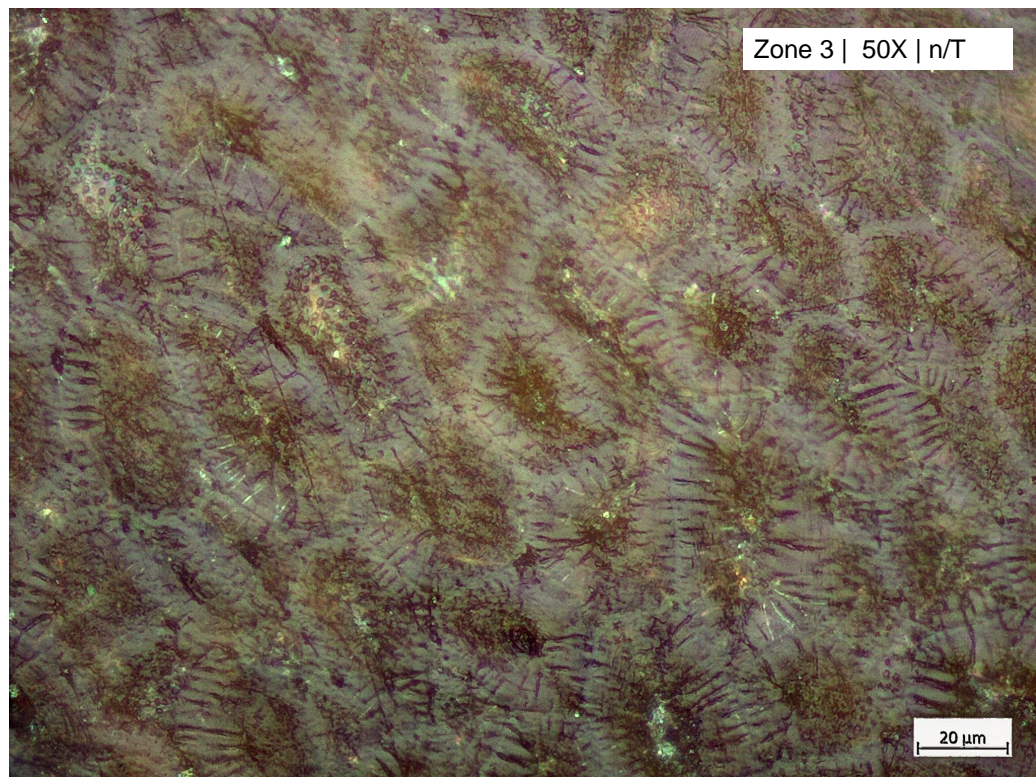


Figure B.14: Compiled microscopy of PKS, zone 3 without Toluidine.

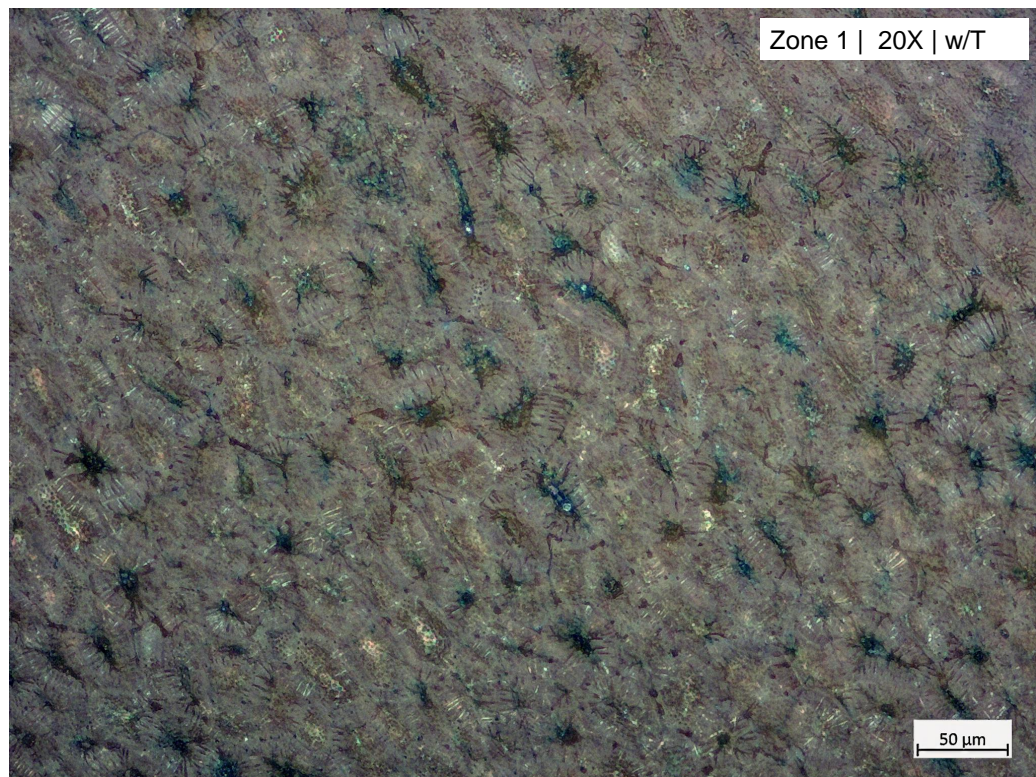


Figure B.15: Compiled microscopy of PKS, zone 1 with Toluidine.

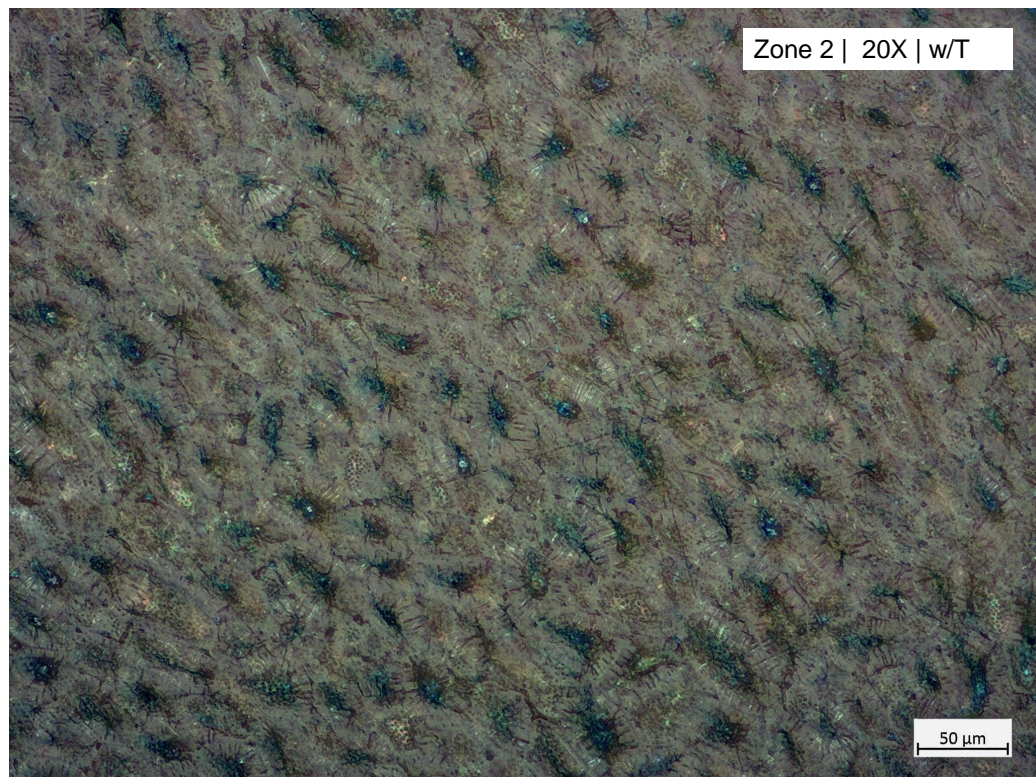


Figure B.16: Compiled microscopy of PKS, zone 2 with Toluidine.



Figure B.17: Compiled microscopy of PKS, zone 3 with Toluidine.

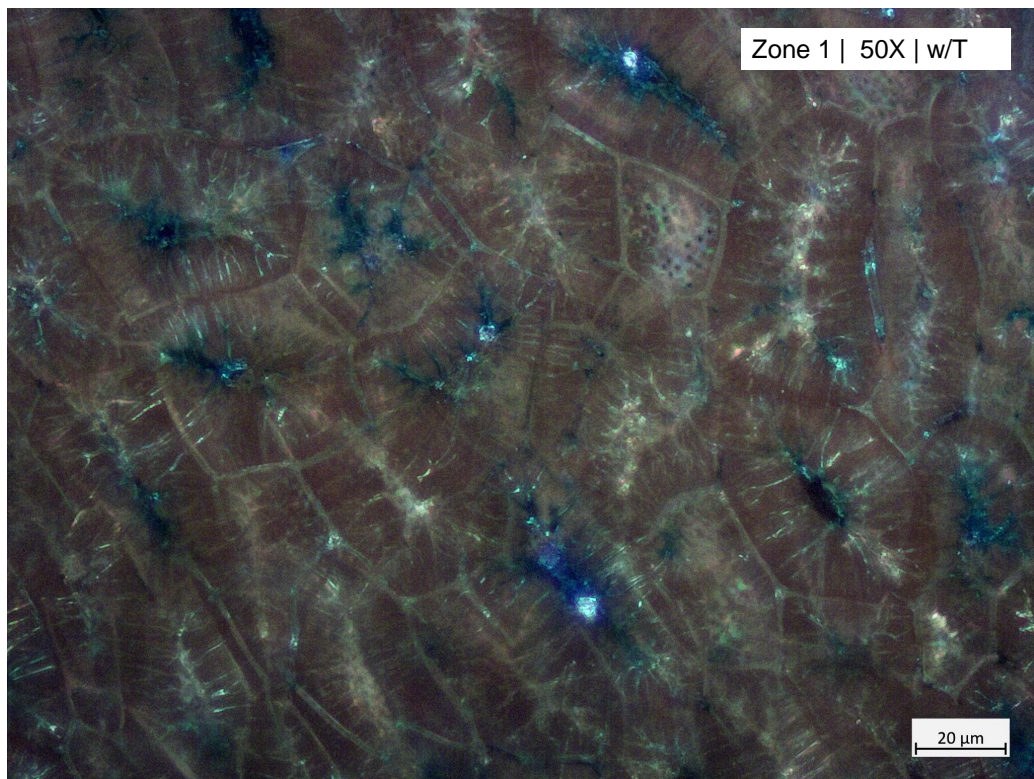


Figure B.18: Compiled microscopy of PKS, zone 1 with Toluidine.

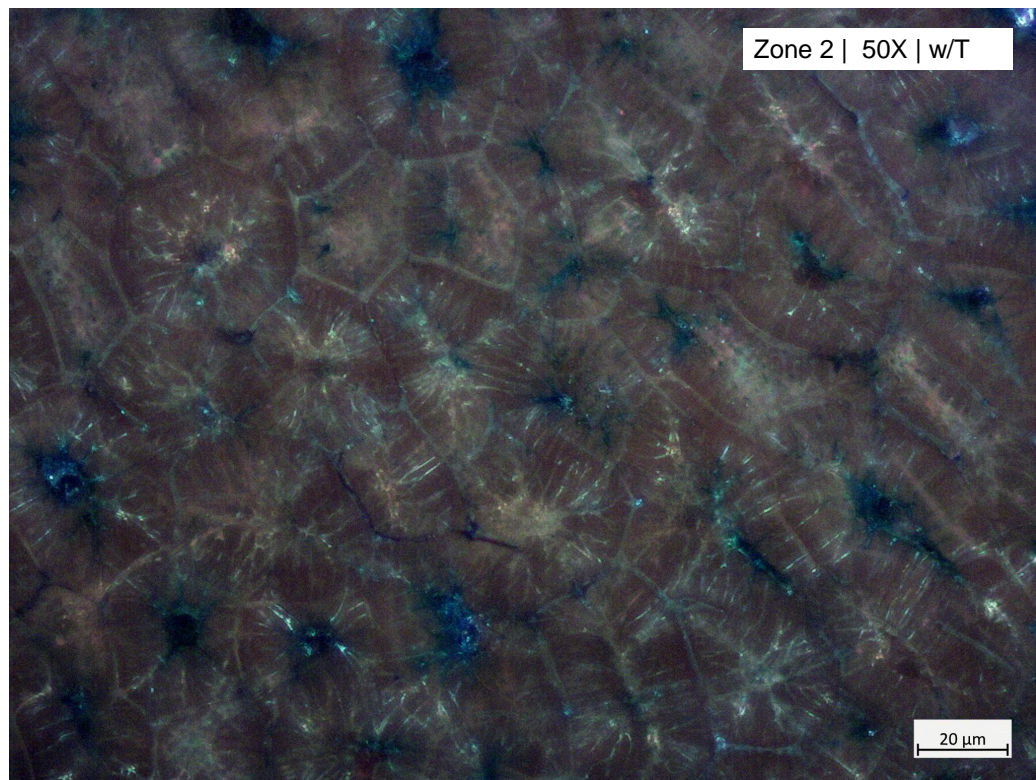


Figure B.19: Compiled microscopy of PKS, zone 2 with Toluidine.

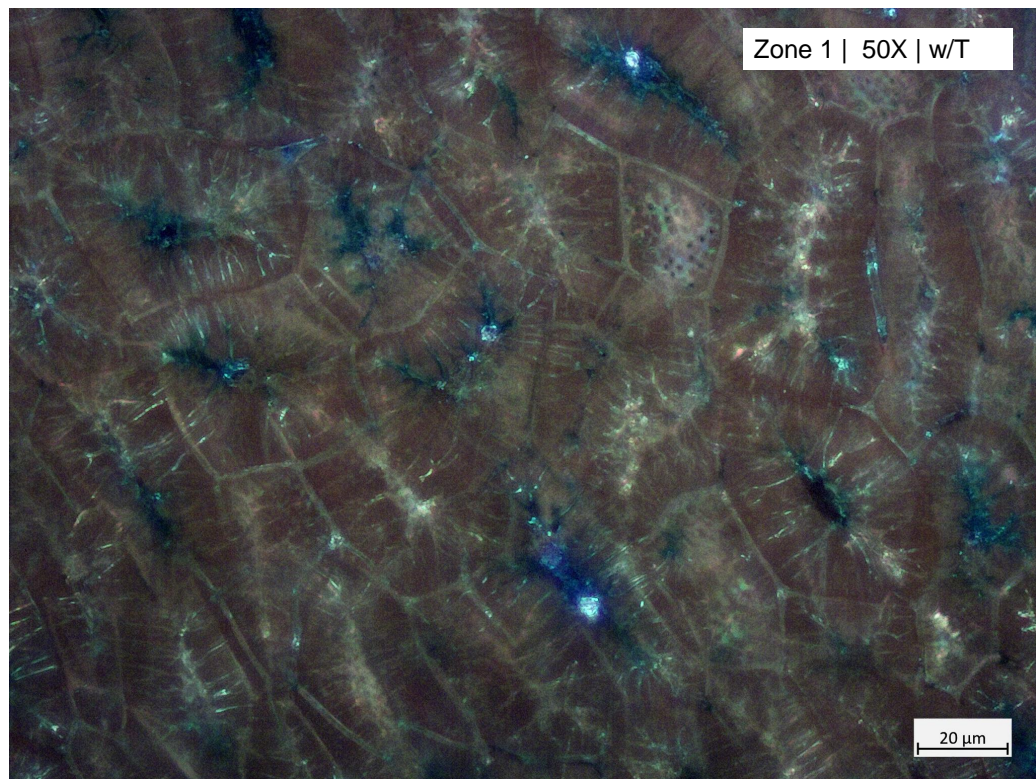


Figure B.20: Compiled microscopy of PKS, zone 3 with Toluidine.

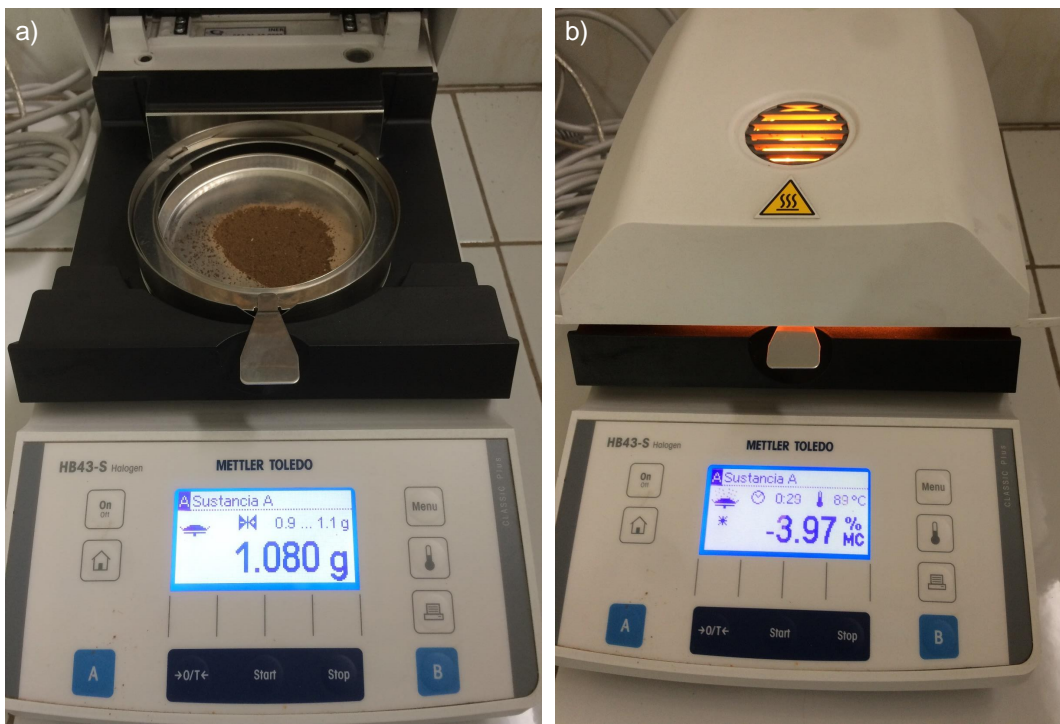


Figure B.21: HB43-S Halogen Mettler Toledo moisture balance before a) and during analysis b).

Table B.15: Milled PKS moisture content determined with the moisture balance.

Initial mass [g]	Moisture content [%]
1.090	7.43
1.080	7.23
1.040	7.12
Average	7.26 ± 0.16

calculations are presented in tables B.16 and B.17.

$$RPD = \left[\frac{(X_1 - X_2)}{X_{mean}} \right] \cdot 100 \quad (B.5)$$

$$RMS = \sqrt{\left(\frac{\sum^n x}{n} \right)^2} \quad (B.6)$$

$$\sigma = \sqrt{\frac{\sum^n (x_i - RMS)^2}{n}} \quad (B.7)$$

B.1.8 Elemental analysis determination

The results of the composition obtained in the elemental analyzer, considering moist biomass, is presented in Table B.18. Moreover, the corrected elemental analysis con-

Table B.16: Determination of water-soluble extractives in PKS samples

Sample	Weight _{sample} [g]	Moisture [%]	Total solids [g]	Dry sample [g]	Weight _{flask} [g]	Weight _{flask+extractives} [g]	Extractives [%]	RPD	RMS
1	10.0028	7.26	92.74	9.2766	164.0369	164.2371	2.16	28.21	2.51
2	10.0012	7.26	92.74	9.2751	168.6123	168.8782	2.87		
Average $\pm\sigma$								2.51 ± 0.50	

Table B.17: Determination of ethanol-soluble extractives in PKS samples

Sample	Weight _{sample} [g]	Moisture [%]	Total solids [g]	Dry sample [g]	Weight _{flask} [g]	Weight _{flask+extractives} [g]	Extractives [%]	RPD	RMS
1	10.0028	7.26	92.74	9.2766	163.6960	164.0108	3.39	7.74	3.27
2	10.0012	7.26	92.74	9.2751	170.7704	171.0617	3.14		
Average $\pm\sigma$								3.27 ± 0.18	

sidering the moisture content in each type of biomass: 10.62wt.% for PKS, 5.93wt.% for the synthetic mixture and 2.91wt.% for the coffee husk; is presented in Table as a normalized composition.

The elemental analysis presented in the previous table is then compared to other types of biomass from literature and a minimum molecular formula is obtained for the different feedstocks by transforming the weight percentages in molar fractions using the molecular weights and then dividing the moles of each component for the moles of the component with the smallest amount. The obtained information is presented in Table B.20.

Table B.18: Elemental analysis results for moist PKS, synthetic mixture and coffee husk

No.	C [wt. %]	H [wt. %]	N [wt. %]	S [wt. %]	O [wt. %]
Palm kernel shells					
S1	49.81	6.02	0.60	0.32	43.25
S2	49.54	8.90	0.53	0.04	40.99
S3	49.72	5.88	0.58	0.37	43.45
Synthetic mixture					
S1	44.01	7.27	0.16	1.76	46.80
S2	43.47	5.24	0.11	1.33	49.85
S3	44.10	7.63	0.15	1.59	46.53
Coffee husk					
S1	45.78	7.22	0.90	0.00	46.10
S2	46.74	7.81	0.90	0.00	44.55
S3	46.12	8.17	0.90	0.00	44.81

Table B.19: Moisture corrected elemental analysis results for moist PKS, synthetic mixture and coffee husk

No.	C [wt.%]	H [wt.%]	N [wt.%]	S [wt.%]	O [wt.%]
Palm kernel shells					
S1	51.97	6.21	0.63	0.33	40.86
S2	51.59	9.16	0.55	0.04	38.66
S3	51.88	6.06	0.61	0.39	41.06
Average	51.81 ± 0.20	7.14 ± 1.75	0.59 ± 0.04	0.25 ± 0.19	40.19 ± 1.33
Synthetic mixture					
S1	45.15	7.41	0.16	1.81	45.48
S2	44.66	5.35	0.11	1.37	48.51
S3	45.23	7.77	0.15	1.63	45.21
Average	45.01 ± 0.31	6.84 ± 1.31	0.14 ± 0.03	1.60 ± 0.22	46.40 ± 1.84
Coffee husk					
S1	46.34	7.29	0.91	0.00	45.46
S2	47.30	7.88	0.91	0.00	43.91
S3	46.67	8.24	0.91	0.00	44.17
Average	46.77 ± 0.48	7.80 ± 0.48	0.91 ± 1.86E - 4	0.00	44.52 ± 0.83

Table B.20: Comparison between the elemental composition for different types on dry basis.

	C [wt.%]	H [wt.%]	N [wt.%]	S [wt.%]	O [wt.%]	Formula	Reference
PKS	51.81	7.14	0.59	0.25	40.19	$C_{1.56}H_{2.57}O$	This work
Synthetic mixture	45.01	6.84	0.14	1.60	46.40	$C_{1.33}H_{2.88}O$	This work
Coffee husk	46.77	7.80	0.91	0.00	44.52	$C_{1.36}H_{2.74}O$	This work
Rice husk	42.30	6.10	1.10	0.10	50.56	$C_{1.12}H_{1.93}O$	[17]
Sugar cane bagasse	49.90	6.00	0.40	0.04	43.15	$C_{1.54}H_{2.22}O$	[17]
Olive husk	52.80	6.70	0.50	0.05	36.70	$C_{1.92}H_{2.92}O$	[19]
Jatropha cake	44.42	6.23	4.33	0.51	44.51	$C_{11.97}H_{20.14}O_{8.99}N$	[18]
Cocoa pod	43.87	5.82	2.23	0.57	47.28	$C_{22.95}H_{36.54}O_{18.55}N$	[18]
Walnut shell	53.50	6.60	1.50	0.10	35.50	$C_{41.61}H_{61.60}O_{20.71}N$	[19]
Hazelnut shell	51.60	6.20	1.60	0.04	40.20	$C_{37.63}H_{54.25}O_{22.55}N$	[19]

Table B.21: Detail of the measurements for the determination of HHV in biomass samples without corrections

Sample	HHV [J kg ⁻¹]	Average HHV [MJ kg ⁻¹]
PKS-S1	19337	
PKS-S2	19300	19.28 ± 0.06
PKS-S3	19214	
SYNT-S1	17529	
SYNT-S2	17521	17.51 ± 0.03
SYNT-S3	17482	
COFFEE HUSK-S1	18204	
COFFEE HUSK-S2	18259	18.22 ± 0.03
COFFEE HUSK-S3	18206	

Table B.22: High calorific value including moisture and sulfur content corrections.

Biomass	HHV _{moist} [MJ kg]	HHV _{dry} [MJ kg]	HHV _{S-free} [MJ kg]
PKS	19.28 ± 0.06	20.79 ± 0.07	20.77 ± 0.07
Synthetic mixture	17.51 ± 0.03	18.61 ± 0.03	18.46 ± 0.03
Coffee husk	18.22 ± 0.03	18.75 ± 0.03	18.75 ± 0.03

B.1.9 Energy content high heating value determination

The detail of the measurements undertaken for determining the HHV for the palm kernel shells and for the synthetic mixture are presented in Table B.21. Additionally and for comparison purposes, another lignin-rich biomass HHV was analyzed, coffee husk. The results of the characterization of coffee husk are presented in Table B.23. The previously showed results are not corrected with the moisture content nor the sulphur content in biomass.

For correcting the HHV of PKS, coffee husk and of the synthetic mixture, a moisture content of 7.26 wt.% is considered for PKS and 2.80 wt.% is considered correspondingly for the coffee husk. The synthetic mixture contains 5.93 wt.% moisture, which is used for its HHV correction. Regarding the sulphur content, PKS showed a 0.25 wt.%, whereas the synthetic mixture had 1.6wt.% and the coffee husks did not require any sulphur correction. The corrected HHVs are presented in Table B.22.

Table B.23: Results from the characterization of coffee husk

Property	Value
Moisture content [wt.%]	2.91 ± 0.13
Elemental analysis ^b	
C [wt.%]	46.77 ± 0.48
H [wt.%]	7.80 ± 0.48
N [wt.%]	0.91 ± 1.86 · 10 ⁻⁴
O ^a [wt.%]	44.52 ± 0.83
Biomass composition ^c	
Cellulose [wt.%]	30.08 ± 1.21
Hemicellulose [wt.%]	26.01 ± 0.13
Lignin [wt.%]	43.91 ± 2.25
Energy content	
Higher heating value [MJ kg ⁻¹]	18.22 ± 0.03

- ^a calculated by difference.
- ^b calculated on dry basis.
- ^c calculated on dry and extractives free basis.

B.1.9.1 Correlation between HHV and the composition for lignin-rich biomass

The results from the linear regression considering the current work, and three other different correlations from literature [20, 21, 22] are presented in Figure B.22.

B.2 Thermal analysis and kinetic model determination

B.2.1 Thermogravimetric analysis (TGA)

The summary of the design of experiments used to evaluate pyrolysis of PKS and of the synthetic mixture is presented in Table B.24. The remaining mass after the pyrolysis tests in % is presented for each run in Table B.25. Similarly, the resulting interval plot considering a 95% of CI for the mean and using the individual standard deviation for calculating the intervals is presented in Figure B.22.

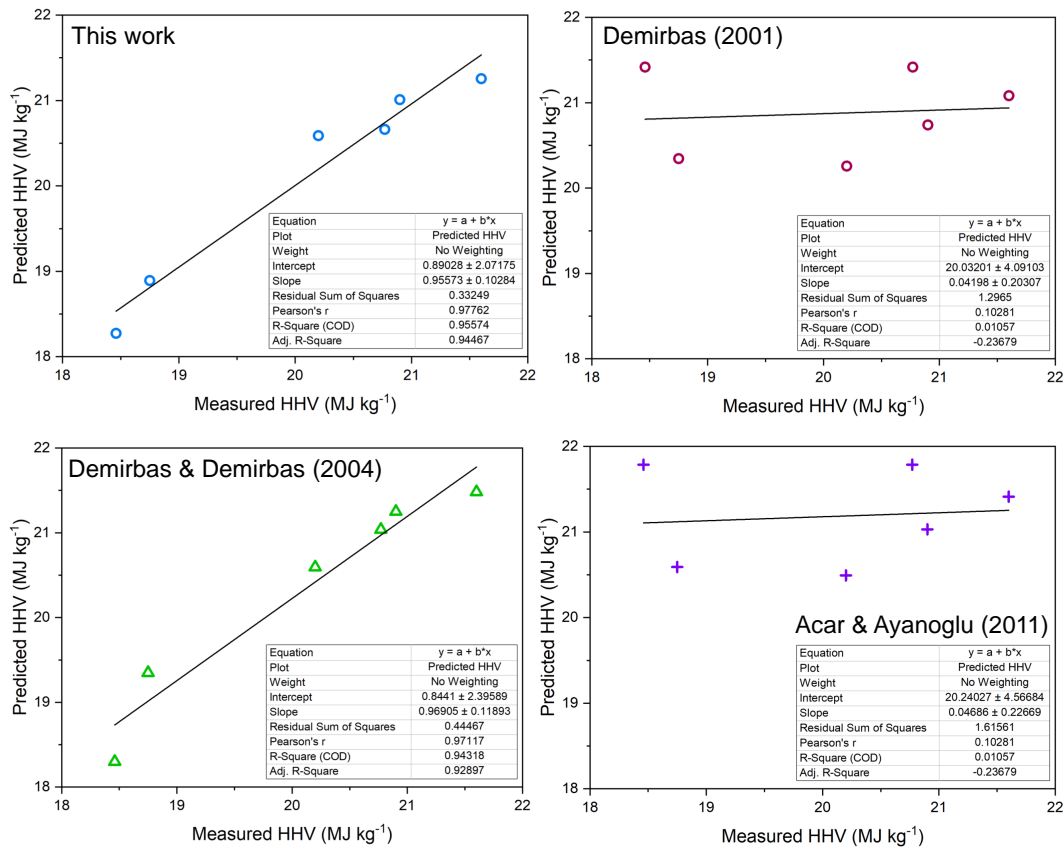


Figure B.22: Linear regressions between predicted and measured HHV for the current work and three other correlations from literature [20, 21, 22].

Table B.24: Summary of the design of experiments for pyrolysis analysis

Design Summary	
Factors	2
Base runs	8
Base blocks	1
Replicates	3
Total runs	24
Total blocks	1
Number of levels	2, 4

Table B.25: Design of experiments for randomized PKS and synthetic mixture pyrolysis tests at different heating rates

StdOrder	Run order	Biomass	Heating rate [°C min ⁻¹]	Remaining mass [%]
15	1	Synthetic mixture	35	32.7021
11	2	PKS	35	15.0431
12	3	PKS	50	19.9571
19	4	PKS	35	16.1665
20	5	PKS	50	14.3801
9	6	PKS	5	6.8308
5	7	Synthetic mixture	5	20.4300
17	8	PKS	5	4.9913
4	9	PKS	50	14.3209
13	10	Synthetic mixture	5	19.2815
14	11	Synthetic mixture	20	25.7405
18	12	PKS	20	12.4919
23	13	Synthetic mixture	35	33.9886
6	14	Synthetic mixture	20	32.0522
22	15	Synthetic mixture	20	26.0368
10	16	PKS	20	13.5940
16	17	Synthetic mixture	50	33.2401
21	18	Synthetic mixture	5	19.2543
8	19	Synthetic mixture	50	39.5680
3	20	PKS	35	18.3042
2	21	PKS	20	12.0033
7	22	Synthetic mixture	35	27.3704
24	23	Synthetic mixture	50	33.4326
1	24	PKS	5	4.1560

Appendix C

Pyrolysis of coarse biomass in a single screw auger reactor

C.1 Determination of residence time distributions using a DEM approach

C.1.1 Convergence analysis for interaction properties in PKS

C.1.2 Density adjustment

Given the non-spherical geometry of PKS, the particle's density is adjusted. The experimentally-determined PKS density is $1286.87 \text{ kg m}^{-3}$. From Table C.1. The $\rho_{\text{bulk}}/\rho_{\text{calibrated}}$ ratio must stay between 0.2-0.5. With this premise, an initial calibrated density of $1000 \text{ [kg m}^{-3}]$ is considered for the DEM simulation.

C.1.3 Simulations for determining particle-particle sliding and rolling friction coefficients.

The complete set of results from the simulation in LIGGGHTS is presented in the next lines.

Table C.1: Comparison of densities for PKS, particle and bulk

$\rho_{\text{calibrated}}$ kg m^{-3}	ρ_{particle} kg m^{-3}	$\rho_{\text{bulk simulated}}$ kg m^{-3}	$\rho_{\text{bulk experimental}}$ kg m^{-3}
1000		421.80	
900	1286.87	469.97	536.64
800		524.57	

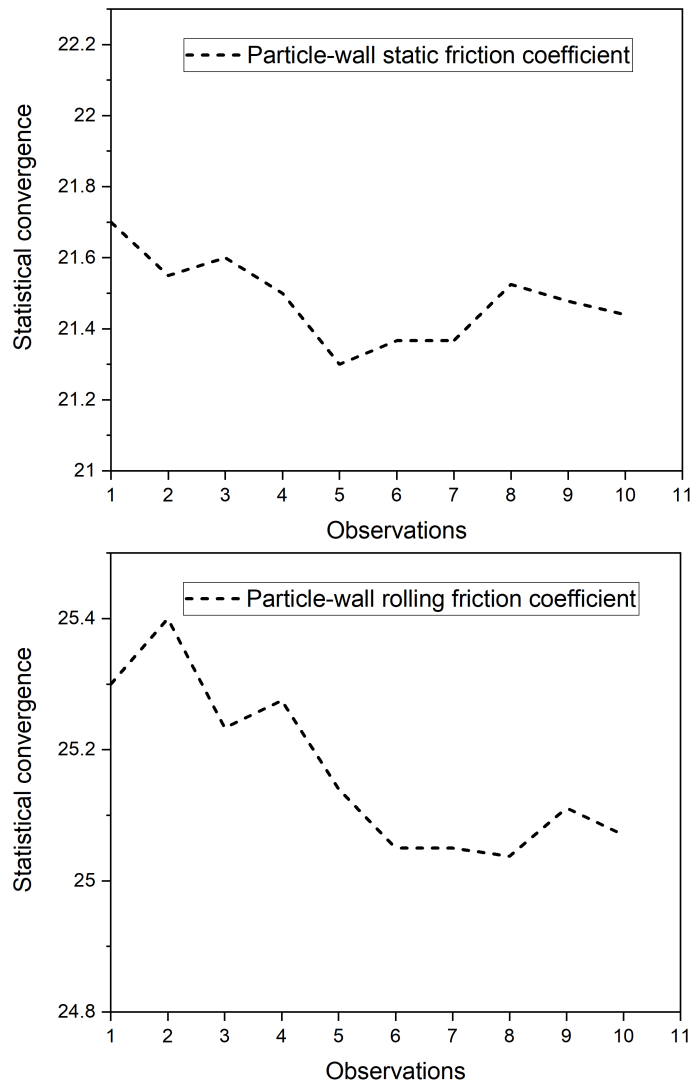


Figure C.1: Convergence of the mean for evaluating the tilting angle using for determining wall-particle coefficients of static friction and rolling friction.

The experimental results for the repose angles in both left and right side are presented in Figure C.6

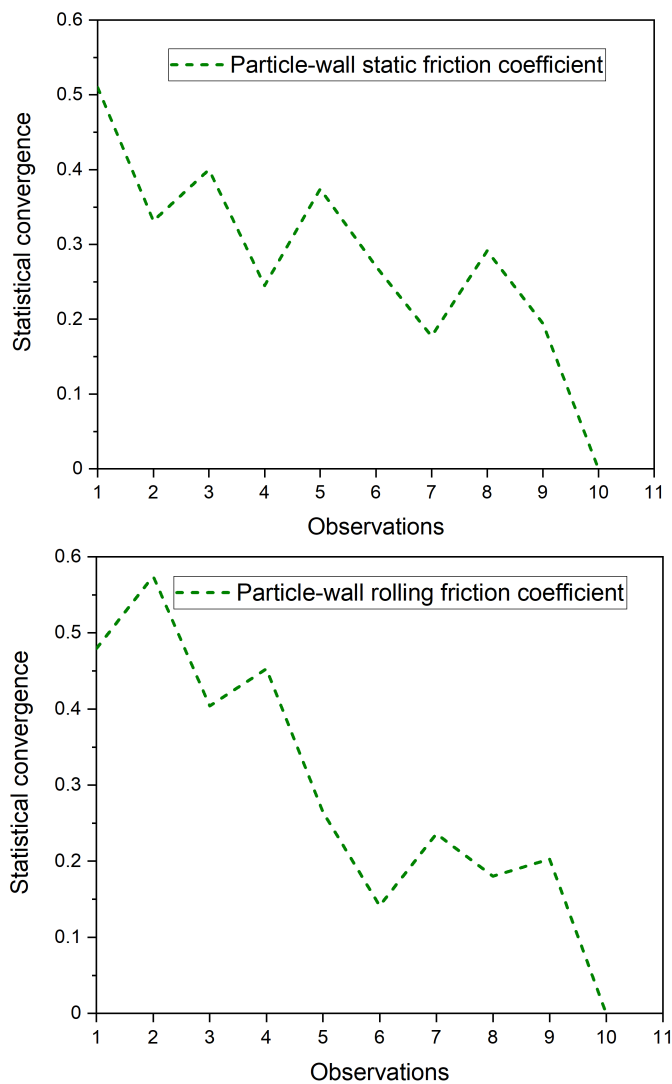


Figure C.2: Convergence of the deviation for evaluating the tilting angle using for determining wall-particle coefficients of static friction and rolling friction.

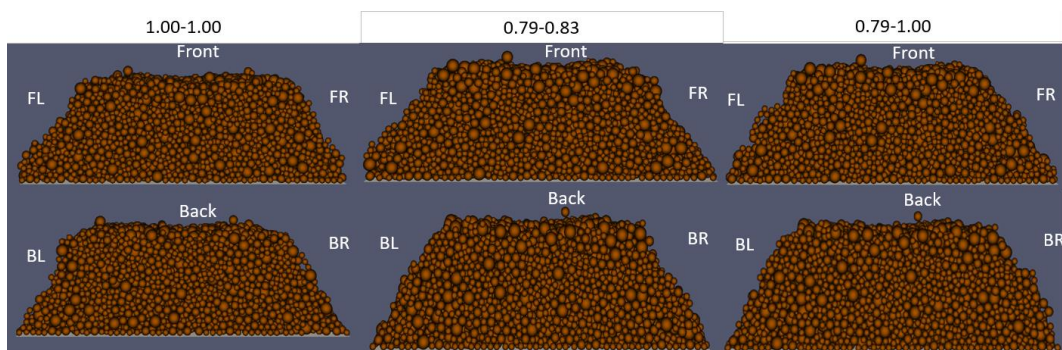


Figure C.3: Results from the simulation in LIGGGHTS for the calculation of repose angle for different combination of sliding and rolling particle-particle friction coefficients. Sliding coefficient-Rolling coefficient. F=front, B=back, L=left, R=right.

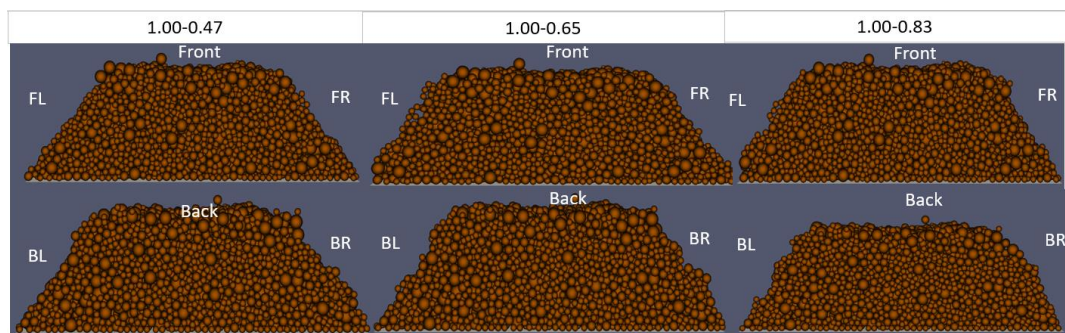


Figure C.4: Results from the simulation in LIGGGHTS for the calculation of repose angle for different combination of sliding and rolling particle-particle friction coefficients. Sliding coefficient-Rolling coefficient. F=front, B=back, L=left, R=right.

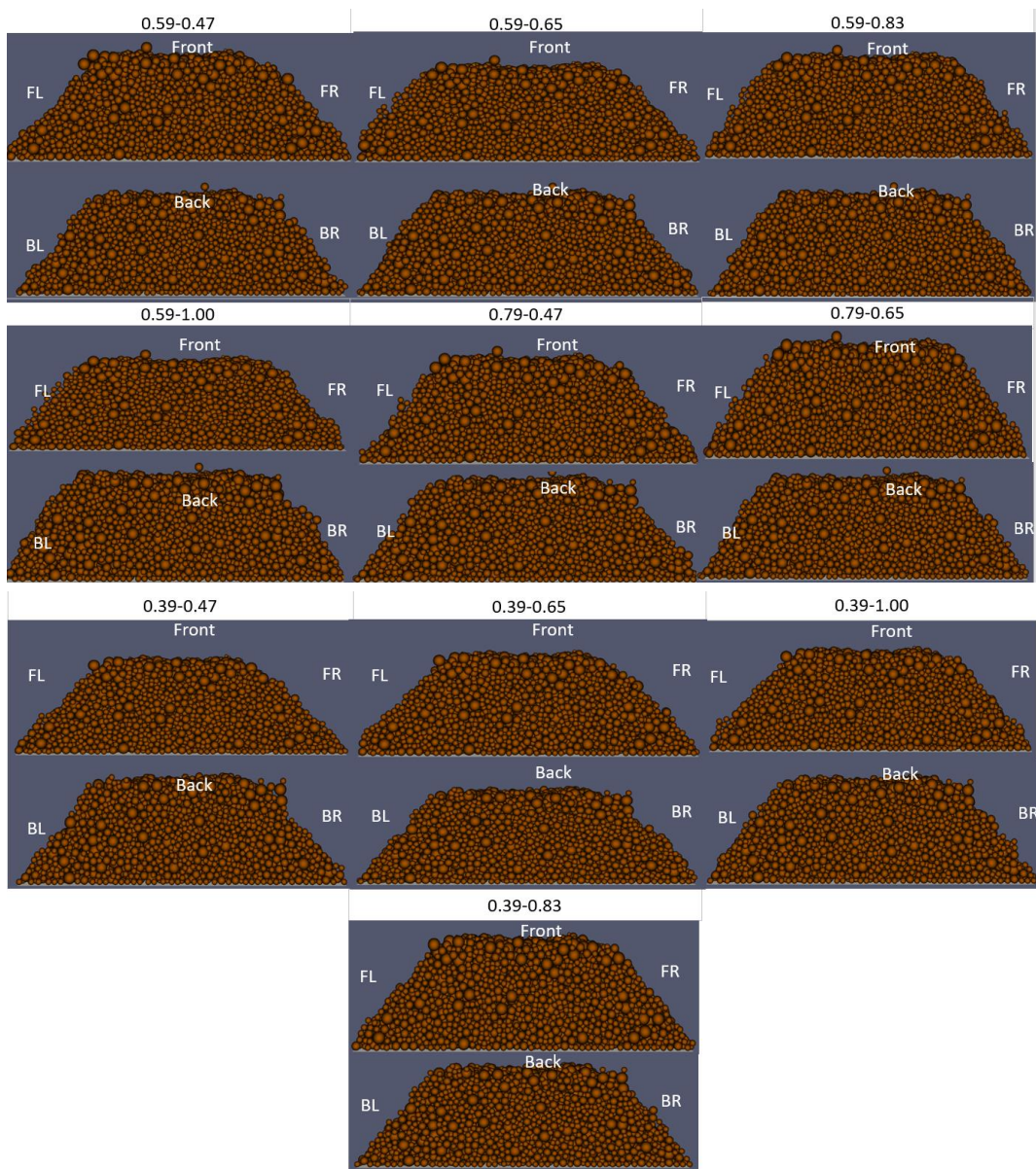


Figure C.5: Results from the simulation in LIGGGHTS for the calculation of repose angle for different combination of sliding and rolling particle-particle friction coefficients. Sliding coefficient-Rolling coefficient. F=front, B=back, L=left, R=right.

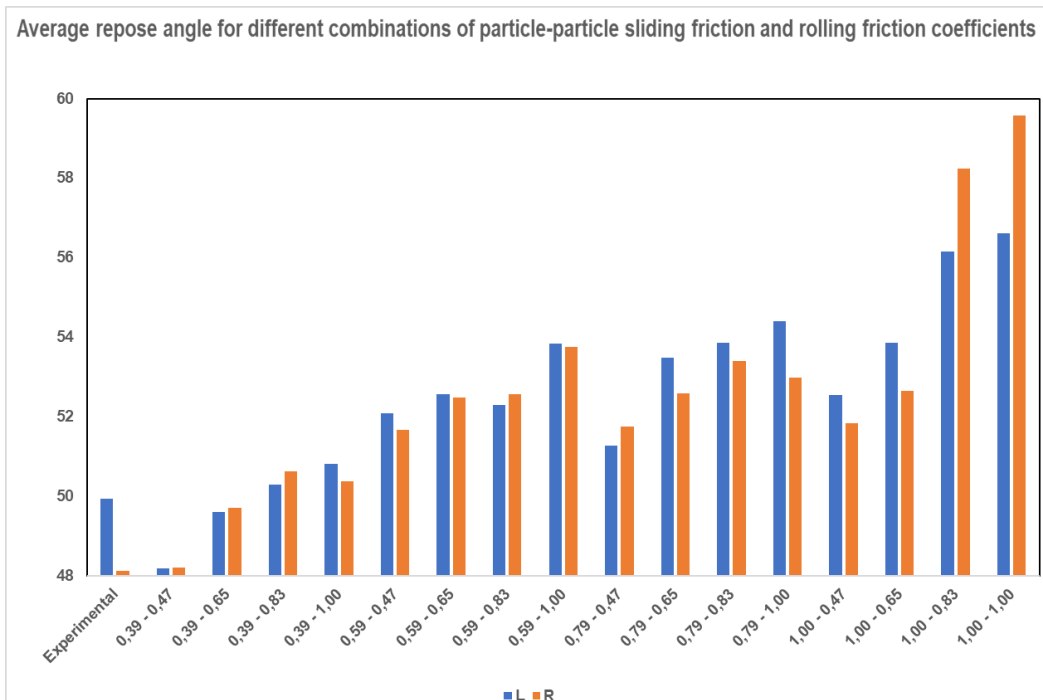


Figure C.6: Repose angle for left and right sides of the experimental set up for finding sliding and rolling friction coefficients between particle-particle. Sliding coefficient-Rolling coefficient. F=front, B=back, L=left, R=right.

Bibliography

- [1] R. McKenna, V. Bertsch, K. Mainzer, and W. Fichtner. Combining local preferences with multi-criteria decision analysis and linear optimization to develop feasible energy concepts in small communities. *European Journal of Operational Research*, 268(3):1092–1110, 2018.
- [2] Wu-Jun Liu, Hong Jiang, and Han-Qing Yu. Development of Biochar-Based Functional Materials: Toward a Sustainable Platform Carbon Material. *Chemical Reviews*, 115(22):12251–12285, 2015.
- [3] Vaibhav Dhyani and Thallada Bhaskar. A comprehensive review on the pyrolysis of lignocellulosic biomass. *Renewable Energy*, 129:695–716, 2018.
- [4] E. Ranzi, T. Faravelli, and F. Manenti. *Pyrolysis, Gasification, and Combustion of Solid Fuels*, volume 49. Elsevier Inc., 1 edition, 2016.
- [5] Raquel Escrivani Guedes, Aderval S. Luna, and Alexandre Rodrigues Torres. Operating parameters for bio-oil production in biomass pyrolysis: A review. *Journal of Analytical and Applied Pyrolysis*, 129(November 2017):134–149, 2018.
- [6] Shurong Wang, Gongxin Dai, Haiping Yang, and Zhongyang Luo. Lignocellulosic biomass pyrolysis mechanism: A state-of-the-art review. *Progress in Energy and Combustion Science*, 62:33–86, 2017.
- [7] Dekui Shen, Rui Xiao, Sai Gu, and Huiyan Zhang. The Overview of Thermal Decomposition of Cellulose in Lignocellulosic Biomass. *Cellulose - Biomass Conversion*, 2013.
- [8] Haiping Yang, Rong Yan, Hanping Chen, Dong Ho Lee, and Chuguang Zheng.

- Characteristics of hemicellulose, cellulose and lignin pyrolysis. *Fuel*, 86(12-13):1781–1788, 2007.
- [9] Gábor Várhegyi, Michael Jerry Antal, Emma Jakab, and Piroska Szabó. Kinetic modeling of biomass pyrolysis. *Journal of Analytical and Applied Pyrolysis*, 42(1):73–87, 1997.
- [10] Xun Wang, Mian Hu, Wanyong Hu, Zhihua Chen, Shiming Liu, Zhiqian Hu, and Bo Xiao. Thermogravimetric kinetic study of agricultural residue biomass pyrolysis based on combined kinetics. *Bioresource Technology*, 219:510–520, 2016.
- [11] Juan A. Conesa, JoséA A. Caballero, A. Marcilla, and R. Font. Analysis of different kinetic models in the dynamic pyrolysis of cellulose. *Thermochimica Acta*, 254(C):175–192, 1995.
- [12] F J Kilzer and A Broido. Speculations on the Nature of Cellulose Pyrolysis. *Pyrolydynamics*, 2(April 1964):151–163, 1965.
- [13] F. Shafizadeh and A. G.W. Bradbury. Thermal degradation of cellulose in air and nitrogen at low temperatures. *Journal of Applied Polymer Science*, 23(5):1431–1442, 1979.
- [14] Victor Pozzobon, Sylvain Salvador, Jean Jacques Bézian, Mouna El-Hafi, Yannick Le Maoult, and Gilles Flamant. Radiative pyrolysis of wet wood under intermediate heat flux: Experiments and modelling. *Fuel Processing Technology*, 128:319–330, 2014.
- [15] R. Vinu and Linda J. Broadbelt. A mechanistic model of fast pyrolysis of glucose-based carbohydrates to predict bio-oil composition. *Energy and Environmental Science*, 5(12):9808–9826, 2012.
- [16] Mettler Toledo. Density Kit for Precision Balances XPR, XSR, XPE, XP, XS. Technical report, Mettler Toledo, 2022.
- [17] A. Williams, J. M. Jones, L. Ma, and M. Pourkashanian. Pollutants from the combustion of solid biomass fuels. *Progress in Energy and Combustion Science*, 38(2):113–137, 2012.

- [18] James O. Titiloye, Muhammad S. Abu Bakar, and Temitope E. Odetoye. Thermochemical characterisation of agricultural wastes from West Africa. *Industrial Crops and Products*, 47:199–203, 2013.
- [19] Ayhan Demirbaş. Fuel characteristics of olive husk and walnut, hazelnut, sunflower, and almond shells. *Energy Sources*, 24(3):215–221, 2002.
- [20] A. Demirbaş. Relationships between lignin contents and heating values of biomass. *Energy Conversion and Management*, 42(2):183–188, 2001.
- [21] Ayhan Demirbaş and A. Hilal Demirbaş. Estimating the calorific values of lignocellulosic fuels. *Energy Exploration and Exploitation*, 22(2):135–143, 2004.
- [22] Sukru Acar and Abdulkadir Ayanoglu. Determination of higher heating values (HHVs) of biomass fuels. *Energy Education Science and Technology Part A: Energy Science and Research*, 28(2):749–758, 2012.
- [23] Tony Bridgwater. Challenges and Opportunities in Fast Pyrolysis of Biomass: Part I. *Johnson Matthey Technology Review*, 62(1):118–130, 2018.
- [24] Andres Anca-Couce, Peter Sommersacher, and Robert Scharler. Online experiments and modelling with a detailed reaction scheme of single particle biomass pyrolysis. *Journal of Analytical and Applied Pyrolysis*, 127(March 2017):411–425, 2017.
- [25] Eliseo Ranzi, Michele Corbetta, Flavio Manenti, and Sauro Pierucci. Kinetic modeling of the thermal degradation and combustion of biomass. *Chemical Engineering Science*, 110:2–12, 2014.
- [26] Andrés Anca-Couce and Nico Zobel. Numerical analysis of a biomass pyrolysis particle model: Solution method optimized for the coupling to reactor models. *Fuel*, 97:80–88, 2012.
- [27] Andrés Anca-Couce. Reaction mechanisms and multi-scale modelling of lignocellulosic biomass pyrolysis. *Progress in Energy and Combustion Science*, 53:41–79, 2016.

- [28] Wai Chun R. Chan, Marcia Kelbon, and Barbara B. Krieger. Modelling and experimental verification of physical and chemical processes during pyrolysis of a large biomass particle. *Fuel*, 64(11):1505–1513, 1985.
- [29] Kenneth M. Bryden and Mathew J. Hagge. Modeling the combined impact of moisture and char shrinkage on the pyrolysis of a biomass particle. *Fuel*, 82(13):1633–1644, 2003.
- [30] Jewel A. Capunitan and Sergio C. Capareda. Assessing the potential for biofuel production of corn stover pyrolysis using a pressurized batch reactor. *Fuel*, 95:563–572, 2012.
- [31] Xinyu Wang, Wei Lv, Li Guo, Ming Zhai, Peng Dong, and Guoli Qi. Energy and exergy analysis of rice husk high-temperature pyrolysis. *International Journal of Hydrogen Energy*, 41(46):21121–21130, 2016.
- [32] Alpha Chemika. Specifications of Cellulose Powder (For Column Chromatography), 2013.
- [33] LOBA Chemie Laboratory Reagents & Fine Chemicals. Certificate of Analysis, 2012.
- [34] SIGMA-ALDRICH. Product Specification, 2021.
- [35] IEA. *World Energy Outlook 2020*. OECD Publishing, Paris, 2020.
- [36] Eliseo Ranzi, Paulo Eduardo Amaral Debiagi, and Alessio Frassoldati. Mathematical Modeling of Fast Biomass Pyrolysis and Bio-Oil Formation. Note II: Secondary Gas-Phase Reactions and Bio-Oil Formation. *ACS Sustainable Chemistry and Engineering*, 5(4):2882–2896, 2017.
- [37] J. N. Brown and R. C. Brown. Process optimization of an auger pyrolyzer with heat carrier using response surface methodology. *Bioresource Technology*, 103(1):405–414, 2012.
- [38] Javaid Akhtar and Noraishah Saidina Amin. A review on operating parameters for optimum liquid oil yield in biomass pyrolysis. *Renewable and Sustainable Energy Reviews*, 16(7):5101–5109, 2012.

- [39] Xiaogang Shi, Frederik Ronsse, and Jan G. Pieters. Finite element modeling of intraparticle heterogeneous tar conversion during pyrolysis of woody biomass particles. *Fuel Processing Technology*, 148:302–316, 2016.
- [40] Morten G. Gronli and Morten C. Melaaen. Mathematical model for wood pyrolysis-comparison of experimental measurements with model predictions. *Energy and Fuels*, 14(4):791–800, 2000.
- [41] Alberto Cuoci, Alessio Frassoldati, Tiziano Faravelli, and Eliseo Ranzi. OpenSMOKE++: An object-oriented framework for the numerical modeling of reactive systems with detailed kinetic mechanisms. *Computer Physics Communications*, 192:237–264, 2015.
- [42] Seiichi Koshizuka, Kazuya Shibata, Masahiro Kondo, and Takuya Matsunaga. Boundary conditions. In Seiichi Koshizuka, Kazuya Shibata, Masahiro Kondo, and Takuya Matsunaga, editors, *Moving Particle Semi-implicit Method*, chapter 4, pages 155–215. Academic Press, London, 2018.
- [43] Haiping Yang, Rong Yan, Hanping Chen, Dong H. Lee, David Tee Liang, and Chuguang Zheng. Pyrolysis of palm oil wastes for enhanced production of hydrogen rich gases. *Fuel Processing Technology*, 87:935–942, 2006.
- [44] C. A. Koufopanos, A. Lucchesi, and G. Maschio. Kinetic modelling of the pyrolysis of biomass and biomass components. *The Canadian Journal of Chemical Engineering*, 67(1):75–84, 1989.
- [45] Morten Grønli, Michael Jerry Antal, and Gábor Várhegyi. A round-robin study of cellulose pyrolysis kinetics by thermogravimetry. *Industrial and Engineering Chemistry Research*, 38(6):2238–2244, 1999.
- [46] Z. Miao, T. E. Grift, A. C. Hansen, and K. C. Ting. Energy requirement for comminution of biomass in relation to particle physical properties. *Industrial Crops and Products*, 33(2):504–513, 2011.
- [47] Ayse E Pütün, Nurgül Özbay, Varol Esin Apaydin, Basak B Uzun, and Funda Ates. Rapid and slow pyrolysis of pistachio shell: Effect of pyrolysis conditions on the product yields and characterization of the liquid product. *International Journal of Energy Research*, 31:506–514, 2007.

- [48] Michaël Becidan, Øyvind Skreiberg, and Johan E. Hustad. Experimental study on pyrolysis of thermally thick biomass residues samples: Intra-sample temperature distribution and effect of sample weight ("scaling effect"). *Fuel*, 86(17-18):2754–2760, 2007.
- [49] Paulo Eduardo Amaral Debiagi, Chiara Pecchi, Giancarlo Gentile, Alessio Frassoldati, Alberto Cuoci, Tiziano Faravelli, and Eliseo Ranzi. Extractives Extend the Applicability of Multistep Kinetic Scheme of Biomass Pyrolysis. *Energy and Fuels*, 29(10):6544–6555, 2015.
- [50] John E. White, W. James Catallo, and Benjamin L. Legendre. Biomass pyrolysis kinetics: A comparative critical review with relevant agricultural residue case studies. *Journal of Analytical and Applied Pyrolysis*, 91(1):1–33, 2011.
- [51] D. Ferdous, A. K. Dalai, S. K. Bej, and R. W. Thring. Pyrolysis of lignins: Experimental and kinetics studies. *Energy and Fuels*, 16(6):1405–1412, 2002.
- [52] Andrés Anca-Couce, Ramin Mehrabian, Robert Scharler, and Ingwald Obernberger. Kinetic scheme of biomass pyrolysis considering secondary charring reactions. *Energy Conversion and Management*, 87(2014):687–696, 2014.
- [53] Eliseo Ranzi, Paulo Eduardo Amaral Debiagi, and Alessio Frassoldati. Mathematical Modeling of Fast Biomass Pyrolysis and Bio-Oil Formation. Note I: Kinetic Mechanism of Biomass Pyrolysis. *ACS Sustainable Chemistry and Engineering*, 5(4):2867–2881, 2017.
- [54] Shiliang Wu, Dekui Shen, Jun Hu, Huiyan Zhang, and Rui Xiao. Cellulose-hemicellulose interactions during fast pyrolysis with different temperatures and mixing methods. *Biomass and Bioenergy*, 95:55–63, 2016.
- [55] T. Hosoya, H. Kawamoto, and S. Saka. Cellulose-hemicellulose and cellulose-lignin interactions in wood pyrolysis at gasification temperature. *Journal of Analytical and Applied Pyrolysis*, 80(1):118–125, 2007.
- [56] Qian Liu, Zhaoping Zhong, Shurong Wang, and Zhongyang Luo. Interactions of biomass components during pyrolysis: A TG-FTIR study. *Journal of Analytical and Applied Pyrolysis*, 90(2):213–218, 2011.

- [57] Maria Silvia Bertran and Bruce E. Dale. Determination of cellulose accessibility by differential scanning calorimetry. *Journal of Applied Polymer Science*, 32(3):4241–4253, 1986.
- [58] Fred Shafizadeh and Peter P. S. Chin. Thermal Deterioration of Wood. In *Wood Technology: Chemical Aspects*, volume 43, chapter 5, pages 57–81. 1977.
- [59] C. Di Blasi, C. Branca, F. E. Sarnataro, and A. Gallo. Thermal runaway in the pyrolysis of some lignocellulosic biomasses. *Energy and Fuels*, 28(4):2684–2696, 2014.
- [60] Haiping Yang, Rong Yan, Hanping Chen, Dong Ho Lee, and Chuguang Zheng. Characteristics of hemicellulose, cellulose and lignin pyrolysis. *Fuel*, 86(12–13):1781–1788, 2007.
- [61] Eric Alberto Ocampo Batlle, York Castillo Santiago, Osvaldo José Venturini, José Carlos Escobar Palacio, Electo Eduardo Silva Lora, Diego Mauricio Yepes Maya, and Alberto Ricardo Albis Arrieta. Thermodynamic and environmental assessment of different scenarios for the insertion of pyrolysis technology in palm oil biorefineries. *Journal of Cleaner Production*, 250:1–16, 2020.
- [62] Statista. Production of major vegetable oils worldwide from 2012/13 to 2021/2022, 2022.
- [63] Soh Kheang Loh. The potential of the Malaysian oil palm biomass as a renewable energy source. *Energy Conversion and Management*, 141:285–298, 2017.
- [64] Wendy Pei Qin Ng, Hon Loong Lam, Foo Yuen Ng, Mustafa Kamal, and Joseph Heng Ee Lim. Waste-to-wealth: Green potential from palm biomass in Malaysia. *Journal of Cleaner Production*, 34(September 2011):57–65, 2012.
- [65] Maham Hussain, Haslinda Zabiri, Lemma Dendena Tufa, Suzana Yusup, and Imtiaz Ali. A kinetic study and thermal decomposition characteristics of palm kernel shell using model-fitting and model-free methods. *Biofuels*, 13(1):105–116, 2022.

- [66] Charalampos Christodoulou, Luca Mazzei, Salvador García-Muñoz, and Eva Sorensen. Modelling of Droplet Absorption and Evaporation during Pharmaceutical Tablet Coating. *Computer Aided Chemical Engineering*, 40:85–90, 2017.
- [67] T C Illingworth and I O Golosnoy. Numerical solutions of diffusion-controlled moving boundary problems which conserve solute. 209:207–225, 2005.
- [68] Aristide Giuliano, Massimo Poletto, and Diego Barletta. Process optimization of a multi-product biorefinery: The effect of biomass seasonality. *Chemical Engineering Research and Design*, 107:236–252, 2016.
- [69] C. Luke Williams, Tyler L. Westover, Rachel M. Emerson, Jaya Shankar Tumuluru, and Chenlin Li. Sources of Biomass Feedstock Variability and the Potential Impact on Biofuels Production. *Bioenergy Research*, 9(1):1–14, 2016.
- [70] Murray R. Gray, William H. Corcoran, and George R. Gavalas. Pyrolysis of a Wood-Derived Material. Effects of Moisture and Ash Content. *Industrial and Engineering Chemistry Process Design and Development*, 24(3):646–651, 1985.
- [71] Victor Pozzobon, Sylvain Salvador, and Jean Jacques Bézian. Biomass gasification under high solar heat flux: Advanced modelling. *Fuel*, 214:300–313, 2018.
- [72] Mathew J. Hagge and Kenneth M. Bryden. Modeling the impact of shrinkage on the pyrolysis of dry biomass. *Chemical Engineering Science*, 57(14):2811–2823, 2002.
- [73] Kamil Kwiatkowski, Konrad Bajer, Agnieszka Celińska, Marek Dudyński, Jakub Korotko, and Marta Sosnowska. Pyrolysis and gasification of a thermally thick wood particle - Effect of fragmentation. *Fuel*, 132:125–134, 2014.
- [74] Colomba Di Blasi. Modelling the fast pyrolysis of cellulosic particles in fluid-bed reactors. *Chemical Engineering Science*, 55(24):5999–6013, 2000.
- [75] A. V. Bridgwater. Principles and practice of biomass fast pyrolysis processes for liquids. *Journal of Analytical and Applied Pyrolysis*, 51(1):3–22, 1999.

- [76] Alex D. Paulsen, Matthew S. Mettler, and Paul J. Dauenhauer. The role of sample dimension and temperature in cellulose pyrolysis. *Energy and Fuels*, 27(4):2126–2134, 2013.
- [77] Jaakko Karvonen, Janni Kunttu, Tommi Suominen, Jyrki Kangas, Pekka Leskinen, and Jáchym Judl. Integrating fast pyrolysis reactor with combined heat and power plant improves environmental and energy efficiency in bio-oil production. *Journal of Cleaner Production*, 183:143–152, 2018.
- [78] Andres Chico-Proano, George Manos, Lazaros G Papageorgiou, and Eric S Fraga. Heating Strategies in Cellulose Pyrolysis as an Alternative For Targeting Energy Efficient Product Distribution. *Chemical Engineering Transactions*, 86:61–66, 2021.
- [79] Kuo Zeng, Daniel Gauthier, Jidong Lu, and Gilles Flamant. Parametric study and process optimization for solar pyrolysis of beech wood. *Energy Conversion and Management*, 106:987–998, 2015.
- [80] Sergey Zinoviev, Franziska Müller-Langer, Piyali Das, Nicolás Bertero, Paolo Fornasiero, Martin Kaltschmitt, Gabriele Centi, and Stanislav Miertus. Next-generation biofuels: Survey of emerging technologies and sustainability issues. *ChemSusChem*, 3(10):1106–1133, 2010.
- [81] Nibal T Albasheh and Jessica L Heier. Biomass and Bioenergy Optimization of lignocellulosic biomass-to-biofuel supply chains with densification : Literature review. *Biomass and Bioenergy*, 144(December 2020):1–10, 2021.
- [82] Rodolfo Daniel Silva-Martínez, Alessandro Sanches-Pereira, Willington Ortiz, Maria Fernanda Gómez Galindo, and Suani Teixeira Coelho. The state-of-the-art of organic waste to energy in Latin America and the Caribbean: Challenges and opportunities. *Renewable Energy*, 156:509–525, 2020.
- [83] Tao Kan, Vladimir Strezov, and Tim J. Evans. Lignocellulosic biomass pyrolysis: A review of product properties and effects of pyrolysis parameters. *Renewable and Sustainable Energy Reviews*, 57:126–1140, 2016.

- [84] Felipe Campuzano, Robert C Brown, and Juan Daniel Martínez. Auger reactors for pyrolysis of biomass and wastes. *Renewable and Sustainable Energy Reviews*, 102(October 2018):372–409, 2019.
- [85] Fabio Codignole Luz, Stefano Cordiner, Alessandro Manni, Vincenzo Mulone, and Vittorio Rocco. Biomass fast pyrolysis in screw reactors: Prediction of spent coffee grounds bio-oil production through a monodimensional model. *Energy Conversion and Management*, 168(May):98–106, 2018.
- [86] A. V. Bridgwater. Review of fast pyrolysis of biomass and product upgrading. *Biomass and Bioenergy*, 38:68–94, 2012.
- [87] Peter Mckendry. Energy production from biomass (part 2): conversion technologies. *Bioresource Technology*, 83(July 2001):47–54, 2002.
- [88] T Schepers. *Biorefineries*. Springer, Hannover, 2019.
- [89] Francesco Cherubini. The biorefinery concept: Using biomass instead of oil for producing energy and chemicals. *Energy Conversion and Management*, 51(7):1412–1421, 2010.
- [90] Yoshiharu Nishiyama, Junji Sugiyama, Henri Chanzy, and Paul Langan. Crystal Structure and Hydrogen Bonding System in Cellulose I α from Synchrotron X-ray and Neutron Fiber Diffraction. *Journal of the American Chemical Society*, 125(47):14300–14306, 2003.
- [91] Masahisa Wada, Ritsuko Hori, Ung Jin Kim, and Sono Sasaki. X-ray diffraction study on the thermal expansion behavior of cellulose I β and its high-temperature phase. *Polymer Degradation and Stability*, 95(8):1330–1334, 2010.
- [92] Shubhangi De, Shubham Mishra, Elangovan Poonguzhali, Mathur Rajesh, and Krishnamurthi Tamilarasan. Fractionation and characterization of lignin from waste rice straw: Biomass surface chemical composition analysis. *International Journal of Biological Macromolecules*, 145:795–803, 2020.
- [93] Bradley Tyson, Christopher M. Pask, Neil George, and Elena Simone. Crystallization Behavior and Crystallographic Properties of dl -Arabinose and dl

- Xylose Diastereomer Sugars. *Crystal Growth and Design*, 22(2):1371–1383, 2022.
- [94] Raissa Alvarenga Carvalho Gomide, Ana Carolina Salgado de Oliveira, Danielle Aparecida Caetano Rodrigues, Cassiano Rodrigues de Oliveira, Odflio Benedito Garrido de Assis, Marali Vilela Dias, and Soraia Vilela Borges. Development and Characterization of Lignin Microparticles for Physical and Antioxidant Enhancement of Biodegradable Polymers. *Journal of Polymers and the Environment*, 28(4):1326–1334, 2020.
- [95] Jie Yu, Nigel Paterson, John Blamey, and Marcos Millan. Cellulose, xylan and lignin interactions during pyrolysis of lignocellulosic biomass. *Fuel*, 191:140–149, 2017.
- [96] Wan Nor Roslam Wan Isahak, Mohamed W.M. Hisham, Mohd Ambar Yarmo, and Taufiq Yap Yun Hin. A review on bio-oil production from biomass by using pyrolysis method. *Renewable and Sustainable Energy Reviews*, 16(8):5910–5923, 2012.
- [97] Eliseo Ranzi, Alberto Cuoci, Tiziano Faravelli, Alessio Frassoldati, Gabriele Migliavacca, and Sauro Pierucci. Chemical Kinetics of Biomass Pyrolysis. *Energy & Fuels*, 22:4292–4300, 2008.
- [98] Güray Yıldız, Frederik Ronsse, Robbie Venderbosch, Ruben van Duren, Sascha R.A. Kersten, and Wolter Prins. Effect of biomass ash in catalytic fast pyrolysis of pine wood. *Applied Catalysis B: Environmental*, 168-169:203–211, 2015.
- [99] Y. Haseli, J. A. Van Oijen, and L. P.H. De Goey. Modeling biomass particle pyrolysis with temperature-dependent heat of reactions. *Journal of Analytical and Applied Pyrolysis*, 90(2):140–154, 2011.
- [100] Cristina řerbănescu. Kinetic analysis of cellulose pyrolysis: A short review. *Chemical Papers*, 68(7):847–860, 2014.
- [101] Sergey Vyazovkin, Konstantinos Chrissafis, Maria Laura Di Lorenzo, Nobuyoshi Koga, Michèle Pijolat, Bertrand Roduit, Nicolas Sbirrazzuoli, and

- Joan Josep Suñol. ICTAC Kinetics Committee recommendations for collecting experimental thermal analysis data for kinetic computations. *Thermochimica Acta*, 590(1-2):1–23, 2011.
- [102] Kouichi Miura. A New and Simple Method to Estimate $f(E)$ and $k_0(E)$ in the Distributed Activation Energy Model from Three Sets of Experimental Data. *Energy and Fuels*, 9(2):302–307, 1995.
- [103] Belinda Wang, Berhane H. Gebreslassie, and Fengqi You. Sustainable design and synthesis of hydrocarbon biorefinery via gasification pathway: Integrated life cycle assessment and technoeconomic analysis with multiobjective superstructure optimization. *Computers and Chemical Engineering*, 52:55–76, 2013.
- [104] Su Shiung Lam and Howard A. Chase. A review on waste to energy processes using microwave pyrolysis. *Energies*, 5(10):4209–4232, 2012.
- [105] Anshu Bharadwaj, Larry L. Baxter, and Allen L. Robinson. Effects of intraparticle heat and mass transfer on biomass devolatilization: Experimental results and model predictions. *Energy and Fuels*, 18(4):1021–1031, 2004.
- [106] D. Radlein, J. Piskorz, and D. S. Scott. Fast pyrolysis of natural polysaccharides as a potential industrial process. *Journal of Analytical and Applied Pyrolysis*, 19(C):41–63, 1991.
- [107] A. V. Bridgwater and G. V.C. Peacocke. Fast pyrolysis processes for biomass. *Renewable and sustainable energy reviews*, 4(1):1–73, 2000.
- [108] Luo, Wang, Liao, and Cen. Mechanism Study of Cellulose Rapid Pyrolysis. *Industrial & Engineering Chemistry Research*, 43(18):5605–5610, 2004.
- [109] Isah Yakub Mohammed, Yousif Abdalla Abakr, Feroz Kabir Kazi, Suzana Yusuf, Ibraheem Alshareef, and Soh Aik Chin. Pyrolysis of Napier Grass in a Fixed Bed Reactor: Effect of Operating Conditions on Product Yields and Characteristics. *BioResources*, 10(4), 2015.
- [110] P. Debiagi, G. Gentile, A. Cuoci, A. Frassoldati, E. Ranzi, and T. Faravelli. A

- predictive model of biochar formation and characterization. *Journal of Analytical and Applied Pyrolysis*, 134(June):326–335, 2018.
- [111] T. Faravelli, A. Frassoldati, G. Migliavacca, and E. Ranzi. Detailed kinetic modeling of the thermal degradation of lignins. *Biomass and Bioenergy*, 34(3):290–301, 2010.
- [112] E Ranzi, A Frassoldati, R Grana, A Cuoci, T Faravelli, A P Kelley, and C K Law. Hierarchical and comparative kinetic modeling of laminar flame speeds of hydrocarbon and oxygenated fuels. *Progress in Energy and Combustion Science*, 38(4):468–501, 2012.
- [113] Andrés Anca-Couce, Nico Zobel, and Hugo Atle Jakobsen. Multi-scale modeling of fixed-bed thermo-chemical processes of biomass with the representative particle model: Application to pyrolysis. *Fuel*, 103:773–782, 2013.
- [114] Andrea Teresa Espinoza Pérez, Mauricio Camargo, Paulo César Narváez Rincón, and Miguel Alfaro Marchant. Key challenges and requirements for sustainable and industrialized biorefinery supply chain design and management: A bibliographic analysis. *Renewable and Sustainable Energy Reviews*, 69(November 2016):350–359, 2017.
- [115] Jin Sun Cha, Sung Hoon Park, Sang Chul Jung, Changkook Ryu, Jong Ki Jeon, Min Chul Shin, and Young Kwon Park. Production and utilization of biochar: A review. *Journal of Industrial and Engineering Chemistry*, 40:1–15, 2016.
- [116] Peter McKendry. Energy production from biomass (Part 1): Overview of biomass. *Bioresource technology*, 83(1):37–46, 2002.
- [117] Yury Maksimuk, Zoya Antonava, Vladimir Krouk, Alina Korsakova, and Vera Kursevich. Prediction of higher heating value (HHV) based on the structural composition for biomass. *Fuel*, 299(December 2020):120860, 2021.
- [118] Ayhan Demirbaş. Calculation of higher heating values of biomass fuels. *Fuel*, 76(5):431–434, 1997.
- [119] Marjorie R. Rover, Alvina Aui, Mark Mba Wright, Ryan G. Smith, and Robert C. Brown. Production and purification of crystallized levoglucosan

- from pyrolysis of lignocellulosic biomass. *Green Chemistry*, 21(21):5980–5989, 2019.
- [120] Tony Bridgwater. Biomass Pyrolysis. (October), 2010.
- [121] Yoichi Kodera and Mamoru Kaiho. Model Calculation of Heat Balance of Wood Pyrolysis. *Journal of the Japan Institute of Energy*, 95(10):881–889, 2016.
- [122] Jaakko Karvonen, Janni Kunttu, Tommi Suominen, Jyrki Kangas, Pekka Leskinen, and Jáchym Judl. Integrating fast pyrolysis reactor with combined heat and power plant improves environmental and energy efficiency in bio-oil production. *Journal of Cleaner Production*, 183:143–152, 2018.
- [123] Netherlands Organisation for Applied Scientific Research. cellulose (#2741), 2004.
- [124] Maximilian B. Gorensen, Rajasi Shukre, and Chau Chyun Chen. Development of a Thermophysical Properties Model for Flowsheet Simulation of Biomass Pyrolysis Processes. *ACS Sustainable Chemistry and Engineering*, 7(9):9017–9027, 2019.
- [125] Angelique T. Conag, Jaye Earl R. Villahermosa, Luis K. Cabatingan, and Alchris W. Go. Energy densification of sugarcane leaves through torrefaction under minimized oxidative atmosphere. *Energy for Sustainable Development*, 42:160–169, 2018.
- [126] Xin Jiat Lee, Lai Yee Lee, Suyin Gan, Suchithra Thangalazhy-Gopakumar, and Hoon Kiat Ng. Biochar potential evaluation of palm oil wastes through slow pyrolysis: Thermochemical characterization and pyrolytic kinetic studies. *Bioresource Technology*, 236:155–163, 2017.
- [127] Colomba Di Blasi. Modeling chemical and physical processes of wood and biomass pyrolysis. *Progress in Energy and Combustion Science*, 34(1):47–90, 2008.
- [128] Homer E. Kissinger. Reaction Kinetics in Differential Thermal Analysis. *Analytical Chemistry*, 29(11):1702–1706, 1957.

- [129] Franz Richter and Guillermo Rein. The Role of Heat Transfer Limitations in Polymer Pyrolysis at the Microscale. *Frontiers in Mechanical Engineering*, 4(November):1–13, 2018.
- [130] A. M.C. Janse, R. W.J. Westerhout, and W. Prins. Modelling of flash pyrolysis of a single wood particle. *Chemical Engineering and Processing: Process Intensification*, 39(3):239–252, 2000.
- [131] Anna Trendewicz, Robert Braun, Abhijit Dutta, and Jack Ziegler. One dimensional steady-state circulating fluidized-bed reactor model for biomass fast pyrolysis. *Fuel*, 133:253–262, 2014.
- [132] Fabio Codignole Luz, Stefano Cordiner, Alessandro Manni, Vincenzo Mulone, and Vittorio Rocco. Pyrolysis in screw reactors: A 1-D numerical tool. *Energy Procedia*, 126:683–689, 2017.
- [133] Hyungseok Nam, Sergio C. Capareda, Nanjappa Ashwath, and Jinjuta Kongkasawan. Experimental investigation of pyrolysis of rice straw using bench-scale auger, batch and fluidized bed reactors. *Energy*, 93:2384–2394, 2015.
- [134] Fabio Codignole Luz, Stefano Cordiner, Alessandro Manni, Vincenzo Mulone, and Vittorio Rocco. Biomass fast pyrolysis in a shaftless screw reactor : A 1-D numerical model. *Energy*, 157:792–805, 2018.
- [135] Matthaus U. Babler, Aekjuthon Phounglamcheik, Marko Amovic, Rolf Ljunggren, and Klas Engvall. Modeling and pilot plant runs of slow biomass pyrolysis in a rotary kiln. *Applied Energy*, 207:123–133, 2017.
- [136] Won Chan Park, Arvind Atreya, and Howard R. Baum. Experimental and theoretical investigation of heat and mass transfer processes during wood pyrolysis. *Combustion and Flame*, 157(3):481–494, 2010.
- [137] R. W. Nachenius, T. A. Van De Wardt, F. Ronsse, and W. Prins. Residence time distributions of coarse biomass particles in a screw conveyor reactor. *Fuel Processing Technology*, 130(C):87–95, 2015.

- [138] Shui Qing Li, L. B. Ma, W. Wan, and Q. Yao. A mathematical model of heat transfer in a rotary kiln thermo-reactor. *Chemical Engineering and Technology*, 28(12):1480–1489, 2005.
- [139] M. Brennan Pecha, Jorge Ivan Montoya Arbelaez, Manuel Garcia-Perez, Farid Chejne, and Peter N. Ciesielski. *Progress in understanding the four dominant intra-particle phenomena of lignocellulose pyrolysis: Chemical reactions, heat transfer, mass transfer, and phase change*, volume 21. Royal Society of Chemistry, 2019.
- [140] Alex D Paulsen, Matthew S Mettler, and Paul J Dauenhauer. The Role of Sample Dimension and Temperature in Cellulose Pyrolysis. 2013.
- [141] Colomba Di Blasi. Numerical simulation of cellulose pyrolysis. *Biomass and Bioenergy*, 7(1-6):87–98, 1994.
- [142] R. S. Miller and J. Bellan. A generalized biomass pyrolysis model based on superimposed cellulose, hemicellulose and lignin kinetics. *Combustion Science and Technology*, 126(1-6):97–137, 1997.
- [143] Colomba Di Blasi. Multi-phase moisture transfer in the high-temperature drying of wood particles. *Chemical Engineering Science*, 53(2):353–366, 1998.
- [144] John F. Siau. *Transport processes in wood*. Number 0. Springer, New York, 1984.
- [145] E Donegan, G Sola, Z Cheng, L Birigazzi, J.G.P Gamarra, M Henry, G Vieilledent, and T Chiti. GlobAllomeTree’s wood density database. Technical Report OCTOBER, CIRAD, UNITUS, FAO, Rome, 2014.
- [146] Xiyan Li and Chungen Yin. A drying model for thermally large biomass particle pyrolysis. *Energy Procedia*, 158:1294–1302, 2019.
- [147] Gabriele A. Nagata, Thiago V. Costa, Maisa T.B. Perazzini, and Hugo Perazzini. Coupled heat and mass transfer modelling in convective drying of biomass at particle-level: Model validation with experimental data. *Renewable Energy*, 149:1290–1299, 2020.

- [148] Colomba Di Blasi, Carmen Branca, Silvio Sparano, and Barbara La Mantia. Drying characteristics of wood cylinders for conditions pertinent to fixed-bed countercurrent gasification. *Biomass and Bioenergy*, 25(1):45–58, 2003.
- [149] Bertil Fredlund. Modelling of heat and mass transfer in wood structures during fire. *Fire Safety Journal*, 20(1):39–69, 1993.
- [150] Jaakko Saastamoinen and Jean-Robert Richard. Simultaneous drying and pyrolysis of solid fuel particles. *Fuel and Energy Abstracts*, 37(6):450, 1996.
- [151] David Humbird, Anna Trendewicz, Robert Braun, and Abhijit Dutta. One-Dimensional Biomass Fast Pyrolysis Model with Reaction Kinetics Integrated in an Aspen Plus Biorefinery Process Model. *ACS Sustainable Chemistry and Engineering*, 5(3):2463–2470, 2017.
- [152] Guillaume Gauthier, Thierry Melkior, Sylvain Salvador, Michele Corbetta, Alessio Frassoldati, Sauro Pierucci, Eliseo Ranzi, Hayat Bennadji, and Elizabeth M Fisher. Pyrolysis of Thick Biomass Particles : Experimental and Kinetic Modelling. In *ICHEAP-11 - 11th International Conference on Chemical Process Engineering*, pages 601–606, Milan, 2013.
- [153] Helena Pereira. The chemical composition of cork. In Helena Pereira, editor, *Cork*, chapter 3, pages 55–99. Elsevier Science, 2007.
- [154] F. Mermoud, F. Golfier, S. Salvador, L. Van De Steene, and J. L. Dirion. Experimental and numerical study of steam gasification of a single charcoal particle. *Combustion and Flame*, 145(1-2):59–79, 2006.
- [155] Edward N. Fuller, Paul D. Schettler, and J. Calvin Giddings. A new method for prediction of binary gas-phase diffusion coefficients. *Industrial and Engineering Chemistry*, 58(5):18–27, 1966.
- [156] Bruce Poling, John Prausnitz, and John O’Connell. *The Properties of Gases and Liquids*, volume 12. McGraw-Hill, New York, 5 edition, 2001.
- [157] Changquan Sun. True density of microcrystalline cellulose. *Journal of Pharmaceutical Sciences*, 94(10):2132–2134, 2005.

- [158] Abhishek Sharma, Vishnu Pareek, and Dongke Zhang. Biomass pyrolysis - A review of modelling, process parameters and catalytic studies. *Renewable and Sustainable Energy Reviews*, 50:1081–1096, 2015.
- [159] Madhumita Patel, Adetoyese Olajire Oyedun, Amit Kumar, and Rajender Gupta. What is the production cost of renewable diesel from woody biomass and agricultural residue based on experimentation? A comparative assessment. *Fuel Processing Technology*, 191(April):79–92, 2019.
- [160] Merck KGaA. Biochemicals, 2019.
- [161] Stephanie Redl, Sumesh Sukumara, Tom Ploeger, Liang Wu, Torbjørn Ølshøj Jensen, Alex Toftgaard Nielsen, and Henk Noorman. Thermodynamics and economic feasibility of acetone production from syngas using the thermophilic production host *Moarella thermoacetica*. *Biotechnology for Biofuels*, 10(1):1–17, 2017.
- [162] ONS. Quarterly Energy prices: December 2019. Technical report, The Office for National Statistics. Department for Business, Energy & Industrial Strategy, 2019.
- [163] Paraskevi Karka, Stavros Papadokonstantakis, Konrad Hungerbühler, and Antonis Kokossis. *Environmental impact assessment of biorefinery products using life cycle analysis*, volume 34. Elsevier, 2014.
- [164] John A. Posada, Akshay D. Patel, Alexander Roes, Kornelis Blok, André P.C. Faaij, and Martin K. Patel. Potential of bioethanol as a chemical building block for biorefineries: Preliminary sustainability assessment of 12 bioethanol-based products. *Bioresource Technology*, 135:490–499, 2013.
- [165] H. H. Khoo, W. L. Ee, and Valerio Isoni. Bio-chemicals from lignocellulose feedstock: Sustainability, LCA and the green conundrum. *Green Chemistry*, 18(7):1912–1922, 2016.
- [166] Sara Rajabi Hamedani, Mauro Villarini, Andrea Colantoni, Michele Moretti, and Enrico Bocci. Life cycle performance of hydrogen production via agro-industrial residue gasification-a small scale power plant study. *Energies*, 11(3), 2018.

- [167] Hanna Karlsson, Serina Ahlgren, Mats Sandgren, Volkmar Passoth, Ola Wallberg, and Per Anders Hansson. Greenhouse gas performance of biochemical biodiesel production from straw: Soil organic carbon changes and time-dependent climate impact. *Biotechnology for Biofuels*, 10(1):1–15, 2017.
- [168] Raili Kajaste, Markku Hurme, and Pekka Oinas. Methanol-Managing greenhouse gas emissions in the production chain by optimizing the resource base. *Aims Energy*, 6(December):1074–1102, 2018.
- [169] Juan D. Medrano-García, Rubén Ruiz-Femenia, and José A. Caballero. *Multi-objective Optimization of a Carbon Dioxide Utilization Superstructure for the Synthesis of Formic and Acetic Acid*, volume 43. Elsevier Masson SAS, 2018.
- [170] Ji Lu Zheng, Ya Hong Zhu, Ming Qiang Zhu, Guo Tao Sun, and Run Cang Sun. Life-cycle assessment and techno-economic analysis of the utilization of bio-oil components for the production of three chemicals. *Green Chemistry*, 20(14):3287–3301, 2018.
- [171] Philip Steele, Maureen E. Puettmann, Venkata Kanthi Penmetsa, and Jerome E. Cooper. Life-cycle assessment of pyrolysis bio-oil production. *Forest Products Journal*, 62(4):326–334, 2012.
- [172] Gábor Várhegyi. Aims and methods in non-isothermal reaction kinetics. *Journal of Analytical and Applied Pyrolysis*, 79(1-2 SPEC. ISS.):278–288, 2007.
- [173] J. Zsakó. Kinetic analysis of thermogravimetric data: XXIX. Remarks on the ‘many curves’ methods. *Journal of Thermal Analysis*, 46(6):1845–1864, 1996.
- [174] Marisa A. Lima, Leonardo D. Gomez, Clare G. Steele-King, Rachael Simister, Oigres D. Bernardinelli, Marcelo A. Carvalho, Camila A. Rezende, Carlos A. Labate, Eduardo R. Deazevedo, Simon J. McQueen-Mason, and Igor Polikarpov. Evaluating the composition and processing potential of novel sources of Brazilian biomass for sustainable biorenewables production. *Biotechnology for Biofuels*, 7(1):1–19, 2014.
- [175] Michael Jerry Antal, Gábor Várhegyi, and Emma Jakab. Cellulose Pyrolysis Kinetics: Revisited. *Industrial and Engineering Chemistry Research*, 37(4):1267–1275, 1998.

- [176] Gao Ningbo, Liu Baoling, Li Aimin, and Li Juanjuan. Continuous pyrolysis of pine sawdust at different pyrolysis temperatures and solid residence times. *Journal of Analytical and Applied Pyrolysis*, 114:155–162, 2015.
- [177] Junmeng Cai, Weixuan Wu, Ronghou Liu, and George W. Huber. A distributed activation energy model for the pyrolysis of lignocellulosic biomass. *Green Chemistry*, 15(5):1331–1340, 2013.
- [178] J. Bensch, J. and J. Brynard, H. New Approach to Density Measurements using Archimedes' Principle. *Nature Physical Science*, 239(9):96, 1972.
- [179] Abhisek Sahoo, Sachin Kumar, and Kaustubha Mohanty. A comprehensive characterization of non-edible lignocellulosic biomass to elucidate their biofuel production potential. *Biomass Conversion and Biorefinery*, 12(11):5087–5103, 2022.
- [180] Ayokunle O. Balogun, Adekunle A. Adeleke, Peter P. Ikubanni, Samuel O. Adegoke, Abdulbaset M. Alayat, and Armando G. McDonald. Kinetics modeling, thermodynamics and thermal performance assessments of pyrolytic decomposition of *Moringa oleifera* husk and *Delonix regia* pod. *Scientific Reports*, 11(1):1–12, 2021.
- [181] Joel Falk, Robert J. Berry, Markus Broström, and Sylvia H. Larsson. Mass flow and variability in screw feeding of biomass powders - Relations to particle and bulk properties. *Powder Technology*, 276:80–88, 2015.
- [182] H. P. S. Abdul Khalil, M. Siti Alwani, and A. K. Mohd Omar. Chemical composition, anatomy, lignin distribution, and cell wall structure of Malaysian plant waste fibers. *BioResources*, 1(2):220–232, 2006.
- [183] C. Scarlata J. Sluiter A. Sluiter, R. Ruiz, , and D. Templeton. Determination of Extractives in Biomass: Laboratory Analytical Procedure (LAP). Technical Report January, National Renewable Energy Laboratory, Colorado, 2005.
- [184] F. A Agblevor, B.R Hames, D Schell, and H. L Chum. Analysis of Biomass Sugars Using a Novel HPLC Method. *Applied Biochemistry and Biotechnology*, 136(1):309–326, 2007.

- [185] Amie Sluiter, Bonnie Hames, Raymond Ruiz, Christian Scarlata, Justin Sluiter, David Templeton, and D. Crocker. Determination of Structural Carbohydrates and Lignin in Biomass. Technical Report April 2008, National Renewable Energy Laboratory, Colorado, 2004.
- [186] A Sluiter, R Ruiz, C Scarlata, J Sluiter, and D Templeton. Determination of Extractives in Biomass: Laboratory Analytical Procedure (LAP); Issue Date 7/17/2005 - 42619.pdf. Technical Report January, National Renewable Energy Laboratory, Colorado, 2008.
- [187] M. Hazwan Hussin, Afidah Abdul Rahim, Mohamad Nasir Mohamad Ibrahim, and Nicolas Brosse. Physicochemical characterization of alkaline and ethanol organosolv lignins from oil palm (*Elaeis guineensis*) fronds as phenol substitutes for green material applications. *Industrial Crops and Products*, 49:23–32, 2013.
- [188] Stylianos D. Stefanidis, Konstantinos G. Kalogiannis, Eleni F. Iliopoulou, Chrysoula M. Michailof, Petros A. Pilavachi, and Angelos A. Lappas. A study of lignocellulosic biomass pyrolysis via the pyrolysis of cellulose, hemicellulose and lignin. *Journal of Analytical and Applied Pyrolysis*, 105:143–150, 2014.
- [189] Elém Patrícia Alves Rocha, Ekaterina Sermyagina, Esa Vakkilainen, Jorge Luiz Colodette, Idalmo Montenegro de Oliveira, and Marcelo Cardoso. Kinetics of pyrolysis of some biomasses widely available in Brazil. *Journal of Thermal Analysis and Calorimetry*, 130(3):1445–1454, 2017.
- [190] H. Hidayat, E. R.P. Keijser, U. Prijanto, J. E.G. Van Dam, and H. J. Heeres. Preparation and properties of binderless boards from *Jatropha curcas* L. seed cake. *Industrial Crops and Products*, 52:245–254, 2014.
- [191] Sergey Vyazovkin, Alan K. Burnham, José M. Criado, Luis A. Pérez-Maqueda, Crisan Popescu, and Nicolas Sbirrazzuoli. ICTAC Kinetics Committee recommendations for performing kinetic computations on thermal analysis data. *Thermochimica Acta*, 520(1-2):1–19, 2011.

- [192] C. D Doyle. Kinetic Analysis of Thermogravimetric Data. *Journal of Applied Polymer Science*, V(15):285–292, 1961.
- [193] Ingwald Obernberger and Gerold Thek. Physical characterisation and chemical composition of densified biomass fuels with regard to their combustion behaviour. *Biomass and Bioenergy*, 27(6):653–669, 2004.
- [194] Sadegh Papari and Kelly Hawboldt. A review on the pyrolysis of woody biomass to bio-oil: Focus on kinetic models. *Renewable and Sustainable Energy Reviews*, 52:1580–1595, 2015.
- [195] A. V. Bridgwater. Renewable fuels and chemicals by thermal processing of biomass. *Chemical Engineering Journal*, 91(2-3):87–102, 2003.
- [196] Jinje Park, Yongwoon Lee, Changkook Ryu, and Young Kwon Park. Slow pyrolysis of rice straw: Analysis of products properties, carbon and energy yields. *Bioresource Technology*, 155:63–70, 2014.
- [197] Paulo Eduardo Amaral Debiagi, Chiara Pecchi, Giancarlo Gentile, Alessio Frassoldati, Alberto Cuoci, Tiziano Faravelli, and Eliseo Ranzi. Extractives Extend the Applicability of Multistep Kinetic Scheme of Biomass Pyrolysis. *Energy and Fuels*, 29(10):6544–6555, 2015.
- [198] Oihana Gordobil, Rosana Moriana, Liming Zhang, Jalel Labidi, and Olena Sevastyanova. Assesment of technical lignins for uses in biofuels and biomaterials: Structure-related properties, proximate analysis and chemical modification. *Industrial Crops and Products*, 83:155–165, 2016.
- [199] J Reyes-Rivera and T Terrazas. Methods and Protocols. In Miguel de Lucas and J. Peter Etchhells, editors, *Xylem: Methods and Protocols*, chapter Ligin Anal, pages 193–211. Springer New York, New York, 2017.
- [200] Silawan Sangthong, Worasak Phetwarotai, Muhammad Saifullah Abu Bakar, Benjamas Cheirsilp, and Neeranuch Phusunti. Phenol-rich bio-oil from pyrolysis of palm kernel shell and its isolated lignin. *Industrial Crops and Products*, 188(September):0–1, 2022.

- [201] Masoud Asadieraghi and Wan Mohd Ashri Wan Daud. In-depth investigation on thermochemical characteristics of palm oil biomasses as potential biofuel sources. *Journal of Analytical and Applied Pyrolysis*, 115:379–391, 2015.
- [202] Zhengjun Shi, Gaofeng Xu, Jia Deng, Mengyao Dong, Vignesh Murugadoss, Chuntao Liu, Qian Shao, Shide Wu, and Zhanhu Guo. Structural characterization of lignin from *D. sinicus* by FTIR and NMR techniques. *Green Chemistry Letters and Reviews*, 12(3):235–243, 2019.
- [203] Gloria Marrugo, Carlos F. Valdés, and Farid Chejne. Characterization of Colombian Agroindustrial Biomass Residues as Energy Resources. *Energy and Fuels*, 30(10):8386–8398, 2016.
- [204] Sergey Vyazovkin, Konstantinos Chrissafis, Maria Laura Di Lorenzo, Nobuyoshi Koga, Michèle Pijolat, Bertrand Roduit, Nicolas Sbirrazzuoli, and Joan Josep Suñol. ICTAC Kinetics Committee recommendations for collecting experimental thermal analysis data for kinetic computations. *Thermochimica Acta*, 590:1–23, 2014.
- [205] Anabel Fernandez, Leandro Rodriguez-Ortiz, Daniela Asensio, Rosa Rodriguez, and Germán Mazza. Kinetic analysis and thermodynamics properties of air/steam gasification of agricultural waste. *Journal of Environmental Chemical Engineering*, 8(4):103829, 2020.
- [206] Paulo Eduardo Amaral Debiagi, Giancarlo Gentile, Matteo Pelucchi, Alessio Frassoldati, Alberto Cuoci, Tiziano Faravelli, and Eliseo Ranzi. Detailed kinetic mechanism of gas-phase reactions of volatiles released from biomass pyrolysis. *Biomass and Bioenergy*, 93:60–71, 2016.
- [207] Karishma Gobin and George Manos. Thermogravimetric study of polymer catalytic degradation over microporous materials. *Polymer degradation and stability*, 86:225–231, 2004.
- [208] Zhongqing Ma, Dengyu Chen, Jie Gu, Binfu Bao, and Qisheng Zhang. Determination of pyrolysis characteristics and kinetics of palm kernel shell using TGA – FTIR and model-free integral methods. *Energy Conversion and Management*, 89:251–259, 2015.

- [209] M. Jeguirim, J. Bikai, Y. Elmay, L. Limousy, and E. Njeugna. Thermal characterization and pyrolysis kinetics of tropical biomass feedstocks for energy recovery. *Energy for Sustainable Development*, 23:188–193, 2014.
- [210] J. Thiagarajan, P. K. Srividhya, and P. Balasubramanian. Thermal behavior and pyrolytic kinetics of palm kernel shells and Indian lignite coal at various blending ratios. *Bioresource Technology Reports*, 4(September):88–95, 2018.
- [211] Dheeraj Minglani, Abhishek Sharma, Harsh Pandey, Ram Dayal, Jyeshtaraj B. Joshi, and Shankar Subramaniam. A review of granular flow in screw feeders and conveyors. *Powder Technology*, 366:369–381, 2020.
- [212] Thomas Forgber, Bhageshvar Mohan, Christoph Kloss, and Stefan Radl. Heat transfer rates in sheared beds of inertial particles at high Biot numbers. *Granular Matter*, 19(1):1–23, 2017.
- [213] Sebastian Romuli, Shkelqim Karaj, and Joachim Müller. Discrete element method simulation of the hulling process of *Jatropha curcas* L. fruits. *Biosystems Engineering*, 155:55–67, 2017.
- [214] D.K. Garnayak, R.C. Pradhan, S.N. Naik, and N. Bhatnagar. Moisture-dependent physical properties of jatropha seed (*Jatropha curcas* L.). *Industrial Crops and Products*, 27(1):123–129, jan 2008.
- [215] Daniel Schiochet Nasato, Christoph Goniva, Stefan Pirker, and Christoph Kloss. Coarse graining for large-scale DEM simulations of particle flow - An investigation on contact and cohesion models. *Procedia Engineering*, 102:1484–1490, 2015.
- [216] M Mousaviraad, M Tekeste, and K A Rosentrater. Calibration and validation of a discrete element model of corn using grain flow simulation in a commercial screw grain auger. In *Transactions of the ASABE*, volume 60, pages 1403–1415, 2017.
- [217] Chawannat Jaroenkhaseemmeesuk and Nakorn Tippayawong. *Technical and Economic Analysis of A Biomass Pyrolysis Plant*, volume 79. Elsevier B.V., 2015.

- [218] Polychronis Spanoudakis, Evangelos Christen, and Nikolaos C. Tsourveloudis. Design and Structural Anlysys of a Front Single-Sided Swingram for an Electric Three-Wheel Motorcycle. In Marek Krawczuk and Magdalena Palacz, editors, *Applications of finite element modeling for mechanical and mechatronic systems*, volume 11, pages 59–75. MDPI, Basel, 2021.
- [219] Michael Rackl and Kevin J. Hanley. A methodical calibration procedure for discrete element models. *Powder Technology*, 307:73–83, 2017.
- [220] R. W. Nachenius, T. A. Van De Wardt, F. Ronsse, and W. Prins. Residence time distributions of coarse biomass particles in a screw conveyor reactor. *Fuel Processing Technology*, 130(C):87–95, 2015.
- [221] Q. F. Hou, K. J. Dong, and A. B. Yu. DEM study of the flow of cohesive particles in a screw feeder. *Powder Technology*, 256:529–539, 2014.
- [222] Lukas von Berg, Andrés Anca-Couce, Christoph Hochenauer, and Robert Scharler. Multi-scale modelling of fluidized bed biomass gasification using a 1D particle model coupled to CFD. *Fuel*, 324(May):124677, 2022.
- [223] C. M. Wensrich and A. Katterfeld. Rolling friction as a technique for modelling particle shape in DEM. *Powder Technology*, 217:409–417, 2012.
- [224] A. O. Raji and J. F. Favier. Model for the deformation in agricultural and food particulate materials under bulk compressive loading using discrete element method. II: Compression of oilseeds. *Journal of Food Engineering*, 64(3):373–380, 2004.
- [225] Sayed M. Derakhshani, Dingena L. Schott, and Gabriel Lodewijks. Reducing computation time of dem simulations of fine granular materials. *Bulk Solids Handling*, 33(6):52–56, 2013.
- [226] Fenglei Qi and Mark Mba Wright. A DEM modeling of biomass fast pyrolysis in a double auger reactor. *International Journal of Heat and Mass Transfer*, 150:119308, 2020.

- [227] Xiaogang Shi, Frederik Ronsse, Jelle Roegiers, and Jan G. Pieters. 3D Eulerian-Eulerian modeling of a screw reactor for biomass thermochemical conversion. Part 1: Solids flow dynamics and back-mixing. *Renewable Energy*, 143(2019):1465–1476, 2019.
- [228] Sayed M. Derakhshani, Dingena L. Schott, and Gabriel Lodewijks. Reducing computation time of dem simulations of fine granular materials. *Bulk Solids Handling*, 33(6):52–56, 2013.
- [229] Andres Chico-Proano, Michelle Romero, A. Narváez C. Ricardo, Boris G. German, Daniel Rivadeneira, George Manos, Lazaros G. Papageorgiou, and Eric S. Fraga. Combined particle model and experimental approach for predicting pyrolysis with palm kernel shells. *Computer Aided Chemical Engineering*, 51:343–348, 2022.
- [230] Paulo Ricardo Schizaki dos Santos, Fernando A. Pedersen Voll, Luiz Pereira Ramos, and Marcos L. Corazza. Esterification of fatty acids with supercritical ethanol in a continuous tubular reactor. *Journal of Supercritical Fluids*, 126:25–36, 2017.
- [231] Kamil Kwiatkowski, Konrad Bajer, Agnieszka Celińska, Marek Dudyński, Jakub Korotko, and Marta Sosnowska. Pyrolysis and gasification of a thermally thick wood particle - Effect of fragmentation. *Fuel*, 132:125–134, 2014.
- [232] John F. Siau. *Transport processes in wood*. Number 0. Springer, New York, 1984.
- [233] Colomba Di Blasi. Multi-phase moisture transfer in the high-temperature drying of wood particles. *Chemical Engineering Science*, 53(2):353–366, 1998.
- [234] Nasser Ayoub, Elsayed Elmoshi, Hiroya Seki, and Yuji Naka. Evolutionary algorithms approach for integrated bioenergy supply chains optimization. *Energy Conversion and Management*, 50(12):2944–2955, 2009.
- [235] Dajun Yue, Maxim Slivinsky, Jason Sumpter, and Fengqi You. Sustainable design and operation of cellulosic bioelectricity supply chain networks with life cycle economic, environmental, and social optimization. *Industrial and Engineering Chemistry Research*, 53(10):4008–4029, 2014.

- [236] Shurong Wang and Zhongyang Luo. Pyrolysis of biomass. *Pyrolysis of Biomass*, 1:1–255, 2017.
- [237] Themis Matsoukas. *Fundamentals of Chemical Engineering Thermodynamics*. Prentice Hall, Crawfordsville, 3 edition, 2016.
- [238] Sidney W. Benson and Jerry H. Buss. Additivity rules for the estimation of molecular properties. Thermodynamic properties. *The Journal of Chemical Physics*, 29(3):546–572, 1958.
- [239] Eric M. Suuberg, Ivan Milosavljevic, and Vahur Oja. Two-regime global kinetics of cellulose pyrolysis: The role of tar evaporation. *Symposium (International) on Combustion*, 26(1):1515–1521, 1996.
- [240] O. Boutin, M. Ferrer, and J. Lédé. Radiant flash pyrolysis of cellulose - Evidence for the formation of short life time intermediate liquid species. *Journal of Analytical and Applied Pyrolysis*, 47(1):13–31, 1998.
- [241] Olga Dorofeeva, Vladimir P. Novikov, and David B. Neumann. NIST-JANAF thermochemical tables. I. Ten organic molecules related to atmospheric chemistry. *Journal of Physical and Chemical Reference Data*, 30(2):475–509, 2001.
- [242] Jing Chao, Kenneth R. Hall, Kenneth N. Marsh, and Randolph C. Wilhoit. Thermodynamic Properties of Key Organic Oxygen Compounds in the Carbon Range C1 to C4. Part 2. Ideal Gas Properties. *Journal of Physical and Chemical Reference Data*, 15(4):1369–1436, 1986.
- [243] Malcom Chase. JANAF-NIST Thermochemical Tables Part I, Al-Co. Technical report, American Institute of Physics and the American Chemical Society, New York, 1998.
- [244] Gennady J. Kabo, Yauheni U. Paulechka, Olga V. Voitkevich, Andrey V. Blokhin, Elena N. Stepurko, Sviataslau V. Kohut, and Yakov V. Voznyi. Experimental and theoretical study of thermodynamic properties of levoglucosan. *Journal of Chemical Thermodynamics*, 85:101–110, 2015.